Investigating Photonic Quantum Computation

by

Casey Robert Myers

A thesis
presented to the University of Waterloo
in fulfilment of the
thesis requirement for the degree of
Doctor of Philosophy
in
Physics

Waterloo, Ontario, Canada, 2007

Author's declaration

I hereby declare that I am the sole author of this thesis. This is a true copy of the thesis, including any required final revisions, as accepted by my examiners.

Casey R. Myers

I understand that my thesis may be made electronically available to the public.

Casey R. Myers

Abstract

The use of photons as qubits is a promising implementation for quantum computation. The inability of photons to interact, especially with the environment, makes them an ideal physical candidate. However, this also makes them a difficult system to perform two qubit gates on. Recent breakthroughs in photonic quantum computing have shown methods around the requirement of direct photon-photon interaction. In this thesis we study three recently discovered schemes for optical quantum computation.

We first investigate the so called linear optical quantum computing (LOQC) scheme, exploring a method to improve the original proposal by constructing a photon-number QND detector that succeeds with a high probability. In doing this we present a new type of LOQC teleporter, one that can detect the presence of a single photon in an arbitrary polarisation state when the input state is a sum of vacuum and multi-photon terms. This new type of teleporter is an improvement on the original scheme in that the entangled states required can be made offline with fewer entangling operations.

We next investigate the so called quantum bus (qubus) scheme for photonic quantum computing. We show a scheme to measure the party of n qubit states by using a single qubus mode, controlled rotations and displacements. This allows for the syndrome measurements of any stabilizer quantum error correcting code. We extend these results to a fault tolerant scheme to measure an arbitrary Pauli operator of weight n, incorporating so called single bit teleportations. We investigate the construction of a Toffoli gate by using a single qubus mode, controlled rotations and displacements that works with a success probability of at least 25%. We also investigate the use of single bit teleportations to construct a universal set of gates on coherent state type logic and in the construction of cluster states.

We finally investigate the optical Zeno gate, a gate that uses the Zeno effect in the form of two photon absorbers to induce a CSIGN. We model realistic two photon absorption and include realistic single photon loss for this gate, examining the use of encoding to overcome the single photon loss, showing that our results are competitive with the leading equivalent LOQC scheme.

Acknowledgements

It has been a long and arduous journey and many people have helped and encouraged me along the way. I would first like to thank my supervisor Raymond Laflamme for his support during my time here at Waterloo. I would like to acknowledge financial support from the Mike and Ophelia Lazaridis Fellowship and I would like to thank Elaine Garner from the University of Waterloo graduate office for arranging the Millennium Graduate Student Bursary during my last months at Waterloo. I would like to thank Andrew White for reminding me that all hope was not lost. I would like to thank Jon Dowling, Alexei Gilchrist and Bill Munro for their help and guidance. I would also like to thank Bill Munro for his ongoing encouragement. I would like to thank Tim Ralph, Gerard Milburn, Andrew White, Pieter Kok, Pavel Lougovski, Hwang Lee, Federico Spedalieri, Paul Cochrane, Aggie Branczyk, Sebastian Louis, Rod van Meter, Peter van Loock, Norbert Lütkenhaus, Kevin Resch, Gregor Weihs, Kae Nemoto and Marcus Silva for useful interactions and discussions during the course of my Ph.D. And I would like to thank Kae Nemoto for giving me a job. I would like to thank my fellow graduate students at the IQC for their support and for putting up with me. These include Jean Christian Boileau, Martin Laforest, Chris Erven, Tim Reid, Jamie Batuwantudawe, Osama Moussa, Lana Sheridan, David Poulin and Marcus Silva. I would especially like to thank Jean Christian Boileau, Martin Laforest, Chris Erven and Marcus Silva for their hospitality. I would like to thank Mauricio Ibarra, Silvia Ibarra and Bertha Morales for their help. I would like to thank my mates Nicholas Whitlock, Michael Bremner, Lucas Kulawik, Paul Tobin, Mark Lombardo and Kevin Sookhee for their friendship throughout the years. I would like to thank my sister Jayde and Mum Judith for their support throughout my Ph.D. And I would like to conclude by thanking Maria for her love, support, patience and understanding.

Contents

List of Figures

List of Tables

Chapter 1

Introduction

The use of quantum systems for computation was first proposed by Benioff in [1] and Feynman in [2] and further developed in [3, 4, 5, 6, 7, 8, 9, 10]. Recently, quantum information processing (QIP) has taken off as a research area. QIP promises to solve some problems that have no known efficient classical algorithms. For example, Shor has shown in [11] that a quantum computer could factor a number that is the product of two prime numbers exponentially faster than any known classical algorithm. In [12, 13] Grover showed a quantum search algorithm that could search an unsorted list quadraticly faster than any known classical algorithm. QIP also offers the possibility of simulating other quantum systems efficiently [2, 14, 15], a task with no known efficient classical equivalent.

Before any quantum system can be used for QIP, a full analysis of the propagation of errors in the system must be made and a method to recover from these errors within an acceptable corruption threshold found. This entails encoding the quantum data with quantum error correction (QEC) codes [16, 17, 18, 19, 20] and leads to a theory of fault tolerance for QIP [21, 22, 23, 24, 25, 26].

Before such a sophisticated theory can be implemented on a physical system, a basic quantum system must first be found. The question of which physical system is best suited to perform scalable quantum computations is still very much open. For a physical system to be a suitable candidate for scalable QIP, the following set of five criteria must be first be met [27] :

1. The physical system must have well characterised qubits.
2. We must have the ability to initialise the state of the qubits to a simple fiducial state, such as $|000\ldots\rangle$.
3. A “universal” set of quantum gates such as generic one qubit gates and a two qubit gate must be implementable.
4. The physical system must have a qubit-specific measurement capability.

5. The physical qubits must have long relevant decoherence times, much longer than the gate operation time.

One of the earliest proposals for the physical implementation of a quantum computer involved using a strong cross Kerr non-linearity to facilitate photon interaction [28, 29]. From this a CNOT gate could be constructed [30], a gate when combined with arbitrary single qubit rotations is universal for quantum computation, provided the size of the non-linearity was on the order of π. The size of this non-linearity is the key reason why this scheme is unrealistic, as it is many orders of magnitude greater than what can currently be made. Even with the advancement of experimental ingenuity, it is unlikely that we will see such a large cross Kerr non-linearity in the foreseeable future.

The fact that photons do no interact directly is the major obstacle for using single photons for QIP. Without a direct interaction, two qubit gates are not possible. However, photons do exhibit other characteristics that make them ideal candidates for QIP. Photons decohere slowly, an ideal trait for quantum computing. Photons also travel well, one reason why they are so widely used for communication. Another advantage is that photons can be experimented with at room temperature. Provided we can overcome the interaction problem, there would just be technical obstacles to be overcome, such as mode matching and single photon production and detection.

Recently, it was shown by Knill *et al.* [31] that a Kerr non-linearity was not required to mediate an interaction between photons. The non-linearity required to make photons interact could be present in the form of single photon detectors and previously prepared entangled ancilla states. This scheme, called linear optics quantum computing (LOQC), required single photon sources, linear optical elements such as beam splitters and phase shifters and photon number detectors with the ability to distinguish between 0, 1 and 2 photons. By teleporting qubits through the gate [32], a CNOT could be performed with success probability that asymptotically approached 1.

Performing a two qubit gate now becomes a state preparation problem, something that can be done offline and need not have a perfect success probability. In [31] Knill *et al.* also showed a method to probabilistically perform a CSIGN (locally equivalent to a CNOT) between photonic qubits with a success probability of 1/16, requiring two single photon ancilla states. In the bigger picture, these probabilistic CSIGN gates will be applied between the pre-prepared entangled ancilla states.

Whilst the LOQC proposal by Knill *et al.* [31] is asymptotically scalable, the number of resources required to perform an experimental are staggering. For a two qubit gate to work with a success probability of 99.99%, 10000 photons would be required on 10^8 beam splitters in a square array. This number of photons could be reduced with the use of QEC [33], since the teleportations using the pre-prepared entangled states fail in a very particular way. When the teleportations fail, Z-measurement errors are induced on the photonic logic [33]. With a parity encoding these errors can be corrected.

Since the seminal work by Knill *et al.* on LOQC, research into optical quantum computing has essential split into three, not necessarily disjointed, branches.

The first branch concerns directly improving the LOQC model, such as simplifications and improvements to the probabilistic CSIGN, as shown by Pittman *et al.* [34] and Ralph *et al.* [35]. In [34], a CNOT was shown to succeed 1/4 of the time. However, this CNOT required the use of a Bell state ancilla. In [35], a simplified CNOT in the coincidence basis was shown that succeeded with a success probability of 1/20. Further simplifications shown in [36] and [37], where the use of photon-number QND detectors were necessary, led to experimental verification. In [38, 39], Knill worked towards optimising the probabilistic CSIGN gate, as have Scheel and Lütkenhaus in [40] and Eisert in [41]. Another direct improvement for LOQC would be through more general and efficient QEC codes, such as the work by Knill *et al.* [33] and Silva *et al.* [42]. Hayes *et al.* [43] have shown that the parity encoding introduced in [31] can be generalised to use an incremental parity encoding, leading to a reduction in the necessary resources for computation.

The second branch moves away from the circuit model of quantum computation, instead concentrating on the cluster state model by Raussendorf [44]. Yoran and Reznik [45] used a variation of the cluster state model to show that the number of resources for LOQC could be reduced by two orders of magnitude. Nielsen showed [46] that with the standard KLM CSIGN gate and ideas from cluster state computation, the number of photons required per two qubit operation could be reduced by another order of magnitude. Later, it was shown by Browne and Rudolph [47] that this number could be reduced by another order of magnitude with the use of so called *fusion* gates. More recently, Ralph *et. al.* [48] have shown that the number of photons required per two qubit gate can be reduced even more by using incremental encoding.

The third branch involves the investigation of different forms of non-linearity to induce photon interaction. Nemoto and Munro [49] build on the idea of using a cross Kerr non-linearity to construct a near deterministic CNOT gate, circumventing the need for a large cross Kerr non-linearity by using weak Kerr non-linearities in conjunction with large coherent bus modes. Franson *et al.* [50] have shown that a CNOT between photonic qubits is possible using the Zeno effect in the form of two photon absorbers. In this scheme, two photon absorption are used to eliminate any photonic terms outside the logical Hilbert while a simple beam splitter type of interaction takes place.

In this thesis we will investigate the first and third branch extensively and briefly touch on the second.

We investigate direct improvements to the LOQC model by exploring the possibility of constructing photon-number QND detectors with near perfect success probability. This leads to investigating possible improvements to the original LOQC asymptotic teleporter.

We investigate two areas of the weak non-linearity model. We first examine the benefits of coherent beam displacements in this model, investigating the measurement of arbitrary stabilizer codes and the construction of entangling three qubit gates. We next examine the use of teleportations in the weak non-linearity scheme, investigating a fault tolerant measurement of arbitrary stabilizer codes, the possibility of efficient computation performed on coherent state logic and the production of cluster states.

We investigate the optical Zeno gate by modelling realistic two photon absorption and include realistic single photon loss. We examine the use of encoding to overcome the realistic single photon loss and compare our results with the leading equivalent LOQC scheme.

1.1 Outline of the dissertation

In Chapter 2 we introduce important background results that are built upon in this thesis. We give a brief overview of quantum optics in Section 2.1, we describe the original proposal for photonic quantum gates in Section 2.2, in Section 2.3 we define a definition for fidelity used in this thesis, we give a brief overview of progress made towards quantum gates with linear optics prior to the LOQC scheme in Section 2.4, we summarise the LOQC proposal in Section 2.5 and the quantum error correction scheme used to recover from teleportation failure in Section 2.6, in Section 2.7 we give a brief overview of improvements and simplifications to the LOQC proposal, we describe the quantum bus scheme for optical quantum gates in Section 2.8 and conclude the chapter in Section 2.9 by describing the optical Zeno gate.

In Chapter 3 we search for a high success probability LOQC photon number QND detector, describing the details for such a gate in Section 3.1 and describing an important application for such a gate in Section 3.2.

In Chapter 4 we investigate the use of displacements in qubus computation. In Section 4.1 we describe a method to measure the parity of n qubits and in Section 4.2 we propose a Toffoli gate.

In Chapter 5 we investigate the use of single qubit teleportations in qubus computation. In Section 5.1 we describe a fault tolerant method to measure the parity of n qubits, in Section 5.2 we provide a detailed analysis of qubus single qubit teleportations, in Section 5.3 we describe a method to perform a universal set of gates on coherent state type qubits and in Section 5.4 we provide a method to construct large cluster states.

in Chapter 6 we perform a full analysis of the optical Zeno effect optical gate. In Section 6.1 we describe an analytical solution for the density matrix when we have a continuous interaction between the qubits and realistic, continuous two photon absorption and single photon loss, in Section 6.2 we describe an analytical solution when the continuous interaction is replaced by a linear array of beam splitters, in Section 6.3 we measure the effect single photon loss has on the CSIGN gate, in Sections 6.4 and 6.5 we encode against the single photon loss and in Section 6.6 we compare our encoded optical Zeno gate against the equivalent leading LOQC gate.

In Chapter 7 we summarise the results from this thesis.

1.2 Additional information for the examiners of this thesis

Chapter 2 is intended as a summary of the important background results that are built upon in this thesis. None of the results in this Chapter are claimed to be original. They are all known results taken from the literature. Sections 2.1, 2.2, 2.4, 2.5 and 2.6 are loosely based on the LOQC review paper written by C.R. Myers and R. Laflamme [51].

Section 4.1 from Chapter 4 and Section 5.1 from Chapter 5 are based on the *Physical Review A* article [52] written with M. Silva, K. Nemoto and W.J. Munro.

Chapter 4 is a result of discussions with M. Silva and W.J. Munro. I am the sole contributor to the details in this chapter. A paper concerning Section 4.2 is currently being written by C.R. Myers.

Chapter 5 is a result of discussions with M. Silva, K. Nemoto and W.J. Munro. C.R. Myers and M. Silva had an equal contribution to the results in this Chapter. A paper concerning Sections 5.2–5.4 is currently being written by C.R. Myers and M. Silva.

The results presented in Chapter 6 are based on the *Physical Review A* article [53] written with A. Gilchrist. C.R. Myers and A. Gilchrist had an equal contribution to the results in this Chapter.

The results presented in Chapter 3 are a result of discussions between C.R. Myers and J.P. Dowling. I am the sole contributor to the results in this chapter. A paper concerning this chapter is currently being written by C.R. Myers and J.P. Dowling.

Chapter 2

Background

In this chapter we describe important background results that are built upon in this thesis. We begin with a brief overview of quantum optics, concentrating on techniques that will be used in this thesis. Next we briefly describe the original photonic quantum gate proposal based on strong Kerr cross non-linearities. After this we describe the fidelity measures that will be used in this thesis. We follow this with a description of progress made towards quantum gates with linear optics prior to the LOQC scheme. Next we summarise the LOQC scheme and the quantum error correction scheme used to recover from teleportation failure. This is followed by a brief overview of improvements and simplifications to the LOQC proposal. We then summarise the quantum bus scheme for implementing quantum gates on photons, emphasising results that will be extending in later chapters. Finally we summarise the optical Zeno gate.

2.1 Quantum Optics

2.1.1 Classical Electromagnetic Field

When we deal with electromagnetic waves classically we look for solutions to the source free Maxwell equations [54], resulting in the electric field $\mathbf{E}(\mathbf{r},t)$ wave equation

$$\nabla^2\mathbf{E}(\mathbf{r},t)-\frac{1}{c^2}\frac{\partial^2}{\partial t^2}\mathbf{E}(\mathbf{r},t)=0. \tag{2.1}$$

The solutions have a plus and minus frequency part [55, 56] :

$$\mathbf{E}(\mathbf{r},t)=i\sum_k\left(\frac{\hbar\omega_k}{2}\right)^{\frac{1}{2}}\left[a_k\mathbf{u}_k(\mathbf{r})e^{-i\omega_k t}-a_k^*\mathbf{u}_k^*(\mathbf{r})e^{i\omega_k t}\right]. \tag{2.2}$$

The a_k are dimensionless (complex) amplitudes and $\mathbf{u}_k(\mathbf{r})$ are orthogonal mode functions, usually plane wave mode functions: $\mathbf{u}_k(\mathbf{r})=\frac{\hat{\mathbf{e}}^{(\lambda)}}{\sqrt{V}}\exp(i\mathbf{k}\cdot\mathbf{r})$, where

V is the volume and $\hat{\mathbf{e}}^{(\lambda)}$ is defined as the unit polarisation vector satisfying $\mathbf{k}\cdot\hat{\mathbf{e}}^{(\lambda)} = 0$ and $\hat{\mathbf{e}}^{(\lambda)}.\hat{\mathbf{e}}^{(\lambda')} = \delta_{\lambda,\lambda'}$ [57].

The energy of a classical electromagnetic field is given by [56]

$$H = \frac{1}{2}\int_V (\epsilon_0 \mathbf{E}^2 + \frac{\mathbf{B}^2}{\mu_0}) d\mathbf{r} = \sum_k \left(\frac{\hbar\omega_k}{2}\right) a_k a_k^*, \tag{2.3}$$

where $\epsilon_0 = 8.854 \times 10^{-12} F \cdot m^{-1}$ is the permittivity of vacuum and $\mu_0 = 4\pi \times 10^{-7} N \cdot A^{-2}$ is the permeability of vacuum such that $\epsilon_0\mu_0 = \frac{1}{c^2}$.

2.1.2 Quantise

We quantise the electromagnetic field by turning the coefficients a_k into operators and imposing the commutation relations:

$$\begin{aligned} \left[\hat{a}_i, \hat{a}_j^\dagger\right] &= \delta_{i,j} \\ \left[\hat{a}_i, \hat{a}_j\right] &= \left[\hat{a}_i^\dagger, \hat{a}_j^\dagger\right] = 0. \end{aligned} \tag{2.4}$$

In terms of these operators the energy is given by

$$\hat{H} = \sum_k \hbar\omega_k \big(\hat{a}_k^\dagger \hat{a}_k + \frac{1}{2}\big). \tag{2.5}$$

If we let

$$\hat{a} = \frac{1}{\sqrt{2}}\Big(\sqrt{\frac{m\omega}{\hbar}}\hat{x} + i\frac{1}{\sqrt{m\hbar\omega}}\hat{p}\Big), \tag{2.6}$$

where $\hat{x}$ and $\hat{p}$ are the usual position and momentum operators,

$$\begin{aligned} \langle x|\hat{p}|\psi\rangle &= -i\hbar\frac{d}{dx}\langle x|\psi\rangle \\ \langle x|\hat{x}|\psi\rangle &= x\langle x|\psi\rangle. \end{aligned} \tag{2.7}$$

The energy of the electromagnetic field becomes

$$\hat{H} = \frac{\hat{p}^2}{2m} + \frac{1}{2}m\omega^2\hat{x}^2, \tag{2.8}$$

where $\omega = \sqrt{k/m}$. This is the Hamiltonian for a harmonic oscillator.

The eigenstates of $\hat{H}$, called Fock states, are labelled $|n\rangle$. We define the number operator $\hat{n}$ as $\hat{n} = \hat{a}^\dagger\hat{a}$ having eigenvalue n:

$$\hat{n}|n\rangle = \hat{a}^\dagger\hat{a}|n\rangle = n|n\rangle. \tag{2.9}$$

The effect of $\hat{a}$ on $|n\rangle$ can be seen by finding the number of photons in $\hat{a}|n\rangle$:

$$\hat{n}\big(\hat{a}|n\rangle\big) = \hat{a}^\dagger\hat{a}^2|n\rangle = \big(\hat{a}\hat{a}^\dagger\hat{a} - \hat{a}\big)|n\rangle = \big(n-1\big)\hat{a}|n\rangle.$$

So $\hat{a}|n\rangle$ is a Fock state with $n-1$ photons. We define this to be $A|n-1\rangle$ for $A \in \mathbb{R}$ and $n \geq 1$. In a similar way we can show that $\hat{a}^\dagger|n\rangle$ is a Fock state with $n+1$ photons, $B|n+1\rangle$. A and B can be worked out using the fact that $\langle n|\hat{n}|n\rangle = n$:

$$\begin{aligned}
\langle n|\hat{n}|n\rangle &= \langle n|\hat{a}^\dagger\hat{a}|n\rangle = A\langle n|\hat{a}^\dagger|n-1\rangle \\
&= \langle n-1|A^2|n-1\rangle = A^2 = n \\
\langle n|\hat{n}|n\rangle &= \langle n|\hat{a}^\dagger\hat{a}|n\rangle = \langle n|\hat{a}\hat{a}^\dagger - 1|n-1\rangle \\
&= B^2 - 1 = n.
\end{aligned}$$

We call $\hat{a}$ an annihilation operator and $\hat{a}^\dagger$ a creation operator:

$$\hat{a}^\dagger|n\rangle = \sqrt{n+1}|n+1\rangle \tag{2.10}$$

$$\hat{a}|n\rangle = \sqrt{n}|n-1\rangle. \tag{2.11}$$

For $n=0$, we define $\hat{a}|0\rangle = 0$, this represents vacuum fluctuations: $\hat{H}|0\rangle = \frac{1}{2}\hbar\omega|0\rangle$ vacuum fluctuation energy of the lowest eigenstate of the Hamiltonian.

The Fock states form an orthonormal set:

$$\begin{aligned}
\langle n|m\rangle &= \delta_{nm} \\
\sum_{n=0}^{\infty}|n\rangle\langle n| &= \mathbb{1}.
\end{aligned}$$

Each Fock state may be built up from creation operators:

$$|n\rangle = \frac{\left(\hat{a}^\dagger\right)^n}{\sqrt{n!}}|0\rangle. \tag{2.12}$$

The matrix form of the annihilation operator can be seen by using the identity operator twice:

$$\begin{aligned}
\hat{a} &= \mathbb{1}\hat{a}\mathbb{1} = \sum_{n=0}^{\infty}|n\rangle\langle n|\hat{a}\sum_{m=0}^{\infty}|m\rangle\langle m| \\
&= \sum_{n=0}^{\infty}\sqrt{n+1}|n\rangle\langle n+1|.
\end{aligned}$$

In matrix form:

$$\hat{a} = \begin{pmatrix} 0 & \sqrt{1} & 0 & 0 & \cdots \\ 0 & 0 & \sqrt{2} & 0 & \cdots \\ 0 & 0 & 0 & \sqrt{3} & \cdots \\ \vdots & \vdots & \vdots & \vdots & \ddots \end{pmatrix}.$$

It should be noted that we only consider monochromatic photonic modes in this thesis. To consider all modes associated with each photon we could use the techniques presented in [58]. In the case that we consider each photon to have a finite frequency width we would include frequency filters in front of each photon source and each photon detector. An analysis of frequency effects in linear optics quantum computing has been shown by Rohde *et al.* [59].

2.1.3 Minimum Uncertainty States

The Heisenberg Uncertainty Principle: for two non-commuting observables $\hat{A}$ and $\hat{B}$, the uncertainty in each is given by the relation:

$$\Delta\hat{A}\Delta\hat{B} \geq \frac{1}{2}|\langle\Big[\hat{A},\hat{B}\Big]\rangle|$$

where $(\Delta\hat{A})^2 = \langle\hat{A}^2\rangle - \langle\hat{A}\rangle^2$.

For example, consider the case when $\hat{A} = \hat{x}$ and $\hat{B} = \hat{p}$. The uncertainty principle becomes the well known result: $\Delta\hat{x}\Delta\hat{p} \geq \frac{\hbar}{2}$.

In Eqn. 2.6 we wrote $\hat{a}$ in terms of $\hat{x}$ and $\hat{p}$. It is often more convenient to write the annihilation operator as a linear combination of the two Hermitian operators:

$$\begin{aligned} \hat{X}_1 &= \hat{a} + \hat{a}^\dagger \\ \hat{X}_2 &= -i\big(\hat{a} - \hat{a}^\dagger\big) \end{aligned} \tag{2.13}$$

where $\hat{X}_1$ (similarly to $\hat{x}$ from before) corresponds to the in-phase component of the electric field amplitude of the spatial-temporal mode and $\hat{X}_2$ (similar to $\hat{p}$ from before) corresponds to the out-of-phase component.

This gives the commutation relation $\Big[\hat{X}_1,\hat{X}_2\Big] = 2i$ and the Heisenberg uncertainty relation

$$\Delta\hat{X}_1\Delta\hat{X}_2 \geq 1. \tag{2.14}$$

Minimum uncertainty states are states that correspond to an equality in Eqn. (2.14). Two important minimum uncertainty states are coherent states and squeezed states, described in the next two sections.

2.1.4 Coherent States

A coherent state $|\alpha\rangle$ is a minimum uncertainty state defined as the eigenstate of an annihilation operator:

$$\hat{a}|\alpha\rangle = \alpha|\alpha\rangle. \tag{2.15}$$

Alternatively, we can define a coherent state with the displacement operator $D(\alpha)$:

$$|\alpha\rangle = D(\alpha)|0\rangle \tag{2.16}$$

where

$$D(\alpha) = \exp(\alpha\hat{a}^\dagger - \alpha^*\hat{a}). \tag{2.17}$$

We can use the Campbell-Baker-Hausdorff operator identity [60]:

$$e^{\hat{A}+\hat{B}} = e^{\hat{A}}e^{\hat{B}}e^{-\frac{1}{2}[\hat{A},\hat{B}]}$$

for $\left[\hat{A},\left[\hat{A},\hat{B}\right]\right]=\left[\hat{B},\left[\hat{A},\hat{B}\right]\right]=0$ to rewrite the displacement operator:

$$\exp(\alpha\hat{a}^\dagger-\alpha^*\hat{a})=\exp\Big(-\frac{|\alpha|^2}{2}\Big)\exp(\alpha\hat{a}^\dagger)\exp(-\alpha^*\hat{a}). \tag{2.18}$$

We can then rewrite the coherent state as

$$|\alpha\rangle=\exp\Big(-\frac{|\alpha|^2}{2}\Big)\exp(\alpha\hat{a}^\dagger)|0\rangle=\exp\Big(-\frac{|\alpha|^2}{2}\Big)\sum_{n=0}^{\infty}\frac{\alpha^n}{\sqrt{n!}}|n\rangle. \tag{2.19}$$

Working out $\Delta\hat{X}_1\Delta\hat{X}_2$ for a coherent state we find $\Delta\hat{X}_1=\Delta\hat{X}_2=1$, showing that coherent states are minimum uncertainty states, since $\Delta\hat{X}_1\Delta\hat{X}_2=1$.

Coherent states are not orthogonal since

$$\begin{aligned}\langle\beta|\alpha\rangle &= \exp\Big(-\frac{1}{2}\big(|\alpha|^2+|\beta|^2\big)+\alpha\beta^*\Big) && (2.20)\\ |\langle\beta|\alpha\rangle|^2 &= \exp\Big(-|\alpha-\beta|^2\Big) && (2.21)\end{aligned}$$

and as such form an over complete set

$$\int|\alpha\rangle\langle\alpha|d^2\alpha=\pi. \tag{2.22}$$

By writing $\alpha=re^{i\theta}$ we know that $d^2\alpha=rdrd\theta$. Using this and Eqn. 2.19 we can explicitly prove Eqn. 2.22 [55]. The inverse of the displacement operator $D^{-1}(\alpha)$ is given by

$$D^\dagger(\alpha)=D^{-1}(\alpha)=D(-\alpha). \tag{2.23}$$

Using the identity [61]

$$e^{\xi B}Ae^{-\xi B}=A+\xi\,[B,A]+\frac{\xi^2}{2!}\,[B,[B,A]]+\frac{\xi^3}{3!}\,[B,[B,[B,A]]]+\cdots, \tag{2.24}$$

we can see how the displacement operator *displaces* annihilation and creation operators:

$$\begin{aligned}D^\dagger(\alpha)\hat{a}D(\alpha) &= \hat{a}+\alpha && (2.25)\\ D^\dagger(\alpha)\hat{a}^\dagger D(\alpha) &= \hat{a}^\dagger+\alpha^*.\end{aligned}$$

The displacement of a coherent state $|\alpha\rangle$ by β results in a phase factor

$$D(\beta)D(\alpha)=\exp\big(i\mathrm{Im}(\beta\alpha^*)\big)D(\alpha+\beta). \tag{2.26}$$

2.1.5 Linear Optics

Linear optical components are passive devices used to interfere optical states with each other. We will use them extensively in this thesis so we will describe them here.

An optical component is said to be linear if its output modes $\hat{b}_j^\dagger$ are a linear combination of its input modes $\hat{a}_j^\dagger$:

$$\hat{b}_j^\dagger = \sum_k M_{jk} \hat{a}_k^\dagger.$$

Linear optical components are made up of phase shifters and beam splitters. A phase shifter, shown in Fig. 2.1 (i), is defined by the transformation $U(P_\phi) : |n\rangle \rightarrow e^{in\phi}|n\rangle$. That is, $\big(\hat{a}_l^\dagger\big)^n|0\rangle \rightarrow e^{in\phi}\big(\hat{a}_l^\dagger\big)^n|0\rangle$. The Hamiltonian for a phase shifter is given by the number operator:

$$\hat{U}_{\text{PS}} = e^{i\phi\hat{H}} = e^{i\phi\hat{n}} = e^{i\phi\hat{a}^\dagger\hat{a}}. \tag{2.27}$$

Using this we see that $e^{i\phi\hat{a}^\dagger\hat{a}}|n\rangle = e^{in\phi}|n\rangle$. The phase operator takes a coherent state $|\alpha\rangle$ to $|e^{i\phi}\alpha\rangle$:

$$\begin{aligned} e^{i\phi\hat{n}}|\alpha\rangle = e^{i\phi\hat{a}^\dagger\hat{a}} \sum_{n=0}^{\infty} \frac{(i\alpha)^n}{\sqrt{n!}}|n\rangle &= \sum_{n=0}^{\infty} \frac{(i\alpha)^n}{\sqrt{n!}} e^{i\phi\hat{a}^\dagger\hat{a}}|n\rangle \\ &= \sum_{n=0}^{\infty} \frac{(i\alpha)^n}{\sqrt{n!}} e^{i\phi n}|n\rangle \\ &= \sum_{n=0}^{\infty} \frac{(i\alpha e^{i\phi})^n}{\sqrt{n!}}|n\rangle \\ &= |e^{i\phi}\alpha\rangle. \end{aligned} \tag{2.28}$$

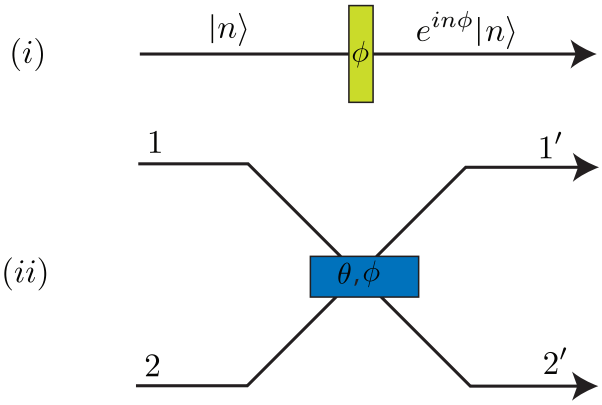

Figure 2.1: (i) Phase shifter ϕ. (ii) Beam splitter described by θ and ϕ. The reflectivity is given by $\cos^2(\theta)$.

A possible Hamiltonian for the beam splitter shown in Fig. 2.1 (ii) is given by

$$\hat{H} = \epsilon\big(e^{i\vartheta}\hat{a}_1^\dagger\hat{a}_2 + e^{-i\vartheta}\hat{a}_1\hat{a}_2^\dagger\big). \tag{2.29}$$

The corresponding unitary transformation is

$$\hat{U}_{\mathrm{BS}} = \exp\Big(i\theta\big(e^{i\vartheta}\hat{a}_1^\dagger\hat{a}_2 + e^{-i\vartheta}\hat{a}_1\hat{a}_2^\dagger\big)\Big), \tag{2.30}$$

where modes 1 and 2 are being acted upon by the beam splitter and $\theta = \epsilon t$, t being measured in units of $\hbar$.

A beam splitter takes the two mode state $|\psi\rangle_{12}$ to $\hat{U}_{\mathrm{BS}}|\psi\rangle_{12}$. Any photonic state can be written as a polynomial function of creation and annihilation operators acting on the vacuum: $|\psi\rangle_{12} = f(\hat{a}_1^\dagger, \hat{a}_2^\dagger, \hat{a}_1, \hat{a}_2)|\mathrm{vac}\rangle_{12}$. We can always use Eqn. 2.4 and generalisations [61, 62] such as:

$$\begin{aligned}\Big[\hat{a}_i, (\hat{a}_j^\dagger)^n\Big] &= \delta_{ij} n (\hat{a}_i^\dagger)^{n-1} \\ \Big[\hat{a}_i^\dagger, (\hat{a}_j)^n\Big] &= -\delta_{ij} n (\hat{a}_i)^{n-1}\end{aligned} \tag{2.31}$$

to write the function $f(\hat{a}_1^\dagger, \hat{a}_2^\dagger, \hat{a}_1, \hat{a}_2)$ with the creation operators to the left of the annihilation operators, something called *normal ordering*, and use the fact that $\hat{a}|0\rangle = 0$ to obtain a function that only depends on the creation operators: $|\psi\rangle_{12} = \tilde{f}(\hat{a}_1^\dagger, \hat{a}_2^\dagger)|\mathrm{vac}\rangle_{12}$. The beam splitter now takes $|\psi\rangle_{12}$ to

$$\begin{aligned}\hat{U}_{\mathrm{BS}}\tilde{f}(\hat{a}_1^\dagger, \hat{a}_2^\dagger)|\mathrm{vac}\rangle_{12} &= \hat{U}_{\mathrm{BS}}\tilde{f}(\hat{a}_1^\dagger, \hat{a}_2^\dagger)\hat{U}_{\mathrm{BS}}^\dagger\hat{U}_{\mathrm{BS}}|\mathrm{vac}\rangle_{12} \\ &= \tilde{f}(\hat{U}_{\mathrm{BS}}\hat{a}_1^\dagger\hat{U}_{\mathrm{BS}}^\dagger, \hat{U}_{\mathrm{BS}}\hat{a}_2^\dagger\hat{U}_{\mathrm{BS}}^\dagger)|\mathrm{vac}\rangle_{12},\end{aligned} \tag{2.32}$$

since $\hat{U}|\mathrm{vac}\rangle = |\mathrm{vac}\rangle$ for any unitary $\hat{U}$ and $\tilde{f}(\hat{a}_1^\dagger, \hat{a}_2^\dagger)$ is a polynomial function of creation operators.

Using Eqn. 2.24 $\hat{U}_{\mathrm{BS}}\hat{a}_1^\dagger\hat{U}_{\mathrm{BS}}^\dagger$ and $\hat{U}_{\mathrm{BS}}\hat{a}_2^\dagger\hat{U}_{\mathrm{BS}}^\dagger$ can be expanded as:

$$\begin{aligned}\hat{U}_{\mathrm{BS}}\hat{a}_1^\dagger\hat{U}_{\mathrm{BS}}^\dagger &= \hat{a}_1^\dagger + i\theta e^{-i\vartheta}\hat{a}_2^\dagger - \frac{1}{2!}\theta^2\hat{a}_1^\dagger - \frac{1}{3!}i\theta^3 e^{-i\vartheta}\hat{a}_2^\dagger + \frac{1}{4!}\theta^4\hat{a}_1^\dagger + \frac{1}{5!}i\theta^5 e^{-i\vartheta}\hat{a}_2^\dagger + \cdots \\ \hat{U}_{\mathrm{BS}}\hat{a}_2^\dagger\hat{U}_{\mathrm{BS}}^\dagger &= \hat{a}_2^\dagger + i\theta e^{i\vartheta}\hat{a}_1^\dagger - \frac{1}{2!}\theta^2\hat{a}_2^\dagger - \frac{1}{3!}i\theta^3 e^{i\vartheta}\hat{a}_1^\dagger + \frac{1}{4!}\theta^4\hat{a}_2^\dagger + \frac{1}{5!}i\theta^5 e^{i\vartheta}\hat{a}_1^\dagger + \cdots\end{aligned}$$

Comparing this with the Maclaurin series for $\cos(x)$ and $\sin(x)$

$$\cos(x) = 1 - \frac{1}{2!}x^2 + \frac{1}{4!}x^4 - \frac{1}{6!}x^6 \cdots \tag{2.33}$$

$$\sin(x) = x - \frac{1}{3!}x^3 + \frac{1}{3!}x^3 - \frac{1}{7!}x^7 \cdots \tag{2.34}$$

we see that

$$\begin{aligned}\hat{U}_{\mathrm{BS}}\hat{a}_1^\dagger\hat{U}_{\mathrm{BS}}^\dagger &= \cos(\theta)\hat{a}_1^\dagger + e^{-i\phi}\sin(\theta)\hat{a}_2^\dagger \\ \hat{U}_{\mathrm{BS}}\hat{a}_2^\dagger\hat{U}_{\mathrm{BS}}^\dagger &= -e^{i\phi}\sin(\theta)\hat{a}_1^\dagger + \cos(\theta)\hat{a}_2^\dagger\end{aligned} \tag{2.35}$$

where we have set $\phi = \vartheta - \frac{\pi}{2}$. We can summarise this by saying that the creation operators $\hat{a}_1^\dagger$ and $\hat{a}_2^\dagger$ are transformed by a beam splitter to give $\Lambda\vec{a}$, where

$$\Lambda = \begin{pmatrix} \cos(\theta) & -e^{i\phi}\sin(\theta) \\ e^{-i\phi}\sin(\theta) & \cos(\theta) \end{pmatrix} \tag{2.36}$$

and

$$\vec{a} = \begin{pmatrix} \hat{a}^\dagger_{1'} \\ \hat{a}^\dagger_{2'} \end{pmatrix} \tag{2.37}$$

Consider the state $|mn\rangle_{12}$ incident on a beam splitter. The output would look like:

$$\begin{aligned} |mn\rangle_{12} &= \frac{\left(\hat{a}^\dagger_1\right)^m}{\sqrt{m!}}\frac{\left(\hat{a}^\dagger_2\right)^n}{\sqrt{n!}}|00\rangle \\ &\rightarrow \frac{1}{\sqrt{m!}}\Big(\sum_{i'}\Lambda_{i'1}\hat{a}^\dagger_{i'}\Big)^m \frac{1}{\sqrt{n!}}\Big(\sum_{j'}\Lambda_{j'2}\hat{a}^\dagger_{j'}\Big)^n|00\rangle \\ &= \frac{1}{\sqrt{m!n!}}\Big(\hat{a}^\dagger_{1'}\cos(\theta) + \hat{a}^\dagger_{2'}e^{-i\phi}\sin(\theta)\Big)^m\Big(-\hat{a}^\dagger_{1'}e^{i\phi}\sin(\theta) + \hat{a}^\dagger_{2'}\cos(\theta)\Big)^n|00\rangle \end{aligned} \tag{2.38}$$

where we have used the notation $|00\rangle$ for the two mode vacuum state $|\mathrm{vac}\rangle_{12}$. For example:

$$\begin{aligned} |10\rangle &\rightarrow \cos(\theta)|10\rangle + e^{-i\phi}\sin(\theta)|01\rangle \\ |01\rangle &\rightarrow -e^{i\phi}\sin(\theta)|10\rangle + \cos(\theta)|01\rangle \\ |11\rangle &\rightarrow -\sqrt{2}e^{i\phi}\cos(\theta)\sin(\theta)|20\rangle + (\cos^2(\theta) - \sin^2(\theta))|11\rangle + \sqrt{2}e^{-i\phi}\cos(\theta)\sin(\theta)|02\rangle \\ |20\rangle &\rightarrow \cos^2(\theta)|20\rangle + \sqrt{2}e^{-i\phi}\cos(\theta)\sin(\theta)|11\rangle + e^{-2i\phi}\sin^2(\theta)|02\rangle \\ |02\rangle &\rightarrow e^{2i\phi}\sin^2(\theta)|20\rangle - \sqrt{2}e^{i\phi}\cos(\theta)\sin(\theta)|11\rangle + \cos^2(\theta)|02\rangle. \end{aligned}$$

Polarisation

In the solution to the source free Maxwell equation in Eqn. 2.2 a polarisation vector $\hat{\mathbf{e}}^{(\lambda)}$ was defined. This polarisation degree of freedom for photons has the two dimensional basis $\{|H\rangle, |V\rangle\}$, corresponding to horizontally and vertically polarised photons. In the 45 degree basis we have $|F\rangle = \frac{1}{\sqrt{2}}\big(|H\rangle + |V\rangle\big)$ and $|S\rangle = \frac{1}{\sqrt{2}}\big(|V\rangle - |H\rangle\big)$. Alternatively $|H\rangle = \frac{1}{\sqrt{2}}\big(|F\rangle - |S\rangle\big)$ and $|V\rangle = \frac{1}{\sqrt{2}}\big(|F\rangle + |S\rangle\big)$. The polarisation equivalent to linear optical elements are polarisers and polarising beam splitters (PBS), shown in Fig. 2.2.

A polariser is able to implement any single qubit operation on the qubit $\alpha|H\rangle_a + \beta|V\rangle_a$. That is, the polariser in Fig. 2.2 (i) takes $\alpha|H\rangle_a + \beta|V\rangle_a$ to $\alpha\left(\cos(\theta)|H\rangle + e^{-i\phi}\sin(\theta)|V\rangle\right)_b + \beta\left(-e^{i\phi}\sin(\theta)|H\rangle + \cos(\theta)|V\rangle\right)_b$, where $|\alpha^2| + |\beta|^2 = 1$.

Polarising beam splitters reflect or transmit photons depending on their polarisation. In Fig. 2.2 (ii) the HV-PBS reflects $|V\rangle$ and transmits $|H\rangle$. For example, the state

$$\begin{aligned} &c_0|H\rangle_c|H\rangle_d + c_1|H\rangle_c|V\rangle_d + c_2|V\rangle_c|H\rangle_d + c_3|V\rangle_c|V\rangle_d \\ &\rightarrow c_0|H\rangle_f|H\rangle_e + c_1|H\rangle_f|V\rangle_f + c_2|V\rangle_e|H\rangle_e + c_3|V\rangle_e|V\rangle_f \end{aligned}$$

where $\sum_{i=0}^{3}|c_i|^2 = 1$.

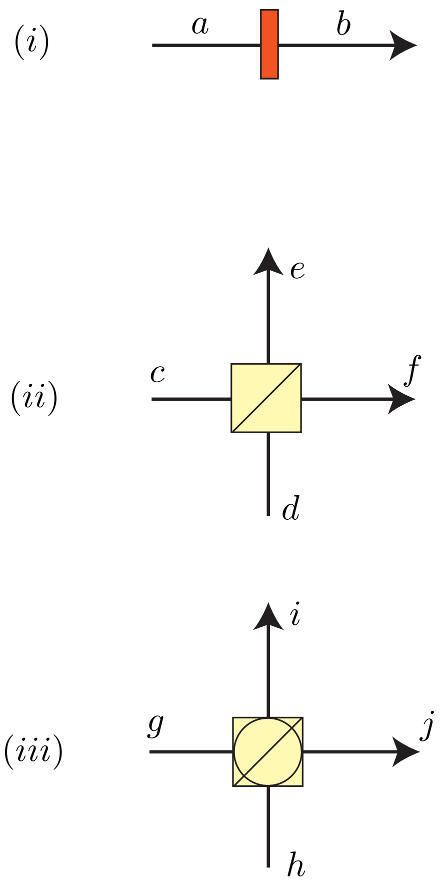

Figure 2.2: (i) Polariser. (ii) HV-Polarising Beam Splitter (PBS) that reflects $|V\rangle$ and transmits $|H\rangle$. (iii) FS-PBS that reflects $|S\rangle$ and transmits $|F\rangle$.

In Fig. 2.2 (iii) the FS-PBS reflects $|S\rangle$ and transmits $|F\rangle$. For example, the state

$$\begin{aligned} &c_0|F\rangle_g|F\rangle_h + c_1|F\rangle_g|S\rangle_h + c_2|S\rangle_g|F\rangle_h + c_3|S\rangle_g|S\rangle_h \\ &\to c_0|F\rangle_j|F\rangle_i + c_1|F\rangle_j|S\rangle_j + c_2|S\rangle_i|F\rangle_i + c_3|S\rangle_i|S\rangle_j . \end{aligned}$$

2.1.6 Homodyne Measurement

A homodyne measurements of a state corresponds to a projection of that state along a straight line in phase space. Physically this corresponds to mixing our optical state on a beam splitter with a strong coherent beam of equal frequency, called a local oscillator, and then detecting the count rate difference. Consider applying a homodyne detection to the state in mode a of Fig. 2.3.

In mode b we have the local oscillator in the state $|\beta e^{i\phi}\rangle, \beta, \phi \in \mathbb{R}$, where ϕ is the phase of the local oscillator. What we observe at the output is the

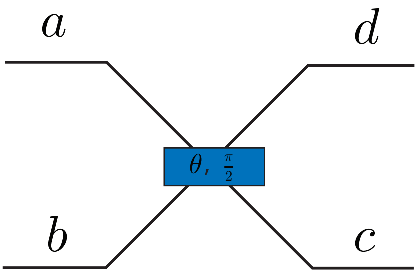

Figure 2.3: Beam splitter of reflectivity $\sqrt{\eta} = \cos(\theta)$.

difference in count between modes c and d [55]: $\langle \hat{c}^\dagger \hat{c} \rangle - \langle \hat{d}^\dagger \hat{d} \rangle$.

If we let $\sqrt{\eta} = \cos(\theta)$ and $\phi = \frac{\pi}{2}$ for the beam splitter in Fig. 2.3 we have

$$\begin{aligned} \hat{c}^\dagger &= \sqrt{\eta}\hat{a}^\dagger - i\sqrt{1-\eta}\hat{b}^\dagger \\ \hat{d}^\dagger &= -i\sqrt{1-\eta}\hat{a}^\dagger + \sqrt{\eta}\hat{b}^\dagger . \end{aligned}$$

We work out the count rates to be:

$$\begin{aligned} \hat{c}^\dagger \hat{c} &= \left(\sqrt{\eta}\hat{a}^\dagger - i\sqrt{1-\eta}\hat{b}^\dagger\right)\left(\sqrt{\eta}\hat{a} + i\sqrt{1-\eta}\hat{b}\right) \\ &= \eta\hat{a}^\dagger\hat{a} + (1-\eta)\hat{b}^\dagger\hat{b} - i\sqrt{(1-\eta)\eta}\left(\hat{b}^\dagger\hat{a} - \hat{b}\hat{a}^\dagger\right) \\ \hat{d}^\dagger \hat{d} &= \left(\sqrt{\eta}\hat{b}^\dagger - i\sqrt{1-\eta}\hat{a}^\dagger\right)\left(\sqrt{\eta}\hat{b} + i\sqrt{1-\eta}\hat{a}\right) \\ &= \eta\hat{b}^\dagger\hat{b} + (1-\eta)\hat{a}^\dagger\hat{a} - i\sqrt{(1-\eta)\eta}\left(\hat{b}\hat{a}^\dagger - \hat{b}^\dagger\hat{a}\right). \end{aligned}$$

The operator $\hat{b}$ is the annihilation operator for the coherent state $|\beta e^{i\phi}\rangle$

$$\langle \hat{b} \rangle = e^{-|\beta|^2} \langle 0| e^{\beta e^{-i\phi}\hat{b}} \hat{b} e^{\beta e^{i\phi}\hat{b}^\dagger} |0\rangle$$

remembering that $\beta \in \mathbb{R}$. Using Eqn. 2.31 we have:

$$\begin{aligned} \hat{b}\sum_{n=0}^{\infty} \frac{\left(\beta e^{i\phi}\hat{b}^\dagger\right)^n}{n!}|0\rangle &= \sum_{n=0}^{\infty}\left(\frac{\left(\beta e^{i\phi}\hat{b}^\dagger\right)^n \hat{b}}{n!} + \frac{n\left(\beta e^{i\phi}\right)^n (\hat{b}^\dagger)^{n-1}}{n!}\right)|0\rangle \\ &= \sum_{n=0}^{\infty} \frac{n\left(\beta e^{i\phi}\right)^n (\hat{b}^\dagger)^{n-1}}{n!}|0\rangle . \end{aligned}$$

So

$$\begin{aligned} \langle \hat{b} \rangle &= e^{-|\beta|^2}\langle 0| e^{\beta e^{i\phi}\hat{b}} \sum_{n=0}^{\infty} \frac{\left(\beta e^{i\phi}\right)^n (\hat{b}^\dagger)^{n-1}}{(n-1)!}|0\rangle \\ &= e^{-|\beta|^2}\langle 0| e^{\beta e^{i\phi}\hat{b}} \sum_{m=0}^{\infty} \frac{\beta e^{i\phi}\left(\beta e^{i\phi}\right)^m (\hat{b}^\dagger)^m}{m!}|0\rangle \\ &= \beta e^{i\phi}, \end{aligned} \tag{2.39}$$

where $m = n - 1$ and $\langle \beta e^{i\phi} | \beta e^{i\phi} \rangle = 1$. Similarly $\langle \hat{b}^\dagger \rangle = \beta e^{-\phi}$ and $\langle \hat{b}^\dagger \hat{b} \rangle = \beta^2$.

With the above we can work out $\langle \hat{c}^\dagger \hat{c} \rangle - \langle \hat{d}^\dagger \hat{d} \rangle$

$$\langle \hat{c}^\dagger \hat{c} \rangle - \langle \hat{d}^\dagger \hat{d} \rangle = \big(2\eta - 1\big)\langle \hat{a}^\dagger \hat{a} \rangle + \big(1 - 2\eta\big)\beta^2 - 2i\sqrt{(1-\eta)\eta}\big(\beta e^{-i\phi}\langle \hat{a} \rangle - \beta e^{i\phi}\langle \hat{a}^\dagger \rangle\big).$$

For a 50/50 beam splitter $\eta = \frac{1}{2}$ and if we let $\phi = \theta - \frac{\pi}{2}$ we have

$$\langle \hat{c}^\dagger \hat{c} \rangle - \langle \hat{d}^\dagger \hat{d} \rangle = \beta\big(e^{-i\theta}\langle \hat{a} \rangle + e^{i\theta}\langle \hat{a}^\dagger \rangle\big). \tag{2.40}$$

That is, when we homodyne detect we measure the operator

$$\hat{x}(\phi) = \beta\big(e^{-i\phi}\hat{a} + e^{i\phi}\hat{a}^\dagger\big). \tag{2.41}$$

For a homodyne measurement of the position quadrature $\hat{X}_1 = \hat{a} + \hat{a}^\dagger$ we choose $\phi = 0$ and for a homodyne measurement of the momentum quadrature $\hat{X}_2 = -i\hat{a} + i\hat{a}^\dagger$ we choose $\phi = \frac{\pi}{2}$.

With homodyne detection we can infer the unknown phase of a coherent state $|e^{i\theta}\alpha\rangle$. If we want to homodyne detect the state $|e^{i\theta}\alpha\rangle$ input into mode a in Fig. 2.3, where $\alpha, \theta \in \mathbb{R}$, we measure $\hat{x}(\phi) = e^{i\phi}\hat{c} + e^{-i\phi}\hat{c}^\dagger$ on the probe beam $|e^{i\phi}\beta\rangle$:

$$\begin{aligned} \langle \hat{x}(\phi) \rangle &= \langle \alpha^* e^{-i\theta} | e^{i\phi}\hat{c} + e^{-i\phi}\hat{c}^\dagger | \alpha e^{i\theta} \rangle \\ &= \alpha e^{i\delta} + \alpha^* e^{-i\delta}, \end{aligned} \tag{2.42}$$

where we have used the results from Eqn. (2.39) and $\delta = \phi + \theta$. If we expand this we have:

$$\begin{aligned} \langle \hat{x}(\phi) \rangle &= \mathrm{Re}[\alpha] + i\mathrm{Im}[\alpha]\Big)\Big(\cos\delta + i\sin\delta\Big) + \Big(\mathrm{Re}[\alpha] - i\mathrm{Im}[\alpha]\Big)\Big(\cos\delta - i\sin\delta \\ &= 2\mathrm{Re}[\alpha]\cos\delta - \mathrm{Im}[\alpha]\sin\delta. \end{aligned} \tag{2.43}$$

For a homodyne measurement of the position $\hat{X}_1 = \hat{a} + \hat{a}^\dagger$ we have $\phi = 0$ in Eqn. (2.41). For a homodyne measurement of the momentum $\hat{X}_2 = -i\hat{a} + i\hat{a}^\dagger$ we have $\phi = \frac{\pi}{2}$ in Eqn. (2.41).

$$\langle \hat{X}_1 \rangle = 2\alpha\cos(\theta) \tag{2.44}$$

$$\langle \hat{X}_2 \rangle = 2\alpha\cos(\theta - \frac{\pi}{2}) = 2\alpha\sin(\theta). \tag{2.45}$$

Provided we knew α in advance, we can induce what the phase θ was from the average result of the homodyne detection.

Alternatively, we could obtain the results in Eqns. 2.44 and 2.45 by directly finding the corresponding projection of $|\alpha\rangle$. That is, to find the results of a homodyne measurement in the $x-$quadrature, we want to find $\langle x|\alpha\rangle$. To find an analytical expression for $\langle x|\alpha\rangle$ we need to solve the ODE resulting from $\langle x|\hat{a}|\alpha\rangle$:

$$\begin{aligned}\langle x|\hat{a}|\alpha\rangle &= \alpha\langle x|\alpha\rangle \\ &= \langle x|\frac{i}{\sqrt{2\hbar\omega m}}\hat{p} + \sqrt{\frac{k}{2\hbar\omega}}\hat{x}|\alpha\rangle \\ &= \Big(\frac{i}{\sqrt{2\hbar\omega m}}(-i)\hbar\frac{d}{dx} + \sqrt{\frac{k}{2\hbar\omega}}x\Big)\langle x|\alpha\rangle \\ &= \frac{1}{\sqrt{2\hbar\omega}}\Big(\frac{\hbar}{\sqrt{m}}\frac{d}{dx} + \sqrt{k}x\Big)\langle x|\alpha\rangle \qquad (2.46)\end{aligned}$$

where we have used Eqns. 2.6 and 2.7. We know that $\omega = \sqrt{\frac{k}{m}}$ and we let $\eta = \frac{\sqrt{km}}{\hbar}$, so $\eta = \frac{\omega m}{\hbar}$ and $\eta = \frac{k}{\omega\hbar}$

$$\Big(\frac{1}{\sqrt{2\eta}}\frac{d}{dx} + \sqrt{\frac{\eta}{2}}x\Big)\langle x|\alpha\rangle = \alpha\langle x|\alpha\rangle. \qquad (2.47)$$

From here we need to solve an ODE, as done in [57], to get

$$\langle x|\alpha\rangle = \big(\frac{\eta}{\pi}\big)^{\frac{1}{4}}\exp\Big(-\big(\mathrm{Im}(\alpha)\big)^2 - \frac{\eta}{2}\big(x-\alpha\sqrt{\frac{2}{\eta}}\big)^2\Big). \qquad (2.48)$$

Since we want $\hat{X} = \hat{a} + \hat{a}^\dagger$ we choose $\eta = \frac{1}{2}$ [63]. That is, from Eqn. 2.6 we have $\hat{a} + \hat{a}^\dagger = \sqrt{\frac{2m\omega}{\hbar}}\hat{x} = \sqrt{2\eta}\hat{x}$. We now have

$$\langle x|\alpha\rangle = \big(2\pi\big)^{-\frac{1}{4}}\exp\Big(-\big(\mathrm{Im}(\alpha)\big)^2 - \frac{1}{4}\big(x-2\alpha\big)^2\Big). \qquad (2.49)$$

If $\alpha \in \mathbb{R}$ we have $\langle x|\alpha\rangle = f(x,\alpha)$ where

$$f(x,\alpha) = \big(2\pi\big)^{-\frac{1}{4}}\exp\Big(-\frac{1}{4}\big(x-2\alpha\big)^2\Big). \qquad (2.50)$$

Also, we can calculate $\langle x|e^{i\theta}\alpha\rangle$

$$\begin{aligned}\langle x|e^{i\theta}\alpha\rangle &= \big(2\pi\big)^{-\frac{1}{4}}\exp\Big(-\alpha^2\sin^2\theta - \frac{1}{4}\big(x-2\alpha\cos(\theta)-2i\alpha\sin(\theta)\big)^2\Big) \\ &= \big(2\pi\big)^{-\frac{1}{4}}\exp\Big(-\frac{1}{4}\big(x-2\alpha\cos(\theta)\big)^2 + ix\alpha\sin(\theta) - 2i\alpha^2\sin(\theta)\cos(\theta)\Big) \\ &= f(x,\alpha\cos(\theta))\exp\Big(i\alpha\sin(\theta)\big(x-2\alpha\cos(\theta)\big)\Big) \\ &= f(x,\alpha\cos(\theta))\exp\Big(i\phi(x)\Big) \qquad (2.51)\end{aligned}$$

where

$$\phi(x) = \alpha\sin(\theta)\big(x-2\alpha\cos(\theta)\big). \qquad (2.52)$$

We see that this gives us the result found in Eqn. 2.44, since this is a Gaussian function with mean $2\alpha\cos(\theta)$ and a standard deviation of 1, a requirement for coherent states.

2.1.7 Master Equations and Photon Absorption

We define the density matrix to be an ensemble average of pure states:

$$\rho = \sum_a p_a |\psi_a\rangle\langle\psi_a| \tag{2.53}$$

with the following properties:

$$\begin{aligned} \mathrm{Tr}\left[\rho\right] &= 1 \\ \rho^2 &= \rho \text{ for pure } \rho \\ \rho^\dagger &= \rho \\ \mathrm{Tr}\left[\rho^2\right] &\leq 1. \end{aligned}$$

A master equation is an operator ordinary differential equation (ODE) that governs the evolution of a density matrix ρ. Given a closed system evolving under the interaction Hamiltonian $\hat{H}_I$, the master equation is given by the Liouvill-von Neumann equation, a generalisation of the Schrödinger equation and the Heisenberg equation of motion [64]

$$\frac{d\rho}{dt} = -i\left[\hat{H}_I, \rho\right] \tag{2.54}$$

where we measure t in units of $\hbar$.

When we consider a quantum optical system that is not closed, the evolution of the system is governed by the Lindblad master equation [65, 66, 64]:

$$\frac{d\rho}{dt} = \dot{\rho} = -i\left[\hat{H}_I, \rho\right] + \frac{1}{2}\sum_k \gamma_k \left(2\hat{A}_k\rho\hat{A}_k^\dagger - \hat{A}_k^\dagger\hat{A}_k\rho - \rho\hat{A}_k^\dagger\hat{A}_k\right) \tag{2.55}$$

where $\gamma_k \geq 0$ and the operators $\hat{A}_k$ are arbitrary linear operators, given in terms of annihilation and creation operators. For example, when $k = 1$ and $A_1 = \hat{a}^n$ we have a master equation describing n photon absorption and when $k = 1$ and $A_1 = \left(\hat{a}^\dagger\right)^n$ we have a master equation describing n photon emission [66]. When using the Lindblad master equation we must assume the system-environment coupling satisfies the Born-Markov approximation [67, 57]. That is, we must assume (i) the system and environment are initially uncorrelated; (ii) the system and environment only weakly interact; (iii) the size of the environment is large and is not significantly affected by the system; (iv) the correlations between the system and environment decay sufficiently rapidly such that the environment has no memory.

If we want to consider the case of just single photon absorption on our system, with no interaction Hamiltonian, we set $\hat{H}_I = 0$, $k = 1$ and $A_1 = \hat{a}$ in Eqn. 2.55 to get

$$\dot{\rho} = \frac{\gamma_1}{2}\left(2\hat{a}\rho\hat{a}^\dagger - \hat{a}^\dagger\hat{a}\rho - \rho\hat{a}^\dagger\hat{a}\right). \tag{2.56}$$

This will be considered equivalent to single photon loss throughout this thesis. The solution for this is given by [68]

$$\rho(t) = \exp\left(\left(\hat{J}+\hat{L}\right)t\right)\rho(0) \tag{2.57}$$

where

$$\begin{aligned}\hat{J}\rho &= \gamma_1 \hat{a}\rho\hat{a}^\dagger \\ \hat{L}\rho &= -\frac{\gamma_1}{2}\left(\hat{a}^\dagger\hat{a}\rho + \rho\hat{a}^\dagger\hat{a}\right).\end{aligned}$$

When there is a limited number of photons in the system being considered, we may not need to use the solution in Eqn. 2.57 explicitly, we may be able to solve the system of first order ODE's. Consider the single photon loss master equation in Eqn. 2.56 when we have the initial state $|n\rangle$. Since we can lose at most one photon, we only need to look at the terms $|n\rangle\langle n|$, $|n-1\rangle\langle n|$, $|n\rangle\langle n-1|$ and $|n-1\rangle\langle n-1|$:

$$\begin{aligned}\dot{\rho}_{n,n} &= \frac{\gamma_1}{2}\left(2(n+1)\rho_{n+1,n+1} - 2n\rho_{n,n}\right) \\ &= -\gamma_1 n\rho_{n,n} \\ \dot{\rho}_{n-1,n} &= \frac{\gamma_1}{2}\left(2\sqrt{n(n+1)}\rho_{n,n+1} - (2n-1)\rho_{n-1,n}\right) \\ &= -\frac{\gamma_1}{2}(2n-1)\rho_{n-1,n} \\ \dot{\rho}_{n-1,n-1} &= \frac{\gamma_2}{2}\left(2n\rho_{n,n} - 2(n-1)\rho_{n-1,n-1}\right)\end{aligned} \tag{2.58}$$

where $\rho_{i,j} = \langle i|\rho|j\rangle$, $\rho_{j,i} = \rho^\dagger_{i,j}$ and $\rho_{n+i,j} = 0, \forall i > 0$ since we start with the state $|n\rangle\langle n|$. Solving the coupled ODE's in Eqn. 2.58 gives

$$\begin{aligned}\rho_{n,n}(t) &= e^{-n\gamma_1 t}\rho_{n,n}(0) \\ \rho_{n-1,n}(t) &= e^{-\frac{1}{2}(2n-1)\gamma_1 t}\rho_{n-1,n}(0) \\ \rho_{n-1,n-1}(t) &= e^{-(n-1)\gamma_1 t}\rho_{n-1,n-1}(0) + ne^{-n\gamma_1 t}\left(e^{\gamma_1 t}-1\right)\rho_{n,n}(0).\end{aligned} \tag{2.59}$$

The initial state $|n\rangle\langle n|$ will evolve to

$$|n\rangle\langle n| \rightarrow ne^{-n\gamma_1 t}\left(e^{\gamma_1 t}-1\right)|n-1\rangle\langle n-1| + e^{-n\gamma_1 t}|n\rangle\langle n|.$$

For the case $n = 1$ this is

$$|1\rangle\langle 1| \rightarrow \left(1-e^{-\gamma_1 t}\right)|0\rangle\langle 0| + e^{-\gamma_1 t}|1\rangle\langle 1|. \tag{2.60}$$

If we want to consider the case of just two photon absorption on our system, with no interaction Hamiltonian, we set $\hat{H}_I = 0$, $k = 1$ and $A_1 = \hat{a}^2$ in Eqn. 2.55 to get

$$\dot{\rho} = \frac{\gamma_2}{2}\left(2\hat{a}^2\rho\left(\hat{a}^\dagger\right)^2 - \left(\hat{a}^\dagger\right)^2\hat{a}^2\rho - \rho\left(\hat{a}^\dagger\right)^2\hat{a}^2\right). \tag{2.61}$$

The general solution to this master equation was initially found in two steps. First a solution for the on-diagonal elements for the density matrix was found [65, 69], followed by a solution for the off-diagonal elements [70, 71]. The general density matrix, denoted $\psi_n(\mu,\tau) = \sqrt{\frac{(n+\mu)!}{n!}}\langle n|\rho(\tau)|n+\mu\rangle$, after time $\tau = \gamma_2 t$, is given by

$$\begin{aligned}
\psi_n(\mu,\tau) &= \sum_{\substack{k=n \\ (k-n\text{ even})}}^{\infty} \frac{(-1)^{k/2-n/2}2^n\Gamma(k/2+n/2+\sigma)}{n!\Gamma(\sigma)\Gamma(k/2-n/2+1)}A_k^\sigma e^{-\lambda_k\tau}, \quad \sigma \neq 0 \\
\psi_n(1,\tau) &= \sum_{\substack{k=n \\ (k-n\text{ even})}}^{\infty} \frac{(-1)^{k/2-n/2}2^{n-1}k\Gamma(k/2+n/2)}{n!\Gamma(k/2-n/2+1)}B_k e^{-k^2\tau},
\end{aligned} \tag{2.62}$$

where

$$\begin{aligned}
A_k^\sigma &= \frac{(k+\sigma)\Gamma(\sigma)}{2^k\sqrt{\pi}} \sum_{\substack{m=k \\ (m-k\text{ even})}}^{\infty} \frac{m!\Gamma(m/2-k/2+1/2)}{(m-k)!\Gamma(m/2+k/2+\sigma+1)}\psi_m(\mu,0), \quad \sigma \neq 0, \\
B_k &= \sum_{\substack{m=k \\ (m-k\text{ even})}}^{\infty} \frac{m!}{2^{m-\sigma(k)}(m/2+k/2)!(m/2-k/2)!}\psi_m(1,0),
\end{aligned}$$

$\sigma = (\mu-1)/2$, $\lambda_k = k(k+\mu-1)+\mu(\mu-1)/2$ and $\delta(k) = \begin{cases} 1 & \text{if } k > 0 \\ 0 & \text{if } k = 0 \end{cases}$

Once again, when there is a limited number of photons in the system being considered, we may not need to solve the two photon absorption master equation with Eqn. 2.62 explicitly, we may be able to solve the system of first order ODE's. Consider the two photon absorption master equation in Eqn. 2.61 when we have the initial state $|n\rangle$. Since we can only lose two photons, we only need to look at the terms $|n\rangle\langle n|$, $|n-2\rangle\langle n|$, $|n\rangle\langle n-2|$ and $|n-2\rangle\langle n-2|$:

$$\begin{aligned}
\dot{\rho}_{n,n} &= \frac{\gamma_2}{2}\left(2(n+2)(n+1)\rho_{n+2,n+2} - 2n(n-1)\rho_{n,n}\right) \\
&= -\gamma_2 n(n-1)\rho_{n,n} \\
\dot{\rho}_{n-2,n} &= \frac{\gamma_2}{2}\left(2\sqrt{(n+2)(n+1)n(n-1)}\rho_{n,n+2} - (n^2-3n+3)\rho_{n-2,n}\right) \\
&= -\frac{\gamma_2}{2}(n^2-3n+3)\rho_{n-2,n} \\
\dot{\rho}_{n-2,n-2} &= \frac{\gamma_2}{2}\left(2n(n-1)\rho_{n,n} - 2(n-2)(n-3)\rho_{n-2,n-2}\right)
\end{aligned} \tag{2.63}$$

where $\rho_{i,j} = \langle i|\rho|j\rangle$, $\rho_{j,i} = \rho_{i,j}^\dagger$ and $\rho_{n+i,j} = 0, \forall i > 0$ since we start with the state $|n\rangle\langle n|$. Solving the coupled ODE's in Eqn. 2.63 gives

$$\begin{aligned}
\rho_{n,n}(t) &= e^{-n(n-1)\gamma_2 t}\rho_{n,n}(0) \\
\rho_{n-2,n}(t) &= e^{-\frac{1}{2}(n^2-3n+3)\gamma_2 t}\rho_{n-2,n}(0) \\
\rho_{n-2,n-2}(t) &= e^{-(n-2)(n-3)\gamma_2 t}\left(\rho_{n-2,n-2}(0) + \frac{n(n-1)}{4n-6}\left(1-e^{-2(2n-3)\gamma_2 t}\right)\rho_{n,n}(0)\right).
\end{aligned} \tag{2.64}$$

The initial state $|n\rangle\langle n|$ will evolve to

$$|n\rangle\langle n| \rightarrow \frac{n(n-1)e^{-(n-2)(n-3)\gamma_2 t}}{4n-6}\left(1-e^{-2(2n-3)\gamma_2 t}\right)|n-2\rangle\langle n-2| + e^{-n(n-1)\gamma_2 t}|n\rangle\langle n|.$$

For the case $n = 2$ this is

$$|2\rangle\langle 2| \rightarrow \left(1-e^{-2\gamma_2 t}\right)|0\rangle\langle 0| + e^{-2\gamma_2 t}|2\rangle\langle 2|. \tag{2.65}$$

2.2 Non-Linear Optical Computing

In this section we describe the first proposal to implement a universal multi-qubit gate with optics [29, 28].

2.2.1 Quantum Optical Fredkin Gate

The first proposal for quantum computation was the quantum optical Fredkin gate [29, 28]. The gate was constructed with single photon optics using the Kerr Effect. A Fredkin gate is a three qubit gate that acts as a controlled swap. The truth table is given in Table 2.1. In this scheme, logical 0 corresponds to the vacuum mode $|0\rangle$ and logical 1 is the single photon Fock state $|1\rangle$.

c_i	a_i	b_i	c_o	a_o	b_o
0	0	0	0	0	0
0	0	1	0	0	1
0	1	0	0	1	0
0	1	1	0	1	1
1	0	0	1	0	0
1	0	1	1	1	0
1	1	0	1	0	1
1	1	1	1	1	1

Table 2.1: The logic for a Fredkin gate. Here subscript i refers to the input qubits, o refers to the output qubits and c is the control qubit.

The optical Kerr effect is defined by a material with an intensity dependent refractive index, that is, a nonlinear crystal that has an index of refraction n proportional to the total intensity I: $n = n_0 + n_2E^2 = n_0 + n_2I$, where n_0 is the normal refractive index and n_2 is the correction term necessary for Kerr materials [72].

The Kerr Hamiltonian is of the form

$$H_I = -\hbar\chi\hat{a}_1^\dagger\hat{a}_1\hat{a}_2^\dagger\hat{a}_2 \tag{2.66}$$

where χ is a coupling constant which depends upon the third-order non-linear susceptibility for the optical Kerr effect and $\hat{a}_1$ and $\hat{a}_2$ are the annihilation modes for the input light.

The optical setup for the Fredkin gate first proposed in [28] is shown below in Fig. 2.4. In this setup we have a Mach-Zehnder interferometer with a Kerr media in either arm. In the top arm the Kerr media has the control beam incident on it. In the bottom arm the Kerr media only has photons incident from mode b, mode d is always the vacuum state. This bottom arm Kerr media is included so that the optical length for photons in both modes a and b is equal. The beam splitter on the left side, BS1, has $\theta = \frac{\pi}{4}, \phi = 0$ and the beam splitter on the right hand side, BS2, has $\theta = \frac{\pi}{4}, \phi = \pi$. The effect of the Kerr media is to act the unitary operator $U = \exp\left(-i\frac{t}{\hbar}H_I\right) = \exp\left(i\epsilon\hat{a}^\dagger\hat{a}\hat{c}^\dagger\hat{c}\right)$ in the top arm and $U = \exp\left(i\epsilon\hat{b}^\dagger\hat{b}\hat{d}^\dagger\hat{d}\right)$ in the bottom arm, where $\epsilon = \frac{t\chi}{\hbar}$ and t is the length of time photons spend inside the Kerr media.

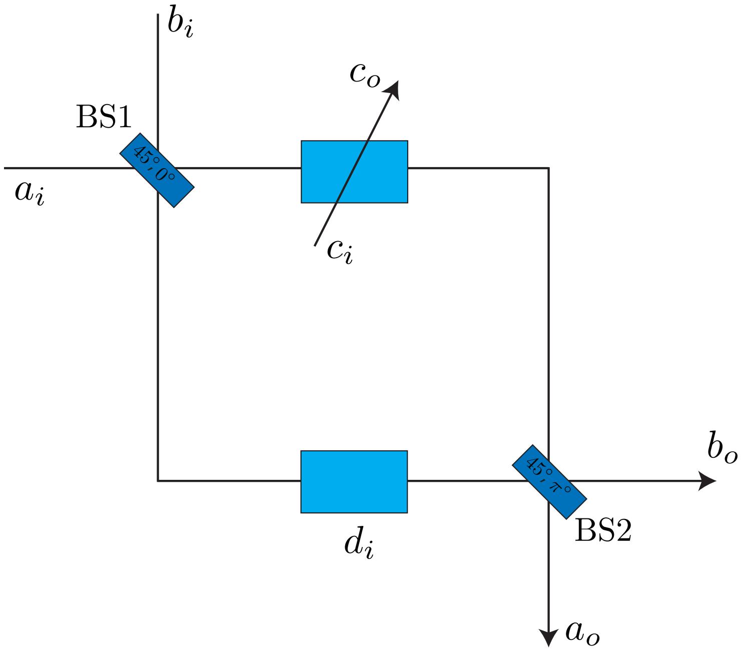

Figure 2.4: The original quantum Fredkin gate [28].

For example, consider the input state $|cab, d\rangle = |010, 0\rangle$

$$\begin{aligned}
|010,0\rangle \quad & \rightarrow \frac{1}{\sqrt{2}}\big(|010,0\rangle + |001,0\rangle\big) \\
& \rightarrow \frac{1}{\sqrt{2}} e^{i\epsilon \hat{c}^\dagger \hat{c} \hat{a}^\dagger \hat{a}} e^{i\epsilon \hat{b}^\dagger \hat{b} \hat{d}^\dagger \hat{d}} \big(|010,0\rangle + |001,0\rangle\big) \\
& = \frac{1}{\sqrt{2}}\big(e^{i\epsilon \hat{c}^\dagger \hat{c} \hat{a}^\dagger \hat{a}}|010,0\rangle + e^{i\epsilon \hat{b}^\dagger \hat{b} \hat{d}^\dagger \hat{d}}|001,0\rangle\big) \\
& = \frac{1}{\sqrt{2}}\big(|010,0\rangle + |001,0\rangle\big) \rightarrow |010,0\rangle
\end{aligned}$$

where mode d is always in the vacuum mode $|0\rangle$ and remember that $e^{i\phi\hat{n}}|m\rangle = e^{im\phi}|m\rangle$.

Next consider the input $|101, 0\rangle$

$$\begin{aligned}
|101,0\rangle \quad & \rightarrow \frac{1}{\sqrt{2}}\big(|101,0\rangle - |110,0\rangle\big) \\
& \rightarrow \frac{1}{\sqrt{2}}\big(-e^{i\epsilon \hat{c}^\dagger \hat{c} \hat{a}^\dagger \hat{a}}|110,0\rangle + e^{i\epsilon \hat{b}^\dagger \hat{b} \hat{d}^\dagger \hat{d}}|101,0\rangle\big) \\
& \rightarrow \frac{1}{\sqrt{2}}\big(-e^{i\epsilon}|110,0\rangle + |101,0\rangle\big) \\
& \rightarrow \frac{1}{2}\big(-e^{i\epsilon}|110,0\rangle + e^{i\epsilon}|101,0\rangle + |101,0\rangle + |110,0\rangle\big).
\end{aligned}$$

If we choose $\epsilon = \pi$ this gives $|110, 0\rangle$. With this choice of ϵ we can show that all the logic gates are as in the Fredkin gate logic table.

There are two major problems with this scheme: (1) it is difficult to achieve the high nonlinearities, especially those required for $\epsilon = \pi$ phase change; (2) at high nonlinearities the crystal exhibits other detrimental affects, such as absorption.

The technique from the scheme presented in Fig. 2.4 can be used to induce a CNOT between optical qubits, as shown in [30].

2.3 Process Fidelity

The fidelity between the two density matrices ρ and σ is given by [73]

$$F(\rho, \sigma) = \Big(\mathrm{Tr}[\sqrt{\sqrt{\rho}\sigma\sqrt{\rho}}\,]\Big)^2. \tag{2.67}$$

This fidelity definition is symmetric: $F(\rho, \sigma) = F(\sigma, \rho)$

When ρ is pure, $\rho = |\psi\rangle\langle\psi|$, the fidelity is equal to the overlap between $|\psi\rangle$ and σ:

$$F(\rho, \sigma) = \langle\psi|\sigma|\psi\rangle, \tag{2.68}$$

where we have used the fact that $\rho^2 = \rho$ for pure ρ.

To quantify gate performance for an imperfect quantum gate, in general a quantum operation $\mathcal{E}(\rho)$, with respect to the ideal quantum gate U, we use the process fidelity F_p. A general quantum operation $\mathcal{E}(\rho)$ on the Hilbert space $\mathcal{H}$ of dimension d is isomorphic to density matrices in $\mathcal{H}\otimes\mathcal{H}$ [74] via

$$\rho_{\mathcal{E}} = \mathcal{I}\otimes\mathcal{E}(|\phi\rangle\langle\phi|), \tag{2.69}$$

where $|\phi\rangle$ is a maximally entangled state $\sum_j |j\rangle|j\rangle/\sqrt{d}$ in $\mathcal{H}\otimes\mathcal{H}$. The process fidelity is then the fidelity between this process density matrix and the one associated with the ideal gate U

$$F_{\mathrm{p}} = F(\rho_{\mathcal{E}}, \rho_U). \tag{2.70}$$

That is, the process fidelity is the overlap between sending half of a maximally entangled state through the imperfect quantum gate $\mathcal{E}$ (Fig. 2.5 (a)) and sending half of a maximally entangled state through the imperfect quantum gate U (Fig. 2.5 (b)).

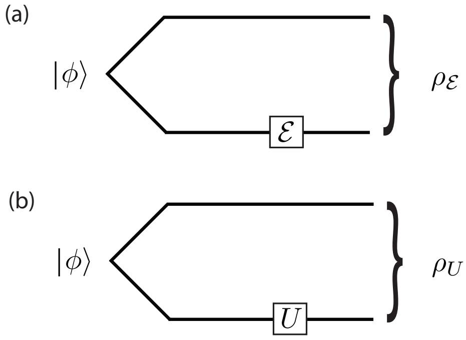

Figure 2.5: Half a maximally entangled state $|\phi\rangle$ goes through a general quantum operation $\mathcal{E}(\rho)$ in part (a) and through the ideal quantum gate in part (b).

The process fidelity is linearly related to the average gate fidelity $\bar{F}$, via $F_{\mathrm{p}} = (\bar{F}d+1)/(d+1)$, where d is the dimension of the system [75, 73].

2.4 Previous Progress with Linear Optics

We saw in Section 2.2.1 that to induce photon interaction we required cross Kerr non-linearities on the order of π. We know we cannot build a deterministic two qubit gate between photons with linear optics alone since Lütkenhaus *et al.* have shown that Bell state measurements with linear optics can work at best 50% of the time [76]. In this section we give the details of some of the prior progress that was made with linear optics for optical QIP before the work by Knill *et al.* in [31].

2.4.1 Decomposition of unitaries

Reck *et al.* showed that we can break *any* unitary into a set of linear optical components [77]. The unitary transformation considered is acting on the creation operators.

A unitary operator U of dimension N can be decomposed into $\frac{N}{2}(N-1)$ beam splitters as follows:

$$U = \left(T_{N,N-1} \cdot T_{N,N-2} \cdot T_{N,N-3} \cdots T_{N,1} \cdot T_{N-1,N-2} \cdot T_{N-1,N-3} \cdots T_{2,1} D\right)^{-1} \tag{2.71}$$

where $T_{p,q}$ is the N dimensional identity with the $\{p, q\}$ elements replaced with the beam splitter matrix (2.36) and D is an $N \times N$ matrix with phases on the diagonal.

The general linear optical network for a unitary matrix U is a triangular array of beam splitters and phase shifters, shown in Fig. 2.6.

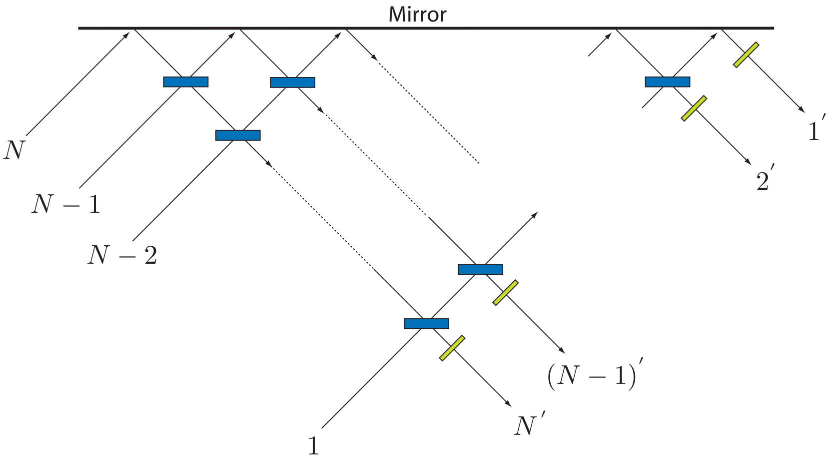

Figure 2.6: General linear optical network for a unitary matrix U.

As an example, we can break the following unitary into a linear optical circuit:

$$U = \begin{pmatrix} 1-\sqrt{2} & \frac{1}{\sqrt{\sqrt{2}}} & \sqrt{\frac{3}{\sqrt{2}}-2} \\ \frac{1}{\sqrt{\sqrt{2}}} & \frac{1}{2} & \frac{1}{2}-\frac{1}{\sqrt{2}} \\ \sqrt{\frac{3}{\sqrt{2}}-2} & \frac{1}{2}-\frac{1}{\sqrt{2}} & \sqrt{2}-\frac{1}{2} \end{pmatrix}.$$

Here we have a unitary matrix with N=3, so we can say that

$$U = \Big(T_{3,2}\cdot T_{3,1}\cdot T_{2,1}\cdot D\Big)^{-1} = D^\dagger\cdot T_{2,1}^\dagger\cdot T_{3,1}^\dagger\cdot T_{3,2}^\dagger.$$

We find that

$$T_{3,2} = \begin{pmatrix} 1 & 0 & 0 \\ 0 & \cos\theta_1 & e^{-i\phi_1}\sin\theta_1 \\ 0 & -e^{i\phi_1}\sin\theta_1 & \cos\theta_1 \end{pmatrix}$$

$$T_{3,1} = \begin{pmatrix} \cos\theta_2 & 0 & e^{-i\phi_2}\sin\theta_2 \\ 0 & 1 & 0 \\ -e^{i\phi_2}\sin\theta_2 & 0 & \cos\theta_2 \end{pmatrix}$$

$$T_{2,1} = \begin{pmatrix} \cos\theta_3 & e^{-i\phi_3}\sin\theta_3 & 0 \\ -e^{i\phi_3}\sin\theta_3 & \cos\theta_3 & 0 \\ 0 & 0 & 1 \end{pmatrix}$$

and

$$D = \begin{pmatrix} e^{i\phi_4} & 0 & 0 \\ 0 & e^{i\phi_5} & 0 \\ 0 & 0 & e^{i\phi_6} \end{pmatrix}.$$

With the solution: $\theta_1 = 12.8^o, \phi_1 = \pi,\ \theta_2 = 20.4^o, \phi_2 = 0,\ \theta_3 = 63.8, \phi_3 = 0,$ $\phi_4 = 180, \phi_5 = 0, \phi_6 = 0$.

2.4.2 Optical Simulation of Quantum Logic

In [78], Cerf *et al.* proposed a scheme for quantum logic with only linear optical devices and a single photon. To simulate n qubits a single photon is put into a superposition of 2^n different paths. The position of the photon corresponds to the logical n-qubit state. For example, consider the $n = 3$ case. We require the photon to be in a superposition of 8 paths, which we write as an 8×1 column vector. The logical state $|000\rangle_L$ corresponds to the photon in path 1, $|1000000\rangle^T$, whereas the logical state $|110\rangle_L$ corresponds to the photon in path 7, $|0000010\rangle^T$.

A $\sqrt{\text{NOT}}$ gate is given by a beam splitter with $\theta = \frac{\pi}{4}$ and $\phi = -\frac{\pi}{2}$, where

$$\sqrt{\text{NOT}} = \frac{1}{\sqrt{2}} \begin{pmatrix} 1 & i \\ i & 1 \end{pmatrix}$$

$$|0\rangle_q = |01\rangle \rightarrow \frac{1}{\sqrt{2}}\big(i|10\rangle + |01\rangle\big)$$
$$|1\rangle_q = |10\rangle \rightarrow \frac{1}{\sqrt{2}}\big(|10\rangle + i|01\rangle\big).$$

Three simple gate implementations proposed by Cerf *et al.* are given in Fig. 2.7. With these, a universal set of gates is possible.

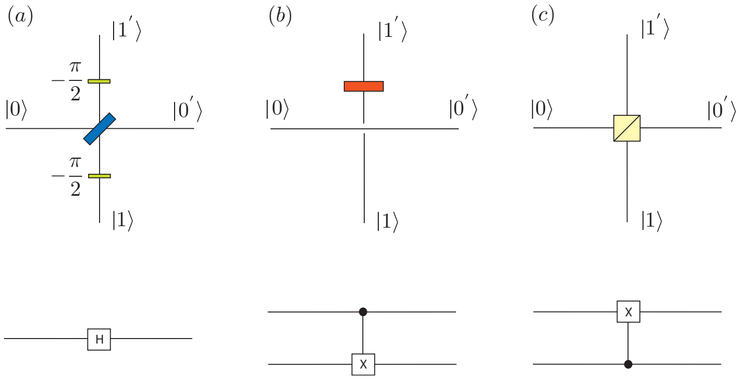

Figure 2.7: A Hadamard, a CNOT and a reverse CNOT .

To implement a Hadamard gate we use a $\theta = \frac{\pi}{4}, \phi = -\frac{\pi}{2}$ beam splitter and two $-\frac{\pi}{2}$ phase shifters, as in part (a) of Fig. 2.7:

$$\begin{aligned} |0\rangle_q = |01\rangle \rightarrow -i|01\rangle \rightarrow -\frac{i}{\sqrt{2}}\big(|01\rangle + i|10\rangle\big) \\ \rightarrow \frac{-i}{\sqrt{2}}\big(|01\rangle + i(-i)|10\rangle\big) = \frac{-i}{\sqrt{2}}\big(|01\rangle + |10\rangle\big) \\ |1\rangle_q = |10\rangle \rightarrow |10\rangle \rightarrow \frac{1}{\sqrt{2}}\big(i|01\rangle + |10\rangle\big) \\ \rightarrow \frac{1}{\sqrt{2}}\big(i|01\rangle + -i|10\rangle\big) = \frac{i}{\sqrt{2}}\big(|01\rangle - |10\rangle\big). \end{aligned}$$

To implement a CNOT we encode a qubit in position and polarisation. The location is the control and the polarisation the target. For the control: $|0\rangle_q = |01\rangle$, $|1\rangle_q = |10\rangle$. For the target: $|0\rangle_q = |H\rangle$, $|1\rangle_q = |V\rangle$. The circuit for this is a polarisation rotator on the upper arm, as in part (b) of Fig. 2.7. If a photon is present in the top arm, its polarisation will be flipped:

$$\begin{aligned} &\big(\alpha|01\rangle + \beta|10\rangle\big) \otimes \big(\gamma|H\rangle + \delta|V\rangle\big) \\ &\rightarrow \alpha\gamma|01\rangle|H\rangle + \alpha\delta|01\rangle|V\rangle + \beta\gamma|10\rangle|V\rangle + \beta\delta|10\rangle|H\rangle \end{aligned}$$

To implement a reverse CNOT we simply need a polarising beam splitter (PBS), where horizontal is reflected. As before, the location is the control and the polarisation the target. This is in part (c) of Fig. 2.7:

$$\begin{aligned}&\big(\alpha|01\rangle + \beta|10\rangle\big) \otimes \big(\gamma|H\rangle + \delta|V\rangle\big)\\ &\quad \rightarrow \alpha\gamma|01\rangle|H\rangle + \alpha\delta|10\rangle|V\rangle + \beta\gamma|10\rangle|H\rangle + \beta\delta|01\rangle|V\rangle\end{aligned}$$

The problem with this scheme is that n qubits requires 2^n paths which in turn requires $2^n - 1$ beam splitters to setup. This is not efficiently scalable. With one qubit encoded in polarisation we still need 2^{n-1} optical paths.

2.5 Linear Optics Quantum Computing

It is not known whether we can efficiently simulate an ideal quantum computer with linear optics alone. A scheme has been suggested by Cerf *et al.* [78], described in Section 2.4.2, that requires an exponential amount of resources. In this section we present the so called linear optics quantum computing (LOQC) scheme from [31]. We show that beam splitters, phase shifters, single photon sources and detectors can efficiently simulate an ideal quantum computer. By efficiently simulate we mean to use a polynomial amount of resources. It is when we allow for detections and feed forward that we can efficiently simulate a quantum computer. The basic resources that are necessary for LOQC are linear optics, as described in Section 2.1.5, single photon sources and photon detectors that can distinguish between 0, 1 and 2 photons.

2.5.1 Qubits in LOQC

In LOQC we encode qubits with dual rail logic. That is, logic that is encoded using the physical location of a photon. Logical 0 is given by $|0\rangle_q = |01\rangle_{ab}$ and logical 1 by $|1\rangle_q = |10\rangle_{ab}$, where mode a is one spatial mode and mode b another.

Polarisation is an equivalent encoding of optical qubits: $|0\rangle_q = |H\rangle$, $|1\rangle_q = |V\rangle$. We can change the representation of the qubit from polarisation to dual rail using a polarising rotator and a polarising beam splitter as can be seen below in Fig. 2.8.

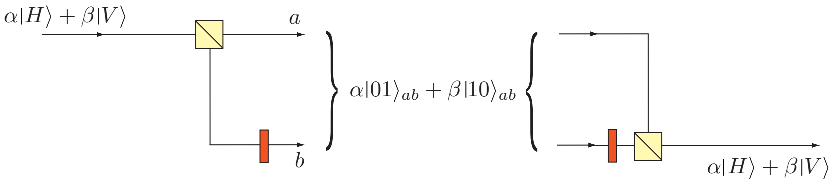

Figure 2.8: Transforming from dual rail to polarisation encoding.

2.5.2 Qubit Operations

For a physical system to be a viable candidate for quantum computation, we need a universal set of gates, as stated in point 3 of DiVincenzo's five criteria [27], seen in Chapter 1. Arbitrary single qubit gates and the CNOT operation is one such universal set [10].

Single qubit operations are easily performed using linear optical elements, shown in the next section. Since it it quite difficult to induce photon interaction, two qubit operations are considerably more difficult. In Section 2.5.4 we show a probabilistic two qubit gate with the use of single photon ancillas and photon detection. The required non-linearity is in the form of measurement. Since it is probabilistic, this two qubit gate is not sufficient for quantum computation. We can build an asymptotically deterministic two qubit gate with the use of quantum teleportation. The resources for this teleported gate can be reduced with the use of quantum error correction, as will be shown in Section 2.6. Once the error rate is below the required threshold we can use the accuracy threshold theorem [79].

2.5.3 Single qubit gates

All single qubit gates can be implemented with just beam splitters and phase shifters. To see this, note that any single qubit unitary, U, can be decomposed into rotations about the Z and Y axis in the Bloch sphere as follows [79]:

$$U = e^{i\alpha} R_z(\beta) R_y(\gamma) R_z(\delta) \tag{2.72}$$

where $R_z(\theta) = e^{-i\frac{\theta}{2}\sigma_z}$ and $R_y(\phi) = e^{-i\frac{\phi}{2}\sigma_y}$. For example, $R_x(\vartheta) = R_z(\frac{\pi}{2}) R_y(-\vartheta) R_z(-\frac{\pi}{2})$. If we can show how to make arbitrary rotations about the Z and Y axis we can perform any arbitrary single qubit operation.

Rotations about the Z axis can simply be performed using a phase shifter on the top mode of a dual rail qubit. This can be seen by looking at how the

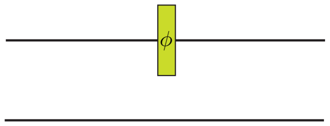

Figure 2.9: Performs a rotation of ϕ about the Z axis: $R_Z(\phi)$.

state $\alpha|0\rangle_q + \beta|1\rangle_q$ is transformed by Fig. 2.9, up to irrelevant global phases:

$$\begin{aligned}
\alpha|0\rangle_q + \beta|1\rangle_q &= \alpha|01\rangle + \beta|10\rangle \\
&\rightarrow \alpha|01\rangle + \beta e^{i\phi}|10\rangle \\
&= e^{i\phi/2}(e^{-i\phi/2}\alpha|0\rangle_q + e^{i\phi/2}\beta|1\rangle_q) \\
&= e^{i\phi/2}e^{-i\phi\sigma_z/2}(\alpha|0\rangle_q + \beta|1\rangle_q) \\
&= e^{i\phi/2}R_Z(\phi)(\alpha|0\rangle_q + \beta|1\rangle_q).
\end{aligned}$$

Rotations of -2θ about the Y axis require a beam splitter of angle θ and $\phi = 0$, up to irrelevant global phases. This can be seen by looking at how the state $\alpha|0\rangle_q + \beta|1\rangle_q$ is transformed by Fig. 2.10.

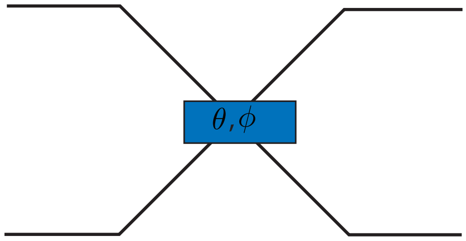

Figure 2.10: Performs a rotation of -2θ about the Y axis: $R_Y(-2\theta)$ when $\phi = 0$.

$$\begin{aligned}
\alpha|0\rangle_q + \beta|1\rangle_q &= \alpha|01\rangle + \beta|10\rangle \\
&\rightarrow \alpha\big(\cos(\theta)|01\rangle - \sin(\theta)|10\rangle\big) + \beta\big(\cos(\theta)|10\rangle + \sin(\theta)|01\rangle\big) \\
&= \cos(\theta)\big(\alpha|01\rangle + \beta|10\rangle\big) - \sin(\theta)\big(\alpha|10\rangle - \beta|01\rangle\big) \\
&= e^{i\theta Y_q}\big(\alpha|0\rangle_q + \beta|1\rangle_q\big) \\
&= R_Y(-2\theta)\big(\alpha|0\rangle_q + \beta|1\rangle_q\big).
\end{aligned}$$

2.5.4 Two qubit gates

In this section we address the question of how to make a two qubit gate with just linear optics, single photon ancillas and photo-detection. Since both the Pauli X and Pauli Z matrices have the same eigenvalues, using the spectral decomposition theorem [79] we know that $X = UZU^\dagger$, for some unitary U. In this case U is the Hadamard matrix H, defined below. This means the CNOT gate and CSIGN gate are equivalent, as shown in Fig. 2.11. In this section we will consider the construction of a CSIGN gate. The CNOT gate is defined as $|x\rangle_L|y\rangle_L \rightarrow |x\rangle_L|y \oplus x \bmod 2\rangle_L$ and the CSIGN gate is defined as $|x\rangle_L|y\rangle_L \rightarrow e^{i\pi x\cdot y}|x\rangle_L|y\rangle_L$, for $x, y \in \{0,1\}$. In terms of matrices, the CNOT, or controlled-X gate is defined by

$$U_{\text{CNOT}} = \begin{pmatrix} 1 & 0 & 0 & 0 \\ 0 & 1 & 0 & 0 \\ 0 & 0 & 0 & 1 \\ 0 & 0 & 1 & 0 \end{pmatrix}, \tag{2.73}$$

the CSIGN, or controlled-Z gate is defined by

$$U_{\text{CZ}} = \begin{pmatrix} 1 & 0 & 0 & 0 \\ 0 & 1 & 0 & 0 \\ 0 & 0 & 1 & 0 \\ 0 & 0 & 0 & -1 \end{pmatrix} \tag{2.74}$$

and the Hadamard is defined by

$$H = \frac{1}{\sqrt{2}}\begin{pmatrix} 1 & 1 \\ 1 & -1 \end{pmatrix} \tag{2.75}$$

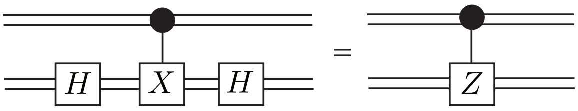

Figure 2.11: The equivalence between the CNOT and CSIGN gate. The double lines here represent dual rail qubits.

To perform a probabilistic CSIGN gate we need the so called non-linear sign shift (NS_{-1}) transformation:

$$|\psi\rangle = \alpha|0\rangle + \beta|1\rangle + \gamma|2\rangle \rightarrow \alpha|0\rangle + \beta|1\rangle - \gamma|2\rangle. \tag{2.76}$$

Nonlinear sign shift gate

As the above transformation is non-linear, that is since the transformation is non-linear in the action of the creation operators, we cannot use linear optics alone. With the use of one single photon ancilla and one vacuum ancilla mode,

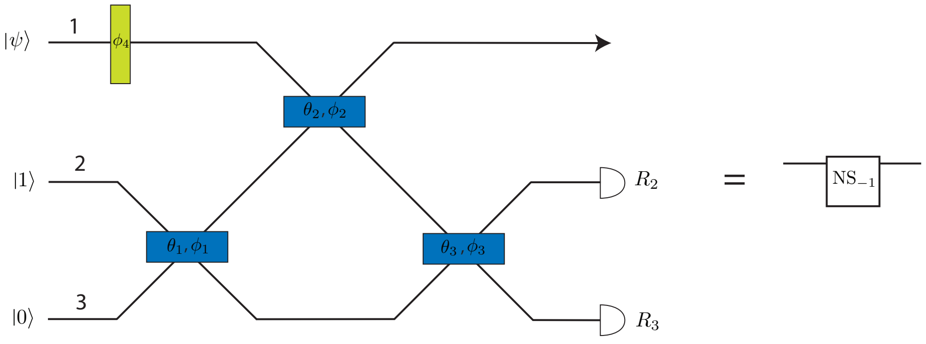

Figure 2.12: The NS_{-1} gate. Here $\theta_1 = 22.5°, \phi_1 = 0°$, $\theta_2 = 65.5302°, \phi_2 = 0°$, $\theta_3 = -22.5°, \phi_3 = 0°$ and $\phi_4 = 180°$. The NS_{-1} transformation takes place when $R_2 = 1$ and $R_3 = 0$. This occurs with a probability of 1/4.

along with photon detection, we can perform this transformation, shown in Fig. 2.12. The input state is given by $\big(\alpha|0\rangle_1 + \beta|1\rangle_1 + \gamma|2\rangle_1\big) \otimes |1\rangle_2 \otimes |0\rangle_3$.

The action of this circuit is to apply the following unitary matrix on the input modes:

$$U\begin{pmatrix} \hat{a}_1^\dagger \\ \hat{a}_2^\dagger \\ \hat{a}_3^\dagger \end{pmatrix} = \begin{pmatrix} 1-\sqrt{2} & \frac{1}{\sqrt{\sqrt{2}}} & \sqrt{\frac{3}{\sqrt{2}}-2} \\ \frac{1}{\sqrt{\sqrt{2}}} & \frac{1}{2} & \frac{1}{2}-\frac{1}{\sqrt{2}} \\ \sqrt{\frac{3}{\sqrt{2}}-2} & \frac{1}{2}-\frac{1}{\sqrt{2}} & \sqrt{2}-\frac{1}{2} \end{pmatrix}\begin{pmatrix} \hat{a}_1^\dagger \\ \hat{a}_2^\dagger \\ \hat{a}_3^\dagger \end{pmatrix}.$$

Notice that beam splitter array for U shown in Fig. 2.12 is different to the array predicted in Section 2.4.1. This is due to the fact that we can break any unitary into two different types of beam splitter arrays, a V array, as shown in Fig. 2.6, or a Λ array, as in Fig. 2.12

When we measure a single photon in mode 2 of Fig. 2.12 and vacuum in mode 3, we have the state $\alpha|0\rangle_1 + \beta|1\rangle_1 - \gamma|2\rangle_1$ output in mode 1. The probability of measuring a single photon in mode 2 and vacuum in mode 3 is $\frac{1}{4}$.

Controlled Sign gate

The NS_{-1} gate is an essential ingredient for the probabilistic CSIGN, since it both provides a way for the state of the system to return to the dual rail basis and applies the necessary phase shift for an entangling gate to be made, as shown by Knill *et al.* [31]. With the use of two NS_{-1} gates we can make a CSIGN gate, as seen in the Fig. 2.13.

Say we start with the input state $|Q_1\rangle = \alpha|0\rangle_q + \beta|1\rangle_q = \alpha|01\rangle_{12} + \beta|10\rangle_{12}$ in modes 1 and 2 and $|Q_2\rangle = \gamma|0\rangle_q + \delta|1\rangle_q = \gamma|01\rangle_{34} + \delta|10\rangle_{34}$ in modes 3 and

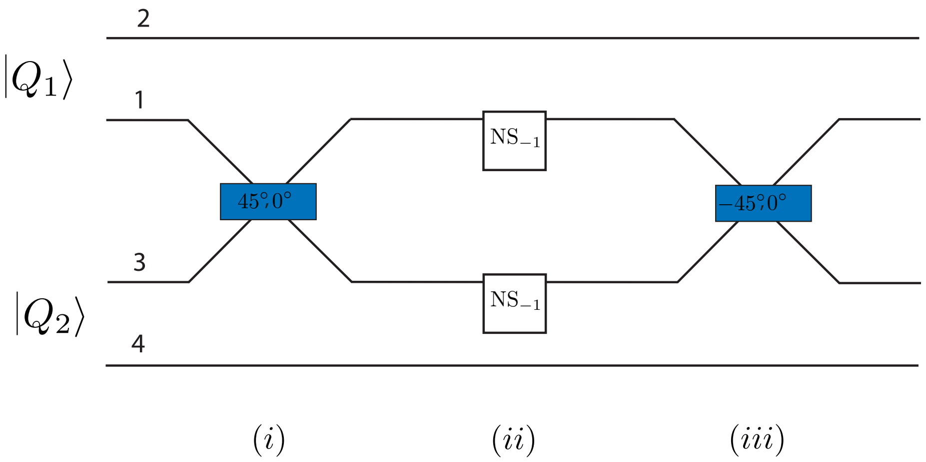

Figure 2.13: A probabilistic CSIGN gate. The probability of success is $\frac{1}{16}$. Qubit 1 $|Q\rangle_1$ is incident on modes 1 and 2 and qubit 2 $|Q\rangle_2$ is incident on modes 3 and 4.

4. After the first beam splitter, (i) in Fig. 2.13, the state $|Q_1\rangle|Q_2\rangle$ becomes:

$$\begin{aligned}\to \alpha\gamma|0101\rangle - \frac{\alpha\delta}{\sqrt{2}}|1100\rangle + \frac{\alpha\delta}{\sqrt{2}}|0110\rangle + \frac{\beta\gamma}{\sqrt{2}}|1001\rangle \\ + \frac{\beta\gamma}{\sqrt{2}}|0011\rangle - \frac{\beta\delta}{\sqrt{2}}|2000\rangle + \frac{\beta\delta}{\sqrt{2}}|0020\rangle.\end{aligned}$$

After the two NS$_{-1}$ gates, (ii) in Fig. 2.13, we have

$$\begin{aligned}\to \alpha\gamma|0101\rangle - \frac{\alpha\delta}{\sqrt{2}}|1100\rangle + \frac{\alpha\delta}{\sqrt{2}}|0110\rangle + \frac{\beta\gamma}{\sqrt{2}}|1001\rangle \\ + \frac{\beta\gamma}{\sqrt{2}}|0011\rangle + \frac{\beta\delta}{\sqrt{2}}|2000\rangle - \frac{\beta\delta}{\sqrt{2}}|0020\rangle.\end{aligned}$$

After the final beam splitter, (iii) in Fig. 2.13, we have

$$\begin{aligned}&\to \alpha\gamma|0101\rangle + \alpha\delta|0110\rangle + \beta\gamma|1001\rangle - \beta\delta|1010\rangle \\ &= \alpha\gamma|00\rangle_q + \alpha\delta|01\rangle_q + \beta\gamma|10\rangle_q - \beta\delta|11\rangle_q.\end{aligned}$$

This gate works with a probability of $\frac{1}{16}$. That is, there is a probability of $\frac{1}{16}$ that we will measure the ancilla state $|10\rangle$ in both NS$_{-1}$ gates. It is important to notice that when the result of the measurement of the ancilla state is other than $|10\rangle$, the gate fails but we know that this failure has occurred. An interesting point worth mentioning is that during the gate, between points (i) and (iii) in Fig. 2.13, the state of the system has terms outside the qubit Hilbert space.

The state

$$\frac{1}{2}\Big(|0101\rangle + |0110\rangle + |1001\rangle - |1010\rangle\Big) \qquad (2.77)$$

is the first building block to performing a CSIGN on photonic qubits with probability arbitrarily close to 1.

Teleporting qubits through a gate

In Fig. 2.13 we have a probabilistic CSIGN . This is not enough to allow scalable quantum computation. The probabilistic CSIGN gate will be used as an entangled state production stage.

To perform a two qubit gate we can teleport [80] the qubits through the gate, as first shown by Gottesman and Chuang [32].

Say we have two arbitrary qubits $|\psi_1\rangle_q$ and $|\psi_2\rangle_q$ that we want to perform a CSIGN on. We could teleport both these qubits and then apply a CSIGN on them, as seen in the Fig. 2.14.

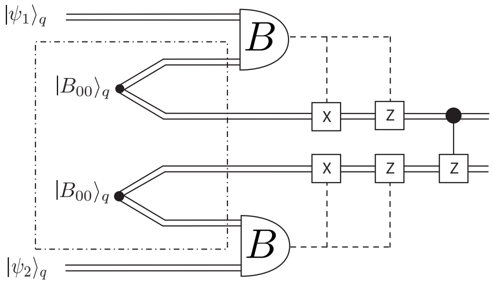

Figure 2.14: An application a CSIGN between qubits $|\psi_1\rangle_q$ and $|\psi_2\rangle_q$. The dashed-dotted box is the state preparation area. In this case just the Bell states $|B_{00}\rangle = (|0101\rangle + |1010\rangle)/\sqrt{2}$ need to be prepared.

Since CSIGN is its own inverse, we can add two CSIGN 's to Fig. 2.14 as seen in Fig. 2.15.

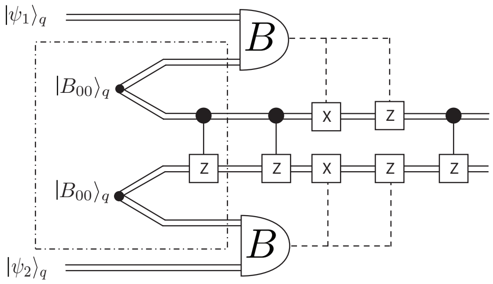

Figure 2.15: An application a CSIGN between qubits $|\psi_1\rangle_q$ and $|\psi_2\rangle_q$.

We now have a CSIGN inside the dashed-dotted box, the state preparation area. To see how the correction gates are transformed by the CSIGN gates outside the box we use the following identities:

$$\begin{aligned}
\text{CSIGN}\left(\sigma_x \otimes \mathbb{1}\right)\text{CSIGN} &= \sigma_x \otimes \sigma_z \\
\text{CSIGN}\left(\mathbb{1} \otimes \sigma_x\right)\text{CSIGN} &= \sigma_z \otimes \sigma_x \\
\text{CSIGN}\left(\sigma_z \otimes \mathbb{1}\right)\text{CSIGN} &= \sigma_z \otimes \mathbb{1} \\
\text{CSIGN}\left(\mathbb{1} \otimes \sigma_z\right)\text{CSIGN} &= \mathbb{1} \otimes \sigma_z .
\end{aligned}$$

Applying these identities gives the circuit shown in Fig. 2.16:

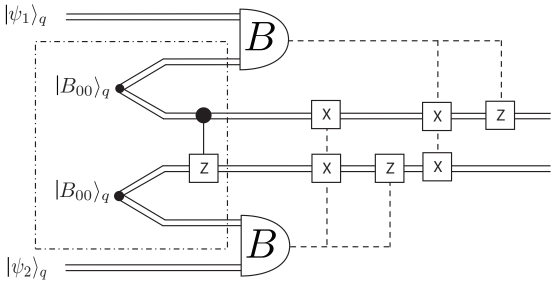

Figure 2.16: An application a CSIGN between qubits $|\psi_1\rangle_q$ and $|\psi_2\rangle_q$.

The problem of performing a CSIGN has now been turned into a state preparation problem. We can apply the CSIGN gate in Fig. 2.13 probabilistically offline. Once we know we have a successful CSIGN preparation state (Eqn. 2.77), we can proceed and teleport the information qubits, as in Fig. 2.16. This way we do not corrupt the quantum information. The next step is to show how we perform teleportation with linear optics.

Basic Teleportation with linear optics

It was shown by Lutkenhaus *et al.* [76] that we cannot distinguish the four Bell states with linear optics alone. With a single beam splitter the best we can do is distinguish the Bell states with a success probability of 1/2. Below we show how this can be used for a basic teleportation, followed by how to generalise to a teleportation with a success probability that asymptotically approaches 1.

Consider teleporting the state $(\alpha|01\rangle + \beta|10\rangle)_{12}$. We only need to look at teleporting the first mode of this state, shown in Fig. 2.17.

First the entangled resource state $\frac{1}{\sqrt{2}}\left(|01\rangle_{34} + |10\rangle_{34}\right)$ is made in part (i) of Fig. 2.17. After the second beam splitter in part (ii) of Fig. 2.17 we have:

$$\rightarrow \frac{1}{2}\Big(\sqrt{2}\alpha|0101\rangle - \alpha|1100\rangle + \alpha|0110\rangle + \beta|1001\rangle + \beta|0011\rangle - \beta|2000\rangle + \beta|0020\rangle\Big). \quad (2.78)$$

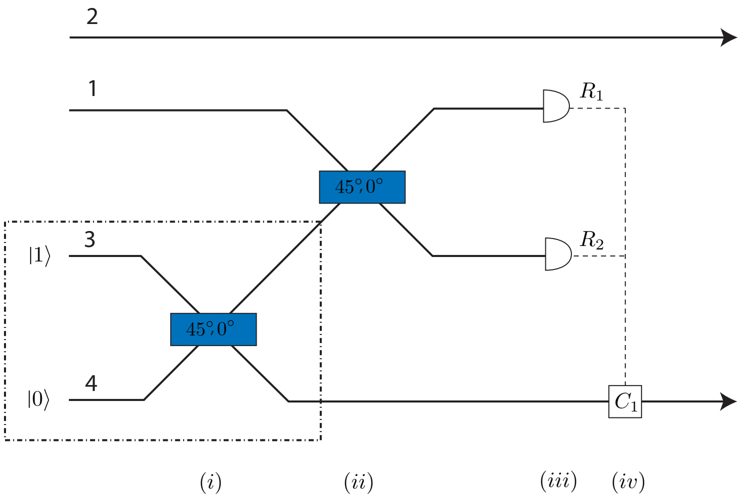

Figure 2.17: Telelportation with linear optics. The teleported qubit appears in modes 2 and 4. The entangled state production is shown in the dotted-dashed box.

If the detectors in part (iii) of Fig. 2.17 measure a total of 1 photon ($R_1 + R_2 = 1$), we can recover the original information in modes 4 and 2:

$$\begin{aligned} R_1 = 0, R_2 = 1: &\quad \frac{1}{2}\big(\alpha|01\rangle + \beta|10\rangle\big) \\ R_1 = 1, R_2 = 0: &\quad \frac{1}{2}\big(-\alpha|01\rangle + \beta|10\rangle\big). \end{aligned}$$

In the case that we measure $R_1 = 1, R_2 = 0$ we need to perform a phase shift correction gate C_1, shown in part (iv) of Fig. 2.17. The probability of successful teleportation is $1/4 + 1/4 = 1/2$. If the detectors measure 0 or 2 photons, the teleportation fails by collapsing the state into $|0\rangle$ or $|1\rangle$. This is equivalent to projecting the qubit in the Z basis, as will be explained in the next section. This occurs with a probability of $1/2$.

The teleported csign

We now have the necessary pieces for a teleported CSIGN gate. We combine the state preparation from Fig. 2.13 with the basic teleportation protocol given in Fig. 2.17 to get the teleported CSIGN circuit shown in Fig. 2.18. The success probability for the state production is $1/16$, as for Fig. 2.13, however this state preparation is performed offline. The success probability for this CSIGN gate is $1/2 \times 1/2 = 1/4$, given that the dashed-dotted box makes the state $\frac{1}{2}\big(|1010\rangle + |1001\rangle - |0110\rangle + |0101\rangle\big)_{5687}$. We know we had a successful CSIGN when $R_1 + R_5 = 1$ and $R_7 + R_3 = 1$, as in Fig. 2.17.

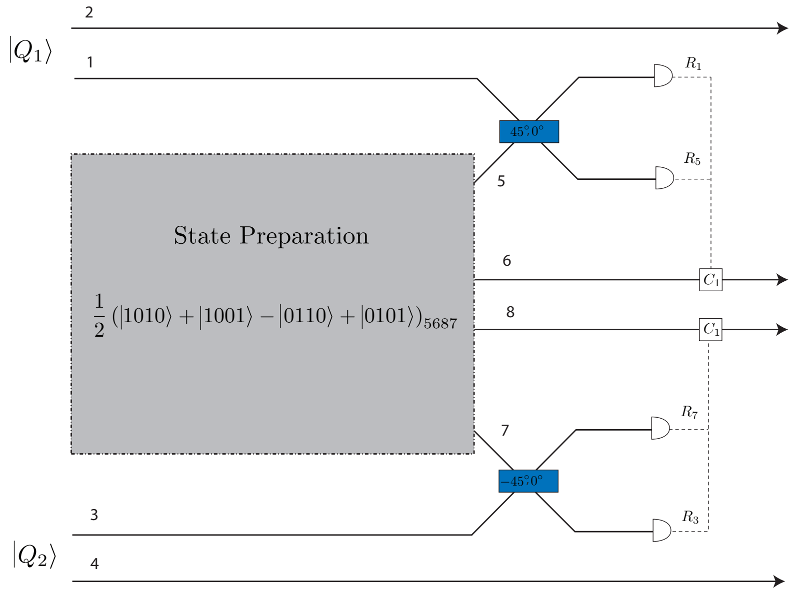

Figure 2.18: Teleported CSIGN gate. The Grey state preparation box contains Fig. 2.13.

Increasing the success probability for teleportaton

We now show how to increase the success probability for teleportation with linear optics asymptotically close to 1. By increasing the complexity of the grey state production box in Fig. 2.18 we increase the teleportation success probability. Eqn. 2.77 can be generalised by increasing the number of entangled photons and modes:

$$|t_n\rangle = \frac{1}{\sqrt{n+1}} \sum_{j=0}^{n} \Big(|1\rangle^{\otimes j} |0\rangle^{\otimes(n-j)} |0\rangle^{\otimes j} |1\rangle^{\otimes(n-j)} \Big)_{12\cdots 2n} \tag{2.79}$$

In the logical basis this is

$$|t_n\rangle_q = \frac{1}{\sqrt{n+1}} \sum_{j=0}^{n} |0\rangle_q^{\otimes j} |1\rangle_q^{\otimes(n-j)}. \tag{2.80}$$

For example, the states $|t_1\rangle$, $|t_2\rangle$, $|t_3\rangle$ and $|t_4\rangle$ are given by

$$\begin{aligned}
|t_1\rangle &= \frac{1}{\sqrt{2}}\left(|0\rangle + |1\rangle\right)_q \\
&= \frac{1}{\sqrt{2}}\left(|01\rangle + |10\rangle\right)_{12} \\
|t_2\rangle &= \frac{1}{\sqrt{3}}\left(|11\rangle + |01\rangle + |00\rangle\right)_q \\
&= \frac{1}{\sqrt{3}}\left(|0011\rangle + |1010\rangle + |1100\rangle\right)_{1234} \\
|t_3\rangle &= \frac{1}{2}\left(|111\rangle + |011\rangle + |001\rangle + |000\rangle\right)_q \\
&= \frac{1}{2}\left(|000111\rangle + |100011\rangle + |110001\rangle + |111000\rangle\right)_{123456} \\
|t_4\rangle &= \frac{1}{\sqrt{5}}\left(|1111\rangle + |0111\rangle + |0011\rangle + |0001\rangle + |0000\rangle\right)_q \\
&= \frac{1}{\sqrt{5}}\left(|00001111\rangle + |10000111\rangle + |11000011\rangle + |01110001\rangle + |11110000\rangle\right)_{12345678}
\end{aligned}$$

where the k^{th} qubit when written in terms of logical qubits is encoded in modes $n+k$ and n.

When we use this preparation state for teleportation the success probability scales as $1 - \frac{1}{n+1} = \frac{n}{n+1}$. In order to use the $|t_n\rangle$ states in the place of the dashed-dotted box in Fig. 2.17, we need a generalised beam splitter. We use the $n+1$ point Fourier transform, also called an $n+1$-splitter, denoted $\hat{F}_{n+1}$. The matrix elements of $\hat{F}_{n+1}$ are given by

$$u\left(\hat{F}_{n+1}\right)_{kl} = \frac{\exp\left(i\frac{2\pi kl}{n+1}\right)}{\sqrt{n+1}} \tag{2.81}$$

where $k, l \in \{0, \cdots, n\}$. Such a general beam splitter can be constructed from an array of beam splitters [77], as shown in Section 2.4.1.

When using the $n+1$ point Fourier transform we only teleport mode 0 of the state $(\alpha|01\rangle + \beta|10\rangle)_{0a}$, as was the case for the basic teleportation in Fig. 2.17. As in part (iii) of Fig. 2.17, we measure all the outputs of the $n+1$ point Fourier transform, modes 0 through to n, as shown in Fig. 2.19.

If we detect k photons and $0 < k < n+1$, then we know the qubit has been teleported to mode $n+k$. In this case we know that modes $n+1, n+2, \cdots, n+k-2, n+k-1$ are in the vacuum state $|0\rangle$ and modes $n+k+1, n+k+2, \cdots, 2n-1, 2n$ are in the single photon state $|1\rangle$. A phase correction on the $(n+k)^{\text{th}}$ qubit will be necessary, depicted as C_i in Fig. 2.19. This phase correction is unknown until after we detect modes 0–n. If we measure either 0 or $n+1$ photons the teleportation has failed.

For example, consider the $n = 2$ case:

$$|t_2\rangle = \frac{1}{\sqrt{3}}\left(|0011\rangle + |1010\rangle + |1100\rangle\right)_{1234}$$

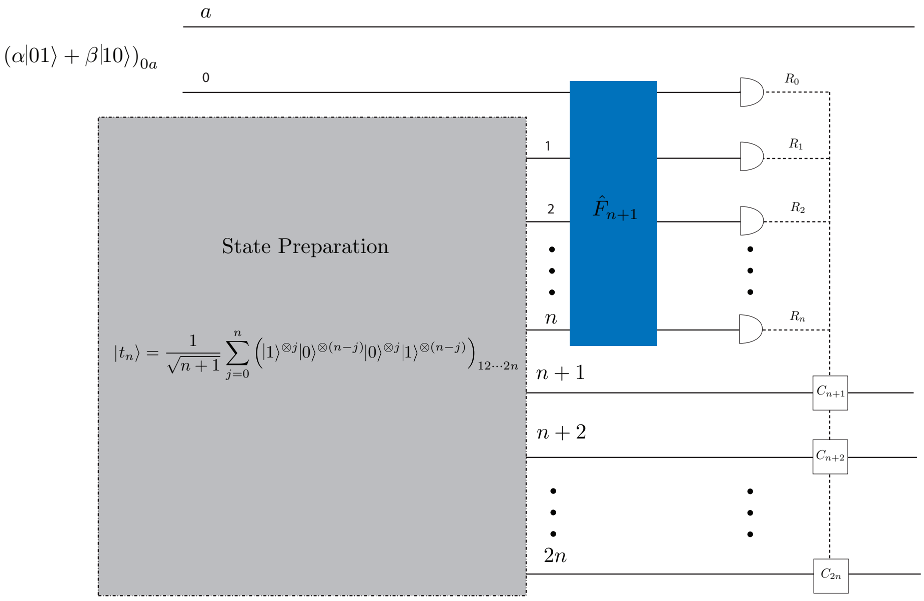

Figure 2.19: Teleportation with $|t_n\rangle$. The dashed-dotted box produces $|t_n\rangle$. The probability of success is $\frac{n}{n+1}$.

and

$$u(F_3) = \begin{pmatrix} 1 & 1 & 1 \\ 1 & e^{\frac{2\pi i}{3}} & e^{-\frac{2\pi i}{3}} \\ 1 & e^{-\frac{2\pi i}{3}} & e^{\frac{2\pi i}{3}} \end{pmatrix}.$$

When F_3 is applied to the incident modes 0, 1 and 2, the modes are transformed as:

$$\begin{aligned}
\hat{a}_0^\dagger &\to \frac{1}{\sqrt{3}}(\hat{a}_0^\dagger + \hat{a}_1^\dagger + \hat{a}_2^\dagger) \\
\hat{a}_1^\dagger &\to \frac{1}{\sqrt{3}}(\hat{a}_0^\dagger + e^{\frac{2\pi i}{3}}\hat{a}_1^\dagger + e^{-\frac{2\pi i}{3}}\hat{a}_2^\dagger) \\
\hat{a}_2^\dagger &\to \frac{1}{\sqrt{3}}(\hat{a}_0^\dagger + e^{-\frac{2\pi i}{3}}\hat{a}_1^\dagger + e^{\frac{2\pi i}{3}}\hat{a}_2^\dagger).
\end{aligned}$$

Once we apply the 3 point Fourier transform to the mode 0 of state $(\alpha|01\rangle + \beta|10\rangle)_{0a}$ and modes 1 and 2 of $|t_2\rangle$, as in Fig. 2.20, we have 19 measurement outcomes: $R_0, R_1, R_2 = 000$, 001, 010, 100, 011, 101, 110, 002, 020, 200, 012, 021, 201, 102, 120, 210, 300, 030 and 003. Only measurements with a total photon number between 0 and $n+1 = 3$ result in a successful teleportation. In this case a total of 1 or 2 photons. The relevant measurement outcomes are given in the Table 2.2 along with the output mode number. We can see what phase correction C_3 or C_4 is needed after detection. The following identities are necessary when

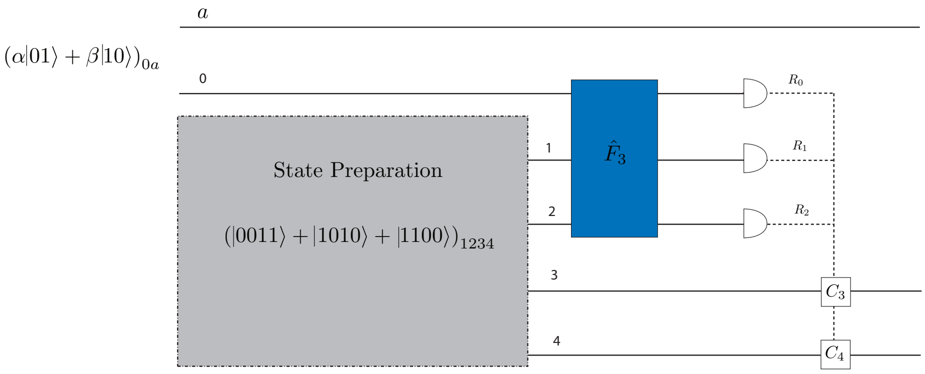

Figure 2.20: Teleportation with $|t_2\rangle$. The dashed-dotted box produces $|t_2\rangle$. The probability of success of this teleportation is 2/3.

calculating this: $e^{i\frac{2}{3}\pi}+e^{-i\frac{2}{3}\pi}=-1$, $e^{i\frac{4}{3}\pi}+e^{-i\frac{4}{3}\pi}=-1$, $e^{i\frac{2}{3}\pi}+1=e^{i\frac{\pi}{3}}$ and $e^{-i\frac{2}{3}\pi}+1=e^{-i\frac{\pi}{3}}$.

The total probability for successful teleportation is $3\left(\frac{1}{9}\right)+3\left(\frac{2}{27}\right)+3\left(\frac{1}{27}\right)=\frac{2}{3}$. This corresponds to $\frac{n}{n+1}$ with n=2. As in the basic teleportation case, successful teleportation is heralded, a failed teleportation projects the quantum information into the Z basis, as will be explained in the next section.

Measurement	Output	Mode	Probability
$\|100\rangle$	$\frac{1}{3}\left(\alpha\|0\rangle+\beta\|1\rangle\right)$	3	$\frac{1}{9}$
$\|010\rangle$	$\frac{1}{3}\left(e^{\frac{2\pi i}{3}}\alpha\|0\rangle+\beta\|1\rangle\right)$	3	$\frac{1}{9}$
$\|001\rangle$	$\frac{1}{3}\left(e^{-\frac{2\pi i}{3}}\alpha\|0\rangle+\beta\|1\rangle\right)$	3	$\frac{1}{9}$
$\|200\rangle$	$\frac{\sqrt{2}}{3\sqrt{3}}\left(\alpha\|0\rangle+\beta\|1\rangle\right)$	4	$\frac{2}{27}$
$\|020\rangle$	$\frac{\sqrt{2}}{3\sqrt{3}}\left(\alpha\|0\rangle+e^{\frac{2\pi i}{3}}\beta\|1\rangle\right)$	4	$\frac{2}{27}$
$\|002\rangle$	$\frac{\sqrt{2}}{3\sqrt{3}}\left(\alpha\|0\rangle+e^{-\frac{2\pi i}{3}}\beta\|1\rangle\right)$	4	$\frac{2}{27}$
$\|110\rangle$	$\frac{1}{3\sqrt{3}}\left(-\alpha\|0\rangle+e^{\frac{i\pi}{3}}\beta\|1\rangle\right)$	4	$\frac{1}{27}$
$\|101\rangle$	$\frac{1}{3\sqrt{3}}\left(-\alpha\|0\rangle+e^{-\frac{i\pi}{3}}\beta\|1\rangle\right)$	4	$\frac{1}{27}$
$\|011\rangle$	$\frac{1}{3\sqrt{3}}\left(-\alpha\|0\rangle-\beta\|1\rangle\right)$	4	$\frac{1}{27}$

Table 2.2: The telelported states when using $|t_2\rangle$ as an entanglement resource.

To understand why teleportation with the $n+1$ point Fourier transform fails with a probability of $1/(n+1)$, we need to take a closer look at $|t_n\rangle$ in terms of physical dual rail qubits. When we expand the sum in Eqn. 2.79 we see that the first term is always of the form $|\overbrace{00\cdots0}^{n}\underbrace{11\cdots1}_{n}\rangle_{12\cdots2n}$ and the last term is always of the form $|\overbrace{11\cdots1}^{n}\underbrace{00\cdots0}_{n}\rangle_{12\cdots2n}$. Since we teleport the state $(\alpha|01\rangle+\beta|10\rangle)_{0a}$, we need to consider the case :

$$(\alpha|01\rangle + \beta|10\rangle)_{0a} \frac{1}{\sqrt{n+1}} \left(|00\cdots011\cdots1\rangle + |11\cdots100\cdots0\rangle\right)_{12\cdots2n} \qquad (2.82)$$

Since modes 0–n are incident on the generalised beam splitter, we know that one measurement outcome will be the $n+1$ photon case and another outcome will the 0 photon case. Both of these possibilities indicate a failed teleportation, since measuring $n+1$ photons leaves the qubit in the state $\beta|0\rangle$ and measuring 0 photons leaves the qubit in the state $\alpha|1\rangle$. The probability for both of these is $\left(|\alpha|^2 + |\beta|^2\right)/(n+1) = 1/(n+1)$, since $|\alpha|^2 + |\beta|^2 = 1$. None of the other terms in the sum in Eqn. 2.79 corrupt the quantum information in this way.

With this in mind, one might be tempted to use the state

$$|t_n\rangle - \left(|\overbrace{00\cdots0}^{n}\underbrace{11\cdots1}_{n}\rangle + |\overbrace{11\cdots1}^{n}\underbrace{00\cdots0}_{n}\rangle\right)_{12\cdots2n} \qquad (2.83)$$

for teleportation. However, both $|00\cdots011\cdots1\rangle$ and $|11\cdots100\cdots0\rangle$ combine with the adjacent terms in the sum in Eqn. 2.82 to produce a successful teleportation. By taking these two terms from the entangled resource state, we are making the new first and last term in Eqn. 2.83 corrupt the quantum information. The probability for this would now be $1/(n-1)$, worse than what we calculated originally.

A possible construction of $|t_n\rangle$ was described in [81, 82], suggesting the use of a controlled beam splitter. In [81] it was suggested that such a controlled beam splitter could be constructed with the use of a controlled phase gate ($|x\rangle|y\rangle \rightarrow e^{ixy\phi}|x\rangle|y\rangle$) with phases other than $\phi = \pi$. In [82], a controlled phase gate with $\phi = \pi/2$ was used to construct $|t_2\rangle$. Taking this as the basis for the proposed controlled beam splitter gate, it would succeed with a probability of $(0.18082)^2 \approx 0.0327$. The algorithm given in [81] to make $|t_n\rangle$ used n controlled beam splitters and n CSIGN gates. The state $|t_n\rangle$ would then be produced with a success probability of

$$P^{\mathrm{KLM}}_{|t_n\rangle} = \left(0.0327 \times \frac{1}{16}\right)^n \approx (0.00204)^n \,. \qquad (2.84)$$

In [43] Hayes *et al.* use so called elimination circuits to produce $|t_n\rangle$. An elimination circuit succeeds with a probability of $12/441 \approx 0.0272$ and $n-1$ elimination circuits are required to produce $|t_n\rangle$, giving a total success probability of

$$P^{\mathrm{Hayes}}_{|t_n\rangle} = (0.0272)^{n-1} \,. \qquad (2.85)$$

In [83] Franson *et al.* propose a scheme that requires $n-1$ CNOT gates. The CNOT gates can either be modifications of a single photon probabilistic CSIGN, such as that shown in Fig. 2.13, or the 1/4 CNOT gate proposed in [34], to be described in Section 2.7.1. The probability of success for producing $|t_n\rangle$ is then

$$P^{\text{Franson}}_{|t_n\rangle} = \left(\frac{1}{4}\right)^{n-1}. \tag{2.86}$$

We next describe a scheme for constructing $|t_n\rangle$ that is ultimately equivalent to that proposed by Fransons *et al.* in [83].

Constructing $|t_n\rangle$

Here we describe a scheme using controlled beam splitters to produce $|t_n\rangle$. The controlled beam splitter used is a modification to the suggestions from [81, 82]. As suggested in [81], we use a controlled phase gate ($|x\rangle|y\rangle \rightarrow e^{ixy\phi}|x\rangle|y\rangle$) with $\phi = \pi/2$ to construct controlled beam splitter gate, shown in Fig. 2.21.

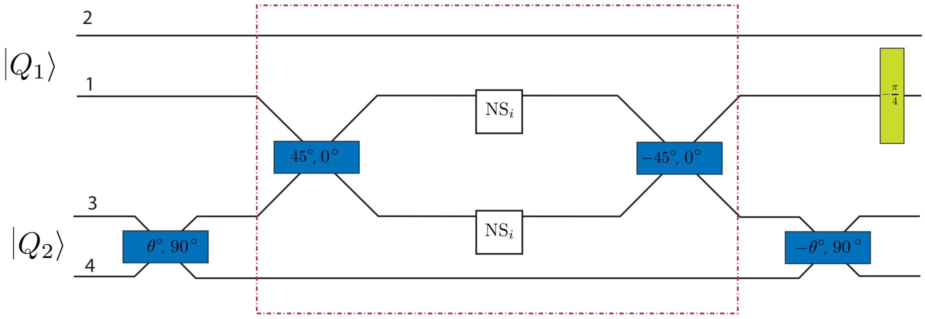

Figure 2.21: A probabilistic controlled beam splitter gate. The probability of success is $(0.18082)^2 \approx 0.0327$. Here $\theta = \frac{1}{2}\arccos\left(\sqrt{2a^2-1}\right)$. Qubit 1 $|Q\rangle_1$ is incident on modes 1 and 2 and qubit 2 $|Q\rangle_2$ is incident on modes 3 and 4. The controlled $\phi = \pi/2$ phase gate is shown in the red dashed-dotted box.

This induces the transformation $|x\rangle_q|y\rangle_q \xrightarrow{\text{C-BS}} |x\rangle_q \left(U_{\text{BS}}\right)^x |y\rangle_q$ where

$$U_{\text{BS}} = \begin{pmatrix} e^{-i\phi_{\text{BS}}}a & -\sqrt{1-a^2} \\ \sqrt{1-a^2} & e^{i\phi_{\text{BS}}}a \end{pmatrix}, \tag{2.87}$$

$$a = \frac{\sqrt{1+\cos^2(2\theta)}}{\sqrt{2}} \tag{2.88}$$

and

$$\phi_{\text{BS}} = \arctan\left(\cos\left(2\theta\right)\right) = \arctan\left(\sqrt{2a^2-1}\right). \tag{2.89}$$

In terms of dual rail qubits this circuits induces the transformation:

$$\begin{aligned}&\left(\alpha|01\rangle + \beta|10\rangle\right)_{12}\left(\gamma|01\rangle + \delta|10\rangle\right)_{34} \rightarrow \alpha|01\rangle_{12}\left(\gamma|01\rangle + \delta|10\rangle\right)_{34} \qquad (2.90)\\ &+ \frac{1}{\sqrt{2}}\beta|10\rangle_{12}\left(\gamma\left(e^{-i\phi_{\text{BS}}}a|01\rangle + \sqrt{1-a^2}|10\rangle\right)_{34} + \delta\left(-\sqrt{1-a^2}|01\rangle + e^{i\phi_{\text{BS}}}a|10\rangle\right)_{34}\right)\end{aligned}$$

and in terms of logical qubits this transformation is:

$$\begin{aligned}&(\alpha|0\rangle_q+\beta|1\rangle_q)\,(\gamma|0\rangle_q+\delta|1\rangle_q)\to\alpha|0\rangle_q\,(\gamma|0\rangle_q+\beta|1\rangle_q)\\&+\beta|1\rangle_q\left(\gamma\left(e^{-i\phi_{\mathrm{BS}}}a|0\rangle_q+\sqrt{1-a^2}|1\rangle_q\right)+\delta\left(-\sqrt{1-a^2}|0\rangle_q+e^{i\phi_{\mathrm{BS}}}a|1\rangle_q\right)\right).\end{aligned}\tag{2.91}$$

The NS$_i$ gate required for the controlled beam splitter was described in [31] and is defined by the transformation $\alpha|0\rangle+\beta|1\rangle+\gamma|2\rangle\to\alpha|0\rangle+\beta|1\rangle+i\gamma|2\rangle$. It can be implemented using Fig. 2.12, choosing $\theta_1=36.53°,\phi_1=88.24°$, $\theta_2=62.25°,\phi_2=-66.52°$, $\theta_3=-36.53°,\phi_3=-11.25°$ and $\phi_4=102.24°$. The NS$_i$ gate succeeds with a probability of 0.18082. The controlled beam splitter gate in Fig. 2.21 therefore succeeds with a probability of $(0.18082)^2\approx0.0327$.

In order to construct $|t_n\rangle_q$ from the state $|0\rangle_q^{\otimes n}$ we need $n-1$ controlled beam splitter gates. The first step is to apply a beam splitter to the first qubit:

$$|\overbrace{00\cdots0}^{n}\rangle_q\to a_1|0\overbrace{00\cdots0}^{n-1}\rangle_q+\sqrt{1-a_1^2}|1\overbrace{00\cdots0}^{n-1}\rangle_q$$

We next perform a controlled beam splitter between modes 1 and 2

$$\to a_1|0\overbrace{00\cdots0}^{n-1}\rangle_q+e^{-i\phi_2}\sqrt{1-a_1^2}a_2|10\overbrace{00\cdots0}^{n-2}\rangle_q+\sqrt{1-a_1^2}\sqrt{1-a_2^2}|11\overbrace{00\cdots0}^{n-2}\rangle_q$$

followed by a controlled beam splitter between modes 2 and 3, and continue in this manner until we perform a controlled beam splitter between modes $n-1$ and n. In total this is $n-1$ controlled beam splitters. The resulting state is

$$\begin{aligned}&a_1|00\cdots0\rangle_q+e^{-i\phi_2}\sqrt{1-a_1^2}a_2|100\cdots0\rangle_q+e^{-i\phi_3}\sqrt{1-a_1^2}\sqrt{1-a_2^2}a_3|1100\cdots0\rangle_q\\&\quad+\cdots+e^{-i\phi_n}\sqrt{1-a_1^2}\sqrt{1-a_2^2}\cdots\sqrt{1-a_{n-1}^2}a_n|11\cdots10\rangle_q\\&\qquad+\sqrt{1-a_1^2}\sqrt{1-a_2^2}\cdots\sqrt{1-a_n^2}|11\cdots1\rangle_q\end{aligned}$$

If we choose $a_1=1/\sqrt{n+1}$, $a_2=1/\sqrt{n}$, $a_3=1/\sqrt{n-1}$, $\cdots$, $a_n=1/\sqrt{2}$ we obtain $|t_n\rangle$. We can correct for the phases by applying n phase gates: a phase gate with $\phi=\phi_2$ to qubit 1, a phase gate with $\phi=\phi_3-\phi_2$ to qubit 2, a phase gate with $\phi=\phi_4-\phi_3$ to qubit 3, $\cdots$, a phase gate with $\phi=\phi_n-\phi_{n-1}$ to qubit $n-1$ and a phase gate with $\phi=\phi_n$ to qubit n.

Constructing $|t_n\rangle$ in this way succeeds with a probability of:

$$P_{|t_n\rangle}=(0.0327)^{n-1}\,.\tag{2.92}$$

Even though this success probability decreases exponentially with the size of $|t_n\rangle$, it is an improvement on both the scheme by Knill *et al.* [81] (Eqn. 2.84) and the scheme by Hayes *et al.* [43] (Eqn. 2.85). We can improve this success probability by using the optimised controlled $\phi=\pi/2$ phase gate described by

Knill in [39] that succeeds with a probability of $1/19.37 \approx 0.0516$, in the place of the red dashed-dotted box in Fig. 2.21:

$$P_{|t_n\rangle} = (0.0516)^{n-1} \,. \tag{2.93}$$

We would require two CNOT gates [79] to induce the controlled beam splitter in Fig. 2.21 since Eqn. 2.87 does not have eigenvalues of ± 1. However, notice that we only use the first column of Eqn. 2.87 to construct $|t_n\rangle$. That is, we only apply the controlled beam splitter to the states $|00\rangle_q$, $|01\rangle_q$ and $|10\rangle_q$, never $|11\rangle_q$. Therefore, the beam splitter matrix in Eqn. 2.94 can be used in the place of Eqn. 2.87 to construct $|t_n\rangle$:

$$U_{\text{BS'}} = \begin{pmatrix} a & e^{-i\phi_{\text{BS}}}\sqrt{1-a^2} \\ e^{i\phi_{\text{BS}}}\sqrt{1-a^2} & -a \end{pmatrix} . \tag{2.94}$$

Since $U_{\text{BS'}}$ has eigenvalues of ± 1 we can transform it into the Pauli X matrix:

$$U_{\text{BS'}} = VXV^{\dagger},$$

where

$$V = \begin{pmatrix} e^{-i\frac{\phi_{\text{BS}}}{2}} \cos\left(\frac{\arcsin(a)}{2}\right) & e^{-i\frac{\phi_{\text{BS}}}{2}} \sin\left(\frac{\arcsin(a)}{2}\right) \\ -e^{i\frac{\phi_{\text{BS}}}{2}} \sin\left(\frac{\arcsin(a)}{2}\right) & e^{i\frac{\phi_{\text{BS}}}{2}} \cos\left(\frac{\arcsin(a)}{2}\right) \end{pmatrix} .$$

A controlled-BS' gate can therefore be made from a CNOT as seen in Fig. 2.22. The single qubit operators V can easily be made with beam splitters. This allows the success probability for constructing $|t_n\rangle$ to be improved to

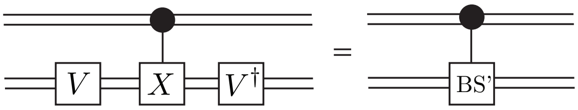

Figure 2.22: The equivalence between the CNOT and a controlled-BS' gate.

$$P_{|t_n\rangle} = (0.0741)^{n-1} \tag{2.95}$$

when we use the 2/27 CNOT gate [39], the best known CNOT construction to date, to be described in Section 2.7.5. This success probability was calculated assuming a resource of single photons. If we instead allow a for a resource of Bell states, we can use the CNOT by Pittman *et al.* from [34], to be described in

Section 2.7.1, in the place of the 2/27 CNOT. This lead to a success probability of

$$P_{|t_n\rangle'} = \left(\frac{1}{4}\right)^{n-1} \tag{2.96}$$

which is the same as the scheme by Franson *et al.* [83] (Eqn. 2.86).

Increasing the Probability for the csign

Since we now have a way of performing near deterministic teleportation with the entangled ancilla state $|t_n\rangle$ and $n+1$ Fourier transform $\hat{F}_{n+1}$, we should be able to use two of these teleportation circuits to apply a CSIGN near deterministically, as in Fig. 2.16. For this we need to apply a CSIGN between the two $|t_n\rangle$ states during state preparation. However, since we do not know which mode will contain the teleported state until after we detect the $n+1$ modes from the generalised beam splitter, we must apply a CSIGN between all potential output modes. There are n possible modes that the quantum information could be teleported into, modes $n+1, \cdots, 2n$, as can be seen in Fig. 2.19. This means the entangled production stage will require a CSIGN to be applied between all n qubits for each $|t_n\rangle$ state, that is, we need to apply n^2 CSIGN gates at the state preparation stage. After the application of the n^2 CSIGN gates to the state $|t_n\rangle|t_n\rangle$ we have

$$|CS_n\rangle = \frac{1}{n+1}\sum_{i,j=0}^{n}(-1)^{(n-1)(n-j)}|1\rangle^{\otimes i}|0\rangle^{\otimes(n-i)}|0\rangle^{\otimes i}|1\rangle^{\otimes(n-i)}|1\rangle^{\otimes j}|0\rangle^{\otimes(n-j)}|0\rangle^{\otimes j}|1\rangle^{\otimes(n-j)}$$

or in the logical basis

$$|CS_n\rangle_q = \frac{1}{n+1}\sum_{i,j=0}^{n}(-1)^{(n-1)(n-j)}|0\rangle_q^{\otimes i}|1\rangle_q^{\otimes(n-i)}|0\rangle_q^{\otimes j}|1\rangle_q^{\otimes(n-j)}. \tag{2.97}$$

For example,

$$\begin{aligned}
|cs_1\rangle_q &= \frac{1}{2}\big(|0\rangle|0\rangle + |0\rangle|1\rangle + |1\rangle|0\rangle - |1\rangle|1\rangle\big)_q \\
|cs_2\rangle_q &= \frac{1}{3}\big(|00\rangle|00\rangle + |00\rangle|01\rangle + |00\rangle|11\rangle + |01\rangle|00\rangle - |01\rangle|01\rangle + |01\rangle|11\rangle \\
&\qquad\qquad + |11\rangle|00\rangle + |11\rangle|01\rangle + |11\rangle|11\rangle\big)_q.
\end{aligned}$$

If we construct $|cs_n\rangle$ from single photons, the success probability is just that for producing two $|t_n\rangle$ states multiplied by $(1/16)^{n^2}$. In [83], when $n \gg 1$, Franson *et al.* use a more sophisticated technique than just applying a CNOT between all possible output modes, only requiring an additional $4n$ CNOT gates.

2.6 Quantum Error Correction in LOQC

2.6.1 Improving LOQC: beyond state preparation

In the last section we showed that scalable quantum computing was possible with linear optical elements, single photon sources and photo-detection. The problem of making a two qubit gate with probability of success arbitrarily close to one was transferred to a state preparation problem. By using generalised entangled states of the form $|t_n\rangle$, the probability of success scaled as $\frac{n}{n+1}$. However, states of the form $|t_n\rangle$ are complicated to make. To date the best schemes need resources that are exponential in n [81, 83, 43]. Instead, we may ask ourselves if we can incorporate quantum error correction into the LOQC proposal. Is it possible to correct for the incorrect measurements in the basic linear optical teleportation in Fig. 2.17? Can we use quantum error correction along with smaller $|t_n\rangle$ states to increase the probability of successful gates giving scalable quantum computing? These questions have been addressed by Knill *et al.* in [33] and elaborated by Knill in [84].

To answer these questions we first need to know what errors are inflicted on the quantum information when an incorrect measurement is made in the teleportation in Fig. 2.17.

In the previous section we went through this basic teleportation with linear optics and showed that if we want to teleport the state $\alpha|01\rangle + \beta|10\rangle$ using the entanglement resource state $\frac{1}{\sqrt{2}}\big(|01\rangle + |10\rangle\big)$, we need to measure 1 and only 1 photon at the photo-detection stage (Fig. 2.17 (iii)). The probability of success was $\frac{1}{2}$. What happens when we measure 0 or 2 photons?

In section 2.5.4 we saw that our input state $\alpha|01\rangle + \beta|10\rangle$ was transformed to Eqn. 2.78 in Fig. 2.17 (ii). If the detectors measure a total of 1 photon $(R_1 + R_2 = 1)$ we recover the original information:

$$\begin{aligned} R_1 = 0, R_2 = 1: &\quad \frac{1}{2}\big(\alpha|01\rangle + \beta|10\rangle\big) \\ R_0 = 1, R_1 = 1: &\quad \frac{1}{2}\big(-\alpha_0|01\rangle + \alpha_1|10\rangle\big). \end{aligned}$$

If the detectors measure a total of 0 or 2 photons ($R_1 + R_2 = 0 \bmod 2$) we have:

$$\begin{aligned} R_1 = 0, R_2 = 0: &\quad \frac{1}{\sqrt{2}}\alpha_0|11\rangle \\ R_0 = 2, R_1 = 0: &\quad -\frac{1}{\sqrt{2}}\alpha_1|00\rangle \\ R_1 = 0, R_2 = 2: &\quad \frac{1}{\sqrt{2}}\alpha_1|00\rangle. \end{aligned}$$

Note that when we measure 0 or 2 photons we have measured our qubit, collapsing our quantum information. This means we are free to add a single photon, or vacuum mode. When we measure 0 photons, we obtain the state $|01\rangle = |0\rangle_q$ and when we measure 2 photons, we obtain $|10\rangle = |1\rangle_q$. When we measure 0 or 2 photons we effectively measure our information qubit in the Z-basis. When we consider teleportation with the generalised entangled states $|t_n\rangle$, the errors resulting from measuring 0 or $n+1$ photons are also Z-projection errors on the quantum information.

With this knowledge we should be able to use quantum error correction to encoded our quantum data and then correct when the teleportation fails, i.e. when the measurement result is either 0 or 2 photons in Fig. 2.17 or 0 or $n+1$ photons in Fig. 2.19. This means we need to find a quantum error correcting (QEC) code that can deal with a projection in the Z basis, where we know which qubit was projected. In the next Section we will define what a quantum error correcting code is and give the details for a code that can deal with Z-projection errors.

2.6.2 Quantum Error Correcting Codes

We can encode our quantum information with code words to protect against errors. Classically, when the error model is given by independent bit flips (X), this can be done via the repetition code: 0 → 000 and 1 → 111.

When we generalise the classical theory to the quantum case, we also have to worry about phase errors (Z operators and the combination of bit flip and phase errors: Y operators). A necessary and sufficient condition [20, 85] for a code with basis code words $\{|\overline{\psi}\rangle\}$ to correct for the set of errors $\{E\}$ is

$$\langle\overline{\psi}_i|E_a^\dagger E_b|\overline{\psi}_j\rangle = C_{ab}\delta_{ij} \tag{2.98}$$

where $|\overline{\psi}_i\rangle, |\overline{\psi}_j\rangle \in \{|\overline{\psi}\rangle\}$ and $E_a, E_b \in \{E\}$.

If we have errors of the form $E_1 = \frac{1}{2}\big(\mathbb{1} + Z\big)$, $E_2 = \frac{1}{2}\big(\mathbb{1} - Z\big)$, our qubit $|\psi\rangle = \alpha|0\rangle_q + \beta|1\rangle_q$ becomes:

$$\begin{aligned} E_1|\psi\rangle &= \alpha|0\rangle_q \\ E_2|\psi\rangle &= \beta|1\rangle_q. \end{aligned}$$

We have measured our qubit in the Z-basis. We can encode to correct for this error using the parity encoding:

$$|\overline{0}\rangle = \frac{1}{\sqrt{2}}\big(|00\rangle_q + |11\rangle_q\big) \tag{2.99}$$

$$|\overline{1}\rangle = \frac{1}{\sqrt{2}}\big(|01\rangle_q + |10\rangle_q\big). \tag{2.100}$$

If we measure the first mode of our encoded qubit in the Z-basis we have

$$\frac{1}{\sqrt{2}}\big(\alpha|00\rangle_q+\alpha|11\rangle_q+\beta|01\rangle_q+\beta|10\rangle_q\big)$$
$$=\frac{1}{\sqrt{2}}\{|0\rangle_q\big(\alpha|0\rangle_q+\beta|1\rangle_q\big)\}+\frac{1}{\sqrt{2}}|1\rangle_q\big(\alpha|1\rangle_q+\beta|0\rangle_q\big)\}$$

and we see that if we measure mode 1 to be a $|0\rangle_q$, we get our original information qubit back and if we measure mode 1 to be a $|1\rangle_q$, we can get our original information qubit back once we apply a bit flip. Now we need to check that this code satisfies condition 2.98 for the errors E_1 and E_2. We assume the errors are on the 1st qubit, so $E_1=\frac{1}{2}\big(\mathbb{1}+Z\big)\otimes\mathbb{1}$ and $E_2=\frac{1}{2}\big(\mathbb{1}-Z\big)\otimes\mathbb{1}$:

$\langle\bar{0}\vert E_1^\dagger\mathbb{1}\vert\bar{0}\rangle=\frac{1}{2}$	$\langle\bar{0}\vert E_2^\dagger\mathbb{1}\vert\bar{0}\rangle=\frac{1}{2}$	$\langle\bar{0}\vert E_1^\dagger E_2\vert\bar{0}\rangle=0$	$\langle\bar{0}\vert E_2^\dagger E_1\vert\bar{0}\rangle=0$
$\langle\bar{0}\vert E_1^\dagger\mathbb{1}\vert\bar{1}\rangle=0$	$\langle\bar{0}\vert E_2^\dagger\mathbb{1}\vert\bar{1}\rangle=0$	$\langle\bar{0}\vert E_1^\dagger E_2\vert\bar{1}\rangle=0$	$\langle\bar{0}\vert E_2^\dagger E_1\vert\bar{1}\rangle=0$
$\langle\bar{1}\vert E_1^\dagger\mathbb{1}\vert\bar{0}\rangle=0$	$\langle\bar{1}\vert E_2^\dagger\mathbb{1}\vert\bar{0}\rangle=0$	$\langle\bar{1}\vert E_1^\dagger E_2\vert\bar{0}\rangle=0$	$\langle\bar{1}\vert E_2^\dagger E_1\vert\bar{0}\rangle=0$
$\langle\bar{1}\vert E_1^\dagger\mathbb{1}\vert\bar{1}\rangle=\frac{1}{2}$	$\langle\bar{1}\vert E_2^\dagger\mathbb{1}\vert\bar{1}\rangle=\frac{1}{2}$	$\langle\bar{1}\vert E_1^\dagger E_2\vert\bar{1}\rangle=0$	$\langle\bar{1}\vert E_2^\dagger E_1\vert\bar{1}\rangle=0$

Table 2.3: Testing condition 2.98 for the errors E_1 and E_2.

But this does not tell us how to correct for the errors E_1 and E_2, only that correction is possible.

2.6.3 Z-measurement QEC Code

How can we correct for the Z-measurement errors E_1 and E_2? There is a formalism called the stabilizer formalism [19, 86] that gives us a way to do this. A stabilizer is defined by a set of operators for an n qubit system whose common eigenvectors define a 2^k-dimensional subspace (the code). That is, the stabilizer is defined as the set of operators $\{M_i\}$ that leave the code word space $\{|\overline{\psi}_j\rangle\}$ invariant: $M_i|\overline{\psi}_j\rangle=|\overline{\psi}_j\rangle$, $\forall i,j$. The operators M_i are formed by tensor products of Pauli operators. We have the two code words: $|\bar{0}\rangle=\frac{1}{\sqrt{2}}\big(|00\rangle_q+|11\rangle_q\big)$ and $|\bar{1}\rangle=\frac{1}{\sqrt{2}}\big(|01\rangle_q+|10\rangle_q\big)$. These are stabilized by the two operators $\mathbb{1}\otimes\mathbb{1}$ and $X\otimes X$.

For a stabilizer code we can detect all errors that are either in the stabilizer or anti-commute with any member of the stabilizer group. If we have the QEC code with code words $|\overline{\psi}_j\rangle$ where M_i is an element of the stabilizer S and E is an error such that $\{M_i,E\}=0$, then $M_iE|\overline{\psi}_j\rangle=-EM_i|\overline{\psi}_j\rangle=-E|\overline{\psi}_j\rangle$ [86]. We see that $E|\overline{\psi}_j\rangle$ is an eigenstate of M_i, measuring M_i will tell us if E has occurred. By measuring all the stabilizer generators we identify the error syndrome with this method.

If a QEC code can correct for errors E and F, then it can also correct for the error $aE+bF$ [86]. From the form of E_1 and E_2 we need only consider correcting the error $Z\otimes\mathbb{1}$. More generally, when we consider correcting for a Z-measurement error on either qubit of the code words in Eqns. 2.99 and 2.100, we need to consider the errors $Z\otimes\mathbb{1}$ and $\mathbb{1}\otimes Z$. Both $Z\otimes\mathbb{1}$ and $\mathbb{1}\otimes Z$ anti-commute with $X\otimes X$.

The operator $X\otimes X$ has the matrix form:

$$X\otimes X=\begin{pmatrix}0&1\\1&0\end{pmatrix}\otimes\begin{pmatrix}0&1\\1&0\end{pmatrix}=\begin{pmatrix}0&0&0&1\\0&0&1&0\\0&1&0&0\\1&0&0&0\end{pmatrix}$$

and has eigenvectors:

$$|XX_{\substack{10\\00}}\rangle=\big(\pm|00\rangle_q+|11\rangle_q\big)/\sqrt{2}$$
$$|XX_{\substack{11\\01}}\rangle=\big(\pm|01\rangle_q+|10\rangle_q\big)/\sqrt{2}$$

with the following eigenvalues:

$$\begin{aligned}(X\otimes X)\,|XX_{00}\rangle&=-|XX_{00}\rangle\\(X\otimes X)\,|XX_{01}\rangle&=-|XX_{01}\rangle\\(X\otimes X)\,|XX_{10}\rangle&=+|XX_{10}\rangle\\(X\otimes X)\,|XX_{11}\rangle&=+|XX_{11}\rangle.\end{aligned}$$

For example, consider the first qubit of our encoded state $|\overline{\psi}\rangle=\alpha|\overline{0}\rangle+\beta|\overline{1}\rangle=\frac{1}{\sqrt{2}}\big(\alpha|00\rangle_q+\alpha|11\rangle_q+\beta|01\rangle_q+\beta|10\rangle_q\big)$ is measured in the Z-basis:

$$|\overline{\psi}\rangle\rightarrow\frac{1}{\sqrt{2}}|0\rangle_q\big(\alpha|0\rangle_q+\beta|1\rangle_q\big)\quad\text{or}\quad\frac{1}{\sqrt{2}}|1\rangle_q\big(\alpha|1\rangle_q+\beta|0\rangle_q\big).$$

What if we measure the first qubit in the $+Z$ eigenstate $|0\rangle_q$? $|\overline{\psi}\rangle$ becomes:

$$\frac{1}{2}\big(\alpha|XX_{10}\rangle-\alpha|XX_{00}\rangle+\beta|XX_{11}\rangle-\beta|XX_{01}\rangle\big).$$

If we measure $X\otimes X$ and get $+1$ we have: $\frac{1}{2\sqrt{2}}\big(\alpha|00\rangle_q+\alpha|11\rangle_q+\beta|01\rangle_q+\beta|10\rangle_q\big)$, our original encoded state. If we measure $X\otimes X$ and get -1 we have: $\frac{1}{2\sqrt{2}}\big(\alpha|00\rangle_q-\alpha|11\rangle_q+\beta|01\rangle_q-\beta|10\rangle_q\big)$, and we need to perform the Z operation on the first qubit to get back our original encoded state.

Now what if we measure the first qubit in the $-Z$ eigenstate $|1\rangle_q$? The state $|\overline{\psi}\rangle$ becomes:

$$\frac{1}{2}\big(\alpha|XX_{00}\rangle+\alpha|XX_{10}\rangle+\beta|XX_{01}\rangle+\beta|XX_{11}\rangle\big).$$

If we measure $X\otimes X$ and get $+1$ we have: $\frac{1}{2\sqrt{2}}\big(\alpha|00\rangle_q+\alpha|11\rangle_q+\beta|01\rangle_q+\beta|10\rangle_q\big)$, our original encoded state. If we measure $X\otimes X$ and get -1 we have: $\frac{1}{2\sqrt{2}}\big(-\alpha|00\rangle_q+\alpha|11\rangle_q-\beta|01\rangle_q+\beta|10\rangle_q\big)$, and we need to perform the Z operation on the first qubit to get back our original encoded state (leaving us with an overall phase factor). This is summarised in Fig. 2.23(a).

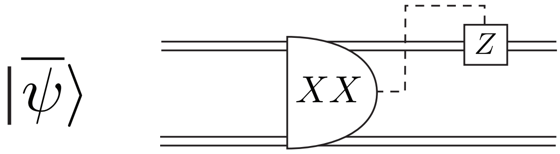

Figure 2.23: Quantum error correction for Z-measurement errors by measuring the stabilizer XX.

2.7 Further developments in LOQC

Since the seminal work by Knill *et al.* [31] many theoretical and practical advances have been made to improve the LOQC protocol. In this section we introduce some of the important theoretical advances that will been built upon in this thesis and that serve as starting points for many of the directions LOQC research is currently taking.

2.7.1 Pittman Bell state CNOT

In [34] Pittman *et al.* constructed a CNOT gate using linear optics, a Bell state ancilla and single photon detection that succeeded with a probability of 1/4. This success probability is four times the success probability for the corresponding gate by Knill *et al.* in [31] (Fig. 2.13). Since this is a probabilistic gate it is not suitable for scalable quantum computation. The Pittman Bell state CNOT is shown in Fig. 2.24. Working in the polarisation basis, the input state is given by

$$\big(\alpha_1|H_{2'}H_{3'}\rangle + \alpha_2|H_{2'}V_{3'}\rangle + \alpha_3|V_{2'}H_{3'}\rangle + \alpha_4|V_{2'}V_{3'}\rangle\big) \otimes \frac{1}{\sqrt{2}}\big(|H_aH_b\rangle + |V_aV_b\rangle\big) \tag{2.101}$$

where the control is incident on mode $2'$ and the target is incident on mode $3'$.

Notice that each detector can detect a maximum of two photons. The CNOT is successfully applied when we detect one photon in both mode c and d. We detect mode c in the F/S basis and mode d in the H/V basis. The four possible detection outcomes that indicate a successful CNOT are $|F_cH_d\rangle$, $|F_cV_d\rangle$, $|S_cH_d\rangle$ and $|S_cV_d\rangle$. The corresponding output state for each of these detections is:

$$\begin{aligned}
&\frac{1}{4}|F_cH_d\rangle\big(\alpha_1|H_2H_3\rangle + \alpha_2|H_2V_3\rangle + \alpha_3|V_2V_3\rangle + \alpha_4|V_2H_3\rangle\big)\\
&\frac{1}{4}|F_cV_d\rangle\big(\alpha_1|H_2V_3\rangle + \alpha_2|H_2H_3\rangle + \alpha_3|V_2H_3\rangle + \alpha_4|V_2V_3\rangle\big)\\
&\frac{1}{4}|S_cH_d\rangle\big(-\alpha_1|H_2H_3\rangle - \alpha_2|H_2V_3\rangle + \alpha_3|V_2V_3\rangle + \alpha_4|V_2H_3\rangle\big)\\
&\frac{1}{4}|S_cV_d\rangle\big(-\alpha_1|H_2V_3\rangle - \alpha_2|H_2H_3\rangle + \alpha_3|V_2H_3\rangle + \alpha_4|V_2V_3\rangle\big).
\end{aligned}$$

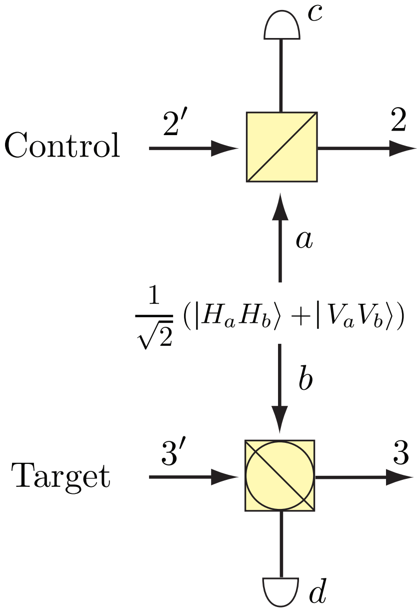

Figure 2.24: The Pittman *et al.* Bell state CNOT [34]. Succeeds with a probability of 1/4 provided we detect one photon in both mode c and d. Detection of mode c is in the F/S basis and detection of mode d is in the H/V basis.

When we detect $|F_cH_d\rangle$ no correction is necessary. When we detect $|F_cV_d\rangle$ we need to apply a polariser to mode 3 such that $H \rightarrow V$ and $V \rightarrow H$. When we detect $|S_cH_d\rangle$ we need to apply a π phase shift to the horizontal photons in mode 2. When we detect $|S_cV_d\rangle$ we need to flip the polarisation in mode 3 and apply the π phase shifter to the horizontal photons in mode 2.

2.7.2 Pittman destructive CNOT

In [36] Pittman *et al.* constructed a simplified version of their Bell state CNOT gate [34]. This simplified CNOT also succeed with a probability of 1/4 and only required one single photon ancilla in the state $(|H\rangle + |V\rangle)/\sqrt{2}$. However, when the ancilla detection indicates a successful CNOT application the output control and target mode also contain terms not in the qubit basis. The number of photons in both the control and target modes needs to be measured. This CNOT gate is destructive in that we must measure the quantum information in order to know the gate worked. The Pittman destructive CNOT is shown in Fig. 2.25. Working in the polarisation basis, the input state is given by

$$\left(\alpha_1|H_{c'}H_{t'}\rangle + \alpha_2|H_{c'}V_{t'}\rangle + \alpha_3|V_{c'}H_{t'}\rangle + \alpha_4|V_{c'}V_{t'}\rangle\right) \otimes \frac{1}{\sqrt{2}}\left(|H_{A'}\rangle + |V_{A'}\rangle\right) \tag{2.102}$$

where the control is incident on mode c' and the target is incident on mode t'.

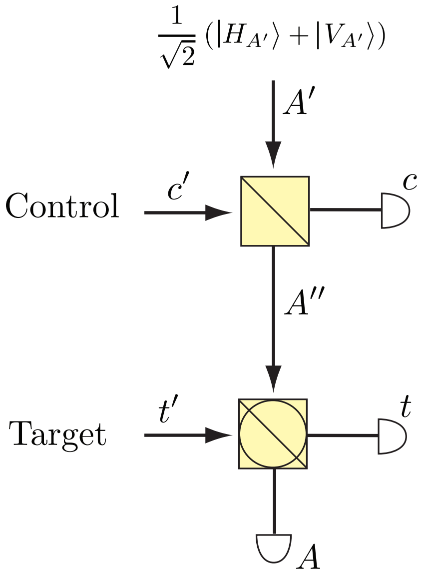

Figure 2.25: The Pittman *et al.* destructive CNOT [36]. Succeeds with a probability of 1/4 provided we detect one photon in mode A and both mode c and t contain only one photon. Mode A is detected in the H/V basis.

Detecting one photon in mode A in the H/V basis gives the output state:

$$\begin{aligned}
&|H_A\rangle\Bigg(\frac{1}{\sqrt{8}}\left(\alpha_1|H_c,H_t\rangle + \alpha_2|H_c,V_t\rangle + \alpha_3|V_c,V_t\rangle + \alpha_4|V_c,H_t\rangle\right) \qquad (2.103)\\
&+\frac{1}{8}(\alpha_4-\alpha_3)\left(|0,2H_t\rangle + |0,2V_t\rangle - \sqrt{2}|0,H_tV_t\rangle\right) + \frac{1}{\sqrt{8}}(\alpha_1-\alpha_2)|H_cV_c,0\rangle\Bigg)\\
&+|V_A\rangle\Bigg(\frac{1}{\sqrt{8}}\left(\alpha_1|H_c,V_t\rangle + \alpha_2|H_c,H_t\rangle + \alpha_3|V_c,H_t\rangle + \alpha_4|V_c,V_t\rangle\right)\\
&+\frac{1}{8}(\alpha_4+\alpha_3)|0,2V_t\rangle + \frac{1}{8}(\alpha_4-\alpha_3)\left(\sqrt{2}|0,H_tV_t\rangle - |0,2H_t\rangle\right) + \frac{1}{\sqrt{8}}(\alpha_2-\alpha_1)|H_cV_c,0\rangle\Bigg).
\end{aligned}$$

If we could measure the presence of one photon in both mode c and t non-destrictively, the ouput state would be:

$$\begin{aligned}
&\tfrac{1}{2\sqrt{2}} && |H_A\rangle\big(\alpha_1|H_cH_t\rangle + \alpha_2|H_cV_t\rangle + \alpha_3|V_cV_t\rangle + \alpha_4|V_cH_t\rangle\big)\\
+\ &\tfrac{1}{2\sqrt{2}} && |V_A\rangle\big(\alpha_1|H_cV_t\rangle + \alpha_2|H_cH_t\rangle + \alpha_3|V_cH_t\rangle + \alpha_4|V_cV_t\rangle\big).
\end{aligned}$$

When we detect $|V_A\rangle$ we need to apply a polariser to mode t such that $H \rightarrow V$ and $V \rightarrow H$.

2.7.3 Ralph Coincidence CNOT

In [35] Ralph *et al.* simplify the probabilistic CSIGN in Fig. 2.13 by removing the lower two beam splitters from each NS_{-1} gate (Fig. 2.12), reducing the number of nested interferometers, leading to the more experimentally feasible circuit shown in Fig. 2.26. The beam splitters corresponding to θ_1, π and θ_4, π in Fig. 2.26 correspond to Hadamard gates, making this a CNOT instead of the CSIGN shown in Fig. 2.13. The success probability is reduced to $(3-\sqrt{2})^2/49 \approx 0.0513$, however this gate works in the coincidence basis, a major advantage for experiments.

Consider the input state

$$(\alpha|10\rangle + \beta|01\rangle)_{12}\,(\gamma|10\rangle + \delta|01\rangle)_{34}\,|0011\rangle_{5678}$$

with the control incident on modes 2 and 1 and the target incident on modes 4 and 3. After the coincidence, shown in the dashed-dotted box in Fig. 2.26, we have

$$\frac{(3-\sqrt{2})}{14}\Bigg(\alpha\gamma\Big(|1100\rangle - |1010\rangle + \sqrt{2}|1001\rangle\Big) + \alpha\delta\Big(|1100\rangle - |1010\rangle - \sqrt{2}|1001\rangle\Big)$$
$$+\beta\gamma\Big(|0020\rangle - |0200\rangle + |0101\rangle + |0011\rangle\Big) + \beta\delta\Big(|0020\rangle - |0200\rangle - |0101\rangle - |0011\rangle\Big)\Bigg)_{15'6'4'}.$$

Notice at this point we have terms outside the dual rail qubit basis, as was the case between points (ii) and (iii) in Fig. 2.13. After the final two beam splitters our output is

$$\frac{(3-\sqrt{2})}{7}\left(\alpha\gamma|1010\rangle + \alpha\delta|1001\rangle + \beta\gamma|0101\rangle + \beta\delta|0110\rangle\right)_{15''6''4''}.$$

We see a CNOT has been implemented with a probability of $(3-\sqrt{2})^2/49 \approx 0.0513$.

2.7.4 Ralph Destructive CNOT

The probabilistic CSIGN gate in Fig. 2.26 was simplified further by Ralph *et al.* in [37] by eliminating the need for single photon ancilla, the simplified gate only needing two vacuum ancilla modes, as shown in Fig. 2.27. The success probability for this gate is $1/9 \approx 0.11$, an improvement on both the original scheme in [31], shown in Fig. 2.13, and the scheme in [35], shown in Fig. 2.26. However, as in the Pittman destructive CNOT gate [36] described in Section 2.7.2, this gate is destructive, requiring the photon number to be measured on the output control and target modes.

Consider the input state

$$(\alpha|01\rangle + \beta|10\rangle)_{12}\,(\gamma|01\rangle + \delta|10\rangle)_{34}\,|00\rangle_{56}$$

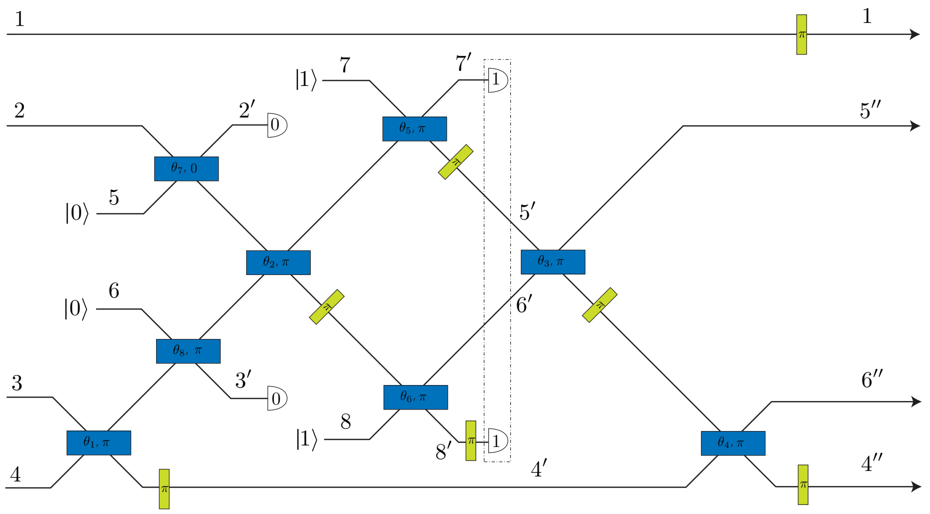

Figure 2.26: Simplified probabilistic CNOT gate shown by Ralph *et al.* in [35]. Here $\theta_1 = \theta_2 = \theta_3 = \theta_4 = \pi/4$, $\theta_5 = \theta_6 = \arccos\left(\sqrt{\frac{3-\sqrt{2}}{7}}\right)$ and $\theta_7 = \theta_8 = \arcsin\left(\sqrt{5-3\sqrt{2}}\right)$. The gate succeeds with a probability of $(3-\sqrt{2})^2/49 \approx 0.0513$. The dashed-dotted box indicates a coincidence measurement.

with the control incident on modes 1 and 2 and the target incident on modes 3 and 4. After we measure $|00\rangle_{5'6'}$ we have

$$\frac{1}{3}\Bigg(\alpha\gamma\Big(|0101\rangle - |0011\rangle + \sqrt{2}\,(|0020\rangle - |0200\rangle)\Big) + \beta\gamma\Big(|1010\rangle - |1100\rangle\Big)$$

$$+\,\alpha\delta\Big(|0110\rangle + |0011\rangle + \sqrt{2}\,(|0002\rangle + |0200\rangle)\Big) + \beta\delta\Big(|1001\rangle + |1100\rangle\Big)\Bigg)_{1'2'3'4'}.$$

To see how a photon number measurement on the output control and target modes leads to a CNOT we transform this state from the dual rail basis to polarisation using the right hand side of Fig. 2.8, giving

$$\frac{1}{3}\Bigg(\alpha\gamma\Big(|H\rangle|H\rangle - |0\rangle|HV\rangle + \sqrt{2}\,(|0\rangle|2V\rangle - |2H\rangle|0\rangle)\Big) + \beta\gamma\Big(|V\rangle|V\rangle - |HV\rangle|0\rangle\Big) \tag{2.104}$$

$$+\,\alpha\delta\Big(|H\rangle|V\rangle + |0\rangle|HV\rangle + \sqrt{2}\,(|0\rangle|2H\rangle + |2H\rangle|0\rangle)\Big) + \beta\delta\Big(|V\rangle|H\rangle + |HV\rangle|0\rangle\Big)\Bigg)_{\mathrm{C,T}}$$

where C and T correspond to control and target, respectively. If we were able to measure the presence of one photon with out destroying the quantum information in both the control and target modes we would have

$$\frac{1}{3}\left(\alpha\gamma|H\rangle|H\rangle + \alpha\delta|H\rangle|V\rangle + \beta\gamma|V\rangle|V\rangle + \beta\delta|V\rangle|H\rangle\right)_{CT}.$$

We see a CNOT has been implemented with a probability of $1/9 \approx 0.11$.

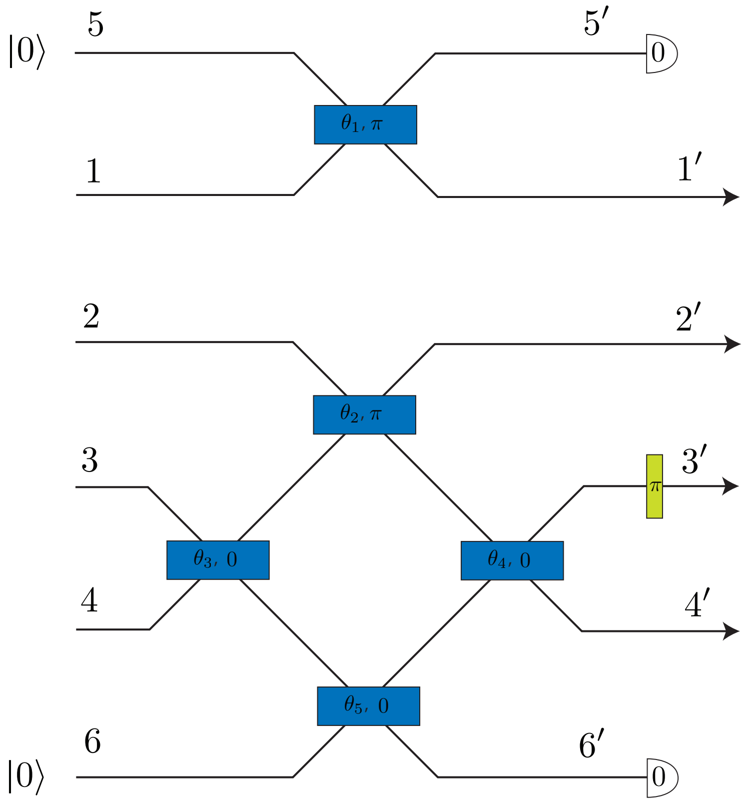

Figure 2.27: Destructive CNOT gate shown by Ralph *et al.* in [37]. Here $\theta_1 = \theta_2 = \theta_5 = \arccos\left(\frac{1}{\sqrt{3}}\right)$ and $\theta_3 = \theta_4 = \pi/4$. The gate succeeds with a probability of $1/9 \approx 0.11$ provided we can measure the number of photons in the control and target without destroying the quantum information.

2.7.5 Bounds on Success Probabilities

The methods described to produce the off-line entangled states $|CS_n\rangle$ necessary for scalable computation with linear optics succeed with a probability that decreases exponentially in the size of the state to be produced, as described at the end of Section 2.5.4. These success probabilities depend solely on the probability of success for the probabilistic CSIGN , whether the CSIGN being used is the one originally proposed by Knill *et al.* [31], described in Fig. 2.13, or one of the more recent schemes described in Sections 2.7.1–2.7.4. For this reason it is important that the CSIGN probability of success is optimised. This can be done in two ways.

First we can optimise the NS_{-1} gate thereby improving the success probability of Fig. 2.13. To date no improvements in the NS_{-1} shown in Fig. 2.12 have been found. Knill [38] has shown that the upper bound for any NS_{-1} gate with one ancilla mode is $1/2$. Scheel *et al.* [40] conjecture that the upper bound for the NS_{-1} gate is 1/4, regardless of the dimensionality of the ancilla space. Eisert has proven this 1/4 bound using convex optimization in [41].

Second, we can directly optimise the probabilistic CSIGN gate without breaking it into NS_{-1} gates. To date the best probabilistic CSIGN gate using single photon ancilla is that proposed by Knill [39] which succeeds with a probability of $2/27 \approx 0.074$ and is shown in Fig. 2.28. Knill has also shown [38] that the probabilistic CSIGN gate has an upper bound of 3/4 when using two ancilla modes, each with a maximum of one photon per mode.

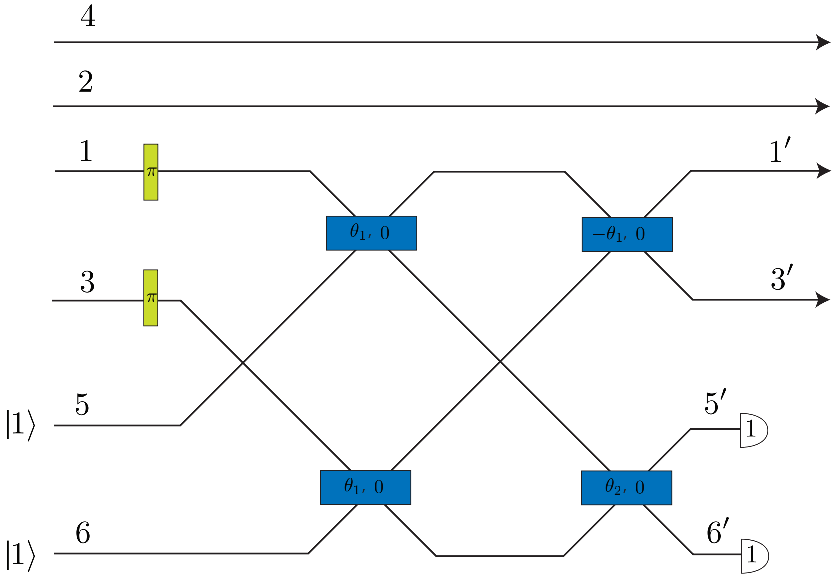

Figure 2.28: A CSIGN gate with success probability $2/27 \approx 0.074$ [39]. Here $\theta_1 = \arccos\left(\frac{1}{\sqrt{3}}\right)$ and $\theta_2 = \frac{1}{2}\arccos\left(\frac{\sqrt{6}}{3}\right)$.

Consider the input state

$$(\alpha|01\rangle + \beta|10\rangle)_{12} (\gamma|01\rangle + \delta|10\rangle)_{34} |11\rangle_{56}$$

with the control incident on modes 1 and 2 and the target incident on modes 3 and 4. After we detect $|11\rangle_{5'6'}$ we have the output:

$$\frac{1}{3}\sqrt{\frac{2}{3}}\,(\alpha\gamma|0101\rangle + \alpha\delta|0110\rangle + \beta\gamma|1001\rangle - \beta\delta|1010\rangle)_{1'23'4}\,.$$

We see a CSIGN has been implemented with a probability of $2/27 \approx 0.074$.

2.7.6 Efficient Parity Encoding

In [87], Gilchrist *et al.* show a generalisation of the parity quantum error correction code described in Eqns. 2.99 and 2.100 in Section 2.6.2, providing a more efficient LOQC two qubit gate. The encoding is based on the incremental encoding in [43]. Qubits are encoded with even and odd parity states:

$$\begin{aligned} |0\rangle^{(n)} &= \frac{1}{\sqrt{2}}\left(|+\rangle^{\otimes n} + |-\rangle^{\otimes n}\right) \\ |1\rangle^{(n)} &= \frac{1}{\sqrt{2}}\left(|+\rangle^{\otimes n} - |-\rangle^{\otimes n}\right) \end{aligned} \tag{2.105}$$

where the physical qubits are defined as $|0\rangle^{(1)} = |0\rangle = |H\rangle$, $|1\rangle^{(1)} = |1\rangle = |V\rangle$ and $|\pm\rangle = \left(|0\rangle \pm |1\rangle\right)/\sqrt{2}$. We see that $|0\rangle^{(n)}$ $\left(|1\rangle^{(n)}\right)$ is just the superposition of all possible even (odd) parity states. Notice that we can write these encoded qubits in terms of the next lower level of encoding:

$$\begin{aligned} |0\rangle^{(n)} &= \frac{1}{\sqrt{2}}\left(|0\rangle^{(n-1)}|0\rangle + |1\rangle^{(n-1)}|1\rangle\right) \\ |1\rangle^{(n)} &= \frac{1}{\sqrt{2}}\left(|0\rangle^{(n-1)}|1\rangle + |1\rangle^{(n-1)}|0\rangle\right). \end{aligned} \tag{2.106}$$

One possible universal set of gates is give by $\{X_\theta, Z_{\frac{\pi}{2}}, \text{CNOT}\}$. The X_θ gate is easily achieved by applying the rotation to any one of the physical qubits. Incidentally, the Pauli Z gate is easily performed on this logic by simply applying a Z operation to each of the physical qubits. The $Z_{\frac{\pi}{2}}$ and CNOT gate need the so called *fusion* gates from [47]. The $Z_{\frac{\pi}{2}}$ and CNOT gates are shown in Fig. 2.29 [87].

The action of the fusion gates f_I and f_{II} are shown in Figs. 2.30 and 2.31, respectively.

We can see the action of the f_I fusion gate by considering what happens when the the following state is incident on Fig. 2.30:

$$\begin{aligned} |\psi\rangle_f &= \left(\alpha|0\rangle^{(n)} + \beta|1\rangle^{(n)}\right)|0\rangle^{(m)} \\ &= \frac{1}{2}\Big(|0\rangle^{(n-1)}\left(\alpha|0\rangle + \beta|1\rangle\right)|0\rangle^{(m-1)}|0\rangle + |0\rangle^{(n-1)}\left(\alpha|0\rangle + \beta|1\rangle\right)|1\rangle^{(m-1)}|1\rangle \\ &\quad + |1\rangle^{(n-1)}\left(\alpha|1\rangle + \beta|0\rangle\right)|0\rangle^{(m-1)}|0\rangle + |1\rangle^{(n-1)}\left(\alpha|1\rangle + \beta|0\rangle\right)|1\rangle^{(m-1)}|1\rangle\Big) \end{aligned} \tag{2.107}$$

where $|\alpha|^2 + |\beta|^2 = 1$ and we have used Eqn. 2.106. We can do this by finding out what f_I does to $c_0|00\rangle + c_1|01\rangle + c_2|10\rangle + c_3|11\rangle$:

$$\begin{aligned} &\left(c_0|HH\rangle + c_1|HV\rangle + c_2|VH\rangle + c_3|VV\rangle\right)_{ab} \\ &\to \frac{1}{\sqrt{2}}\left(c_0|H_cF_e\rangle - c_0|H_cS_f\rangle + \sqrt{2}c_1|H_cV_c\rangle + c_2|2F_e\rangle - c_2|2S_f\rangle + c_3|V_cF_c\rangle + c_3|V_cS_f\rangle\right) \\ &= \frac{1}{\sqrt{2}}\left(|F_e\rangle(c_0|H_c\rangle + c_3|V_c\rangle) + |S_f\rangle(-c_0|H_c\rangle + c_3|V_c\rangle) + \sqrt{2}c_1|H_cV_c\rangle + c_2|2F_e\rangle + c_2|2S_f\rangle\right) \end{aligned}$$

where we have used the polarisation definitions given in Section 2.1.5. If we

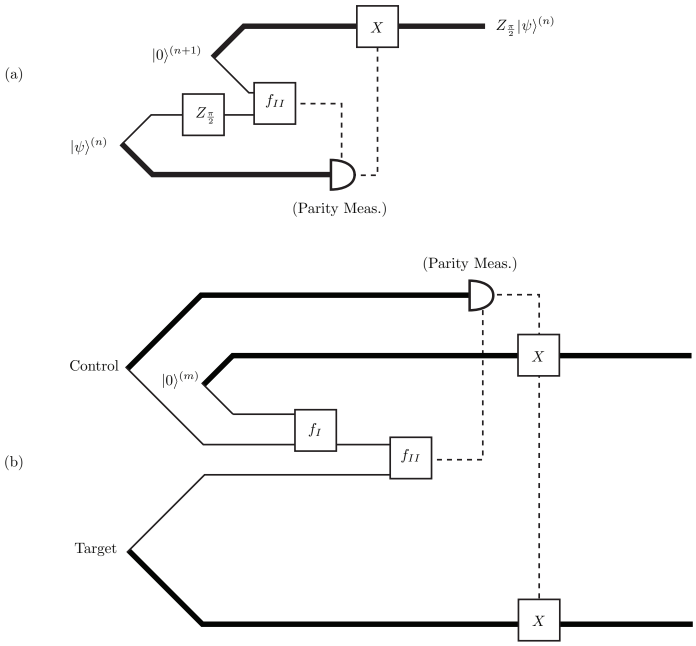

Figure 2.29: **(a)** Applies a $Z_{\frac{\pi}{2}}$ to a qubit encoded via Eqn. 2.105. **(b)** Performs a CNOT between qubits encoded via Eqn. 2.105 [87]. In each case the parity measurement is conditional on the outcome of the f_{II} gate.

apply this to $|\psi\rangle_f$ in Eqn. 2.107 we find after we detect one photon in Fig. 2.30

$$\begin{aligned}|\psi\rangle_f \to &\frac{1}{2\sqrt{2}}\Big(\alpha\left(\pm|0\rangle^{(n-1)}|0\rangle^{(m-1)}|0\rangle + |1\rangle^{(n-1)}|1\rangle^{(m-1)}|1\rangle\right)\\ &+\beta\left(|0\rangle^{(n-1)}|1\rangle^{(m-1)}|1\rangle \pm |1\rangle^{(n-1)}|0\rangle^{(m-1)}|0\rangle\right)\Big)\end{aligned} \tag{2.108}$$

where the ± depends on a detection in mode e or f and can be corrected with a Z gate. The probability for detecting one photon in Fig. 2.30 is $1/2$. If we were to detect two photons in Fig. 2.30, Eqn. 2.107 would become:

$$|\psi\rangle_f \to \pm\frac{1}{2\sqrt{2}}\left(\alpha|1\rangle^{(n-1)} + \beta|0\rangle^{(n-1)}\right)|0\rangle^{(m-1)} \tag{2.109}$$

where once gain the ± is a result of which mode the photons are detected in. The probability for detecting two photons in Fig. 2.30 is $1/4$. If we were to detect zero photons in Fig. 2.30, Eqn. 2.107 would become:

$$|\psi\rangle_f \to \frac{1}{2}\left(\alpha|0\rangle^{(n-1)} + \beta|1\rangle^{(n-1)}\right)|1\rangle^{(m-1)}|\varsigma\rangle \tag{2.110}$$

where the state $|\varsigma\rangle$ has both a horizontally and vertically polarised photon in the same mode, a state outside the logical Hilbert space. The probability for detecting zero photons in Fig. 2.30 is $1/4$.

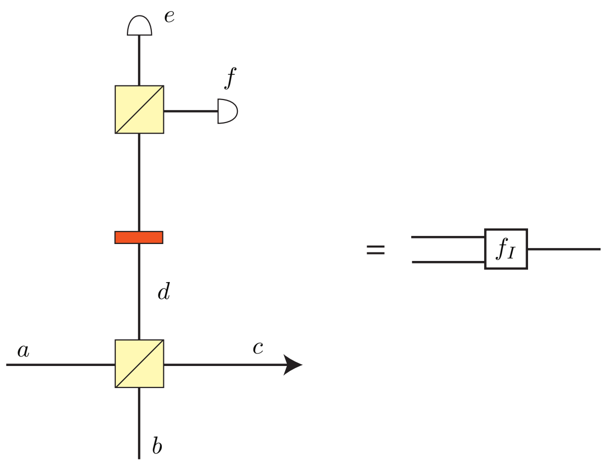

Figure 2.30: Type I fusion gate.

Notice that when we detect the incorrect photon number, that is, zero or two photons, the logical qubit is not destroyed, the level of encoding is reduced by one. We can either re-encode to the original level, or perform the the gate operation can on this new level. This is the so called *incremental* encoding. The probability for a successful measurement outcome for the f_I gate is $\frac{1}{2}$. The f_I fusion gate can be used to build up resource states such as $|0\rangle^{(m)}$, as described in [87].

We can see the action of the f_{II} fusion gate by considering what happens when $|\psi\rangle_f$ in Eqn. 2.107 is incident on Fig. 2.31. We can do this by finding out what f_{II} does to $c_0|00\rangle + c_1|01\rangle + c_2|10\rangle + c_3|11\rangle$:

$$\begin{aligned}
&(c_0|HH\rangle + c_1|HV\rangle + c_2|VH\rangle + c_3|VV\rangle)_{ab} \\
&\to \frac{1}{2}\big(c_0|F_gF_e\rangle - c_0|S_hF_e\rangle - c_0|F_gS_f\rangle + c_0|S_hS_f\rangle + \sqrt{2}c_1|2F_g\rangle - \sqrt{2}c_1|2S_h\rangle \\
&\qquad + \sqrt{2}c_2|2F_e\rangle - \sqrt{2}c_2|2S_f\rangle + c_3|F_gF_e\rangle + c_3|S_hF_e\rangle + c_3|F_gS_f\rangle + c_3|S_hS_f\rangle\big) \\
&= \frac{1}{2}\big((c_0 + c_3)\left(|F_eF_g\rangle + |S_fS_h\rangle\right) + (c_3 - c_0)\left(|F_eS_h\rangle + |S_fF_g\rangle\right) \\
&\qquad + \sqrt{2}\left(c_1|2F_g\rangle - c_1|2S_h\rangle + c_2|2F_e\rangle - c_2|2S_f\rangle\right)\big).
\end{aligned}$$

If we apply this to $|\psi\rangle_f$ in Eqn. 2.107 we find after we detect one photon output from each PBS in Fig. 2.31

$$|\psi\rangle_f \to \frac{1}{2\sqrt{2}}\left(\alpha|0\rangle^{(n+m-1)} + \beta|1\rangle^{(n+m-1)}\right) \tag{2.111}$$

where we need to apply the Pauli Z gate when we we detect $|1001\rangle_{efgh}$ and $|0110\rangle_{efgh}$ in Fig. 2.31. The probability for detecting one photon in each mode in Fig. 2.31 is 1/2. If we were to detect two photons in mode g or h in Fig.

2.31, Eqn. 2.107 would become:

$$|\psi\rangle_f \rightarrow \pm\frac{1}{2\sqrt{2}}\left(\alpha|0\rangle^{(n-1)}+\beta|1\rangle^{(n-1)}\right)|1\rangle^{(m-1)}. \tag{2.112}$$

The probability for detecting two photons in mode g or h Fig. 2.31 is 1/4. If we were to detect two photons in mode e or f in Fig. 2.31, Eqn. 2.107 would become:

$$|\psi\rangle_f \rightarrow \pm\frac{1}{2\sqrt{2}}\left(\alpha|1\rangle^{(n-1)}+\beta|0\rangle^{(n-1)}\right)\gamma|0\rangle^{(m-1)} \tag{2.113}$$

where once gain the ± is a result of which mode the photons are detected in. The probability for detecting two photons in mode e or f Fig. 2.31 is 1/4.

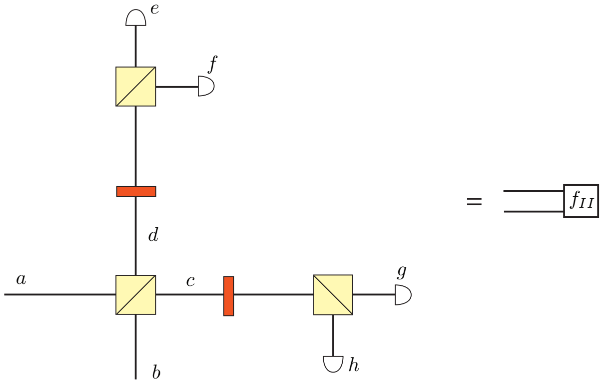

Figure 2.31: Type II fusion gate.

Once again notice that when we detect the incorrect photon number, that is, two photons in one mode, the logical qubits are not destroyed, the level of encoding is reduced by one. The probability for a successful measurement outcome for the f_{II} gate is $\frac{1}{2}$. The f_{II} fusion gate can also be used to build up resource states such as $|0\rangle^{(m)}$, as described in [87].

Using Eqns. 2.111–2.113 we can see how the $Z_{\frac{\pi}{2}}$ gate works in Fig. 2.29(a). If we start with the state $|\psi\rangle_f$ in Eqn. 2.107 with $m = n+1$ and detect one photon output from each PBS for f_{II} we have

$$|0\rangle^{(n-1)}\left(e^{i\frac{\pi}{4}}\alpha|0\rangle^{(n)}+e^{-i\frac{\pi}{4}}\beta|1\rangle^{(n)}\right)+|1\rangle^{(n-1)}\left(e^{i\frac{\pi}{4}}\beta|0\rangle^{(n)}+e^{-i\frac{\pi}{4}}\alpha|1\rangle^{(n)}\right)$$

up to a Z correction. In this case we perform a parity measurement on the rest of the input qubit modes, resulting in a $Z_{\frac{\pi}{2}}$.

If we detect two photons output from each PBS for f_{II} we have

$$\pm e^{-i\frac{\pi}{4}}\left(\alpha|0\rangle^{(n-1)}+\beta|1\rangle^{(n-1)}\right)|1\rangle^{(n)} \quad \text{or} \quad \pm\, e^{i\frac{\pi}{4}}\left(\alpha|1\rangle^{(n-1)}+\beta|0\rangle^{(n-1)}\right)|0\rangle^{(n)}.$$

The probability for this unsuccessful $Z_{\frac{\pi}{2}}$ is 1/2. We can either re-encode or attempt the $Z_{\frac{\pi}{2}}$ gate on $\alpha|0\rangle^{(n-1)}+\beta|1\rangle^{(n-1)}$. If we continue attempting the

$Z_{\frac{\pi}{2}}$ gate on qubit as the level of encoding is reduce, the probability of success for the $Z_{\frac{\pi}{2}}$ gate is

$$P_{Z_{\frac{\pi}{2}}} = 1 - \left(\frac{1}{2}\right)^n . \tag{2.114}$$

Using Eqns. 2.108–2.113 we can see how the CNOT gate works in Fig. 2.29(b). If we start with the state $|\psi\rangle_f \left(\gamma|0\rangle^{(n)} + \delta|1\rangle^{(n)}\right)$, with $m = n$ and detect one photon output from each PBS for f_{II} we have

$$|0\rangle^{n-1}\left(\alpha\gamma|0\rangle^{(n-1)}|0\rangle^{(n-1)} + \alpha\delta|0\rangle^{(n-1)}|1\rangle^{(n-1)} + \beta\gamma|0\rangle^{(n-1)}|1\rangle^{(n-1)} + \beta\delta|1\rangle^{(n-1)}|0\rangle^{(n-1)}\right)$$
$$+ |1\rangle^{n-1}\left(\alpha\gamma|1\rangle^{(n-1)}|1\rangle^{(n-1)} + \alpha\delta|1\rangle^{(n-1)}|0\rangle^{(n-1)} + \beta\gamma|0\rangle^{(n-1)}|0\rangle^{(n-1)} + \beta\delta|0\rangle^{(n-1)}|1\rangle^{(n-1)}\right)$$

up to a Z correction. In this case we perform a parity measurement on the rest of the control qubit modes, resulting in a CNOT . The probability that both the f_I and the f_{II} gate fail is 3/4. As mentioned above, when these gates fail the qubit has its parity encoding reduced by one. When we continue attempting the CNOT on the reduced encoding, the probability of success is given by

$$P_{\text{CNOT}} = 1 - \left(\frac{3}{4}\right)^n . \tag{2.115}$$

We compare the probability of success for the CNOT described in Eqn. 2.115 with that described in Section 2.5, remembering that the success probability scaled as $\left(\frac{n}{n+1}\right)^2$ when we use $|t_n\rangle$ states for teleportation. This comparison is shown in Fig. 2.32. Notice that after $n = 2$, the proposal in [87] has a higher success probability for a given n than the original LOQC proposal in [31].

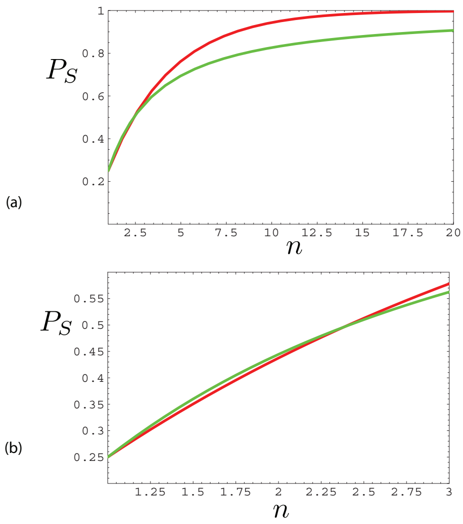

Figure 2.32: The probability of success for a probabilistic CSIGN gate as the number of photons n is increased. The Red curve represents the model from [87] whereas the Green curve represents the model from [31]. Part (b) shows the success probability for small n.

2.7.7 Non Destructive Measurements with Linear Optics

Photon number QND detector

In [88] Kok *et al.* show a method to detect the presence of a single photon in an optical state without destroying the photon's polarisation information using linear optics and projective measurements. This type of measurement is termed a quantum nondemolition (QND) measurement [89, 90] since the backaction action of the measurement only affects unwanted observables, such as the photon number of ancilla modes in this case.

The scheme proposed by Kok *et al.* to detect the presence of a single photon in the state

$$|\psi_{\rm in}\rangle = b_0|0\rangle_a + b_1\big(\alpha|H\rangle + \beta|V\rangle\big)_a + b_2\big(\mu|2H\rangle + \chi|HV\rangle + \nu|2V\rangle\big)_a \qquad (2.116)$$

without destroying the polarisation encoding, where $|\alpha|^2 + |\beta|^2 = |\mu|^2 + |\chi|^2 + |\nu|^2 = |b_0|^2 + |b_1|^2 + |b_2|^2 = 1$, is shown in Fig. 2.33. Here $|2H\rangle_a$ represents two horizontal photons in mode a and $|HV\rangle_a$ represents a horizontal and vertical photon both in mode a. There are four ancilla modes in the state $|VHVH\rangle_{cdef}$. When we detect modes c_1' and d_1', there are a maximum of 4 photons in the system. This means there are 15 possible measurement outcomes. If we condition on a coincidence in modes c_1' and d_1' there are again a maximum of 4 photons in the system when we measure modes c_2' and d_2', since the ancilla modes c_2 and d_2 are input into to the system after we measure modes c_1' and d_1'. Given that we detect a coincidences in modes c_1' and d_1' and in modes c_2' and d_2' we have

$$\begin{aligned} b_1 \cos^2\left(\frac{1}{2}\arccos\left(-\frac{1}{3}\right)\right)\sin^4\left(\frac{1}{2}\arccos\left(-\frac{1}{3}\right)\right)\left(\alpha|H\rangle+\beta|V\rangle\right)_{a'} \\ = \frac{4}{27}b_1\left(\alpha|H\rangle+\beta|V\rangle\right)_{a'}. \end{aligned} \tag{2.117}$$

Notice that the probability of success $16|b_1|^2/729$ is dependent on b_1. In the case that $b_1 = 1$ and $b_0 = b_2 = 0$, the probability of success is $16/729 \approx 0.0219$.

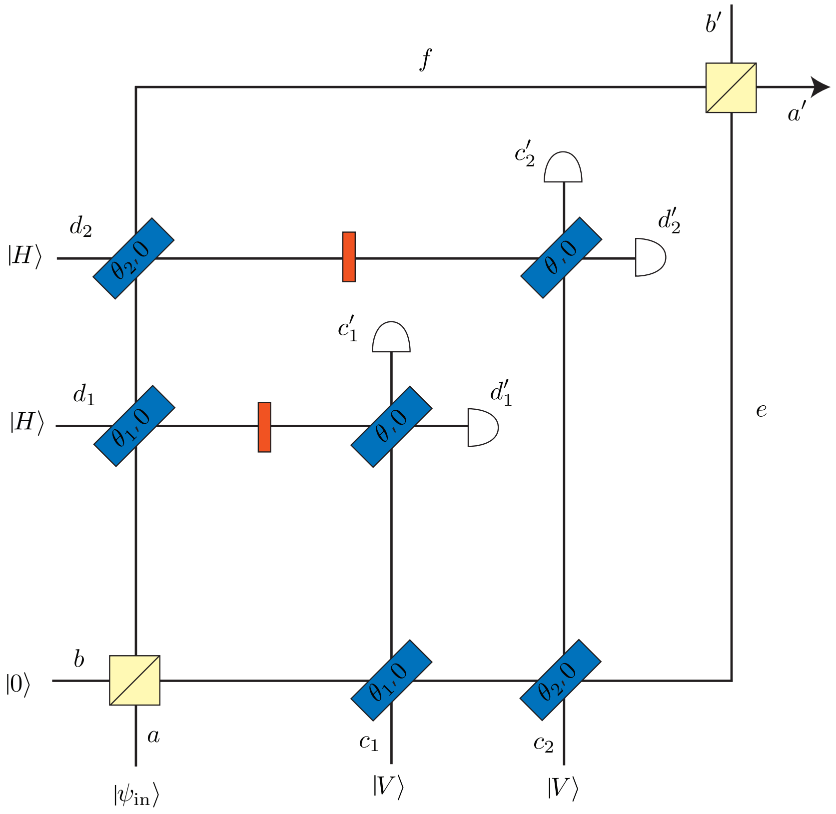

Figure 2.33: Photon number QND detector [88]. Detects the presence of a single photon in an arbitrary polarisation state from the state $|\psi_{\text{in}}\rangle = b_0|0\rangle_a + b_1\left(\alpha|H\rangle+\beta|V\rangle\right)_a + b_2\left(\mu|2H\rangle + \chi|HV\rangle + \nu|2V\rangle\right)_a$. When $\theta = \frac{\pi}{4}$ and $\theta_1 = \theta_2 = -\frac{1}{2}\arccos\left(\frac{1}{3}\right)$, the success probability for this circuit is $(4/27)^2 \approx 0.0219$. There is an ancilla photon in the state $|V\rangle$ in modes c_1 and c_2, and an ancilla photon in the state $|H\rangle$ in modes d_1 and d_2. Mode b has a vacuum input. The polariser transforms H to V and vice versa.

An alternate scheme was also proposed by Kok *et al.* in [88] to detect the presence of a single photon in Eqn.(2.116) when $b_2 = 0$, by using teleportation with the use of a polarisation-entangled state from a parametric down converter

$$|\Psi_{\text{PDC}}\rangle = (1-\epsilon^2)|0\rangle + \frac{\epsilon}{\sqrt{2}}\left(|H\rangle|V\rangle - |V\rangle|H\rangle\right) + O(\epsilon^2). \tag{2.118}$$

If we consider this scheme in terms of dual rail encoding, the circuit to detect the presence of a single photon in either mode a or b in the state

$$|\Psi_1\rangle = b_0|00\rangle_{ab} + b_1\big(\alpha|10\rangle + \beta|01\rangle\big)_{ab} + b_2\big(\mu|20\rangle + \chi|11\rangle + \nu|01\rangle\big)_{ab} \quad (2.119)$$

with $b_2 = 0$ is shown in Fig. 2.34. The corresponding dual rail state for the parametric down converter is given by

$$|\Psi_{\rm PDC}\rangle = (1-\epsilon^2)|0000\rangle_{cdef} + \frac{\epsilon}{\sqrt{2}}\left(|1001\rangle - |0110\rangle\right)_{cdef} + O(\epsilon^2). \quad (2.120)$$

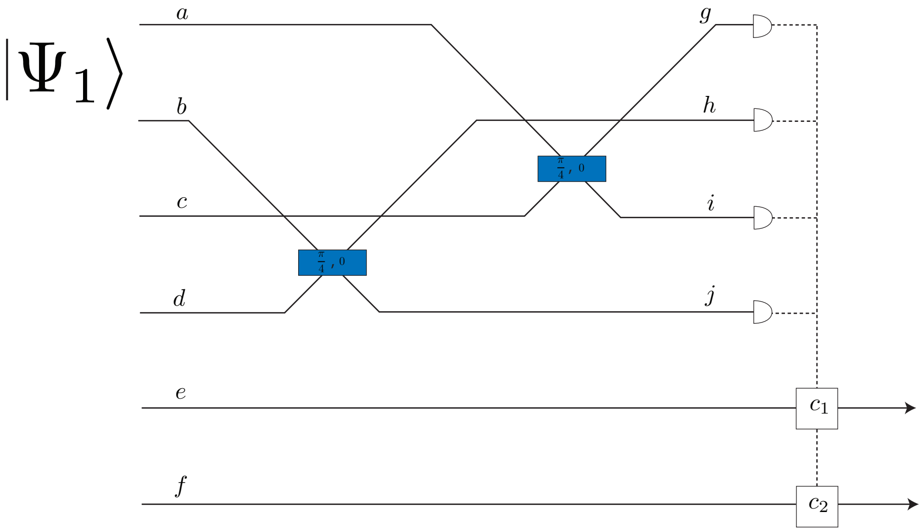

Figure 2.34: Photon number QND detector [88]. Detects the presence of a single photon in either mode a or b in the state $|\Psi_1\rangle = b_0|00\rangle_{ab} + b_1\big(\alpha|10\rangle + \beta|01\rangle\big)_{ab}$. The ancilla state is $(1-\epsilon^2)|0000\rangle_{cdef} + \frac{\epsilon}{\sqrt{2}}\left(|1001\rangle - |0110\rangle\right)_{cdef}$. Success is indicated with a detection of either $|1001\rangle_{ghij}$, $|0110\rangle_{ghij}$, $|1100\rangle_{ghij}$ or $|0011\rangle_{ghij}$. The total probability of success is $\epsilon^2|b_1|^2/2$.

There are four detection outcomes that indicate success:

$$\begin{aligned}
&-\frac{\epsilon b_1}{2\sqrt{2}}\left(\alpha|10\rangle + \beta|01\rangle\right)_{ef}|1001\rangle_{ghij}\\
&\frac{\epsilon b_1}{2\sqrt{2}}\left(\alpha|10\rangle + \beta|01\rangle\right)_{ef}|0110\rangle_{ghij}\\
&\frac{\epsilon b_1}{2\sqrt{2}}\left(\alpha|10\rangle - \beta|01\rangle\right)_{ef}|1100\rangle_{ghij}\\
&\frac{\epsilon b_1}{2\sqrt{2}}\left(-\alpha|10\rangle + \beta|01\rangle\right)_{ef}|0011\rangle_{ghij}.
\end{aligned}$$

The total probability of success is $\epsilon^2|b_1|^2/2$. If we consider $b_2 \neq 0$ in Eqn.2.119, the fidelity for the output from Fig. 2.34 becomes vanishing small once $|b_2|^2 \gg \epsilon^2|b_1|^2$ [88].

Polarisation QND detector

In [91] Pryde *et al.* show a method to indirectly detect the polarisation of a photon by using ancilla photons. This scheme is shown in Fig. 2.35. In the case that we ignore the top beam splitter in Fig. 2.35, that is, set $\theta_2 = \pi/2$, the state

$$(\alpha|H\rangle + \beta|V\rangle)_s \left(\frac{\sqrt{3}}{2}|H\rangle + \frac{1}{2}|V\rangle\right)_m \tag{2.121}$$

is transformed to

$$\frac{\alpha}{\sqrt{3}}\left(|0,2V\rangle - |2H,0\rangle + \frac{1}{\sqrt{2}}|H,H\rangle + \frac{1}{\sqrt{2}}|0,HV\rangle\right)_{c,e} + \frac{\beta}{\sqrt{2}}\left(|HV,0\rangle + |V,V\rangle\right)_{c,e}.$$

When we detect one photon in either mode e_H or e_V we have

$$\frac{\alpha}{\sqrt{6}}|H\rangle_c|H\rangle_e$$
$$\frac{\beta}{\sqrt{2}}|V\rangle_c|V\rangle_e.$$

We see we have measured the polarisation of the photon initially incident in mode s non-destructively. The probability of success in this case is dependent on the input state and is given by $\left(|\alpha|^2 + 3|\beta|^2\right)/6$. If we were to set the top beam splitter to $\theta_2 = \arccos\left(\sqrt{\frac{2}{3}}\right)$ the success probability can be made independent of the input state. In this case the state

$$(\alpha|H\rangle + \beta|V\rangle)_s \left(\frac{\sqrt{3}}{2}|H\rangle + \frac{1}{2}|V\rangle\right)_m |0\rangle_a \tag{2.122}$$

is transformed to

$$\frac{\alpha}{\sqrt{3}}\left(|0,2V,0\rangle - |2H,0,0\rangle + \frac{1}{\sqrt{2}}|H,H,0\rangle + \frac{1}{\sqrt{2}}|0,HV,0\rangle\right)_{c,e,b} + \frac{\beta}{\sqrt{3}}\left(\frac{1}{\sqrt{2}}|H,V,0\rangle + |H,0,V\rangle + |0,V,V\rangle\right)_{c,e,b}.$$

When we detect vacuum in mode b and one photon in either mode e_H or e_V we have

$$\frac{\alpha}{\sqrt{6}}|H\rangle_c|H\rangle_e|0\rangle_b$$
$$\frac{\beta}{\sqrt{6}}|V\rangle_c|V\rangle_e|0\rangle_b.$$

The probability of success in this case is $\left(|\alpha|^2 + |\beta|^2\right)/6 = 1/6$, independent of the input state.

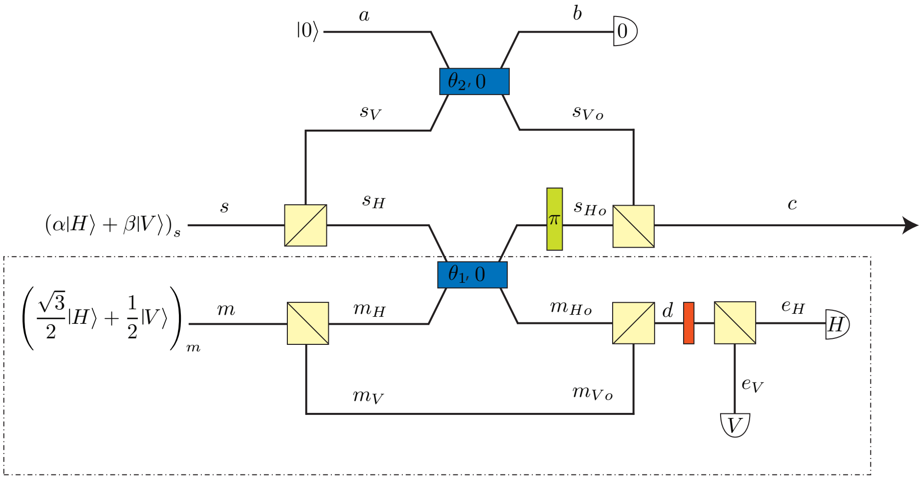

Figure 2.35: A polarisation QND detector [91]. We set $\theta_1 = \arccos\left(\frac{1}{\sqrt{3}}\right)$. When $\theta_2 = \pi/2$ the device succeeds with a probability $|\alpha|^2/6 + |\beta|^2/2$ if we detect 1 photon in either mode e_H or e_V. When $\theta_2 = \arccos\left(\sqrt{\frac{2}{3}}\right)$ the device succeeds with a probability of $1/6$ if we detect vacuum in mode b and 1 photon in either mode e_H or e_V. The QND device is enclosed in the dashed-dotted box. The polariser here transforms d_H to $\frac{1}{\sqrt{2}}(d_H + d_V)$ and d_V to $\frac{1}{\sqrt{2}}(-d_H + d_V)$.

2.8 Quantum Bus Computation

In [49, 92] Nemoto *et al.* build on the idea of using a cross Kerr non-linearity [29, 28], described in Section 2.2, to construct a near deterministic CNOT gate. Nemoto *et al.* circumvent the need for a large cross Kerr non-linearity by using weak Kerr non-linearities in conjunction with large coherent bus modes. The weak Kerr non-linearities induce a phase shift on the coherent bus mode that is dependent on the logical state of the polarisation qubits. This phase shift is measured via homodyne detection, thus inducing a CNOT for a sufficiently large bus mode α and non-linearity θ: $\alpha\theta \gg 1$. The relatively low number of photon interactions and optical components makes this scheme particularly attractive. This model of computation is named quantum bus, or "qubus" computation [93].

It is unlikely that Kerr materials will be used to induce the nonlinearities required for qubus computation since the phase shift θ predicted for Kerr media is on the order of 10^{-18}radians [94, 88]. One promising area is electromagnetically induced transparency [95, 96, 97]. It has been suggested a θ as large as 10^{-2}radians could be obtained experimentally [63].

An advantage the qubus scheme has over LOQC is that it is deterministic, given the right scaling for α and θ. This scaling for qubus computation is the source of the necessary non-linearity required to induce photon-photon interaction. This is in contrast to LOQC, which requires projective measurements in conjunction with offline entangled state production. This scaling is also a disadvantage for qubus computation since it makes the scheme heavily dependent on experimental progress in making large nonlinearities. Another possible drawback to the qubus scheme was shown by Shapiro *et al.* [98] when considering a continuous-time multi-mode model for the nonlinear medium inside an optical fibre, resulting in phase noise terms.

2.8.1 Controlled rotations

In Section 2.1.5 we described the effect a phase shifter has on a coherent state, transforming $|\alpha\rangle$ to $|e^{i\phi}\alpha\rangle$. In phase space this corresponds to a rotation by the angle ϕ. We can use this fact to induce a controlled rotation on a coherent state. In optics we can use the cross Kerr non-linearity, described by the Hamiltonian in Eqn. 2.66, to induce a controlled rotation. If the state $\big(c_0|0\rangle + c_1|1\rangle\big)_1|\alpha\rangle_2$ evolves according to Eqn. 2.66, we obtain the state $c_0|0\rangle_1|\alpha\rangle_2 + c_1|1\rangle_1|e^{i\theta}\alpha\rangle_2$ when $\theta = \chi t$. In general, the state $\big(c_0|0\rangle + c_n|n\rangle\big)_1|\alpha\rangle_2$ evolves to $c_0|0\rangle_1|\alpha\rangle_2 + c_n|n\rangle_1|e^{in\theta}\alpha\rangle_2$. The qubit states are left unaffected by this transformation and the coherent probe beam is conditionally rotated.

2.8.2 Parity Gate

In [49] Nemoto and Munro used controlled rotations to construct a parity gate on polarisation logic, shown in Fig. 2.36.

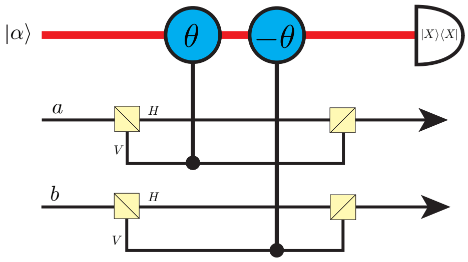

Figure 2.36: Qubus polarisation parity gate.

Consider the following state incident on Fig. 2.36

$$(c_0|HH\rangle + c_1|HV\rangle + c_2|VH\rangle + c_3|VV\rangle)_{ab}\,|\alpha\rangle \tag{2.123}$$

where $|\alpha\rangle$ is a large coherent bus mode and $|H\rangle \equiv |0\rangle$ and $|V\rangle \equiv |1\rangle$. After the two controlled rotations we have

$$(c_0|HH\rangle + c_3|VV\rangle)_{ab}\,|\alpha\rangle + c_1|HV\rangle_{ab}|e^{-i\theta}\alpha\rangle + c_2|VH\rangle_{ab}|e^{i\theta}\alpha\rangle. \tag{2.124}$$

The phase space representation of this is shown in Fig. 2.37.

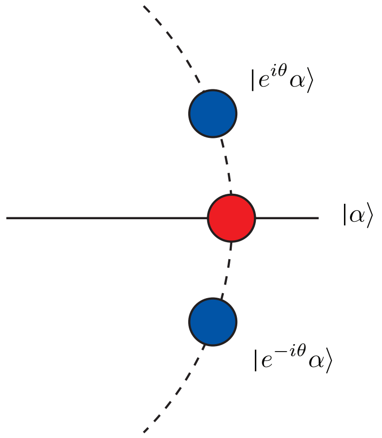

Figure 2.37: Phase space representation for the polarisation parity gate in Fig. 2.36.

To distinguish the parity, we homodyne detect the probe beam in the $x-$direction. In Section 2.1.6, we noted that $\langle x|e^{i\theta}\alpha\rangle = f(x, \alpha\cos(\theta))e^{i\phi(x)}$ for $\alpha, \theta \in \mathbb{R}$, where

$$f(x, \alpha) = \big(2\pi\big)^{-\frac{1}{4}} \exp\Big(-\frac{1}{4}\big(x - 2\alpha\big)^2\Big)$$
$$\phi(x) = \alpha\sin(\theta)\big(x - 2\alpha\cos(\theta)\big).$$

Since we are detecting in the $x-$direction, the states $|e^{i\theta}\alpha\rangle$ and $|e^{-i\theta}\alpha\rangle$ are indistinguishable up to a phase factor: $\langle x|e^{\pm i\theta}\alpha\rangle = f(x, \alpha\cos(\theta))e^{\pm i\phi(x)}$. Eqn. 2.37 becomes:

$$\big(c_0|HH\rangle + c_3|VV\rangle\big)f(x, \alpha) + \big(e^{-i\phi(x)}c_1|HV\rangle + e^{i\phi(x)}c_2|VH\rangle\big)f(x, \alpha\cos(\theta)). \tag{2.125}$$

The peak separation is given by $X_d = 2\alpha(1 - \cos(\theta))$ and the mid-point (cross over point between the Gaussian curves $f(x, \alpha\cos(\theta))$ and $f(x, \alpha)$) is $X_0 = 2\alpha\cos(\theta) + \frac{1}{2}\big(2\alpha - 2\alpha\cos(\theta)\big) = \alpha(1 + \cos(\theta))$ as can be seen below in Fig. 2.38.

We can expand X_d using Eqn. 2.33: $X_d = 2\alpha[1 - 1 + \frac{1}{2!}\theta^2 - \frac{1}{4!}\theta^4 + \cdots] \approx \alpha\theta^2$, for small θ. Provided

$$X_d \approx \alpha\theta^2 \gg 1, \tag{2.126}$$

the overlap between the two curves in Fig. 2.38 is small. In the case that $X > X_0$, Eqn. 2.125 approximately becomes

$$c_0|HH\rangle_{ab} + c_3 d_1|VV\rangle_{ab}$$

and in the case that $X < X_0$ Eqn. 2.125 approximately becomes

$$c_1 e^{-i\phi(X)}|HV\rangle_{ab} + c_2 e^{i\phi(X)}|VH\rangle_{ab}.$$

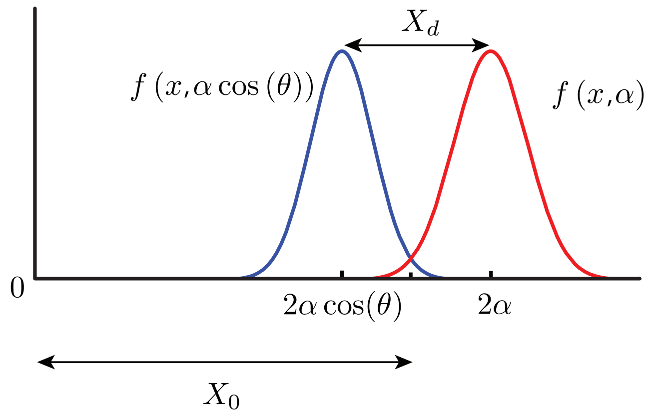

Figure 2.38: Plot showing $f(X, \alpha)$ and $f(X, \alpha\cos(\theta))$.

Feed-forward can be used to give the state $c_1|HV\rangle + c_2|VH\rangle$ when $X < X_0$, for example, by applying a phase shifter on horizontal photons in mode b. We see that Fig. 2.36 acts as a parity gate. With two parity gates we can distinguish all four Bell states, which is the basis for the CNOT Nemoto and Munro construct in [49], described in Section 2.8.4.

2.8.3 Probability of Error

We calculate the probability of Fig. 2.36 incorrectly identifying the parity as the overlap between $f(x, \alpha)$ and $f(x, \alpha\cos(\theta))$:

$$\begin{aligned} P_{\text{err}} &= \int_{X_0}^{\infty} f^2(x, \alpha\cos(\theta))dx + \int_{-\infty}^{X_0} f^2(x, \alpha)dx \\ &= \frac{1}{\sqrt{2\pi}}\left(\int_{X_0}^{\infty} \exp\left(-\frac{1}{2}(x - 2\alpha\cos(\theta))^2\right)dx + \int_{-\infty}^{X_0} \exp\left(-\frac{1}{2}(x-2\alpha)^2\right)dx\right) \\ &= \frac{1}{\sqrt{\pi}}\left(\int_{\frac{X_d}{2\sqrt{2}}}^{\infty} e^{-y^2}dy + \int_{-\infty}^{-\frac{X_d}{2\sqrt{2}}} e^{-y^2}dy\right) \end{aligned}$$

where $y = \frac{1}{\sqrt{2}}\big(x - 2\alpha\cos(\theta)\big)$ for the left hand integral and $y = \frac{1}{\sqrt{2}}\big(x - 2\alpha\big)$ for the right. Since

$$\int_{-\infty}^{z} e^{-t^2}dt = -\int_{\infty}^{-z} e^{-x^2}dx = \int_{-z}^{\infty} e^{-x^2}dx,$$

the probability of error becomes

$$\begin{aligned} P_{\text{err}} = \frac{2}{\sqrt{\pi}}\int_{\frac{X_d}{2\sqrt{2}}}^{\infty} e^{-y^2}dy &= \text{Erfc}\left[\frac{X_d}{2\sqrt{2}}\right] \\ &\approx \text{Erfc}\left[\frac{\alpha\theta^2}{\sqrt{8}}\right]. \end{aligned} \tag{2.127}$$

2.8.4 Single Photon Ancilla CNOT

Using two parity gates a CNOT can be constructed [49], as shown in Fig. 2.39. This CNOT is based on the Pittman destructive CNOT [36], described in Section 2.7.2. We effectively replace each PBS in the Pittman destructive CNOT (Fig. 2.25) with a parity gate.

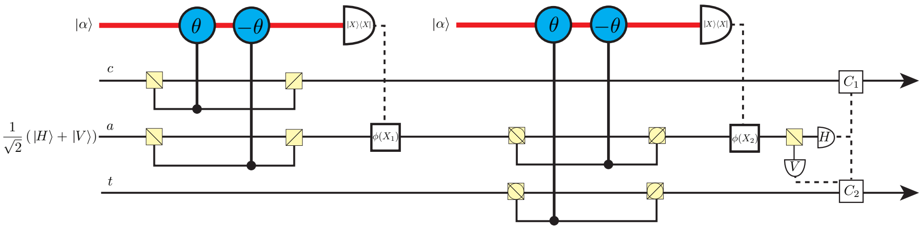

Figure 2.39: CNOT gate acting on polarisation logic using two of the parity gates from Fig. 2.36 [49]. This CNOT is based on the Pittman Bell state CNOT [34]. The correction gate C_1 is either $\mathbb{1}$ of X and C_2 is either X or $\mathbb{1}$.

Consider the state

$$(c_0|H\rangle + c_1|V\rangle)_c \otimes \frac{1}{\sqrt{2}}(|H\rangle + |V\rangle)_a \otimes (d_0|H\rangle + d_1|V\rangle)_t$$

incident on Fig. 2.39. The single photon ancilla can be produced from a coherent state and controlled rotations [92]. After the first parity gate we have

$$\begin{aligned}
&(c_0|HH\rangle + c_1|VV\rangle)_{ca} \otimes (d_0|H\rangle + d_1|V\rangle)_t \\
&= \frac{1}{2}\Big(c_0d_0\,(|HFF\rangle - |HFS\rangle - |HSF\rangle + |HSS\rangle) \\
&\quad + c_0d_1\,(|HFF\rangle + |HFS\rangle - |HSF\rangle - |HSS\rangle) \\
&\quad + c_1d_0\,(|VFF\rangle - |VFS\rangle + |VSF\rangle - |VSS\rangle) \\
&\quad + c_1d_1\,(|VFF\rangle + |VFS\rangle + |VSF\rangle + |VSS\rangle)\Big)_{cat}
\end{aligned}$$

where we have assumed we detect $X_1 > X_0$ in the first homodyne detection and F and S represent 45 degree polarisation states, as defined in Section 2.1.5.

After the second homodyne detection, if we measure $X_2 > X_0$ we have

$$\begin{aligned}
&\frac{1}{2}\Big(c_0d_0|HFF\rangle + c_0d_0|HSS\rangle + c_0d_1|HFF\rangle - c_0d_1|HSS\rangle \\
&+ c_1d_0|VFF\rangle - c_1d_0|VSS\rangle + c_1d_1|VFF\rangle + c_1d_1|VSS\rangle\Big)_{cat}
\end{aligned}$$

otherwise, if we measure $X_2 < X_0$ we have

$$\begin{aligned}
&\frac{1}{2}\Big(e^{i\phi(X_2)}\big(-c_0d_0|H\rangle + c_0d_1|H\rangle - c_1d_0|V\rangle + c_1d_1|V\rangle\big)|FS\rangle \\
&+ e^{-i\phi(X_2)}\big(-c_0d_0|H\rangle - c_0d_1|H\rangle + c_1d_0|V\rangle + c_1d_1|V\rangle\big)|SF\rangle\Big)_{cat}.
\end{aligned}$$

In the case that $X_2 > X_0$, when we detect mode a to be $|H\rangle$ the output state is

$$\frac{1}{2}\left(c_0d_0|HH\rangle + c_0d_1|HV\rangle + c_1d_0|VV\rangle + c_1d_1|VH\rangle\right)_{ct}$$

and when we detect mode a to be $|V\rangle$ we have

$$\frac{1}{2}\left(c_0d_0|HV\rangle + c_0d_1|HH\rangle + c_1d_0|VH\rangle + c_1d_1|VV\rangle\right)_{ct}$$

and require $C_2 = X$.

In the case that $X_2 < X_0$, we must correct for the phase factors $e^{\pm i\phi(X_2)}$. When we detect mode a to be $|H\rangle$ the output state is

$$\frac{1}{2}\left(c_0d_0|HH\rangle + c_0d_1|HV\rangle - c_1d_0|VV\rangle - c_1d_1|VH\rangle\right)_{ct}$$

and require $C_1 = Z$. When we detect mode a to be $|V\rangle$ we have

$$\frac{1}{2}\left(-c_0d_0|HV\rangle - c_0d_1|HH\rangle + c_1d_0|VH\rangle + c_1d_1|VV\rangle\right)_{ct}$$

and require $C_1 = Z$ and $C_2 = X$.

2.8.5 Bell State Ancilla CNOT

An alternative CNOT can also be constructed [92] using two parity gates that is based on the Pittman Bell state [34], described in Section 2.7.1. As in the previous section, this CNOT replaces each PBS in the Pittman scheme (Fig. 2.24) with a parity gate, as shown in Fig. 2.40.

Consider the state

$$\left(\beta_0|HH\rangle + \beta_1|HV\rangle + \beta_2|VH\rangle + \beta_3|VV\rangle\right)_{ct} \otimes \frac{1}{\sqrt{2}}\left(|HH\rangle + |VV\rangle\right)_{ba}$$

incident on Fig. 2.40. We first consider the top parity gate. In the case that we homodyne detect $X_1 > X_0$ we have

$$\begin{aligned}\frac{1}{2}\Big(&|F\rangle_c\left(\beta_0|HHH\rangle + \beta_1|HHV\rangle + \beta_2|VVH\rangle + \beta_3|VVV\rangle\right)_{bat}\\ &+|S\rangle_c\left(-\beta_0|HHH\rangle - \beta_1|HHV\rangle + \beta_2|VVH\rangle + \beta_3|VVV\rangle\right)_{bat}\Big).\end{aligned}$$

When we measure $|F\rangle_c$ no correction is necessary. When we measure $|S_c\rangle$ we require C_1 to transform $|H\rangle_b \to -|H\rangle_b$.

In the case that we homodyne detect $X_1 < X_0$ we have

$$\begin{aligned}\frac{1}{2}\Big(&|F\rangle_c\left(\beta_0|VVH\rangle + \beta_1|VVV\rangle + \beta_2|HHH\rangle + \beta_3|HHV\rangle\right)_{bat}\\ &+|S\rangle_c\left(-\beta_0|VVH\rangle - \beta_1|VVV\rangle + \beta_2|HHH\rangle + \beta_3|HHV\rangle\right)_{bat}\Big).\end{aligned}$$

When we measure $|F\rangle_c$ we require C_1 to flip the polarisation on mode b. When we measure $|S_c\rangle$ we require C_1 flip the polarisation on mode b and to transform

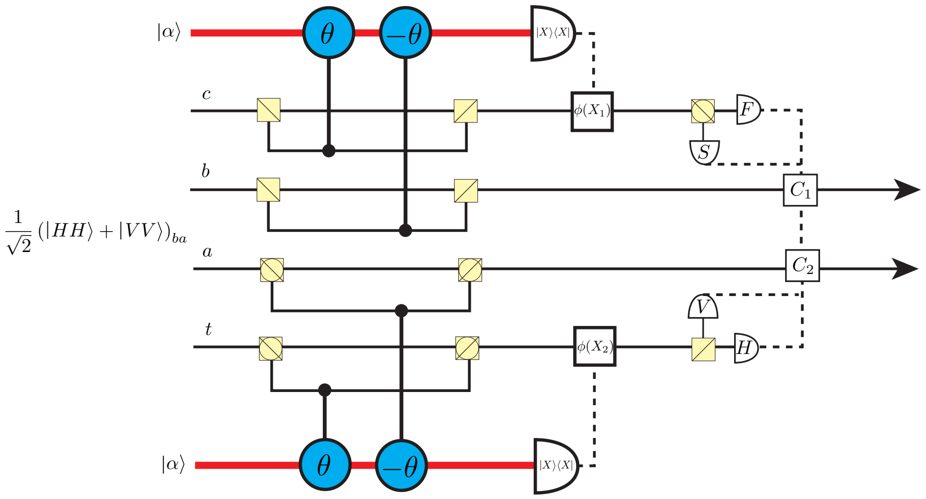

Figure 2.40: CNOT gate acting on polarisation logic using two of the parity gates from Fig. 2.36 [92]. This CNOT is based on the Pittman Bell state CNOT [34]. The correction gate C_1 and C_2 apply the gates X and Z as needed.

$|H\rangle_b \to -|H\rangle_b$. In both these cases, if we also flip the polarisation on mode a, we have the state $(\beta_0|HHH\rangle + \beta_1|HHV\rangle + \beta_2|VVH\rangle + \beta_3|VVV\rangle)\,bat$, as for the $X_1 > X_0$ case. Even though this is not necessary for Fig. 2.40 to function as a CNOT , for the sake of simplicity we assume the top parity gate produces the state

$$\begin{aligned}
&\frac{1}{2}(\beta_0|HHH\rangle + \beta_1|HHV\rangle + \beta_2|VVH\rangle + \beta_3|VVV\rangle)\,bat \\
&= \frac{1}{4}\Bigg(\Big((\beta_0+\beta_1)\,|H\rangle_b + (\beta_2+\beta_3)\,|V\rangle_b\Big)|FF\rangle_{at} \\
&\quad + \Big(-(\beta_0+\beta_1)\,|H\rangle_b + (\beta_2+\beta_3)\,|V\rangle_b\Big)|FS\rangle_{at} \\
&\quad + \Big((-\beta_0+\beta_1)\,|H\rangle_b + (-\beta_2+\beta_3)\,|V\rangle_b\Big)|SF\rangle_{at} \\
&\quad + \Big((\beta_0-\beta_1)\,|H\rangle_b + (-\beta_2+\beta_3)\,|V\rangle_b\Big)|SS\rangle_{at}\Bigg).
\end{aligned}$$

When we homodyne detect after the bottom parity gate in Fig. 2.40, we have

$$\begin{aligned}
&\frac{1}{2}|H\rangle_t\Big(\beta_0|HH\rangle + \beta_1|HV\rangle + \beta_2|VV\rangle + \beta_3|VH\rangle\Big)_{ba} \\
+&\frac{1}{2}|V\rangle_t\Big(\beta_0|HV\rangle + \beta_1|HH\rangle + \beta_2|VH\rangle + \beta_3|VV\rangle\Big)_{ba}
\end{aligned}$$

for $X_2 > X_0$. If we measure $|V\rangle_t$ we require C_2 to flip polarisation on mode a.

When $X_2 < X_0$, we have

$$\frac{1}{2}|H\rangle_t\Big(\beta_0|HH\rangle - \beta_1|HV\rangle + \beta_2|VV\rangle - \beta_3|VH\rangle\Big)_{ba}$$
$$+\frac{1}{2}|V\rangle_t\Big(-\beta_0|HV\rangle + \beta_1|HH\rangle - \beta_2|VH\rangle + \beta_3|VV\rangle\Big)_{ba}.$$

If we measure $|H\rangle_t$ we need to apply the transformations $|V\rangle_b \rightarrow -|V\rangle_b$ and $|V\rangle_a \rightarrow -|V\rangle_a$. If we measure $|V\rangle_t$ we require C_2 to flip the polarisation on mode a and to apply the transformations $|V\rangle_b \rightarrow -|V\rangle_b$ and $|V\rangle_a \rightarrow -|V\rangle_a$.

2.8.6 Displacements

In Sections 2.8.4 and 2.8.5 two qubus CNOT constructions were presented that were based on the parity gate from Fig. 2.36. The operation of this parity gate can be improved by allowing the use of displacements on the coherent probe beam.

Displacements of a state can easily be implemented by mixing the state with a large coherent state on a weak beam splitter, the size of the coherent state amplitude and beam splitter reflectivity deciding the displacement [55]. For example, consider displacing the state $f\left(\hat{a}^\dagger, \hat{a}\right)|\text{vac}\rangle$, where $f()$ is a polynomial function of $\hat{a}^\dagger$ and $\hat{a}$ that can be written in normal ordered form, as described in Section 2.1.5: $\tilde{f}\left(\hat{a}^\dagger\right)|\text{vac}\rangle = \sum_{j=0}^{n} c_j \left(\hat{a}^\dagger\right)^j |\text{vac}\rangle$. From Eqn. 2.25 we know that

$$D(\gamma)\tilde{f}(\hat{a}^\dagger) = \sum_{j=0}^{n} c_j \left(\hat{a}^\dagger - \gamma^*\right)^j D(\gamma). \tag{2.128}$$

If we instead consider a $\theta, \phi = \pi$ beam splitter with $\tilde{f}\left(\hat{a}^\dagger\right)|\text{vac}\rangle$ and $|\beta\rangle$ incident we have

$$\tilde{f}(\hat{a}^\dagger)|\text{vac}\rangle \otimes |\beta\rangle \rightarrow \tilde{f}\left(\cos(\theta)\hat{a}^\dagger - \sin(\theta)\hat{b}^\dagger\right) e^{-\frac{|\beta|^2}{2}} e^{\beta\left(\sin(\theta)\hat{a}^\dagger + \cos(\theta)\hat{b}^\dagger\right)}|\text{vac}\rangle$$
$$= \sum_{j=0}^{n} c_j \sum_{l=0}^{j} \left[\binom{j}{l} \left(\hat{a}^\dagger \cos(\theta)\right)^l (-\sin(\theta))^{j-l} D(\beta\sin(\theta))\right] \tag{2.129}$$
$$\otimes \left[D(\beta\cos(\theta)) \sum_{m=0}^{j-l} \binom{j-l}{m} \left(\hat{b}^\dagger\right)^m (\beta^* \cos(\theta))^{j-l-m}\right] |\text{vac}\rangle$$

where we have used the binomial theorem: $(x+a)^n = \sum_{k=0}^{n} \binom{n}{k} x^k a^{n-k}$ for n a positive integer. We assume that $\sin(\theta) \ll 1$ and $|\beta| \gg 1$ such that $\sin(\theta)\beta \approx \gamma$. For instance, we could choose $\sin(\theta) \approx 1/|\gamma|^2$ and $\beta \approx |\gamma|^2\gamma$. In the case that $\gamma \gg 1$, the term $\sin^p(\theta)\beta \approx 0$ for $p > 1$. Eqn. 2.129 then becomes

$$\approx \left[\sum_{j=0}^{n} c_j \left(\hat{a}^\dagger - \beta^* \sin(\theta)\right)^j D(\beta\sin(\theta))|\text{vac}\rangle\right] \otimes |\beta\cos(\theta)\rangle \tag{2.130}$$

where $\cos^j(\theta) \approx \sqrt{1 - \frac{1}{|\gamma|^4}} \approx 1 - \frac{1}{2|\gamma|^4} \approx 1$. Eqn. 2.130 is equivalent to Eqn. 2.128 when $\gamma = \beta \sin(\theta)$.

Homodyne Detection

One possible improvement that can be made on the parity gate in Fig. 2.36 is to displace the coherent bus mode in between controlled rotations, as shown in Fig. 2.41 [93].

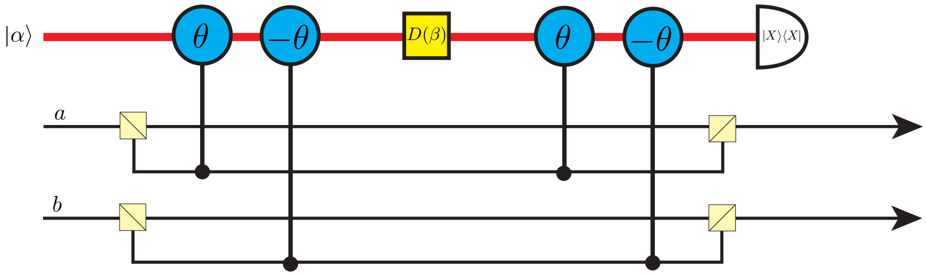

Figure 2.41: An alternative parity gate [93]. If we choose $\beta = -2\alpha\cos(\theta)$ the parity gate operates with negligible error provided $\alpha\theta^2 \gg 1/2$.

Consider the state

$$\Big(\beta_0|HH\rangle + \beta_1|HV\rangle + \beta_2|VH\rangle + \beta_3|VV\rangle\Big)_{ab}|\alpha\rangle$$

incident on Fig. 2.41. After the first two controlled rotations we have

$$\Big(\beta_0|HH\rangle + \beta_3|VV\rangle\Big)_{ab}|\alpha\rangle + \beta_1|HV\rangle_{ab}|e^{-i\theta}\alpha\rangle + \beta_2|VH\rangle_{ab}|e^{i\theta}\alpha\rangle.$$

We now displacement the probe beam with $\beta = -2\alpha\cos(\theta)$. Using Eqn. 2.26 we find:

$$\begin{aligned} D\left(-2\alpha\cos(\theta)\right)|\alpha\rangle &= |\alpha\big(1 - 2\cos(\theta)\big)\rangle \\ D\left(-2\alpha\cos(\theta)\right)|e^{\pm i\theta}\alpha\rangle &= e^{\pm 2i\alpha^2\cos(\theta)\sin(\theta)}|\alpha\big(e^{\pm i\theta} - 2\cos(\theta)\big)\rangle \\ &= e^{\pm 2i\alpha^2\cos(\theta)\sin(\theta)}|-e^{\mp i\theta}\alpha\rangle. \end{aligned}$$

After the displacement, we have:

$$\begin{aligned} \Big(\beta_0|HH\rangle + \beta_3|VV\rangle\Big)|\alpha\big(1 - 2\cos(\theta)\big)\rangle + \beta_1 e^{-2i\alpha^2\cos(\theta)\sin(\theta)}|HV\rangle|-e^{i\theta}\alpha\rangle \\ + \beta_2 e^{2i\alpha^2\cos(\theta)\sin(\theta)}|VH\rangle|-e^{-i\theta}\alpha\rangle \end{aligned}$$

where we have assumed $\alpha \in \mathbb{R}$. After the final two controlled rotations in Fig. 2.41 we have:

$$\begin{aligned} &\Big(\beta_0|HH\rangle + \beta_3|VV\rangle\Big)|\alpha\big(1 - 2\cos(\theta)\big)\rangle \\ &+\Big(\beta_1 e^{-2i\alpha^2\cos(\theta)\sin(\theta)}|HV\rangle + \beta_2 e^{2i\alpha^2\cos(\theta)\sin(\theta)}|VH\rangle\Big)|-\alpha\rangle. \end{aligned}$$

The phases $e^{\pm 2i\alpha^2\cos(\theta)\sin(\theta)}$ can be corrected once we homodyne detect the probe beam. After we homodyne detect we have

$$\Big(\beta_0|HH\rangle + \beta_3|VV\rangle\Big)f(x,\alpha(1-2\cos(\theta))) + \Big(\beta_1|HV\rangle + \beta_2|VH\rangle\Big)f(x,-\alpha)$$

where $f(x,\beta)$ is as defined in Eqn. 2.50. The peak separation between $f(x,-\alpha)$ and $f(x,\alpha(1-2\cos(\theta)))$ is given by $X_d = 4\alpha(1-\cos(\theta))$ and the midpoint is $X_0 = -2\alpha\cos(\theta)$. For these two parity Bell states to be distinguishable we require $X_d \approx 2\alpha\theta^2 \gg 1$, for small θ. That is,

$$\alpha\theta^2 \gg \frac{1}{2} \tag{2.131}$$

which is a factor of two improvement on the scaling in Eqn. 2.126. The probability of error can be calculated out to be

$$\begin{aligned} P_{\text{err}} &= \int_{X_0}^{\infty} f^2(x,-\alpha)dx + \int_{-\infty}^{X_0} f^2(x,\alpha(1-2\cos(\theta))dx = \text{Erfc}\left[\frac{X_d}{2\sqrt{2}}\right] \qquad (2.132)\\ &\approx \text{Erfc}\left[\frac{\alpha\theta^2}{\sqrt{2}}\right]. \end{aligned}$$

This is an improvement on Eqn. 2.127 since Erfc $[x] \to 1$ as $x \to 0$.

Photon Number Detection

Another improvement that can be made on the parity gate in Fig. 2.36 is to displace the coherent bus mode prior to measurement [92, 93], so we can perform a photon number detection instead of a homodyne detection. This allows the scaling of α and θ in Eqn. 2.126 to be improved by more than the constant factor shown in Eqn. 2.131. This is shown in Fig. 2.42. The photon number detection can be made with a photon number QND detector made from controlled rotations [99, 92].

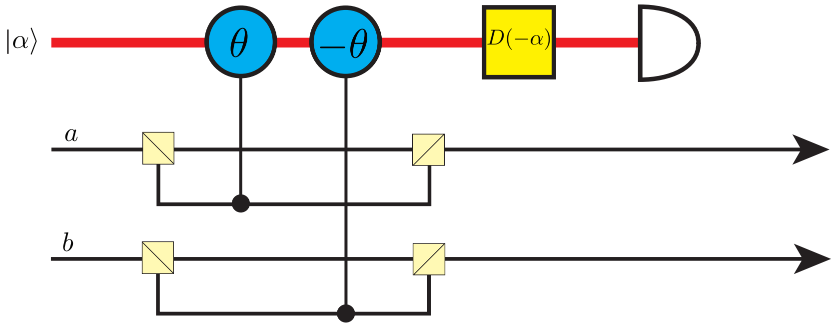

Figure 2.42: An alternative parity gate [92, 93]. The parity gate operates with an error $\ll 1$ provided $\alpha\theta \gg 1$.

As with the parity gate in Fig. 2.36, after the two controlled rotations we have

$$(c_0|HH\rangle + c_3|VV\rangle)_{ab}\,|\alpha\rangle + c_1|HV\rangle_{ab}|e^{-i\theta}\alpha\rangle + c_2|VH\rangle_{ab}|e^{i\theta}\alpha\rangle.$$

After we displace the coherent probe beam we have

$$\Big(c_0|HH\rangle_{ab} + c_3|VV\rangle_{ab}\Big)|0\rangle + e^{i|\alpha|^2\sin(\theta)}c_1|HV\rangle_{ab}|\alpha(e^{-i\theta}-1)\rangle \\ + e^{-i|\alpha|^2\sin(\theta)}c_2|VH\rangle_{ab}|\alpha(e^{i\theta}-1)\rangle.$$

The phase space representation of this is shown in Fig. 2.43.

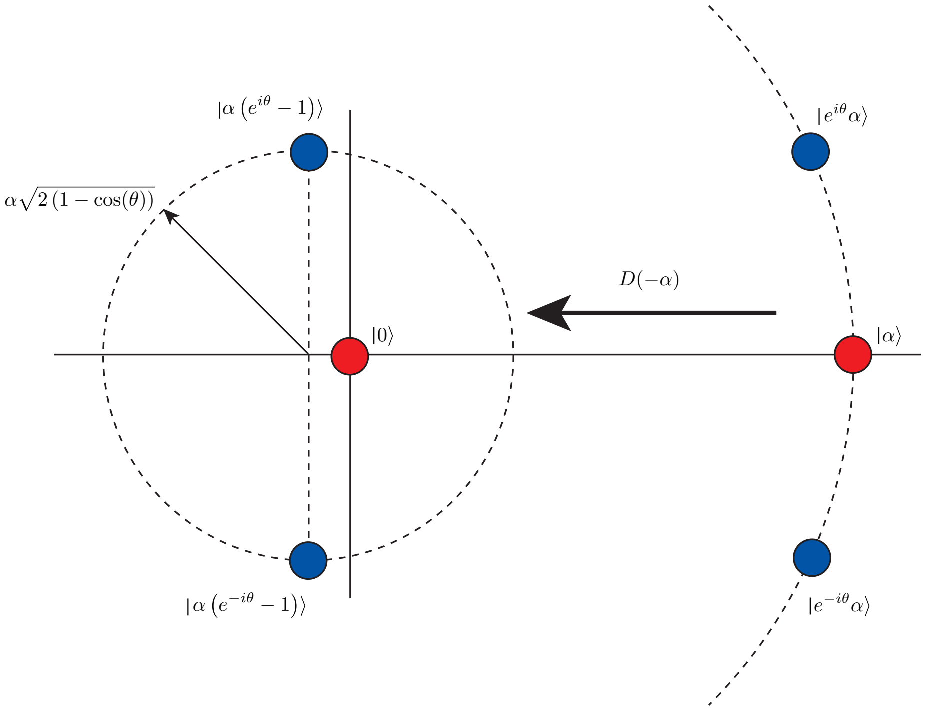

Figure 2.43: Phase space representation for the polarisation parity gate with a photon number detection in Fig. 2.42.

The phases $e^{\pm i|\alpha|^2\sin(\theta)}$ can easily be taken care of after we measure the probe beam. The mean photon number in the state $|\alpha(e^{\pm i\theta}-1)\rangle$ is given by

$$n_p = |\alpha(e^{\pm i\theta}-1)|^2 = 2\alpha^2\big(1-\cos(\theta)\big) \approx \alpha^2\theta^2 \tag{2.133}$$

for small θ. To distinguish the $n_p = 0$ case from the $n_p > 0$ case we require

$$\alpha\theta \gg 1 \tag{2.134}$$

which is a quadratic improvement compared to Eqn. 2.126. This scaling is thought to be near optimal [92]. After we perform a photon number detection on the probe beam in Fig. 2.42 we have

$$\begin{aligned} c_0|HH\rangle_{ab} + c_3|VV\rangle_{ab} \quad &\text{for } \ n_p = 0 \\ c_1 e^{i\phi(n_p)}|HV\rangle_{ab} + c_2 e^{-i\phi(n_p)}|VH\rangle_{ab} \quad &\text{for } \ n_p > 0. \end{aligned} \tag{2.135}$$

The phases $\pm\phi(n_p)$ result from the fact that $\langle n|\alpha\rangle = e^{-\frac{|\alpha|^2}{2}}\frac{\alpha^n}{\sqrt{n!}}$. When considering the states $|\alpha(e^{\pm i\theta} - 1)\rangle$ we have

$$\begin{aligned} \langle n|\alpha\big(e^{\pm i\theta} - 1\big)\rangle = e^{-\frac{n_p}{2}}\frac{\big(\alpha(e^{\pm i\theta} - 1)\big)^n}{\sqrt{n!}} &= e^{-\frac{n_p}{2}}\frac{\alpha^n}{\sqrt{n!}} e^{\pm i\frac{n\theta}{2}}(\pm 2i)^n \sin^n\left(\frac{\theta}{2}\right) \\ &= e^{-\frac{n_p}{2}}\frac{(2\alpha)^n}{\sqrt{n!}}\sin^n\left(\frac{\theta}{2}\right) e^{\pm i\frac{n}{2}(\theta+\pi)}. \end{aligned} \tag{2.136}$$

The resulting phase $\phi(n_p)$ is then given by

$$\phi(n_p) = \frac{n_p}{2}\big(\theta + \pi\big) \approx n_p\frac{\pi}{2} \tag{2.137}$$

for small θ, since $\alpha^2\theta^3 \approx 0$. The output from Fig. 2.42 is then given by

$$\begin{aligned} c_0|HH\rangle_{ab} + c_3|VV\rangle_{ab} \quad &\text{for } \ n_p = 0 \\ (i)^{n_p}\left(c_1|HV\rangle_{ab} + (-1)^{n_p} c_2|VH\rangle_{ab}\right) \quad &\text{for } \ n_p > 0. \end{aligned} \tag{2.138}$$

The phase $(-1)^{n_p}$ can be corrected for with feed forward phase shifters. Note however that bucket detectors could not be used for the $n_p > 0$ case since that would result in the maximally mixed state [93]

$$\big(c_1|HV\rangle + c_2|VH\rangle\big)\big(c_1^*\langle HV| + c_2^*\langle VH|\big) + \big(c_1|HV\rangle - c_2|VH\rangle\big)\big(c_1^*\langle HV| - c_2^*\langle VH|\big).$$

2.8.7 QEC with Qubus Computation

In [100] Yamaguchi *et al.* described a method to measure the stabilizers for the 3-qubit bit-flip code with qubus type parity gates. The 3-qubit bit-flip code is defined by the stabilizers ZZI and IZZ and is encoded by the code words $|\bar{0}\rangle = |000\rangle$, $|\bar{1}\rangle = |111\rangle$. By measuring both stabilizers we can determine whether there was a bit flip error on either qubit 1,2 or 3 and the location of the error. In terms of parity gates, we can measure the Pauli operator ZZI by measuring the parity of qubits 1 and 2 and we can measure the Pauli operator IZZ by measuring the parity of qubits 2 and 3. This is shown in Fig. 2.44(c).

Note, in Fig. 2.44(a) we have depicted the parity gate without spatially separating the polarisation of the photonic qubits. This is a notational shortcut that will be used throughout this thesis. We assume that only vertically polarised photons induce a controlled rotation. It is also worth noting that controlled rotations may also be applied to physical qubits other than photons [93].

The state incident on Fig. 2.44(c) is $|\overline{\psi}_{\text{in}}\rangle = \big(c_0|000\rangle + c_1|111\rangle\big)_{abc}|\alpha\rangle|\alpha\rangle$. There are four cases to consider: no error, $|\overline{\psi}_{\text{in}}\rangle$; an error on qubit 1, $XII|\overline{\psi}_{\text{in}}\rangle$;

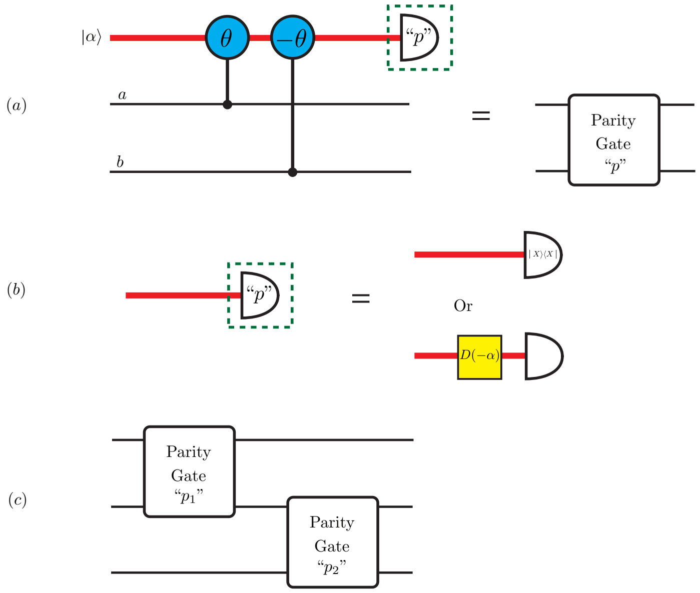

Figure 2.44: **(a)** Qubus parity gate. **(b)** How the probe beam is measured, allowing for either the parity gate in Fig. 2.36 or the parity gate in Fig. 2.42. **(c)** Two parity gates combined to measure the Pauli operators ZZI and IZZ [100].

an error on qubit 2, $IXI|\overline{\psi}_{\text{in}}\rangle$; an error on qubit 3, $IIX|\overline{\psi}_{\text{in}}\rangle$. Directly before we measure the probe beams in Fig. 2.44(c) we have the four cases:

$$\begin{aligned}
|\overline{\psi}_{\text{in}}\rangle &= \big(c_0|000\rangle + c_1|111\rangle\big)|\alpha\rangle|\alpha\rangle \to \big(c_0|000\rangle + c_1|111\rangle\big)|\alpha\rangle|\alpha\rangle \qquad (2.139)\\
IIX|\overline{\psi}_{\text{in}}\rangle &= \big(c_0|001\rangle + c_1|110\rangle\big)|\alpha\rangle|\alpha\rangle \to c_0|001\rangle|\alpha\rangle|e^{i\theta}\alpha\rangle + c_1|110\rangle|\alpha\rangle|e^{-i\theta}\alpha\rangle\\
IXI|\overline{\psi}_{\text{in}}\rangle &= \big(c_0|010\rangle + c_1|101\rangle\big)|\alpha\rangle|\alpha\rangle \to c_0|010\rangle|e^{-i\theta}\alpha\rangle|e^{-i\theta}\alpha\rangle + c_1|101\rangle|e^{i\theta}\alpha\rangle|e^{i\theta}\alpha\rangle\\
XII|\overline{\psi}_{\text{in}}\rangle &= \big(c_0|100\rangle + c_1|011\rangle\big)|\alpha\rangle|\alpha\rangle \to \big(c_0|100\rangle|e^{i\theta}\alpha\rangle + c_1|011\rangle|e^{-i\theta}\alpha\rangle\big)|\alpha\rangle.
\end{aligned}$$

Once we measure the probe beams, the location of the bit flip error will be known.

We can simplify Fig. 2.44(c) such that we only need one probe beam [100], as shown in Fig. 2.45.

Fig. 2.45 measures the stabilizers ZZI and IZZ, provided $\theta_1 + \theta_2 + \theta_3 = 0$. Consider the four cases from Eqn. 2.139 when we let $\theta_1 = \theta$, $\theta_2 = 2\theta$ and $\theta_3 = -3\theta$.

$$\begin{aligned}
\big(c_0|000\rangle + c_1|111\rangle\big)_{abc}|\alpha\rangle &\to c_0|000\rangle_{abc}|\alpha\rangle + c_1|111\rangle_{abc}|\alpha\rangle \qquad (2.140)\\
\big(c_0|001\rangle + c_1|110\rangle\big)_{abc}|\alpha\rangle &\to c_0|001\rangle_{abc}|e^{-3i\theta}\alpha\rangle + c_1|110\rangle_{abc}|e^{3i\theta}\alpha\rangle\\
\big(c_0|010\rangle + c_1|101\rangle\big)_{abc}|\alpha\rangle &\to c_0|010\rangle_{abc}|e^{2i\theta}\alpha\rangle + c_1|101\rangle_{abc}|e^{-2i\theta}\alpha\rangle\\
\big(c_0|100\rangle + c_1|011\rangle\big)_{abc}|\alpha\rangle &\to c_0|100\rangle_{abc}|e^{i\theta}\alpha\rangle + c_1|011\rangle_{abc}|e^{-i\theta}\alpha\rangle.
\end{aligned}$$

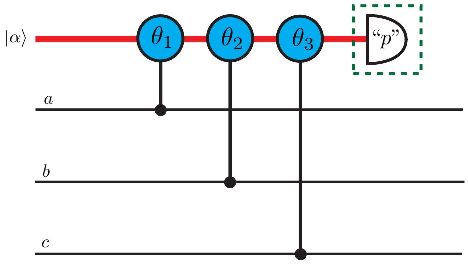

Figure 2.45: Simplified version of Fig. 2.44(c) to measure the parity of three qubits [100].

When we measure the probe state to be $|e^{\pm im\theta}\alpha\rangle$, where $m \in \{0, 1, 2, 3\}$, we know whether there was no error ($m = 0$) or whether qubit m had a bit flip.

Similar methods can be applied to measure the stabilizer operators for Shor's 9-qubit code. The natural question that arises is: can we use techniques similar to those above to measure the syndromes for an arbitrary stabilizer code? This question will be addressed in Chapters 4 and 5.

2.9 Zeno gate

In [50, 101] Franson *et al.* proposed an optical CSIGN gate using the evanescent coupling of photonic qubits in a dual core optical fibre. Unwanted two photon terms are produced during the coupling and are suppressed by the quantum Zeno effect [102]. This scheme is particularly attractive when compared to LOQC since there is no need for ancilla photons or high efficiency detectors. The non-linearity required for the photon-photon interaction takes the form of two photon absorbers used to frequently measuring the qubits, that is, induce the quantum Zeno effect, to suppress the two photon terms.

The interaction Hamiltonian governing the evanescent coupling is given by

$$\hat{H}_I = \epsilon(\hat{a}_1^\dagger \hat{a}_2 + \hat{a}_1 \hat{a}_2^\dagger) \tag{2.141}$$

where $\hat{a}_j$ is the annihilation operator for core j, $j \in \{1, 2\}$. This is just the beam splitter Hamiltonian given in Eqn. 2.29 in Section 2.1.5 with $\theta = \epsilon t$ and $\vartheta = 0$ ($\phi = -\pi/2$ in Eqn. 2.36).

The basis states used in this scheme are $|0\rangle_L = |\text{vac}\rangle = |0\rangle$ and $|1\rangle_L = \hat{a}^\dagger|\text{vac}\rangle = |1\rangle$, where the states on the right are Fock states. Under this interaction Hamiltonian after a time t the basis states evolve to:

$$\begin{array}{rcl} |00\rangle & \rightarrow & |00\rangle \\ |01\rangle & \rightarrow & \cos(\epsilon t)|01\rangle - i\sin(\epsilon t)|10\rangle \\ |10\rangle & \rightarrow & \cos(\epsilon t)|10\rangle - i\sin(\epsilon t)|01\rangle \\ |11\rangle & \rightarrow & \cos(2\epsilon t)|11\rangle - \frac{i}{\sqrt{2}}\sin(2\epsilon t)\big(|20\rangle + |02\rangle\big). \end{array} \tag{2.142}$$

Notice that there is no choice of interaction time such that the two photon terms disappear and we have an entangling two qubit gate. That is, we can choose $2\epsilon t = n\pi$ with $n = 0, 1, 2, \cdots$ to eliminate the two photon terms, however, for each choice of n, we have our original state up to local phase shifts. For example, consider the $n = 1$ case. We see that $|01\rangle \rightarrow -i|10\rangle$, $|10\rangle \rightarrow -i|01\rangle$ and $|11\rangle \rightarrow -|11\rangle$. If the $|11\rangle$ term was unchanged we would have an entangling gate.

Instead of letting the system evolve under H_I for some time $\epsilon t = n\pi/2$, consider breaking the evolution into N increments, each one evolving the system for a time $\epsilon t = n\pi/2N$ and in between each of these evolution increments absorbing the two photon terms.

The states $|01\rangle$ and $|10\rangle$ evolve to

$$\begin{array}{rcl} |01\rangle & \rightarrow & (U_1)^N|01\rangle \\ |10\rangle & \rightarrow & (U_1)^N|10\rangle \end{array} \tag{2.143}$$

where U_1 is the interaction Hamiltonian H_I in the $\{|01\rangle, |10\rangle\}$ basis:

$$U_1 = \left(\begin{array}{cc} \cos(\epsilon t) & -i\sin(\epsilon t) \\ -i\sin(\epsilon t) & \cos(\epsilon t) \end{array} \right) \tag{2.144}$$

and

$$(U_1)^N = \left(\begin{array}{cc} \cos(N\epsilon t) & -i\sin(N\epsilon t) \\ -i\sin(N\epsilon t) & \cos(N\epsilon t) \end{array} \right).$$

Choosing $n = 1$, $\epsilon t = \frac{\pi}{2N}$, we have

$$\begin{array}{rcl} |01\rangle & \rightarrow & -i|10\rangle \\ |10\rangle & \rightarrow & -i|01\rangle. \end{array} \tag{2.145}$$

The state $|11\rangle$ evolves to

$$|11\rangle \rightarrow \big(|11\rangle\langle 11|U_2\big)^N |11\rangle \tag{2.146}$$

where U_2 is the interaction Hamiltonian H_I in the $\{|11\rangle, |20\rangle, |02\rangle\}$ basis:

$$U_2 = \left(\begin{array}{ccc} \cos(2\epsilon t) & -\frac{i}{\sqrt{2}}\sin(2\epsilon t) & -\frac{i}{\sqrt{2}}\sin(2\epsilon t) \\ -\frac{i}{\sqrt{2}}\sin(2\epsilon t) & \frac{1}{2}\big(1+\cos(2\epsilon t)\big) & \frac{1}{2}\big(\cos(2\epsilon t)-1\big) \\ -\frac{i}{\sqrt{2}}\sin(2\epsilon t) & \frac{1}{2}\big(\cos(2\epsilon t)-1\big) & \frac{1}{2}\big(1+\cos(2\epsilon t)\big) \end{array} \right) \tag{2.147}$$

and

$$\Big(|11\rangle\langle 11|U_2\Big)^N = \left(\begin{array}{ccc} \cos^N(2\epsilon t) & -\frac{i}{\sqrt{2}}\sin(2\epsilon t)\cos^{N-1}(2\epsilon t) & -\frac{i}{\sqrt{2}}\sin(2\epsilon t)\cos^{N-1}(2\epsilon t) \\ 0 & 0 & 0 \\ 0 & 0 & 0 \end{array} \right).$$

Again setting $n = 1$, $\epsilon t = \frac{\pi}{2N}$, we have

$$|11\rangle \rightarrow \cos^N(\frac{\pi}{N})|11\rangle. \tag{2.148}$$

Taking the limit $N \rightarrow \infty$ we have

$$|11\rangle \rightarrow \lim_{N\rightarrow\infty} \cos^N(\frac{\pi}{N})|11\rangle = |11\rangle. \tag{2.149}$$

For the choice of $n = 1$, $\epsilon t = \frac{\pi}{2N}$, we have induced the gate

$$\mathbb{S} = \begin{pmatrix} 1 & 0 & 0 & 0 \\ 0 & 0 & -i & 0 \\ 0 & -i & 0 & 0 \\ 0 & 0 & 0 & 1 \end{pmatrix}. \tag{2.150}$$

This $\mathbb{S}$ gate can be used to make a CSIGN . If we have a $\pi/2$ phase shift on each qubit before the application of $\mathbb{S}$ and SWAP the outputs afterwards we have a

CSIGN . This can be seen in Eqn. 2.151 and Fig. 2.46

$$\textsc{swap} \cdot \mathbb{S} \cdot (P \otimes P) = \begin{pmatrix} 1 & 0 & 0 & 0 \\ 0 & 1 & 0 & 0 \\ 0 & 0 & 1 & 0 \\ 0 & 0 & 0 & -1 \end{pmatrix} \tag{2.151}$$

where

$$\textsc{swap} = \begin{pmatrix} 1 & 0 & 0 & 0 \\ 0 & 0 & 1 & 0 \\ 0 & 1 & 0 & 0 \\ 0 & 0 & 0 & 1 \end{pmatrix} \tag{2.152}$$

and

$$P = \begin{pmatrix} 1 & 0 \\ 0 & i \end{pmatrix}. \tag{2.153}$$

In terms of photons a SWAP operation is easy to perform.

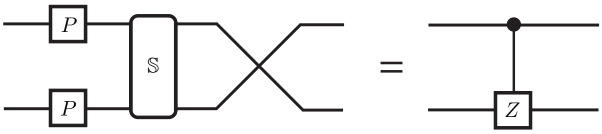

Figure 2.46: The equivalence between the CSIGN and $\mathbb{S}$ gate.

Chapter 3

High Probability LOQC photon number QND Detectors

In Section 2.5.4 we described the original scheme to implement a probabilistic CSIGN gate [31] that succeeded with a probability of $1/16 \approx 0.0625$. The purpose of this gate was to construct the $|CS_n\rangle$ state necessary for a near deterministic CSIGN between optical qubits, allowing for scalable optical quantum computation. In Sections 2.7.1 and 2.7.3 we described two of the first modifications to this probabilistic CSIGN gate, with one proposal using entangled ancilla to increase the success probability [34] and the other allowing for detections in the coincidence basis to simplify the CSIGN, leading to a more experimentally feasible gate [35]. In Section 2.7.5 the best bounds to date were described for the probabilistic CSIGN using only single photon ancilla. The best probabilistic CSIGN yet proposed succeeds with a probability of $2/27 \approx 0.074$ [39].

When we allow for destructive gates, that is gates that allow terms output in the control and target modes outside the logical dual rail basis, the success probability increases above that of the 2/27 gate, as described in Sections 2.7.2 [36] and 2.7.4 [37]. These gates alone cannot be used to construct the $|CS_n\rangle$ states. However, if we had a near deterministic photon number QND detector, these gates could be used. In fact, near deterministic photon number QND detectors would facilitate the search for other destructive gates with higher success probabilities.

In Section 2.7.7 we saw the Kok *et al.* construction [88] of a photon number QND detector using linear optics, single photon ancilla and projective measurements. This scheme, shown in Fig. 2.33, detected the presence of a single photon in the state

$$|\psi_{\text{in}}\rangle = b_0|0\rangle_a + b_1\big(\alpha|H\rangle + \beta|V\rangle\big)_a + b_2\big(\mu|2H\rangle + \chi|HV\rangle + \nu|2V\rangle\big)_a \tag{3.1}$$

without destroying the polarisation information, succeeding with a probability of approximately 2%. To see that a QND circuit such as Fig. 2.33 could be used to correct the proposals in Sections 2.7.2 and 2.7.4, notice that Eqn. 3.1 is equivalent to each mode in Eqns. 2.103 and. 2.104. While the Kok *et al.* construction was an elegant proof of principle that such a QND detector could be made with an interferometer, such a low success probability renders the scheme impractical. This leads to the aim of this chapter, to construct a near deterministic photon number QND detector.

Other proposals would also benefit from a near deterministic photon number QND detector. For example, the optical Zeno gate proposed by Franson *et al.* in [50], used extensively in Chapter 6, requires the use of a two photon absorber. In the continuous interaction case in Chapter 6 this two photon absorption is considered to be doped into the optical fibre. In the beam splitter case, an interferometric near deterministic photon number QND detector could be used. Another example is the scheme by Spedalieri [103] to exploit the Zeno effect to beat loss in LOQC. In this scheme the transformation $b_0|0\rangle + b_1\left(\alpha|H\rangle + \beta|V\rangle\right) \rightarrow \alpha|H\rangle + \beta|V\rangle$ is necessary. This could be achieved with the teleportation scheme from [88], shown in Fig. 2.34, however this only succeeds with a probability of 1/2. A near deterministic photon number QND detector could induce this transformation.

3.1 The Search for an Improved LOQC QND detector

An mentioned above, the aim of this chapter is to find an LOQC circuit that induces the transformation

$$b_0|0\rangle + b_1\big(\alpha|H\rangle + \beta|V\rangle\big) + b_2\big(\mu|2H\rangle + \chi|HV\rangle + \nu|2V\rangle\big) \rightarrow \alpha|H\rangle + \beta|V\rangle \tag{3.2}$$

with a high success probability.

The first question to ask is whether we can modify Fig. 2.33 to increase the success probability above 2%. One might at first think adding an additional ancilla photon in the state $\left(|H\rangle + |V\rangle\right)/\sqrt{2}$ in mode b might help. However, on closer analysis we see that this would just result in a horizontally polarised photon in the lower half of Fig. 2.33 and a vertically polarised photon in the upper half of Fig. 2.33, neither of which would interfere with the ancilla modes or the photons in the state $|\psi_{\text{in}}\rangle$. Another possible way the success probability might be improved is by using additional ancilla photons in modes p and q, as well as an additional coincidence measurement, as shown in Fig. 3.1. In this case the transformation in Eqn. 3.2 is induced, however the probability of success is reduced to $(4/27)^3 \approx 0.00325$. This raises the question of what can been gained by using additional photons.

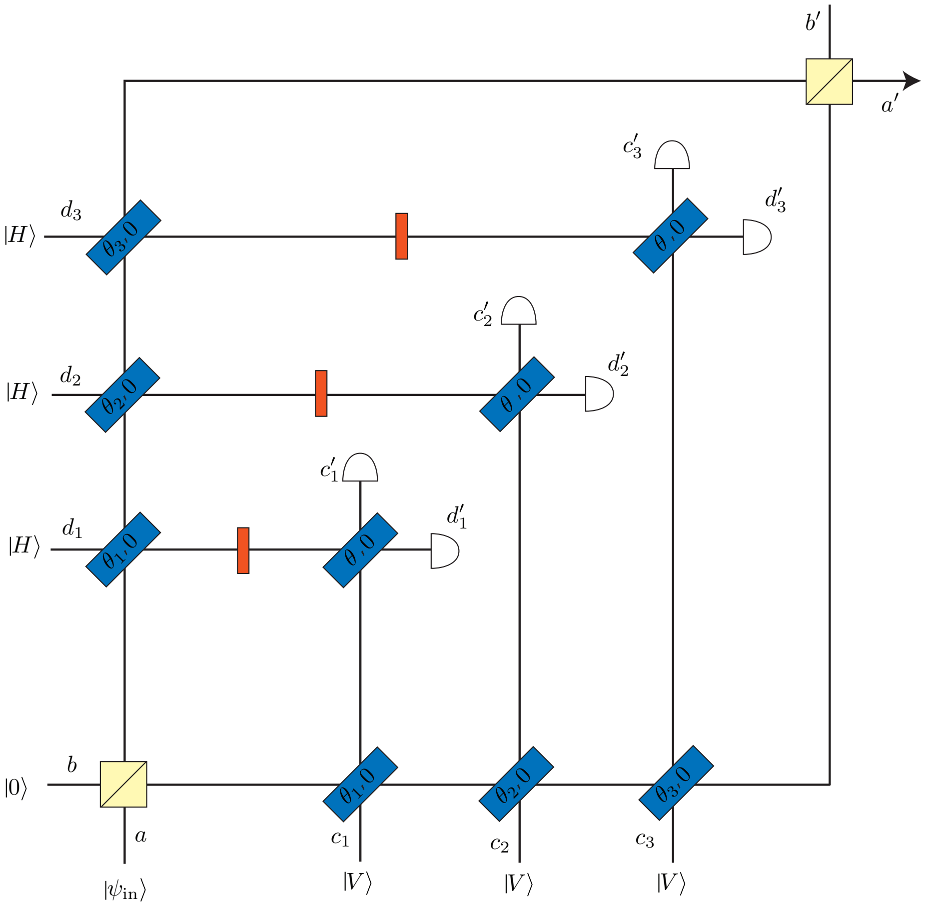

Figure 3.1: An attempt to improve the success probability of the Kok *et al.* [88] photon number QND detector in Fig. 2.33. Detects the presence of a single photon in an arbitrary polarisation state from the state $|\psi_{\text{in}}\rangle = b_0|0\rangle_a + b_1\big(\alpha|H\rangle + \beta|V\rangle\big)_a + b_2\big(\mu|2H\rangle + \chi|HV\rangle + \nu|2V\rangle\big)_a$. When $\theta = \frac{\pi}{4}$ and $\theta_1 = \theta_2 = \theta_3 = -\frac{1}{2}\arccos\left(\frac{1}{3}\right)$, the success probability for this circuit is $(4/27)^3 \approx 0.00325$. There is an ancilla photon in the state $|V\rangle$ in modes c_1, c_2 and c_3, and an ancilla photon in the state $|H\rangle$ in modes d_1, d_2 and d_3. Mode b has a vacuum input. The polariser transforms H to V and vice versa.

If we had the state

$$\begin{aligned}|\psi_{\text{in}}\rangle =& b_0|0\rangle + b_1\big(\alpha|H\rangle + \beta|V\rangle\big) + b_2\big(\mu|2H\rangle + \chi|HV\rangle + \nu|2V\rangle\big)\\ &+ b_3\big(\lambda_1|3H\rangle + \lambda_2|2H,V\rangle + \lambda_3|2V,H\rangle + \lambda_4|3V\rangle\big) \qquad (3.3)\end{aligned}$$

where $\sum_{i=1}^{4}|\lambda_i|^2 = 1$, we can use a modified version of Fig. 3.1 to eliminate all but the b_1 term. If we apply Fig. 2.33 to Eqn. 3.3 we have the state

$$4b_1\big(\alpha|H\rangle+\beta|V\rangle\big)/27+b_3\big(\lambda_1'|3H\rangle+\lambda_2'|2H,V\rangle+\lambda_3'|2V,H\rangle+\lambda_4'|3V\rangle\big) \tag{3.4}$$

Now if we apply Fig. 3.1 with $\theta=\frac{\pi}{4}$ and $\theta_1=\pi/4$, $\theta_2=\frac{1}{2}\arccos\left(\frac{1}{9}\right)$ and $\theta_3=\pi/4$ we have

$$\frac{4}{27}\cos^2(\theta_1)\cos^2(\theta_2)\cos^2(\theta_3)\sin(\theta_1)\sin(\theta_2)\sin(\theta_3)b_1\big(\alpha|H\rangle+\beta|V\rangle\big) \tag{3.5}$$

$$=\left(\frac{4}{27}\right)\left(\frac{5}{108}\right)b_1\big(\alpha|H\rangle+\beta|V\rangle\big). \tag{3.6}$$

We see that we can induce the transformation

$$\begin{aligned}&b_0|0\rangle+b_1\big(\alpha|H\rangle+\beta|V\rangle\big)+b_2\big(\mu|2H\rangle+\chi|HV\rangle+\nu|2V\rangle\big)\\&+b_3\big(\lambda_1|3H\rangle+\lambda_2|2H,V\rangle+\lambda_3|2V,H\rangle+\lambda_4|3V\rangle\big)\\&\rightarrow\alpha|H\rangle+\beta|V\rangle.\end{aligned}$$

This can be generalised to states with any number of photons in arbitrary polarisations:

$$b_0|0\rangle+b_1\big(\alpha|H\rangle+\beta|V\rangle\big)+b_2\big(\mu|2H\rangle+\chi|HV\rangle+\nu|2V\rangle\big)+\sum_{n=3}^{N}b_n\sum_{j=1}^{n+1}\eta_j^{(n)}|(n-j)H,jV\rangle \tag{3.7}$$

where $\sum_{j=1}^{n+1}|\eta_j^{(n)}|^2=1$. Using Fig. 2.33, we first eliminate the vacuum and two photon terms, giving the state

$$4b_1\big(\alpha|H\rangle+\beta|V\rangle\big)/27+\sum_{n=3}^{N}b_n\sum_{j=1}^{n+1}\eta_j'^{(n)}|(n-j)H,jV\rangle. \tag{3.8}$$

Notice that the higher photon number cases corresponding to b_n do not contribute to any other photon number case $b_{n'}$ (for $n\neq n'$), as can be seen by looking at how Fig. 3.2 transforms the general state $|nV,mH\rangle_{fe}\equiv|n,m\rangle_{fe}$

$$\begin{aligned}&|n,m\rangle_{fe}\rightarrow \qquad (3.9)\\&(-1)^{n-2}\sin^{n+m-2}(\theta_i)\cos^2(\theta_i)\Bigg(\sqrt{n\,(m+1)}\left(\frac{(n+1)}{2}\cos^2(\theta_i)-1\right)|n-1,m+1\rangle_{hg}\\&\qquad+\sqrt{m\,(n+1)}\left(\frac{(m+1)}{2}\cos^2(\theta_i)-1\right)|n+1,m-1\rangle_{hg}\Bigg)\end{aligned}$$

where we have used the fact that only the states $|20\rangle$ and $|02\rangle$ incident on the $\theta=\pi/4$ beam splitter allow for a coincidence at c_i' and d_i' [104].

We then apply the circuit in Fig. 3.3 $N-2$ times, increasing the number of ancilla photons by two each time, starting with 6 ancilla photons as in Fig. 3.1

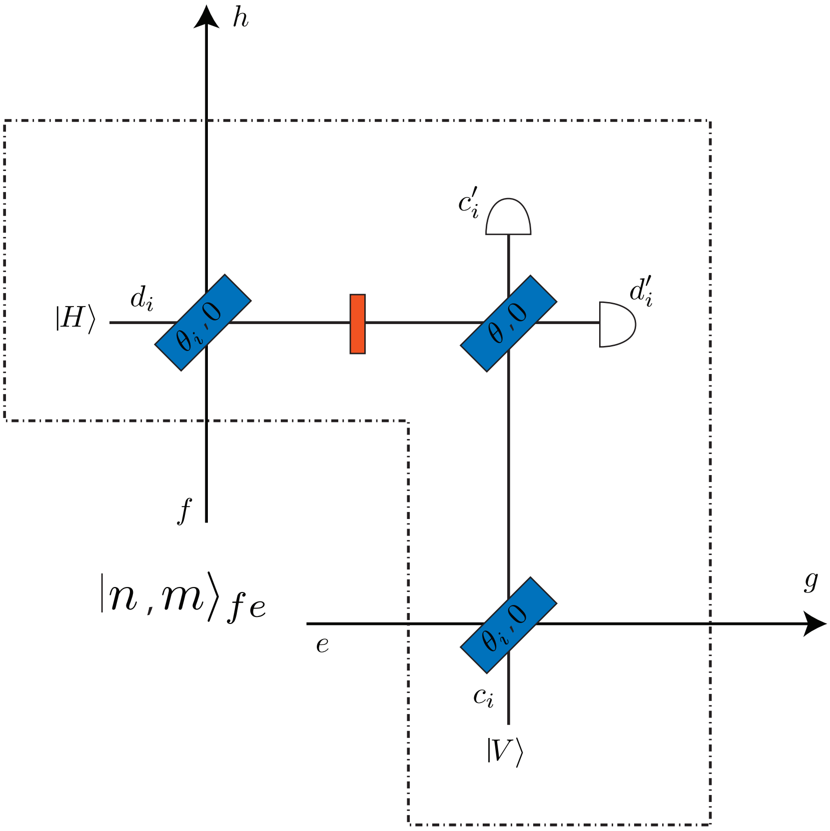

Figure 3.2: The transformation of the state $|n, m\rangle_{fe}$ in a generalised Kok *et al.* [88] photon number QND detector. A coincidence measurement in modes c_i' and d_i' induces transformation 3.9. Here $\theta = \frac{\pi}{4}$ and there is an ancilla photon in the state $|V\rangle$ in modes c_i and an ancilla photon in the state $|H\rangle$ in modes d_i. The polariser transforms H to V and vice versa.

and ending with $2N$ ancilla photons. The final state is

$$\frac{4}{27} b_1 \prod_{n=3}^{N} \prod_{i=1}^{n} \cos^2\left(\theta_i^{(n)}\right) \sin\left(\theta_i^{(n)}\right) (\alpha|H\rangle + \beta|V\rangle) . \tag{3.10}$$

We analytically calculated possible beam splitter reflectivities for the $N = 3$,

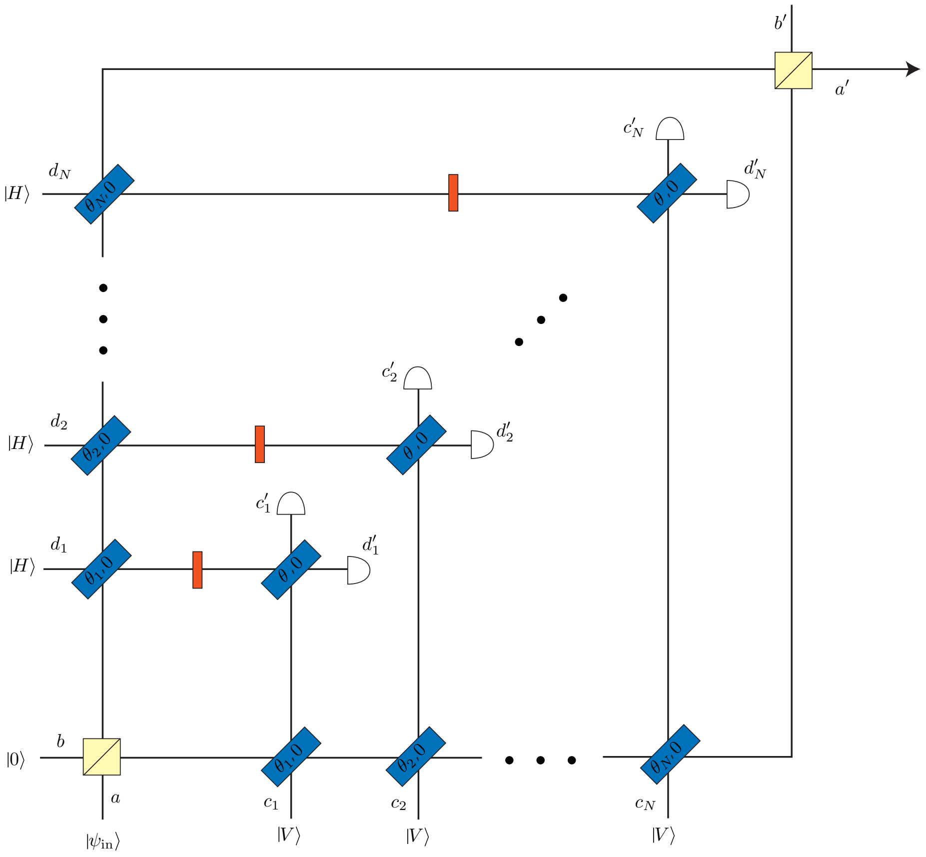

Figure 3.3: Detects the presence of a single photon in an arbitrary polarisation state from the state $|\psi_{\text{in}}\rangle = b_1\big(\alpha|H\rangle + \beta|V\rangle\big)_a + b_N \sum_{j=0}^{N} \eta_j |(N-j)H, jV\rangle_a$. There is an ancilla photon in the state $|V\rangle$ in modes $c_1, c_2, \cdots, c_N$, and an ancilla photon in the state $|H\rangle$ in modes $d_1, d_2, \cdots, d_N$. Mode b has a vacuum input. The polariser transforms H to V and vice versa.

$N = 4$ and $N = 5$ case using Eqn. 3.9:

$$\theta_1^{(3)} = \theta_3^{(3)} = \frac{\pi}{4}, \theta_2^{(3)} = \frac{1}{2} \arccos\left(\frac{1}{9}\right); \prod_{i=1}^{3} \cos^2(\theta_i^{(3)}) \sin(\theta_i^{(3)}) = \frac{5}{108}$$

$$\theta_1^{(4)} = \theta_3^{(4)} = \theta_4^{(4)} = \arccos\left(\sqrt{\frac{2}{5}}\right), \theta_2^{(4)} = \frac{\pi}{4}; \prod_{i=1}^{4} \cos^2(\theta_i^{(4)}) \sin(\theta_i^{(4)}) = \frac{6}{625}\sqrt{\frac{6}{5}}$$

$$\theta_1^{(5)} = \arccos\left(\frac{1}{\sqrt{3}}\right), \theta_2^{(5)} = \arccos\left(\sqrt{\frac{2}{5}}\right), \theta_3^{(5)} = \theta_5^{(5)} = \frac{\pi}{4}, \theta_1^{(4)} = \arccos\left(\frac{1}{3}\right);$$

$$\prod_{i=1}^{5} \cos^2(\theta_i^{(5)}) \sin(\theta_i^{(5)}) = \frac{1}{405\sqrt{5}}.$$

When $N = 3$ the success probability is 4.7×10^{-5}, when $N = 4$ the success probability is 5.2×10^{-9} and when $N = 5$ the success probability is 6.3×10^{-12}.

It is clear that these success probabilities are too low to be of any practical use. Even in the best case scenario, that is, when $\cos^2\left(\theta_i^{(n)}\right)\sin\left(\theta_i^{(n)}\right)$ is maximised at $\theta_i^{(n)} = -\arccos\left(\frac{1}{3}\right)$, which does not work as a general solution, the probability of success scales as 3.3×10^{-3}, 4.8×10^{-4} and 7.1×10^{-5} for the $N = 3$, $N = 4$ and $N = 5$ cases, respectively.

It is evident that using single photon ancilla cannot increase the success probability of the transformation in Eqn. 3.2. We have shown above that additional single photon ancilla can generalise the transformation, but at this point we only need a QND photon number detector that works on states containing up to two photons. The next step is to consider the use of entanglement, motivated by the near deterministic LOQC teleporter from [31], described in Section 2.5.4. With no apparent way to add entanglement to Fig. 2.33 we investigate the LOQC teleporter as a potential near deterministic QND photon number detector.

3.1.1 Entanglement as a Resource

A photon number QND detector based on teleportation was shown in [88] that succeeded with a probability of 1/2, as described in Section 2.7.7. We considered the desired transformation to be in the dual rail basis, so Eqn. 3.2 becomes

$$\begin{aligned}|\Psi_1\rangle = b_0|00\rangle_{ab} + b_1\big(\alpha|10\rangle + \beta|01\rangle\big)_{ab} + b_2\big(\mu|20\rangle + \chi|11\rangle + \nu|02\rangle\big)_{ab}\\ \to \alpha|10\rangle + \beta|01\rangle.\end{aligned} \tag{3.11}$$

This scheme, shown in Fig. 2.34, used the output of a parametric down converter $|\Psi_{\mathrm{PDC}}\rangle$ as a resource. Since this resource state had a vacuum term, the two photon terms in transformation 3.11 could not be eliminated. If we instead just consider the resource state

$$\frac{1}{\sqrt{2}}\left(|1001\rangle - |0110\rangle\right)_{cdef}, \tag{3.12}$$

as shown in Fig. 3.4, we can perform the transformation in Eqn. 3.11 with a success probability of 1/2.

Since Fig. 3.4 is a teleportation circuit, one might at first think that we can directly use the near deterministic LOQC teleporter from [31] as a near deterministic photon number QND detector. However, notice that the $\frac{n}{n+1}$ LOQC teleporter, shown in Fig. 2.19 of Section 2.7.7, will not function as a photon number QND detector. If the state $b_0|00\rangle_{0a} + b_1\big(\alpha|10\rangle + \beta|01\rangle\big)_{0a} + b_2\big(\mu|20\rangle + \chi|11\rangle + \nu|02\rangle\big)_{0a}$ was incident on modes 0 and a we would have the vacuum term $|00\rangle_{0a}$ and the two photon terms $|02\rangle_{0a}$ and $|11\rangle_{0a}$ in the output, since only mode 0 of the input state is teleported. We can eliminate the remaining two photon terms using three more LOQC teleporters, one to eliminate the $|02\rangle_{0a}$ and two to eliminate the $|11\rangle_{0a}$ term after the use of a

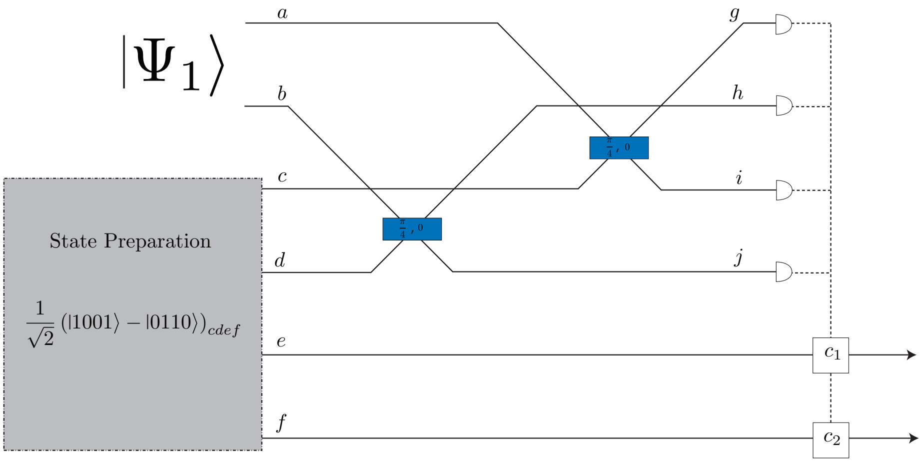

Figure 3.4: Photon number QND detector [88]. Detects the presence of a single photon in either mode a or b in the state $|\Psi_1\rangle = b_0|00\rangle_{ab} + b_1\left(\alpha|10\rangle + \beta|01\rangle\right)_{ab} + b_2\left(\mu|20\rangle + \chi|11\rangle + \nu|02\rangle\right)_{ab}$. Success is indicated with a detection of either $|1001\rangle_{ghij}$, $|0110\rangle_{ghij}$, $|1100\rangle_{ghij}$ or $|0011\rangle_{ghij}$. The total probability of success is $|b_1|^2/2$.

$\theta = \pi/4, \phi = 0$ beam splitter, the effect of the beam splitter needing to be reversed on the state $\alpha|01\rangle_{0a} + \beta|10\rangle_{0a}$ after the application of the four LOQC teleporters. However, there is no way to eliminate the vacuum term $b_0|00\rangle_{oa}$ with LOQC teleporters alone.

On a closer analysis of Fig. 3.4 we notice that both modes of $|\Psi_1\rangle$ are teleported. However, as described above, we cannot simply use two general LOQC teleporters on each mode of the state $|\Psi_1\rangle$ since the output will still have the vacuum term $b_0|00\rangle$ and two photon term $b_2|11\rangle$. Notice that the entangled state used in Fig 3.4, shown in Eqn. 3.12, is not equivalent to either $|t_1\rangle \otimes |t_1\rangle$ or $|t_2\rangle$. In order to construct a near deterministic photon number QND detector we propose a generalisation of Fig. 3.4, using an as yet unknown entangled state to teleport both modes of the state $|\Psi_1\rangle$ simultaneously. To ensure the output from our proposed photon number QND detector are in either the state $|01\rangle$ or $|10\rangle$, we impose two restrictions. First, we deviate from the generalised LOQC teleporter in [31] and dictate before hand which modes will contain the teleported state. We do this by only leaving two modes of our entangled state unmeasured, as opposed to the n modes left unmeasured in Fig. 2.19. Second, the last two modes of the entangled must be either $|01\rangle$ or $|10\rangle$, so the none of the states $|00\rangle$, $|20\rangle$, $|02\rangle$ or $|11\rangle$ can be output. With this in mind, we now need to find the form of the entangled states that will induce the transformation in Eqn. 3.11, as well as increase the probability of success as we increase the number of modes in the entangled state. We limit the entangled state considered to states with $2n$ modes and n photons, such that each mode has a maximum of one photon, a similar restriction to that for the $|t_n\rangle$ states.

We first investigate entangled states that are one level more complex than those considered in Eqn. 3.12, that is, six modes states that have three photons. This is shown in Fig. 3.5. We need to search for the entangled state incident on modes 1–6 that induces 3.11. We considering a superposition of all possible six mode states containing three photons, with a maximum of one photon in each mode and only those states in which modes 5 and 6 are either $|01\rangle_{56}$ or $|10\rangle_{56}$. This is a superposition of twelve states:

$$\Big(\chi_0|110001\rangle + \chi_1|110010\rangle + \chi_2|101001\rangle + \chi_3|101010\rangle + \chi_4|100101\rangle + \chi_5|100110\rangle$$

$$+ \chi_6|011001\rangle + \chi_7|011010\rangle + \chi_8|010101\rangle + \chi_9|010110\rangle + \chi_{10}|001101\rangle + \chi_{11}|001110\rangle\Big)$$

where the modes are labelled 1 through to 6 and $\sum_{i=0}^{11}|\chi_i|^2 = 1$.

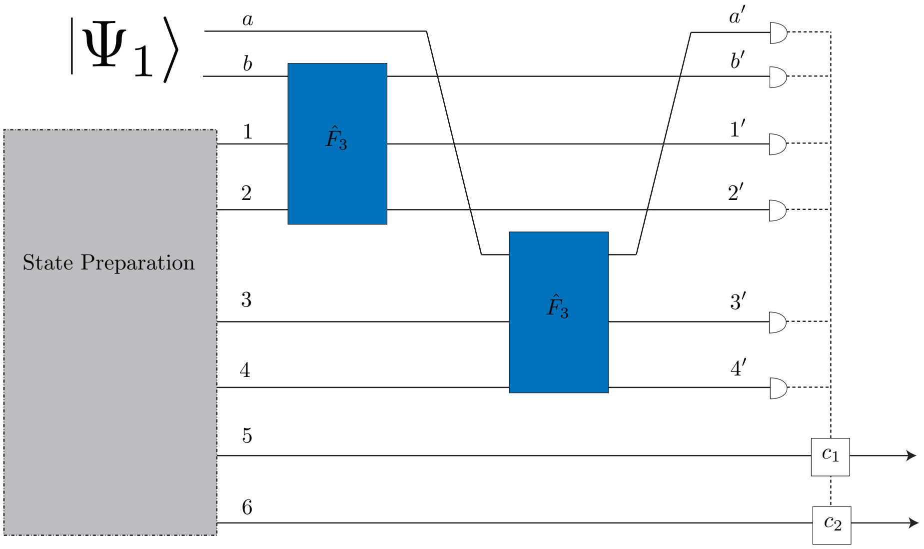

Figure 3.5: Photon Number QND detector with linear optics using two tri-splitters. The success probability is $2|b_1|^2/3$.

Measuring a total of three photons ensures the b_0 and b_2 terms in $|\Psi_1\rangle$ are eliminated. Out of the 56 possible three photon measurements on modes $a', b', 1', 2', 3'$ and $4'$, 36 lead to successful teleportation, given that only $\chi_0 = \chi_3 = \chi_{10} = 1$ and all other $\chi_i = 0$. That is, one possible entangled state incident on modes 1–6 that induces the transformation in Eqn. 3.11 is

$$\frac{1}{\sqrt{3}}\left(\left(|110001\rangle + |101010\rangle + |001101\rangle\right)_{123456}\right. \qquad (3.13)$$

The 36 measurements that perform a successful photon number QND measurement are shown in Table 3.1.

$\|110100\rangle$	$\|100110\rangle$	$\|010110\rangle$	$\|200100\rangle$	$\|002100\rangle$	$\|010200\rangle$
$\|110010\rangle$	$\|100101\rangle$	$\|010101\rangle$	$\|200010\rangle$	$\|002010\rangle$	$\|010020\rangle$
$\|110001\rangle$	$\|100011\rangle$	$\|010011\rangle$	$\|200001\rangle$	$\|002001\rangle$	$\|010002\rangle$
$\|101100\rangle$	$\|011100\rangle$	$\|001110\rangle$	$\|020100\rangle$	$\|100200\rangle$	$\|001200\rangle$
$\|101010\rangle$	$\|011010\rangle$	$\|001101\rangle$	$\|020010\rangle$	$\|100020\rangle$	$\|001020\rangle$
$\|101001\rangle$	$\|011001\rangle$	$\|001011\rangle$	$\|020001\rangle$	$\|100002\rangle$	$\|001002\rangle$

Table 3.1: The detections on modes $b', 1', 2', a', 3', 4'$ that lead to a successful photon number QND measurement for the circuit in Fig. 3.5

Given the entangled state in Eqn. 3.13 and only accepting an output in modes 5 and 6 when we detect a measurement from Table 3.1, Fig. 3.5 succeeds as a photon number QND detector with a probability of $2|b_1|^2/3$, an improvement on $|b_1|^2/2$ probability found in [88] (Fig. 3.4).

Notice that only the measurement outcomes that detect at least one photon from both tri-splitters in Fig. 3.5 lead to success. Detecting either 0 or 3 photons from either tri-splitter results in failure. The necessary corrections c_1 and c_2 in Fig. 3.5 are simply the phase shifters with $\phi = \pm 2\pi/3$. We can always choose either c_1 or c_2 to be the identity. A SWAP correction may also be necessary. Alternatively we can just relabel the modes of the output qubit.

We repeat the above analysis for both the 8 mode and 10 mode entangled state case, shown in Fig. 3.6 for $n = 4$ and $n = 5$, respectively. For the $n = 4$ case we consider a superposition of $2 \times \binom{6}{3} = 40$ states incident on modes 1–8 of Fig. 3.6. Provided we detect at least one photon from each 4-splitter, that is, out of the 330 possible 4 photon detections, we only allow the 260 that have at least one photon from each 4-splitter, the entangled state

$$\frac{1}{2}\left(|11100010\rangle + |10011010\rangle + |00011101\rangle + |11010001\rangle\right), \tag{3.14}$$

induces a photon number QND detector with a probability of $3|b_1|^2/4$, where we label the modes 1 through to 8. The necessary corrections in this case are phase shifters with $\phi = \pi, \pm\pi/2$.

For the $n = 5$ case we consider a superposition of $2 \times \binom{8}{4} = 140$ states incident on modes 1–10 of Fig. 3.6. Provided we detect at least one photon from each 5-splitter, that is, out of the 2002 possible 5 photon detections, we only allow the 1750 that have at least one photon from each 5-splitter, the entangled state

$$\frac{1}{\sqrt{5}}\left(|0000111101\rangle + |1000111010\rangle + |1100110001\rangle + |1110100010\rangle + |1111000001\rangle\right), \tag{3.15}$$

induces a photon number QND detector with a probability of $4|b_1|^2/5$, where we label the modes 1 through to 10. The necessary corrections in this case are phase shifters with $\phi = \pm 2\pi/5, \pm 4\pi/5$.

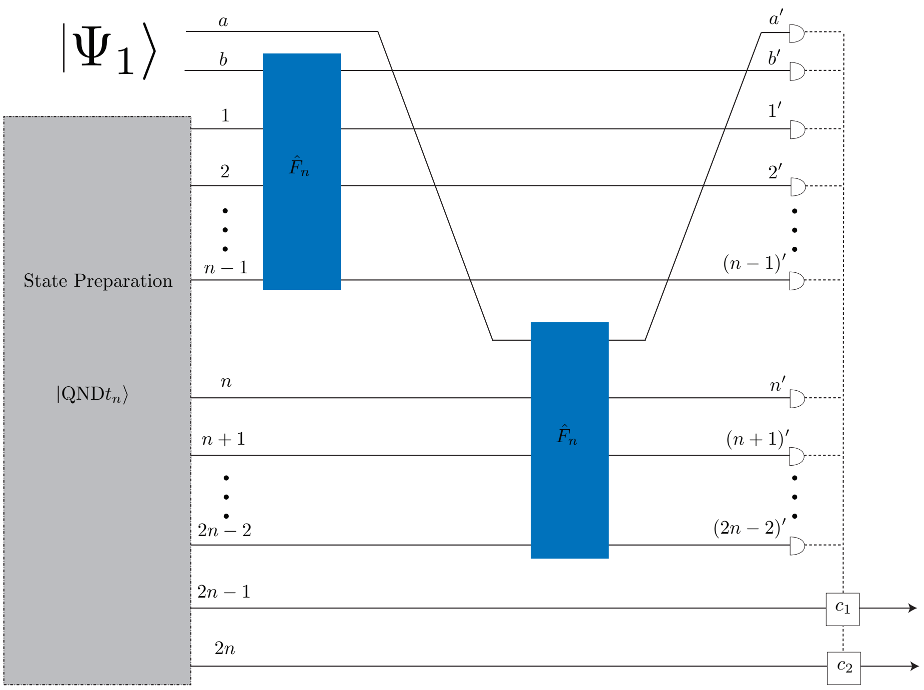

Figure 3.6: Photon Number QND detector with linear optics using two n-splitters. The success probability is $|b_1|^2 \left(\frac{n-1}{n}\right)$.

We see from the three cases considered above that the probability of success for our photon number QND detector increases as the number of modes and photons in our entangled resource increases. To find what the necessary entangled state looks like for the general n case, we could attempt to use a state made up of a superposition of $2 \times \binom{2n-2}{n-1}$ states and then search for which amplitudes in the superposition can be set to zero. However, from the three cases considered we recognise a pattern that leads to the general entangled state of n

photons in $2n$ modes, given as the superposition of n states in Eqn. 3.16.

$$
\begin{aligned}
|\mathrm{QND}t_n\rangle = \frac{1}{\sqrt{n}}\Bigg(& |\overbrace{00\cdots0}^{n-1}\rangle_{1,2,\cdots,n-1}|\overbrace{11\cdots1}^{n-1}\rangle_{n,n+1,\cdots,2n-2}|01\rangle_{2n-1,2n} \\
& +|1\overbrace{00\cdots0}^{n-2}\rangle_{1,2,\cdots,n-1}|\overbrace{11\cdots1}^{n-2}0\rangle_{n,n+,1\cdots,2n-2}|10\rangle_{2n-1,2n} \\
& +|11\overbrace{00\cdots0}^{n-3}\rangle_{1,2,\cdots,n-1}|\overbrace{11\cdots1}^{n-3}00\rangle_{n,n+,1\cdots,2n-2}|01\rangle_{2n-1,2n} \\
& \quad \vdots \\
& +|\overbrace{11\cdots1}^{n-3}00\rangle_{1,2,\cdots,n-1}|11\overbrace{00\cdots0}^{n-3}\rangle_{n,n+,1\cdots,2n-2}|A_{n-2}\rangle_{2n-1,2n} \\
& +|\overbrace{11\cdots1}^{n-2}0\rangle_{1,2,\cdots,n-1}|1\overbrace{00\cdots0}^{n-2}\rangle_{n,n+,1\cdots,2n-2}|A_{n-1}\rangle_{2n-1,2n} \\
& +|\overbrace{11\cdots1}^{n-1}\rangle_{1,2,\cdots,n-1}|\overbrace{00\cdots0}^{n-1}\rangle_{n,n+,1\cdots,2n-2}|A_{n}\rangle_{2n-1,2n}\Bigg),
\end{aligned}
\tag{3.16}
$$

where $|A_{n-2}\rangle = |10\rangle, |A_{n-1}\rangle = |01\rangle, |A_n\rangle = |10\rangle$ for n even and $|A_{n-2}\rangle = |01\rangle, |A_{n-1}\rangle = |10\rangle, |A_n\rangle = |01\rangle$ for n odd. This state induces a photon number QND measurement with a success probability that scales as $|b_1|^2\left(\frac{n-1}{n}\right)$, provided we only detect a total of n photons and ignore the detection outcomes in which we detect either 0 or n photons from either n-splitter. The necessary corrections c_1 and c_2 in Fig. 3.6 are simply the phase shifters $\phi = m\,(2\pi/n)$, where $m \in \{1, 2, \cdots, n-1\}$. We can always choose either c_1 or c_2 to be the identity. A SWAP correction may also be necessary. Alternatively we can just relabel the modes of the output qubit.

It is worth mentioning that the photon number QND detector in Fig. 3.6 also functions for a state $|\Psi_1\rangle$ that has any number of photons in arbitrary polarisation state, such as the dual rail equivalent of Eqn. 3.7:

$$
b_0|0,0\rangle + b_1\big(\alpha|1,0\rangle + \beta|0,1\rangle\big) + b_2\big(\mu|2,0\rangle + \chi|1,1\rangle + \nu|0,2\rangle\big) + \sum_{n=3}^{N} b_n \sum_{j=1}^{n+1} \eta_j^{(n)}|(n-j), j\rangle
\tag{3.17}
$$

where $\sum_{j=1}^{n+1}|\eta_j^{(n)}|^2 = 1$ and $\sum_{k=0}^{N}|b_k|^2 = 1$. This is due to the fact that the entangled resource state in Eqn. 3.16 dictates that the output from the teleporter is either $|01\rangle_{2n-1,2n}$ or $|10\rangle_{2n-1,2n}$.

It is clear that when Eqn. 3.16 is incident on modes 1–2n of Fig. 3.6, the vacuum (b_0) and two photon (b_2) terms in $|\Psi_1\rangle$ are eliminated, since the output modes of the device, modes $2n-1$ and $2n$ in Fig. 3.6, can only be in the states $|01\rangle_{2n-1,2n}$ and/or $|10\rangle_{2n-1,2n}$. However, it is not clear that Eqn. 3.16 induces the transformation in Eqn. 3.11 with a probability that scales as $|b_1|^2\left(\frac{n-1}{n}\right)$.

We explain this using a similar technique to that used when explaining how the states $|t_n\rangle$ perform teleportation with a success probability of $\frac{n}{n+1}$, described in Section 2.5.4.

Consider the case

$$\begin{aligned}
&b_1\big(\alpha|10\rangle+\beta|01\rangle\big)_{ab} \qquad (3.18)\\
&\otimes\Big(|\overbrace{11\cdots1}^{n-m-1}\overbrace{00\cdots0}^{m}\rangle_{1,2,\cdots,n-1}|\overbrace{11\cdots1}^{m}\overbrace{00\cdots0}^{n-m-1}\rangle_{n,n+,1\cdots,2n-2}|A_{n-m}\rangle_{2n-1,2n}\Big)
\end{aligned}$$

where $m=1,\cdots,n-2$. In order to show how this term teleports $\alpha|10\rangle+\beta|01\rangle$ we also need to consider the terms directly before and after this one in the entangled resource in Eqn. 3.16:

$$\begin{aligned}
&b_1\big(\alpha|10\rangle+\beta|01\rangle\big)_{ab} \qquad (3.19)\\
&\otimes\Big(|\overbrace{11\cdots1}^{n-m-2}\overbrace{00\cdots0}^{m+1}\rangle_{1,2,\cdots,n-1}|\overbrace{11\cdots1}^{m+1}\overbrace{00\cdots0}^{n-m-2}\rangle_{n,n+,1\cdots,2n-2}|A_{n-m-1}\rangle_{2n-1,2n}\\
&\quad+|\overbrace{11\cdots1}^{n-m-1}\overbrace{00\cdots0}^{m}\rangle_{1,2,\cdots,n-1}|\overbrace{11\cdots1}^{m}\overbrace{00\cdots0}^{n-m-1}\rangle_{n,n+,1\cdots,2n-2}|A_{n-m}\rangle_{2n-1,2n}\\
&\quad+|\underbrace{11\cdots1}_{n-m}\underbrace{00\cdots0}_{m-1}\rangle_{1,2,\cdots,n-1}|\underbrace{11\cdots1}_{m-1}\underbrace{00\cdots0}_{n-m}\rangle_{n,n+,1\cdots,2n-2}|A_{n-m+1}\rangle_{2n-1,2n}\Big)
\end{aligned}$$

where if n and m have the same parity then $|A_{n-m-1}\rangle=|01\rangle,|A_{n-m}\rangle=|10\rangle,|A_{n-m+1}\rangle=|01\rangle$ and if n and m have different parity then $|A_{n-m-1}\rangle=|10\rangle,|A_{n-m}\rangle=|01\rangle,|A_{n-m+1}\rangle=|10\rangle$. Expanding this we have

$$\begin{aligned}
&=\alpha|0\overbrace{11\cdots1}^{n-m-2}\overbrace{00\cdots0}^{m+1}\rangle_{b,1,2,\cdots,n-1}|1\overbrace{11\cdots1}^{m+1}\overbrace{00\cdots0}^{n-m-2}\rangle_{a,n,n+,1\cdots,2n-2}|A_{n-m-1}\rangle_{2n-1,2n}\\
&\ +\alpha|0\overbrace{11\cdots1}^{n-m-1}\overbrace{00\cdots0}^{m}\rangle_{b,1,2,\cdots,n-1}|1\overbrace{11\cdots1}^{m}\overbrace{00\cdots0}^{n-m-1}\rangle_{a,n,n+,1\cdots,2n-2}|A_{n-m}\rangle_{2n-1,2n}\\
&\ +\alpha|0\underbrace{11\cdots1}_{n-m}\underbrace{00\cdots0}_{m-1}\rangle_{b,1,2,\cdots,n-1}|1\underbrace{11\cdots1}_{m-1}\underbrace{00\cdots0}_{n-m}\rangle_{a,n,n+,1\cdots,2n-2}|A_{n-m+1}\rangle_{2n-1,2n}\\
&\ +\beta|1\overbrace{11\cdots1}^{n-m-2}\overbrace{00\cdots0}^{m+1}\rangle_{b,1,2,\cdots,n-1}|0\overbrace{11\cdots1}^{m+1}\overbrace{00\cdots0}^{n-m-2}\rangle_{a,n,n+,1\cdots,2n-2}|A_{n-m-1}\rangle_{2n-1,2n}\\
&\ +\beta|1\overbrace{11\cdots1}^{n-m-1}\overbrace{00\cdots0}^{m}\rangle_{b,1,2,\cdots,n-1}|0\overbrace{11\cdots1}^{m}\overbrace{00\cdots0}^{n-m-1}\rangle_{a,n,n+,1\cdots,2n-2}|A_{n-m}\rangle_{2n-1,2n}\\
&\ +\beta|1\underbrace{11\cdots1}_{n-m}\underbrace{00\cdots0}_{m-1}\rangle_{b,1,2,\cdots,n-1}|0\underbrace{11\cdots1}_{m-1}\underbrace{00\cdots0}_{n-m}\rangle_{a,n,n+,1\cdots,2n-2}|A_{n-m+1}\rangle_{2n-1,2n}
\end{aligned}$$

We see that there are two states, shown in blue, that have $n-m$ and $m+1$ photons incident on the top and bottom n-splitters in Fig. 3.6, respectively. However the states incident on each n-splitter are not identical, the modes have been shifted by one, that is, one of the blue states incident on the top n-splitter is of the form

$$|\overbrace{11\cdots1}^{p}\overbrace{00\cdots0}^{n-p}\rangle_{b,1,2,\cdots,n-1} \tag{3.20}$$

whereas the other is of the form

$$|0\underbrace{11\cdots1}_{p}\underbrace{00\cdots0}_{n-1-p}\rangle_{b,1,2,\cdots,n-1} \tag{3.21}$$

where $p = n-m$ here. We need to show that the amplitude for each of the states resulting from the state in Eqn. 3.20 incident on an n-splitter is the same as the amplitude for the corresponding states resulting from the state in Eqn. 3.21 incident on an n-splitter. We can do this by recalling the definition of a n-splitter from Eqn. 2.81 in Section 2.5.4. The output from an n-splitter with Eqn. 3.20 incident is given by

$$\prod_{l=1}^{p}\left(\sum_{j=0}^{n-1}\hat{F}_{jl}\hat{a}_j^{\dagger}\right) = \prod_{l=1}^{p}\left(\sum_{j=0}^{n-1}\frac{1}{\sqrt{n}}e^{i\frac{2\pi}{n}lj}\hat{a}_j^{\dagger}\right) \tag{3.22}$$

and the output from an n-splitter with Eqn. 3.20 incident is given by

$$\begin{aligned}\prod_{l=2}^{p+1}\left(\sum_{j=0}^{n-1}\hat{F}_{jl}\hat{a}_j^{\dagger}\right) &= \prod_{k=1}^{p}\left(\sum_{j=0}^{n-1}\frac{1}{\sqrt{n}}e^{i\frac{2\pi}{n}(k+1)j}\hat{a}_j^{\dagger}\right) \\ &= \prod_{k=1}^{p}\left(\sum_{j=0}^{n-1}\frac{1}{\sqrt{n}}e^{i\frac{2\pi}{n}kj}e^{i\frac{2\pi}{n}j}\hat{a}_j^{\dagger}\right)\end{aligned} \tag{3.23}$$

where in this case mode b would take the place of mode 0. If we apply a phase shift of $e^{-i\frac{2\pi}{n}j}$ to each mode j of the output of the n-spliter, $\hat{a}_j^{\dagger} \rightarrow e^{-i\frac{2\pi}{n}j}\hat{a}_j^{\dagger}$, when Eqn. 3.23 is incident, then we can see that the amplitude for each state in Eqn. 3.22 is the same as the corresponding state from Eqn. 3.23. That is, the amplitude for each state in the output from an n-splitter cannot be altered by phase shifters, only the relative phases can be affected. If we do not apply these phase shifters, the teleported state resulting from measuring the output of the n-splitter with Eqns. 3.20 and 3.21 incident will either be of the form $\alpha|10\rangle + e^{i\varphi}\beta|01\rangle$ or $\alpha|01\rangle + e^{i\varphi}\beta|10\rangle$. This same reasoning is also true when we have $n-m-1$ and $m+1$ photons incident on the top and bottom n-splitters in Fig. 3.6, respectively, shown in red in Eqn. 3.19.

Now that we have shown how Eqn. 3.16 teleports the b_1 state from $|\Psi_1\rangle$ using Fig. 3.6, we need to show how it fails, and what the probability of failure is. For this we need to consider the case

$$\begin{aligned}
&b_1\big(\alpha|10\rangle+\beta|01\rangle\big)_{ab} \qquad (3.24)\\
&\otimes\Bigg(|\overbrace{00\cdots0}^{n-1}\rangle_{1,2,\cdots,n-1}|\overbrace{11\cdots1}^{n-1}\rangle_{n,n+1,\cdots,2n-2}|01\rangle_{2n-1,2n}\\
&+|\overbrace{11\cdots1}^{n-1}\rangle_{1,2,\cdots,n-1}|\overbrace{00\cdots0}^{n-1}\rangle_{n,n+,1\cdots,2n-2}|A_n\rangle_{2n-1,2n}\Bigg)/\sqrt{n}
\end{aligned}$$

$$\begin{aligned}
=b_1\Bigg(&\alpha|0\,\overbrace{00\cdots0}^{n-1}\rangle_{b,1,2,\cdots,n-1}|\overbrace{11\cdots1}^{n}\rangle_{a,n,n+1,\cdots,2n-2}|01\rangle_{2n-1,2n}\\
&+\alpha|0\,\overbrace{11\cdots1}^{n-1}\rangle_{b,1,2,\cdots,n-1}|1\,\overbrace{00\cdots0}^{n-1}\rangle_{a,n,n+,1\cdots,2n-2}|A_n\rangle_{2n-1,2n} \qquad (3.25)\\
&+\beta|1\,\overbrace{00\cdots0}^{n-1}\rangle_{b,1,2,\cdots,n-1}|0\,\overbrace{11\cdots1}^{n-1}\rangle_{a,n,n+1,\cdots,2n-2}|01\rangle_{2n-1,2n}\\
&+\beta|\overbrace{11\cdots1}^{n}\rangle_{b,1,2,\cdots,n-1}|0\,\overbrace{00\cdots0}^{n-1}\rangle_{a,n,n+,1\cdots,2n-2}|A_n\rangle_{2n-1,2n}\Bigg)/\sqrt{n}
\end{aligned}$$

We see that when we have n photons incident on the bottom n-splitter in Fig. 3.6, shown in green above, the teleported state is $\alpha|01\rangle_{2n-1,2n}$. This occurs with a probability of $|b_1|^2|\alpha|^2/n$. When we have n photons incident on the top n-splitter in Fig. 3.6, shown in cyan above, the teleported state is $\beta|A_n\rangle_{2n-1,2n}$, where $|A_n\rangle=|10\rangle$ for n even and $|A_n\rangle=|01\rangle$ for n odd. This occurs with a probability of $|b_1|^2|\beta|^2/n$. The total probability of measuring either n photons from the top n-splitter in Fig. 3.6 or n photons from the bottom n-splitter is $|b_1|^2\left(|\alpha|^2+|\beta|^2\right)/n=|b_1|^2/n$. Therefore, the probability of success for Fig. 3.6 acting as a photon number QND detector is $|b_1|^2-\frac{|b_1|^2}{n}=|b_1|^2\left(\frac{n-1}{n}\right)$.

Notice that the probability of success resembles that for the near deterministic teleportation in [31]. The entangled resource we require for a photon number QND detector closely resembles the $|t_n\rangle$ states from [31]. We can see this explicitly when we write the state in Eqn. 3.16 in terms logical qubits, using the definition in Section 2.5.1. We label the first qubit in Eqn. 3.16 as mode 1 and $2n-2$, the second as mode and $2n-3$ and so on until the $(n-1)^{\text{th}}$ qubit which is labelled as modes $n-1$ and n. The n^{th} qubit is labelled as modes $2n-1$ and $2n$. The $n=3$ case in Eqn. 3.13 becomes

$$\frac{1}{\sqrt{3}}\left((|000\rangle+|101\rangle+|110\rangle\right)_q, \qquad (3.26)$$

the $n=4$ case in Eqn. 3.14 becomes

$$\frac{1}{2}\left(|0000\rangle+|1001\rangle+|1100\rangle+|1111\rangle\right)_q, \qquad (3.27)$$

and the $n = 5$ case in Eqn. 3.15 becomes

$$\frac{1}{\sqrt{5}} \left(|00000\rangle + |10001\rangle + |11000\rangle + |11101\rangle + |11110\rangle \right)_q . \tag{3.28}$$

In general the entangled resource in Eqn. 3.16 becomes

$$|\mathrm{QND}t_n\rangle_q = \frac{1}{\sqrt{n}} \sum_{j=0}^{n-1} |1\rangle_q^{\otimes(n-1-j)} |0\rangle_q^{\otimes j} |(1 + (n-1-j) \bmod 2) \bmod 2\rangle_q . \tag{3.29}$$

The n^{th} mode in Eqn. 3.29, $|(1 + (n-1-j) \bmod 2) \bmod 2\rangle_q$, is effectively the parity of the number times 1 appears in the first $n-1$ modes. From this we see that we can make $|\mathrm{QND}t_n\rangle$ from $|t_{n-1}\rangle_q \otimes |0\rangle_q$ by applying $n-1$ CNOT gates between each of the first $n-1$ qubits and the n^{th} qubit. That is, we need to apply a CNOT between the 1st and n^{th} qubit, the 2nd and n^{th} qubit, $\cdots$, the $(n-2)^{\text{th}}$ and n^{th} qubit and between the $(n-1)^{\text{th}}$ and n^{th} qubit.

3.2 An Improved LOQC teleporter

In Fig. 3.6 we described a photon number QND detector that succeeded with a probability of $|b_1|^2 \left(\frac{n-1}{n}\right)$, provided the state $|\Psi_1\rangle$ from Eqn. 3.11 is incident on modes a and b. If we set $b_0 = b_2 = 0$ and $b_1 = 1$, Fig. 3.6 becomes a teleporter. When we compare this teleporter with that proposed by Knill *et al.* [31], shown in Fig. 2.19, we notice two differences. First, we teleport both modes of our quantum states. When we teleport with the n photon entangled resource state $|\mathrm{QND}t_n\rangle$, the probability of success is the same as when the LOQC teleporter uses the $n-1$ photon entangled state $|t_{n-1}\rangle$. By teleporting both modes of our quantum state we have reduced the success probability of teleportation by a factor of $\frac{n^2-1}{n^2}$. Second, since we only leave two modes of our entangled resource state $|\mathrm{QND}t_n\rangle$ unmeasured, we dictate the modes in which the teleported state will appear. This has important consequences when we consider applying a near deterministic CSIGN to optical qubits.

In Fig. 3.7 we show the teleportation of two optical qubits using the resource states $|\mathrm{QND}t_n\rangle$, after which we apply a CSIGN . Since the correction gates c_1, c_2, c_3 and c_4 are always phase shifters of the form $\phi = m\,(2\pi/n)$, where $m \in \{1, 2, \cdots, n-1\}$, we can commute the CSIGN gate through these:

$$U_{\mathrm{CZ}} \cdot \left[\begin{pmatrix} 1 & 0 \\ 0 & e^{i\phi_1} \end{pmatrix} \otimes \begin{pmatrix} 1 & 0 \\ 0 & e^{i\phi_2} \end{pmatrix} \right] \cdot U_{\mathrm{CZ}} = \begin{pmatrix} 1 & 0 \\ 0 & e^{i\phi_1} \end{pmatrix} \otimes \begin{pmatrix} 1 & 0 \\ 0 & e^{i\phi_2} \end{pmatrix}$$

This leads to Fig. 3.8.

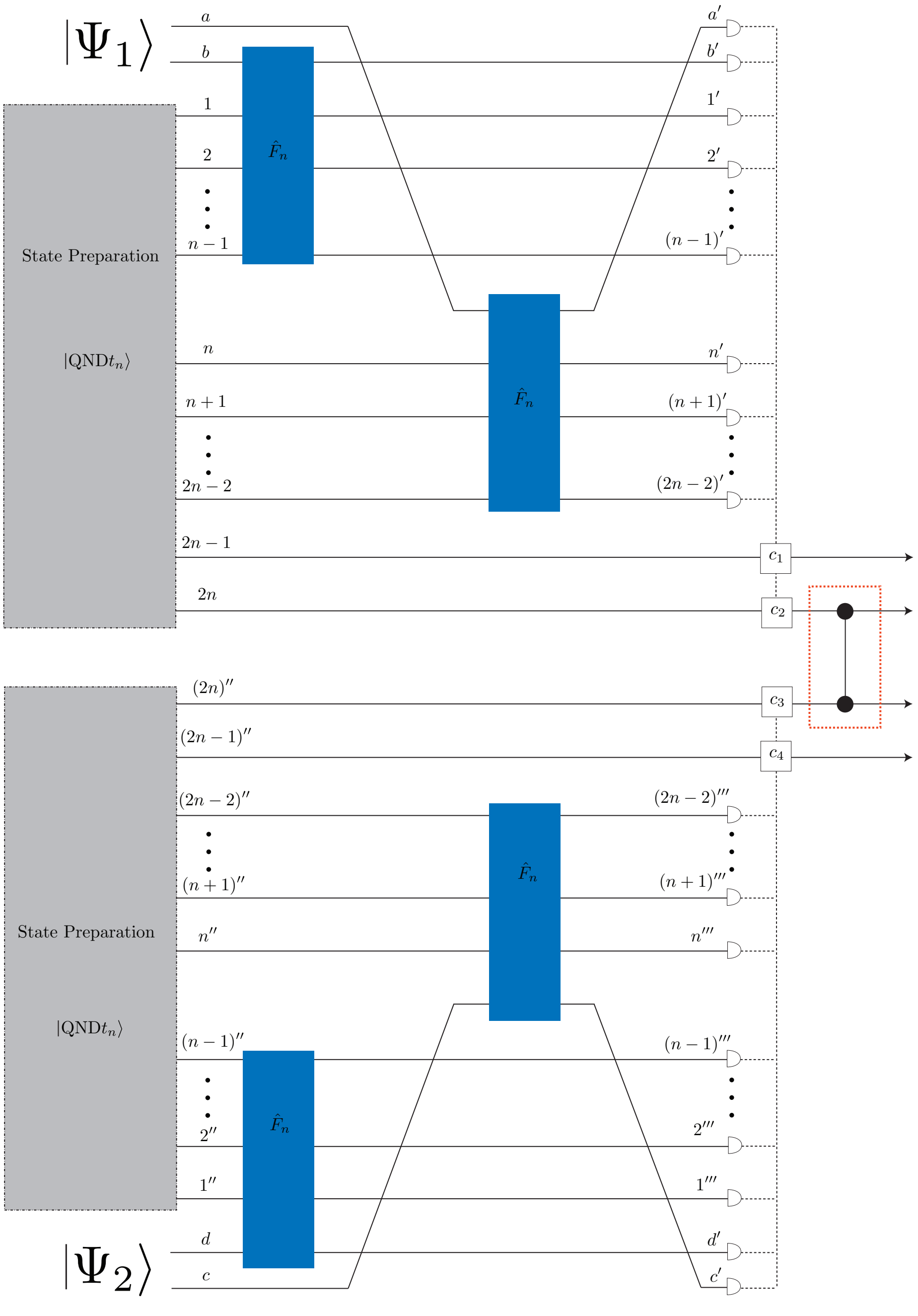

Figure 3.7: Applying a CSIGN after two teleportations, each with the entangled resource state $|\mathrm{QND}t_n\rangle$. The CSIGN gate is shown in the red dashed box.

Fig. 3.8 applies a CSIGN gate to optical qubits with a success probability that asymptotically approaches 1. If we compare this to the teleported gate proposed in [31], we notice that our entangled resource state requires only one

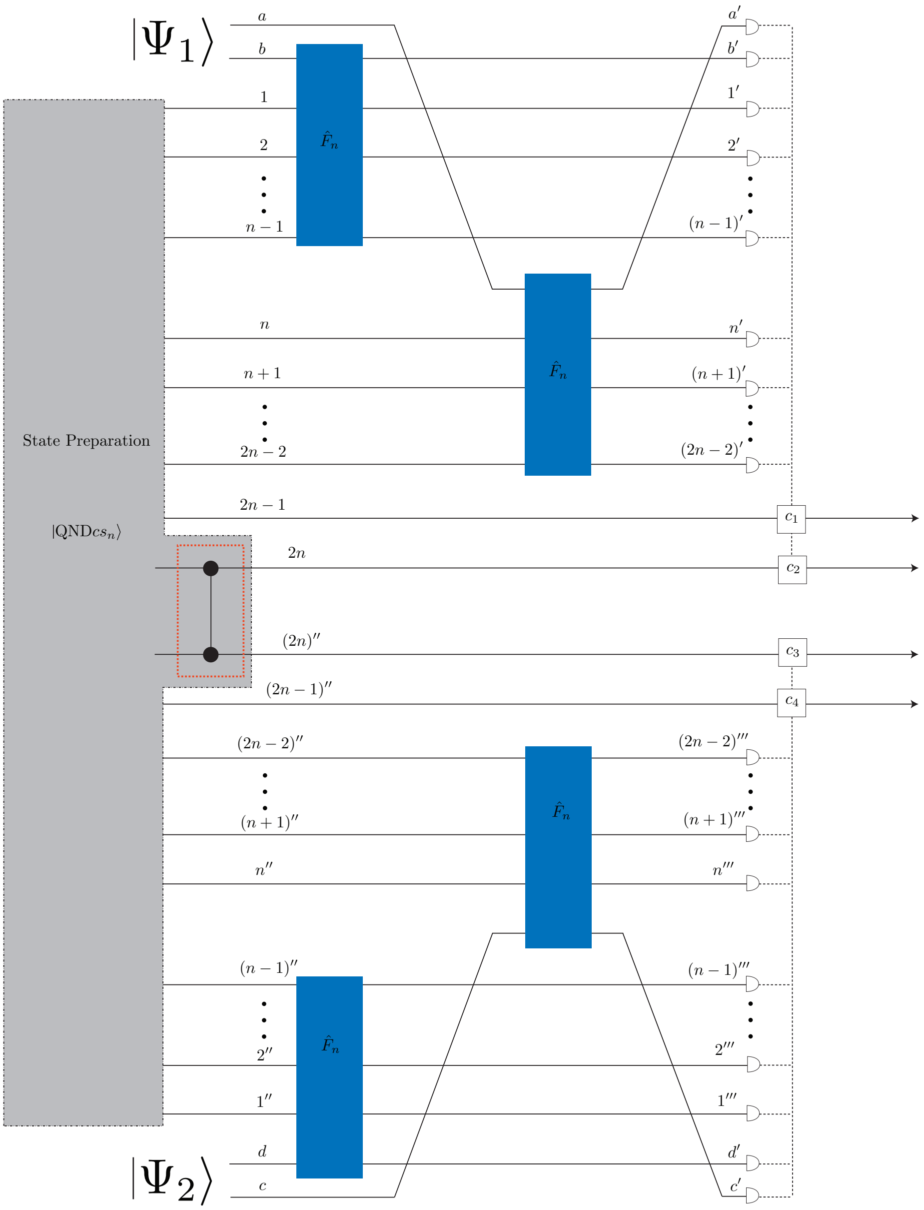

Figure 3.8: Commuting the CSIGN through two teleportations such that it now acts on the entangled resources state $|\mathrm{QND}t_n\rangle \otimes |\mathrm{QND}t_n\rangle$.

application of a probabilistic CSIGN gate as opposed to the n^2 probabilistic CSIGN applications necessary in [31]. This is also an improvement of the scheme by Franson *et al.* [83] that required an additional $4n$ probabilistic CSIGN gates to be applied to the teleporter entangled states.

When we use two copies of $|\mathrm{QND}t_{n+1}\rangle$, the CSIGN shown in Fig. 3.8 succeeds with a probability of $\left(\frac{n}{n+1}\right)^2$. In this case, to produce the one copy of $|\mathrm{QND}t_{n+1}\rangle$ we require $n-1$ probabilistic CNOT gates to produce $|t_n\rangle$ in addition to n probabilistic CNOT gates to entangle the two states $|t_n\rangle_q \otimes |0\rangle_q$. To produce the entangled resource state shown in the grey box in Fig. 3.8 therefore requires $2\,(n-1+n)+1 = 4n-1$ probabilistic CNOT gates. This leads to the following probability of success for producing $|\mathrm{QND}cs_n\rangle$:

$$P_{|\mathrm{QND}cs_n\rangle} = (p_1)^{4n-1} \tag{3.30}$$

where either $p_1 = 0.0741$ when we consider using the $2/27$ single photon probabilistic CNOT from [39], described in Section 2.7.5, or $p_1 = 1/4$ when we consider using the $1/4$ Bell state probabilistic CNOT from [34], described in Section 2.7.1. When we compare this with the scheme from Franson *et al.* [83], given by

$$\begin{aligned} P^{\mathrm{Franson}(1)}_{|cs_n\rangle} &= (p_1)^{n^2+2n-2}, \\ P^{\mathrm{Franson}(2)}_{|cs_n\rangle} &= (p_1)^{6n-2} \quad \text{for}\, n \gg 1, \end{aligned} \tag{3.31}$$

we find that Fig. 3.8 requires $n^2 - 2n - 1$ less probabilistic CNOT gates for small n and $2n-1$ less probabilistic CNOT gates when $n \gg 1$. Using Fig. 3.8 to perform near deterministic two qubit operations of optical qubits allows for a quadratic reduction in resources when $n \geq 3$ for small n and a linear reduction in resources when $n \gg 1$.

It is unlikely that entangled states of large numbers of photons will be used to construct LOQC two qubit gates due to the vast number of resources required, the experimental challenge in making such large entangled states and since we can use small n entangled states in conjunction with concatenated error correction [33] to produce a scalable two qubit gate. The CSIGN gate presented in Fig. 3.8 suffers from the same errors as the original LOQC CSIGN, as discussed in the next Section.

3.2.1 QEC

When we considered Eqn. 3.24 incident on Fig. 3.6 we saw that the error resulting from measuring n photons from the bottom n-splitter in Fig. 3.6 was $\alpha|10\rangle + \beta|01\rangle \rightarrow \alpha|01\rangle$ and the error resulting from measuring n photons from the top n-splitter in Fig. 3.6 was either $\alpha|10\rangle + \beta|01\rangle \rightarrow \beta|01\rangle$ when n was odd or $\alpha|10\rangle + \beta|01\rangle \rightarrow \beta|10\rangle$ when n was even.

In the case that n is even, this error is identical to the Z-measurement error resulting from the LOQC teleportation in Fig. 2.19 and can be corrected by using the party code in Eqns. 2.99 and 2.100.

In the case that n is odd, it appears that this is not the case, the error would not satisfy the condition in Eqn. 2.98 given the code words in Eqns. 2.99 and 2.100. However, if we incorporate a SWAP correction on the output modes when n is odd and we measure n photons from the top n-splitter in Fig. 3.6, the error is identical to the Z-measurement error.

Chapter 4

Qubus Computation: Displacements

In Section 2.8 we described an alternative scheme to the origin proposal [28] to use Kerr non-linearites for the construction of quantum gates. This alternate scheme incorporated weak Kerr non-linearites in conjunction with a strong coherent quantum bus mode to induce a CNOT on photonic qubits [49, 92]. The weak non-linearities effectively induced a controlled rotation on the bus mode dependent on the polarisation of the photonic qubit. The two CNOT gates described in Sections 2.8.4 and 2.8.5 were based on the parity gate in Fig. 2.36. In Section 2.8.6 we described two methods by which the parity gate in Fig. 2.36 could be improved by displacing the probe beam. We build on the results from Section 2.8.6 in this Chapter, investigating other possible uses for displacements in qubus computation.

In Section 4.1 we address the question raised at the end of Section 2.8.7: whether we can use techniques similar to those in Section 2.8.7 to measure the syndromes for an arbitrary stabilizer code. Since the quantum gates proposed in [49, 92] allow for a universal set of gates, we know that in principle we can measure the syndrome for any stabilizer, using standard techniques [21]. However, we wish to investigate the possibility of directly using qubus gates to measure the syndromes of any stabilizer code without the need to break the problem into the standard array of CNOT gates. This will involve first showing how the syndromes for the 7-qubit code can be measured directly with a single coherent probe beam, controlled rotations and displacements, generalising this scheme to any stabilizer code.

The next question addressed in this Chapter is whether we can construct a Toffoli gate directly with qubus gates, once again avoiding the need to break the problem into the standard array of CNOT gates. In Section 4.2 we show a method that uses controlled rotations and displacements to induce a Toffoli gate on photonic qubits that succeeds 50% of the time.

4.1 Measuring Stabilizers with Displacements

4.1.1 The 7-qubit Code

We begin by investigating the $[[7,1,3]]$ stabilizer code [105]. This code can correct a single arbitrary quantum error in any of the 7 qubits, and it has been used extensively in studies of fault-tolerance in quantum computers due to the fact that it allows for simple constructions of fault-tolerant encoded gates [26]. The stabilizer generators for the 7-qubit code are given in Table 4.1.

M_1	X	X	X	X	I	I	I
M_2	X	X	I	I	X	X	I
M_3	X	I	X	I	X	I	X
M_4	Z	Z	Z	Z	I	I	I
M_5	Z	Z	I	I	Z	Z	I
M_6	Z	I	Z	I	Z	I	Z

Table 4.1: The stabilizer generators for the 7-qubit code [105].

The codewords are given by

$$\begin{aligned} |\bar{0}\rangle =& \frac{1}{2\sqrt{2}}\left(|0000000\rangle + |1111000\rangle + |1100110\rangle + |1010101\rangle \right. \\ & \left. + |0011110\rangle + |0101101\rangle + |0110011\rangle + |1001011\rangle\right) \qquad (4.1) \\ |\bar{1}\rangle =& \frac{1}{2\sqrt{2}}\left(|0000111\rangle + |1111111\rangle + |1100001\rangle + |1010010\rangle \right. \\ & \left. + |0011001\rangle + |0101010\rangle + |0110100\rangle + |1001100\rangle\right). \end{aligned}$$

In order to detect both the location and type of error that has corrupted a single qubit in the state $c_0|\bar{0}\rangle + c_1|\bar{1}\rangle$, we must measure the six multi-qubit Pauli operators $M_1, \cdots, M_6$. By measuring M_1, M_2 and M_3 the location of any Z error is given and by measuring M_4, M_5 and M_6 the location of any bit flip error is given. Consider the measurement of M_4, that is, consider detecting the presence of a bit flip error on one of the first four qubits in $c_0|\bar{0}\rangle + c_1|\bar{1}\rangle$. Notice that this entails simply measuring the parity of the first four qubits, an even parity indicating no bit flip and an odd parity indicating a one bit flip error. This same rationale is true for the measurement of M_5 and M_6. That is, measurement of M_5 is equivalent to measuring the parity on qubits 1,2,5 and 6 and measurement of M_6 is equivalent to measuring the parity on qubits 1,3,5 and 7. This is also true for the measurement of M_1, M_2 and M_3, since we can simply change the basis with Hadamard gates.

For an arbitrary stabilizer code, various multi-qubit Pauli operators must be measured, each of which is always equivalent to the measurement of only the parity of a subset of qubits. We can see this by considering the arbitrary stabilizer M_i that is comprised of just Z operators. By definition, we know that $M_i|\bar{\psi}\rangle = |\bar{\psi}\rangle$. For this to be true, we know that the qubits in the codewords that correspond to the location of the Z operators in M_i must have an even parity. For M_i to detect the error E, E must anti-commute with M_i: $M_iE|\bar{\psi}\rangle = -EM_i|\bar{\psi}\rangle = -E|\bar{\psi}\rangle$, as described in Section 2.6.3. This means, once the error E has corrupted $|\bar{\psi}\rangle$, the parity of the qubits in the codewords that correspond to the location of the Z operators in M_i must now have an odd parity.

When M_i is comprised of both X and Z operators, we simply conjugate M_i with Hadamard operators in the location of the X operators: $M_i \to \widetilde{M}_i = \widetilde{H}M_i\widetilde{H}$. Once again, by definition of M_i, we know that $\widetilde{M}_i\widetilde{H}|\bar{\psi}\rangle = \widetilde{H}|\bar{\psi}\rangle$, since $M_i|\bar{\psi}\rangle = \widetilde{H}\widetilde{H}M_i\widetilde{H}\widetilde{H}|\bar{\psi}\rangle = \widetilde{H}\widetilde{H}|\bar{\psi}\rangle = |\bar{\psi}\rangle$. This means the parity of the qubits in $\widetilde{H}|\bar{\psi}\rangle$ that correspond to the location of the Z operators in $\widetilde{M}_i$ must have an even parity. To detect an error E we again use the fact that E must anti-commute with M_i: $\widetilde{M}_i\left(\widetilde{H}E\widetilde{H}\right)\widetilde{H}|\bar{\psi}\rangle = -\left(\widetilde{H}E\widetilde{H}\right)\widetilde{H}|\bar{\psi}\rangle$. This means, once the error E has corrupted $|\bar{\psi}\rangle$, the parity of the qubits in the $\widetilde{H}|\bar{\psi}\rangle$ that correspond to the location of the Z operators in $\widetilde{M}_i$ must now have an odd parity.

4.1.2 Single Coherent Probe Beam

As described above, the measurement of M_4 for the 7-qubit code is equivalent to measuring the parity of the first 4 qubits in $c_0|\bar{0}\rangle + c_1|\bar{1}\rangle$. Ideally we would want to do this with just one coherent probe beam, four controlled rotations and a single probe detection, following a direct analogy with the circuit depicted in Fig. 2.44(a). However this is not possible. The best we can do is have some even states go to $|\alpha\rangle$ and the rest go to $|\alpha e^{\pm 2i\theta}\rangle$ while the odd states go to $|\alpha e^{\pm i\theta}\rangle$. The circuit that performs this is shown in Fig. 4.1(a). In phase space we have five points consisting of three for the even states ($|\alpha\rangle, |\alpha e^{\pm 2i\theta}\rangle$) and two for the odd states ($|\alpha e^{\pm i\theta}\rangle$), as can be seen in Fig. 4.1(b). If we were to homodyne detect the probe beam at this stage, we would partially decode our encoded state $c_0|\bar{0}\rangle + c_1|\bar{1}\rangle$ since we can distinguish the state $|\alpha\rangle$ from $|\alpha e^{\pm 2i\theta}\rangle$.

We now need to determine what operations must be done before we measure the probe beam so that we only distinguish states of different parity on the first four qubits, and nothing more. It turns out that either homodyne or photon number detection can be used, depending on the operations applied before the measurement.

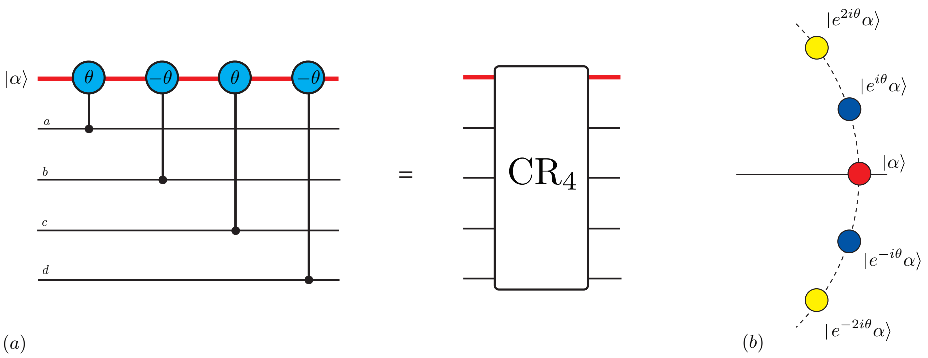

Figure 4.1: **(a)** First attempt at using controlled rotations to measure the parity of four qubits with a single probe beam. CR = controlled rotation. **(b)** Phase space representation of probe beam after part **(a)**. The red and yellow circles correspond even states and the blue circles correspond to odd states.

4.1.3 Photon number detection

Parity measurement for 4 qubits

In order for a photon number detection of the probe beam to only distinguish odd from even parity states, we require the yellow and red circles in Fig. 4.1(b) to be equidistant from the origin situated on a circle and the blue circles to be also be equidistant from the origin situated on a different, concentric circle. If we incorporate displacements in conjunction with applications of Fig. 4.1(a), we can take the five cirlces in phase space to just three. This is shown in Fig. 4.2(a).

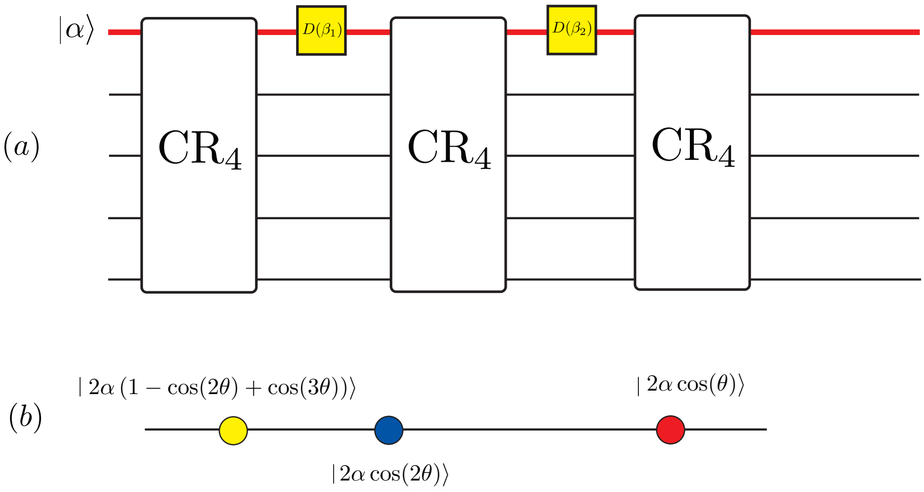

Figure 4.2: **(a)** Controlled rotations and displacements used to transform the 5 circles in Fig. 4.1(b) to just three. **(b)** Phase representation of the probe beam.

To understand how to calculate the necessary displacements to transform Fig. 4.1(b) to Fig. 4.2(b), we consider the five possible cases. For instance, consider the five states $|0000\rangle, |1111\rangle, |1000\rangle, |0111\rangle, |0100\rangle$ incident on Fig. 4.2(a). We begin with three applications of Fig. 4.1(a) and a displacement in between each:

$$\begin{aligned}
|1000\rangle : |\alpha\rangle &\xrightarrow{\text{CR}_4} |e^{i\theta}\alpha\rangle \xrightarrow{D(\beta_1)} |\alpha\left(e^{i\theta}+B_1\right)\rangle \xrightarrow{\text{CR}_4} |e^{i\theta}\alpha\left(e^{i\theta}+B_1\right)\rangle \\
&\xrightarrow{D(\beta_2)} |\alpha\left(e^{i\theta}\left(e^{i\theta}+B_1\right)+B2\right)\rangle \xrightarrow{\text{CR}_4} |\alpha\left(e^{i\theta}\left(e^{i\theta}\left(e^{i\theta}+B_1\right)+B2\right)\right)\rangle \\
|0111\rangle : |\alpha\rangle &\xrightarrow{\text{CR}_4} |e^{-i\theta}\alpha\rangle \xrightarrow{D(\beta_1)} |\alpha\left(e^{-i\theta}+B_1\right)\rangle \xrightarrow{\text{CR}_4} |e^{-i\theta}\alpha\left(e^{-i\theta}+B_1\right)\rangle \\
&\xrightarrow{D(\beta_2)} |\alpha\left(e^{-i\theta}\left(e^{-i\theta}+B_1\right)+B2\right)\rangle \xrightarrow{\text{CR}_4} |\alpha\left(e^{-i\theta}\left(e^{-i\theta}\left(e^{-i\theta}+B_1\right)+B2\right)\right)\rangle \\
|1010\rangle : |\alpha\rangle &\xrightarrow{\text{CR}_4} |e^{2i\theta}\alpha\rangle \xrightarrow{D(\beta_1)} |\alpha\left(e^{2i\theta}+B_1\right)\rangle \xrightarrow{\text{CR}_4} |e^{2i\theta}\alpha\left(e^{2i\theta}+B_1\right)\rangle \\
&\xrightarrow{D(\beta_2)} |\alpha\left(e^{2i\theta}\left(e^{2i\theta}+B_1\right)+B2\right)\rangle \xrightarrow{\text{CR}_4} |\alpha\left(e^{2i\theta}\left(e^{2i\theta}\left(e^{2i\theta}+B_1\right)+B2\right)\right)\rangle \\
|0101\rangle : |\alpha\rangle &\xrightarrow{\text{CR}_4} |e^{-2i\theta}\alpha\rangle \xrightarrow{D(\beta_1)} |\alpha\left(e^{-2i\theta}+B_1\right)\rangle \xrightarrow{\text{CR}_4} |e^{-2i\theta}\alpha\left(e^{-2i\theta}+B_1\right)\rangle \\
&\xrightarrow{D(\beta_2)} |\alpha\left(e^{-2i\theta}\left(e^{-2i\theta}+B_1\right)+B2\right)\rangle \xrightarrow{\text{CR}_4} |\alpha\left(e^{-2i\theta}\left(e^{-2i\theta}\left(e^{-2i\theta}+B_1\right)+B2\right)\right)\rangle \\
|1001\rangle : |\alpha\rangle &\xrightarrow{\text{CR}_4} |\alpha\rangle \xrightarrow{D(\beta_1)} |\alpha\left(1+B_1\right)\rangle \xrightarrow{\text{CR}_4} |\alpha\left(1+B_1\right)\rangle \\
&\xrightarrow{D(\beta_2)} |\alpha\left(1+B_1+B2\right)\rangle \xrightarrow{\text{CR}_4} |\alpha\left(1+B_1+B2\right)\rangle
\end{aligned}$$

where $\beta_1 = \alpha B_1$, $\beta_2 = \alpha B_2$ and we have ignored the phases associated with the displacements (Eqn. 2.26) for now. We see that the real part of the state resulting from transforming $|1000\rangle$ is identical to the real part for $|0111\rangle$ and the imaginary part for $|1000\rangle$ is negative the imaginary part for $|0111\rangle$. This is also true for $|1010\rangle$ and $|0101\rangle$. If we simply set the imaginary part of each resulting state to 0, we have two simultaneous equations that need to be solved. Solving for B_1 and B_2 gives

$$\begin{aligned}
B_1 &= -4\cos^2\left(\frac{\theta}{2}\right)\left(2\cos(\theta)-1\right) \qquad (4.2)\\
B_2 &= 1+2\cos(\theta)+2\cos(3\theta)
\end{aligned}$$

As can be seen in Fig. 4.2(b), the three points in phase space are given by

$$\begin{aligned}
|1000\rangle &: |\alpha\rangle \rightarrow |2\alpha\cos(2\theta)\rangle \\
|0111\rangle &: |\alpha\rangle \rightarrow |2\alpha\cos(2\theta)\rangle \\
|1010\rangle &: |\alpha\rangle \rightarrow |2\alpha\left(1-\cos(2\theta)+\cos(2\theta)\right)\rangle \\
|0101\rangle &: |\alpha\rangle \rightarrow |2\alpha\left(1-\cos(2\theta)+\cos(2\theta)\right)\rangle \\
|1001\rangle &: |\alpha\rangle \rightarrow |2\alpha\cos(\theta)\rangle.
\end{aligned}$$

If we now displace the probe beam by $D(\alpha(\cos(2\theta)-\cos(3\theta)-\cos(\theta)-1)$, as in Fig. 4.3(a), the phase space representation, shown in Fig. 4.3(b), is such that the even parity states can be distinguished from the odd parity states with a photon number detection of the probe beam. That is, $|\text{odd}\rangle \rightarrow |-4\alpha\sin^2(\theta/2)(2\sin^2(\theta)+\cos(\theta))\rangle$ and $|\text{even}\rangle \rightarrow |\pm 2\alpha\sin^2(\theta)(2\cos(\theta)-1)\rangle$

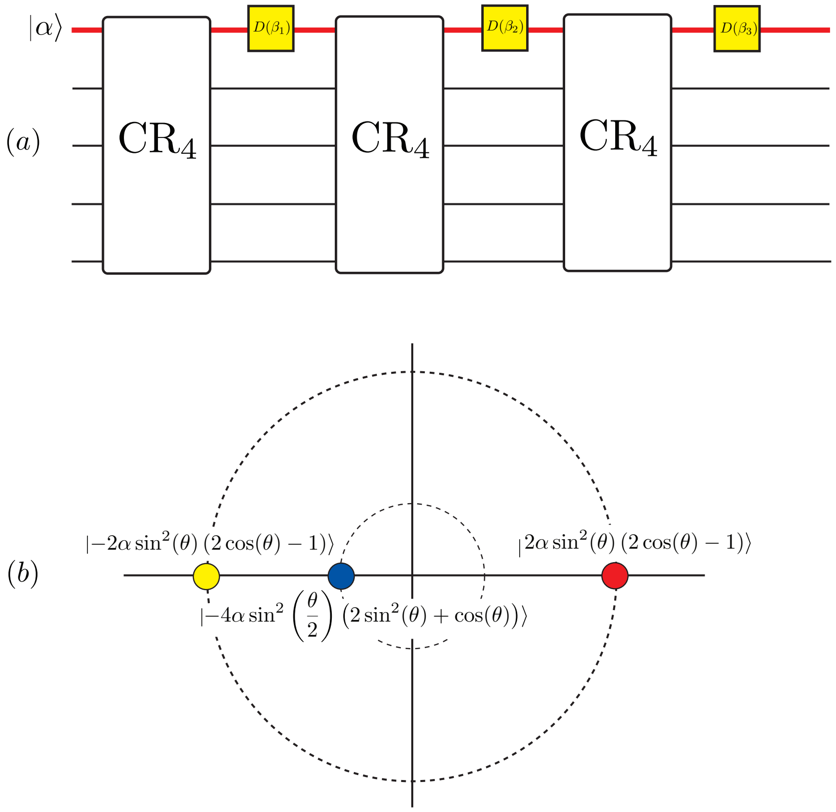

Figure 4.3: **(a)** Controlled rotations and displacements used to measure the parity of four qubits, provided $D(\beta_1) = D(-4\alpha\cos^2(\theta/2)\big(2\cos(\theta)-1\big))$, $D(\beta_2) = D(\alpha\big(1+2\cos(\theta)+2\cos(3\theta)\big))$, $D(\beta_3) = D(\alpha(\cos(2\theta)-\cos(3\theta)-\cos(\theta)-1)$ and we perform a photon number detection on the probe beam. **(b)** Phase representation of the probe beam before detection.

Phase correction

The phases associated with the displacements (Eqn. 2.26) can easily be taken care of after the photon number measurement with appropriate phase shifters on each mode for the odd and even state case. In the case that we detect an even state we know that

$$\begin{aligned}\big(|\text{even}_1\rangle + c_6|1010\rangle + c_7|0101\rangle\big)|\alpha\rangle \rightarrow\ & |\text{even}_1\rangle|2\alpha\sin^2(\theta)(2\cos(\theta)-1)\rangle \\ & + \big(e^{i\phi_1}c_6|1010\rangle + e^{-i\phi_1}c_7|0101\rangle\big)|-2\alpha\sin^2(\theta)(2\cos(\theta)-1)\rangle\end{aligned} \tag{4.3}$$

where $|\text{even}_1\rangle = c_0|0000\rangle + c_1|1111\rangle + c_2|1100\rangle + c_3|1001\rangle + c_4|0110\rangle + c_5|0011\rangle$ and $\phi_1 = \alpha^2\big(2\sin(\theta) + \sin(2\theta) + 2\sin(3\theta) + 3\sin(4\theta) + \sin(6\theta)\big)$. We can easily correct for these phases after the photon number measurement by having a phase shift of $e^{-i\phi_1/2}$ on modes 1 and 3 and a phase shift of $e^{i\phi_1/2}$ on modes 2 and 4. For the even state case, when we perform a photon number detection on the probe there may be an additional phase of -1 when the number of photons detected is odd, as described in Section 2.8.6. When we measure an odd number of photons we have

$$|\text{even}_1\rangle - c_6|1010\rangle - c_7|0101\rangle \tag{4.4}$$

which can be corrected with a phase shift of $e^{-i\pi/2}$ on modes 1 and 3 and a phase shift of $e^{i\pi/2}$ on modes 2 and 4.

In the case that we detect an odd state we know that

$$\big(|\text{odd}_1\rangle + |\text{odd}_2\rangle\big)|\alpha\rangle \rightarrow \big(e^{i\phi_2}|\text{odd}_1\rangle + e^{-i\phi_2}|\text{odd}_2\rangle\big)|\bar{\alpha}\rangle \tag{4.5}$$

where $\bar{\alpha} = -4\alpha\sin^2(\theta/2)(2\sin^2(\theta) + \cos(\theta))$, $|\text{odd}_1\rangle = c_0|0001\rangle + c_1|0100\rangle + c_2|0111\rangle + c_3|1101\rangle$, $|\text{odd}_2\rangle = c_4|0010\rangle + c_5|1000\rangle + c_6|1011\rangle + c_7|1110\rangle$ and $\phi_2 = 2\alpha^2\big(\sin(\theta) - \sin(2\theta) - \sin(3\theta) - \sin(6\theta)/2\big)$. We can easily correct for these phases after the photon number measurement by having a phase shift of $e^{i\phi_2}$ on modes 1 and 3 and a phase shift of $e^{-i\phi_2}$ on modes 2 and 4.

Scaling

For a photon number measurement of the probe beam to distinguish the odd from even states we require

$$\begin{aligned}&\big(2\alpha\sin^2(\theta)\,(2\cos(\theta) - 1)\big)^2 - \left(2\alpha\sin^2\left(\frac{\theta}{2}\right)(1 + \cos(\theta) - \cos(2\theta))\right)^2\\ &= 16\alpha^2\sin^4\left(\frac{\theta}{2}\right)(2\cos(3\theta) + 2\cos(2\theta) - 1) \gg 1.\end{aligned}$$

For small θ we can expand cos() and sin() as in Eqns. 2.33 and 2.34 to give

$$\alpha\theta^2 \gg \frac{1}{\sqrt{3}}. \tag{4.6}$$

Parity measurement of n qubits

We can use a similar method to Fig. 4.3(a) to measure the parity for a state of any size. If we have n qubits then the probe beam can at best be transformed to $n + 1$ points in phase space using n controlled rotations in the $\theta, -\theta, \theta, -\theta$ pattern for the controlled rotations, shown in Fig. 4.4. We can see this by considering the $n = 4$ example in Fig. 4.1(b). We know the 16 possible 4 qubit states $|x_1, x_2, x_3, x_4\rangle$, where $x_1, x_2, x_3, x_4 \in \{0, 1\}$, take the probe beam to 5 possible circles in phase space. When we consider $n = 5$, the 32 possible 5 qubit states are given by $|x_1, x_2, x_3, x_4\rangle \otimes |0\rangle$ and $|x_1, x_2, x_3, x_4\rangle \otimes |1\rangle$. The states $|x_1, x_2, x_3, x_4\rangle \otimes |0\rangle$ take the probe beam to the circles shown in Fig. 4.1(b). Since the fifth controlled rotation is $+\theta$, the states $|x_1, x_2, x_3, x_4\rangle \otimes |1\rangle$ also take the probe beam to the circles shown in Fig. 4.1(b), as well as the circle $|e^{3i\theta}\alpha\rangle$. That is, when $n = 5$, we have 6 circles in phase space. As n increases by 1, we can use the same reasoning to see that the number of circles in phase space also increases by 1. When n is even, the circles in phase space are given by $|e^{\pm i\frac{n}{2}}\alpha\rangle, |e^{\pm i(\frac{n}{2}-1)}\alpha\rangle, \cdots, |e^{\pm i\theta}\alpha\rangle, |\alpha\rangle$. When n is odd, the circles in phase space are given by $|e^{i\frac{n+1}{2}}\alpha\rangle, |e^{\pm i\frac{n-1}{2}}\alpha\rangle, |e^{\pm i(\frac{n-1}{2}-1)}\alpha\rangle, \cdots, |e^{\pm i\theta}\alpha\rangle, |\alpha\rangle$. The parity of the state incident on Fig. 4.4 is the same as the final probe beam's exponent. Using displacements and a photon number detector we are able to measure the parity.

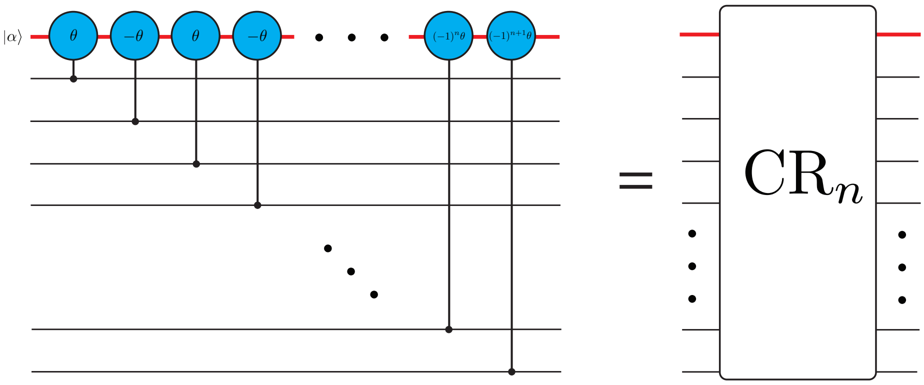

Figure 4.4: The application of n controlled rotations (CR_n) on one probe beam to create $n + 1$ circles in phase space.

To only distinguish the odd and even parity states we need a sufficient number of displacements in conjunction with CR_n circuits to take the $n + 1$ circles in phase space to just three. When n is even, we need to set the imaginary component of $\frac{n}{2}$ probe states to 0.

In the case that $\frac{n}{2}$ is also even, we need to set the real component of the $\frac{n}{4}$ probe beams corresponding to odd states equal, requiring $\frac{n}{4} - 1$ equations. We also need to set the real component for the $\frac{n}{4}$ probe beams corresponding to even states equal, also requiring $\frac{n}{4} - 1$ equations. This is a total of $n - 2$ simultaneous equations that need to be solved. We therefore require $n - 2$ displacements.

In the case that $\frac{n}{2}$ is odd, we need to set the real component of the $\frac{1}{2}(\frac{n}{2} + 1)$ probe beams corresponding to odd states equal, requiring $\frac{1}{2}(\frac{n}{2} + 1) - 1$ equations. We also need to set the real component for the $\frac{1}{2}(\frac{n}{2} - 1)$ probe beams corresponding to even states equal, also requiring $\frac{1}{2}(\frac{n}{2} - 1) - 1$ equations. This is a total of $n - 2$ simultaneous equations that need to be solved. We therefore require $n-2$ displacements.

When n is odd, we need to set the imaginary component of $\frac{n-1}{2}+1$ probe states to 0. When setting the real components to each other, the odd n case is identical to the even case with $n \rightarrow n+1$. We therefore require $\frac{n+1}{2}-2+\frac{n-1}{2}+1=n-1$ displacements.

To be able to distinguish the parity of an n qubit state with a single photon number measurement of the strong coherent probe beam we require $n-1$ displacements and n^2-n controlled rotations when n is even and n displacements and n^2 controlled rotations. The additional displacement is to set the circles in phase space for each parity equidistant from the origin.

Phase correction for the parity measurement of n qubits

When we measure the parity of n qubits by performing a photon number detection of the probe beam, the phases associated with the displacements can be corrected by using n phase shifters. This is apparent when we use the fact that θ is small.

In order to measure the parity of an n qubit state we must find the displacements $A_1, A_2, \cdots, A_m$ that satisfy

$$\alpha e^{-i\varphi(\beta)}\left(e^{i\beta\theta}\left(\cdots e^{i\beta\theta}\left(e^{i\beta\theta}\left(e^{i\beta\theta}(e^{i\beta\theta}+A_1)+A_2\right)+A_3\right)\cdots+A_{m-1}\right)+A_m\right)=\gamma_\beta \tag{4.7}$$

where $m=n-1$, $\beta \in \left\{0, \pm 1, \pm 2, \cdots, \pm\left(\frac{n}{2}-1\right), \pm\frac{n}{2}\right\}$ for n even and $m=n$, $\beta \in \left\{0, \pm 1, \pm 2, \cdots, \pm\left(\frac{n-1}{2}-1\right), \pm\frac{n-1}{2}, \pm\frac{n+1}{2}\right\}$ for n odd. From the symmetry of the phase space representation of the probe beam after the initial application of CR_n, we can assume the displacements $\alpha A_1, \alpha A_2, \cdots, \alpha A_m \in \mathbb{R}$. This also dictates the form of γ_β. When β is odd, $\gamma_\beta=\gamma$. When β is even, $\gamma_0=\gamma'$ and $\gamma_\beta=-\gamma'$ for $\beta \neq 0$, where $\gamma, \gamma' \in \mathbb{R}$. We find the overall phase $\varphi(\beta)$ due to the displacements using Eqn. 2.26:

$$\varphi(\beta)=\alpha^2 \sum_{k=1}^{m-1} A_k \sum_{j=1}^{k} \sin(j\beta\theta) A_{k-1} \tag{4.8}$$

where $A_0=\mathbb{1}$. In the case that $\theta \ll 1$ and $m\beta \ll \frac{1}{\theta}$, we can expand $\sin(j\beta\theta) \approx j\beta\theta$ using Eqn. 2.34:

$$\varphi(\beta) \approx \alpha^2 \sum_{k=1}^{m-1} A_k \sum_{j=1}^{k} j\beta\theta A_{k-1}=\alpha^2\beta\theta \sum_{k=1}^{m-1} A_k \sum_{j=1}^{k} j A_{k-1}=\beta\phi \tag{4.9}$$

where $\phi=\alpha^2\theta \sum_{k=1}^{m-1} A_k \sum_{j=1}^{k} j A_{k-1}$ is independent of β.

To see how we can correct for the phases $\varphi(\beta)$ we need to first look at what the n qubit state looks like after the initial application of Fig. 4.4:

$$\sum_{\beta} |\text{state}(\beta)\rangle |e^{i\beta\theta}\alpha\rangle \tag{4.10}$$

where $|\text{state}(\beta)\rangle$ is the sum of n qubit states with the same probe beam after Fig. 4.4. For example, when $n = 5$, $|\text{state}(2)\rangle = c_1|10100\rangle + c_2|10001\rangle + c_3|00101\rangle + c_4|10111\rangle + c_5|11101\rangle$, for arbitrary c_1, c_2, c_3, c_4, c_5. When n is even, the sum is either over the even or the odd elements of $\left\{0, \pm 1, \pm 2, \cdots, \pm\left(\frac{n}{2} - 1\right), \pm\frac{n}{2}\right\}$. When n is odd, the sum is either over the even or the odd elements of $\{0, \pm 1, \pm 2, \cdots, \pm\left(\frac{n-1}{2} - 1\right), \pm\frac{n-1}{2}, \pm\frac{n+1}{2}\}$.

After the application of m CR$_n$ circuits and m displacements, Eqn. 4.10 becomes

$$\sum_{\beta \neq 0} e^{-i\beta\phi} |\text{state}(\beta)\rangle |-\gamma'\rangle + |\text{state}(0)\rangle |\gamma'\rangle \tag{4.11}$$

or

$$\sum_{\beta} e^{-i\beta\phi} |\text{state}(\beta)\rangle |\gamma\rangle, \tag{4.12}$$

depending on the parity of our n qubit state. To correct for the phases $\varphi(\beta) \approx \beta\phi$ we simply apply phases shifters ϕ to the odd numbered modes and $-\phi$ to the even numbered modes.

For the even state case, there will also be a -1 phase factor when the probe beam detection results in an odd number of photons. Unfortunately this phase factor cannot be corrected for in general, so when the probe beam detection indicates the parity of our n qubits was even, half of the time we will pick up a -1 phase factor on some of the even terms which cannot necessarily be corrected.

Scaling for the parity measurement of n qubits

We can solve Eqn. 4.7 analytically for the cases $m = 5$ and $m = 7$.

To measure the parity of either 5 or 6 qubits, the displacements required in Fig. 4.4 with $n = 5$ or 6 are given by

$$\begin{aligned}
A_1 &= -\frac{1}{2}\left(1 + 4\cos(\theta) + 2\cos(3\theta) + 2\cos(5\theta)\right)\sec(2\theta) \qquad (4.13)\\
A_2 &= 4\cos^2(\frac{\theta}{2})\left(1 + 2\cos(\theta)\right)\left(-3 + 6\cos(\theta) - 4\cos(2\theta) + 2\cos(3\theta)\right)\\
A_3 &= -\left(1 + 2\cos(\theta) + 4\cos(2\theta) + 2\cos(3\theta) + 2\cos(4\theta) + 2\cos(6\theta)\right)\\
A_4 &= \left(1 - 2\cos(\theta) + 2\cos(2\theta)\right)\left(1 + 2\cos(\theta) + 2\cos(2\theta) + 2\cos(3\theta)\right)\\
A_5 &= \frac{1}{2}\left(1 + \cos(\theta)\right)\sec(\theta)\sum_{n=0}^{7} c_n \cos(n\theta)
\end{aligned}$$

where $c_0 = 1, c_1 = 1, c_2 = -5, c_3 = 2, c_4 = 0, c_5 = 2, c_6 = -3$ and $c_7 = 1$.

This takes probe beam for the even parity states to

$$|\pm\alpha\left(2 - \cos(\theta) - \cos(2\theta) - \cos(3\theta) + 2\cos(5\theta) - \cos(6\theta)\right)\rangle \tag{4.14}$$

and the probe beam for the odd parity states to

$$|-\alpha\left(1 + \cos(\theta) - 5\cos(2\theta) + \cos(3\theta) + 2\cos(5\theta) - \cos(6\theta) + \sec(2\theta)\right)\rangle. \tag{4.15}$$

To be able to distinguish the parity of 5 or 6 qubits with a photon number detection of the probe beam we require

$$\alpha\theta^4 \gg \frac{1}{\sqrt{11}}. \tag{4.16}$$

To measure the parity of either 7 or 8 qubits, the displacements required in Fig. 4.4 with $n = 7$ or 8 are given by

$$\begin{aligned}
A_1 &= -\frac{2\cos^2\left(\frac{\theta}{2}\right)\sec(3\theta)}{1 + 2\cos(\theta)} \sum_{n=0}^{7} c_n \cos(n\theta) \\
A_2 &= \frac{1}{1 - 2\cos(\theta) + 2\cos(2\theta)} \sum_{n=0}^{9} c_n \cos(n\theta) \\
A_3 &= -2\sum_{n=0}^{9} c_n \cos(n\theta) \\
A_4 &= \frac{1}{1 + 2\cos(\theta)} \sum_{n=0}^{11} c_n \cos(n\theta) \\
A_5 &= -\sec(\theta) \sum_{n=0}^{10} c_n \cos(n\theta) \\
A_6 &= 1 + 2\cos(\theta) + 2\cos(3\theta) + 2\cos(5\theta) + 2\cos(7\theta) \\
A_7 &= \frac{-1}{2\left(1 + \cos(2\theta) - \cos(3\theta) + \cos(4\theta) + \cos(6\theta)\right)} \sum_{n=0}^{16} c_n \cos(n\theta)
\end{aligned} \tag{4.17}$$

where the coefficients for Eqn. 4.17 are given in Table 4.2. This takes probe beam for the even parity states to

$$|\pm 1024\alpha \cos^4\left(\frac{\theta}{2}\right)\sin^6\left(\frac{\theta}{2}\right)\left(1 - 2\cos(\theta) + \cos(2\theta) - 2\cos(3\theta) - \cos(5\theta)\right)\rangle \tag{4.18}$$

and the probe beam for the odd parity states to

$$|\frac{32\alpha\left(1 + 2\cos(\theta)\right)^2 \sin^6\left(\frac{\theta}{2}\right)}{1 + \cos(2\theta) - \cos(3\theta) + \cos(4\theta) + \cos(6\theta)} \sum_{n=0}^{10} c_n \cos(n\theta)\rangle \tag{4.19}$$

	A_1	A_2	A_3	A_4	A_5	A_7
c_0	-1	1	1	9	2	2
c_1	6	4	3	20	3	9
c_2	-2	2	3	16	4	-6
c_3	4	6	3	16	4	-3
c_4	-2	0	3	14	3	-4
c_5	4	6	2	14	3	6
c_6	0	-2	2	12	2	2
c_7	2	4	1	10	2	6
c_8	0	0	1	6	1	-5
c_9	0	2	1	4	1	1
c_{10}	0	0	0	2	1	-4
c_{11}	0	0	0	2	0	3
c_{12}	0	0	0	0	0	2
c_{13}	0	0	0	0	0	0
c_{14}	0	0	0	0	0	0
c_{15}	0	0	0	0	0	-2
c_{16}	0	0	0	0	0	1

Table 4.2: The coefficients for Eqn. 4.17.

where the coefficients for the odd probe beam are $c_0 = -2, c_1 = -2, c_2 = -1, c_3 = 0, c_4 = 1, c_5 = c_6 = 0, c_7 = 1, c_8 = 0, c_9 = 1$ and $c_{10} = 1$.

To be able to distinguish the parity of 7 or 8 qubits with a photon number detection of the probe beam we require

$$\alpha\theta^6 \gg \frac{1}{\sqrt{2223}}. \tag{4.20}$$

From Eqns. 4.6, 4.16 and 4.20, we expect the the scaling of α and θ to be $\alpha\theta^{m-1} \gg \cdots$ to be able to distinguish the parity of n qubits, where $m = n - 1$ for odd n and $m = n - 2$ for even n, with the photon number detection of a single coherent probe beam. We can verify this numerically.

4.1.4 Arbitrary detection

The method presented in the previous Section required a number discriminating photo-detector. However, when the detection of the probe beam indicated the measurement of an odd number of photons, a phase factor of -1 is be introduced that cannot necessarily be corrected. For the reason we generalise the results from Section 4.1.3 such that the probe beam states for both the even parity and odd parity states each correspond to a separate, single circle in phase space. In this way we can perform a photon number or homodyne detection on the probe beam without any additional phases being introduced, provided we can correct for the phase associated with the displacements, which will be discussed later in this Section.

Parity measurement for 4 qubits

We again consider the $n = 4$ example. As in the previous section, after applying Fig. 4.1(a), we have five circles in phase space. To use homodyne detection to distinguish the parity we will again take advantage of the symmetry in Fig. 4.1(b). We want $|\alpha\rangle$ and $|\alpha e^{\pm 2i\theta}\rangle$ to become one circle in phase space centred at the origin and $|\alpha e^{\pm i\theta}\rangle$ to become another circle on the x-axis $|\alpha R\rangle$, where $R \in \mathbb{R}$. To induce this transformation we will require five displacements, since we need to solve five simultaneous equations, in conjunction with 6 applications of Fig. 4.1(a), as shown in Fig. 4.5.

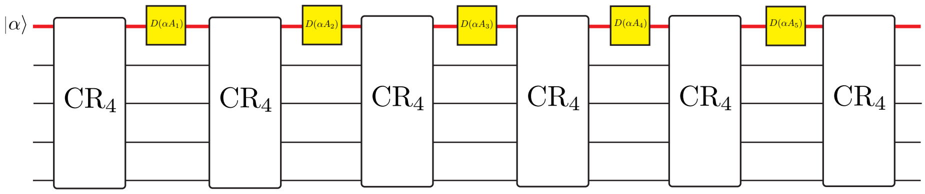

Figure 4.5: Controlled rotations and displacements used to measure the parity of four qubits when we perform a homodyne detection on the probe beam. The displacements are given in Eqn. 4.23.

The equations to be solved are:

$$\alpha e^{i\beta\theta}\left(e^{i\beta\theta}\left(e^{i\beta\theta}\left(e^{i\beta\theta}\left(e^{i\beta\theta}(e^{i\beta\theta} + A_1) + A_2\right) + A_3\right) + A_4\right) + A_5\right) = \delta_\beta \tag{4.21}$$

where $\delta_{0,\pm 2} = 0$, $\delta_{\pm 1} = \alpha R$ and due to the symmetry of Fig. 4.1(b) we can assume the displacements $\alpha A_1, \alpha B_2, \alpha C_3, \alpha D_4$ and αE_5 are real. We can simplify Eqn. 4.21:

$$e^{4i\beta\theta}A_1 + e^{3i\beta\theta}A_2 + e^{2i\beta\theta}A_3 + e^{i\beta\theta}A_4 + A_5 = e^{-i\beta\theta}\delta_\beta - e^{5i\beta\theta}. \tag{4.22}$$

Solving for A_1, A_2, A_3, A_4 and A_5 in Eqn. 4.22 gives:

$$\begin{aligned}
A_1 &= \frac{-\csc^4\left(\frac{\theta}{2}\right)}{16+32\cos(\theta)} \sum_{n=0}^{5} c_n \cos(n\theta) \\
A_2 &= \frac{\csc^4\left(\frac{\theta}{2}\right)}{8+16\cos(\theta)} \sum_{n=0}^{6} c_n \cos(n\theta) \\
A_3 &= \frac{\cos(\theta)\csc^4\left(\frac{\theta}{2}\right)}{8} \sum_{n=0}^{4} c_n \cos(n\theta) \\
A_4 &= \frac{-\csc^4\left(\frac{\theta}{2}\right)}{8+16\cos(\theta)} \sum_{n=0}^{5} c_n \cos(n\theta) \\
A_5 &= \frac{\csc^4\left(\frac{\theta}{2}\right)}{16+32\cos(\theta)} \sum_{n=0}^{3} c_n \cos(n\theta)
\end{aligned} \tag{4.23}$$

where the coefficients for Eqn. 4.23 are given in Table 4.3.

	A_1	A_2	A_3	A_4	A_5
c_0	$R-2$	$R+2$	$-R$	$R+1$	$R+2$
c_1	$2(2-R)$	$-(R+3)$	2	$-2(R+1)$	$-2(R+3)$
c_2	$2(R-1)$	$R+3$	$2(R-2)$	$R+1$	$2(R+3)$
c_3	2	-3	$2(3-R)$	$-(2R+1)$	$-2(R+1)$
c_4	-4	$R+2$	-2	$R+2$	0
c_5	2	-2	0	$-(R+1)$	0
c_6	0	1	0	0	0

Table 4.3: The coefficients for Eqn. 4.23.

In the limit of small θ, these displacements become:

$$\begin{aligned}
\alpha A_1 &\approx -\frac{\alpha R}{3\theta^4} \\
\alpha A_2 &\approx \frac{4\alpha R}{3\theta^4} \\
\alpha A_3 &\approx -\frac{2\alpha R}{\theta^4} \\
\alpha A_4 &\approx \frac{4\alpha R}{3\theta^4} \\
\alpha A_5 &\approx -\frac{\alpha R}{3\theta^4}.
\end{aligned} \tag{4.24}$$

Eqn. 4.24 shows that we are free to choose the distance between the origin and αR to be arbitrarily large, at the expense of using arbitrarily large displacements. We also see that the displacements are on the order of θ^{-4}.

The phases associated with the displacements can easily be taken care of with 4 phase shifters after the homodyne measurement, as described in the previous section.

Parity measurement for n qubits

We can also use the above method to distinguish the parity of any given state of n qubits using Fig. 4.4 in conjunction with displacements. As in the photodetection case in the previous section, we need to consider the case of odd and even n separately.

If n is even, we have $\frac{n}{2}$ points above and below the x-axis. Due to this symmetry, we need $\frac{n}{2}$ simultaneous equations to set the imaginary components of these probe beam states to 0.

In the case that $\frac{n}{2}$ is also even, we need to set the real component of the $\frac{n}{4}$ probe beams corresponding to odd states to αR and we need to set the real component for the $\frac{n}{4}+1$ probe beams corresponding to even states to 0. This is a total of $n+1$ simultaneous equations that need to be solved. We therefore require $n+1$ displacements.

In the case that $\frac{n}{2}$ is odd, we need to set the real component of the $\frac{1}{2}(\frac{n}{2}+1)$ probe beams corresponding to odd states to αR and we need to set the real component for the $\frac{1}{2}(\frac{n}{2}-1)+1$ probe beams corresponding to even states to 0. This is a total of $n+1$ simultaneous equations that need to be solved. We therefore require $n+1$ displacements.

If n is odd, we need to set the imaginary component of $\frac{n-1}{2}+1$ probe states to 0. When setting the real components to either 0 or αR, the odd n case is identical to the even case with $n \rightarrow n+1$. We therefore require $\frac{n-1}{2}+1+\frac{n+1}{2}+1=n+2$ displacements.

When n is even we require $n(n+2)$ controlled rotations and when n is odd we require $n(n+3)$ controlled rotations.

As an example, we analytically find the displacements necessary to measure the parity of 5 or 6 qubits. This involves solving an extended version of Eqn. 4.21

with seven displacements. Solving for these seven displacements gives:

$$\begin{aligned}
A_1 &= \frac{\csc^6\left(\frac{\theta}{2}\right)}{32\left(1+2\cos(\theta)\right)^2\left(1+2\cos(\theta)+2\cos(2\theta)\right)}\sum_{n=0}^{10} c_n\cos(n\theta)\\
A_2 &= \frac{-\csc^6\left(\frac{\theta}{2}\right)}{32\left(3+6\cos(\theta)+4\cos(2\theta)+2\cos(3\theta)\right)}\sum_{n=0}^{11} c_n\cos(n\theta)\\
A_3 &= \frac{\left(2\cos(\theta)-1\right)\csc^6\left(\frac{\theta}{2}\right)}{32\left(1+2\cos(\theta)\right)}\sum_{n=0}^{9} c_n\cos(n\theta)\\
A_4 &= \frac{-\left(2\cos(\theta)-1\right)\csc^6\left(\frac{\theta}{2}\right)}{32\left(1+2\cos(\theta)\right)^2}\sum_{n=0}^{10} c_n\cos(n\theta)\\
A_5 &= \frac{\csc^6\left(\frac{\theta}{2}\right)}{32\left(1+2\cos(\theta)\right)}\sum_{n=0}^{10} c_n\cos(n\theta)\\
A_6 &= \frac{\csc^6\left(\frac{\theta}{2}\right)}{32\left(3+6\cos(\theta)+4\cos(2\theta)+2\cos(3\theta)\right)}\sum_{n=0}^{11} c_n\cos(n\theta)\\
A_7 &= \frac{\csc^6\left(\frac{\theta}{2}\right)}{32\left(1+2\cos(\theta)\right)^2\left(1+2\cos(\theta)+2\cos(2\theta)\right)}\sum_{n=0}^{10} c_n\cos(n\theta)
\end{aligned} \tag{4.25}$$

where the coefficients for Eqn. 4.25 are given in Table 4.4.

	A_1	A_2	A_3	A_4	A_5	A_6	A_7
c_0	$2(R+1)$	$R-7$	$-(2R+3)$	$2-R$	$-7(R+1)$	$3(1-R)$	$-(4R+3)$
c_1	$-(4R+5)$	$2(7-R)$	$3R+5$	$2R-5$	$13(R+1)$	$7R-5$	$2(4R+3)$
c_2	$4R+5$	$R-14$	$-(3R+4)$	$5-3R$	$-(12R+13)$	$4-7R$	$-(8R+7)$
c_3	$-4(R+1)$	$6(2-R)$	$4(R+1)$	$R-4$	$11R+15$	$2(3R-2)$	$7R+6$
c_4	$2R+3$	$2(R-5)$	$-4(R+1)$	$3-2R$	$-5(2R+3)$	$4(1-R)$	$-3(2R+1)$
c_5	$-(2R+3)$	$2(5-R)$	$2R+3$	$R-3$	$4(2R+3)$	$5R-3$	$5R+3$
c_6	$2(R+2)$	$R-9$	$-2(R+1)$	$2(2-R)$	$-(7R+9)$	$2-5R$	$-(5R+3)$
c_7	$-(R+2)$	$7-2R$	$2R+3$	$R-2$	$6R+7$	$4R-3$	$3R+1$
c_8	1	$2R-5$	$-(R+3)$	$1-R$	$-(5R+4)$	$3-2R$	$-2R$
c_9	-2	$4-R$	1	$R-2$	$3R+1$	$2R-1$	$2R$
c_{10}	1	-3	0	$1-R$	$-R$	$-2R$	$-R$
c_{11}	0	1	0	0	0	R	0

Table 4.4: The coefficients for Eqn. 4.25.

In the limit of small θ, these displacements become:

$$\begin{aligned}
\alpha A_1 &\approx -\frac{2\alpha R}{45\theta^6} \\
\alpha B_1 &\approx \frac{4\alpha R}{15\theta^6} \\
\alpha C_1 &\approx -\frac{2\alpha R}{3\theta^6} \\
\alpha D_1 &\approx \frac{8\alpha R}{9\theta^6} \\
\alpha E_1 &\approx -\frac{2\alpha R}{3\theta^6} \\
\alpha F_1 &\approx \frac{4\alpha R}{15\theta^6} \\
\alpha G_1 &\approx -\frac{22\alpha R}{45\theta^6}.
\end{aligned} \tag{4.26}$$

Eqn. 4.26 shows that we are free to choose the distance between the origin and αR to be arbitrarily large, at the expense of using displacements that are on the order of θ^{-2} larger than the displacements in the $n = 4$ case.

We expect the displacements for the parity measurement of n qubits with a single homodyne detection to scale as θ^{-n} when n is even and as $\theta^{-(n+1)}$ when n is odd. We can verify this numerically.

As with the $n = 4$ case, the phases associated with the displacements for the general n qubit case can easily be taken care of with n phase shifters after the homodyne measurement, as described in the previous section.

4.2 Constructing a Three Qubit Gate with Displacements

In this Section we investigate the construction of a three qubit gate with the use of a single coherent probe beam, controlled rotations and displacements. Specifically, we investigate the construction of a Toffoli gate.

The standard arbitrary three qubit state is given by:

$$c_0|000\rangle + c_1|001\rangle + c_2|010\rangle + c_3|100\rangle + c_4|011\rangle + c_5|101\rangle + c_6|110\rangle + c_7|111\rangle \tag{4.27}$$

where $\sum_{i=0}^{7} |c_i|^2 = 1$. If we apply a Toffoli gate to this state it becomes

$$c_0|000\rangle + c_1|001\rangle + c_2|010\rangle + c_3|100\rangle + c_4|011\rangle + c_5|101\rangle + c_6|111\rangle + c_7|110\rangle. \tag{4.28}$$

Consider applying a Hadamard gate to qubit 3 of Eqn. 4.27, as shown in Eqn. 4.29. If we could distinguish the red from the green terms, without obtaining any quantum information, we would have a three qubit entangling gate.

$$\frac{1}{\sqrt{2}}\Big(c_0\big(|000\rangle + |001\rangle\big) + c_1\big(|000\rangle - |001\rangle\big) + c_2\big(|010\rangle + |011\rangle\big) + c_3\big(|100\rangle + |101\rangle\big) + c_4\big(|010\rangle - |011\rangle\big) + c_5\big(|100\rangle - |101\rangle\big) + c_6\big(|110\rangle + |111\rangle\big) + c_7\big(|110\rangle - |111\rangle\big)\Big). \tag{4.29}$$

By distinguishing the red from green terms is Eqn. 4.29, we have effectively induced a controlled-controlled-(iY) gate on Eqn. 4.27. In the case that we pick out the red terms, we need to make a Z correction on qubit 3. While this gate is not locally equivalent to a Toffoli gate, it is just as powerful, in terms of universal quantum computing. We could use a controlled phase gate with $\phi = \pi/2$ on qubits 1 and 2 to convert this gate into a Toffoli gate.

4.2.1 Three Qubit Gate with Controlled Rotations

Ideally, a single coherent probe beam and controlled rotations would be sufficient to distinguish the red from green terms in Eqn. 4.29. To investigate this possibility we consider the state

$$\Big(c_0|000\rangle + c_1|001\rangle + c_2|010\rangle + c_3|100\rangle + c_4|011\rangle + c_5|101\rangle + c_6|110\rangle + c_7|111\rangle\Big)|\alpha\rangle \tag{4.30}$$

incident on Fig 4.6.

At point (ii), after the first three controlled rotations, we have

$$c_0|000\rangle|\alpha\rangle + c_1|001\rangle|\alpha e^{in_3\theta}\rangle + c_2|010\rangle|\alpha e^{in_2\theta}\rangle + c_3|100\rangle|\alpha e^{in_1\theta}\rangle + c_4|011\rangle|\alpha e^{i(n_2+n_3)\theta}\rangle + c_5|101\rangle|\alpha e^{i(n_1+n_3)\theta}\rangle + c_6|110\rangle|\alpha e^{i(n_1+n_2)\theta}\rangle + c_7|111\rangle|\alpha e^{i(n_1+n_2+n_3)\theta}\rangle. \tag{4.31}$$

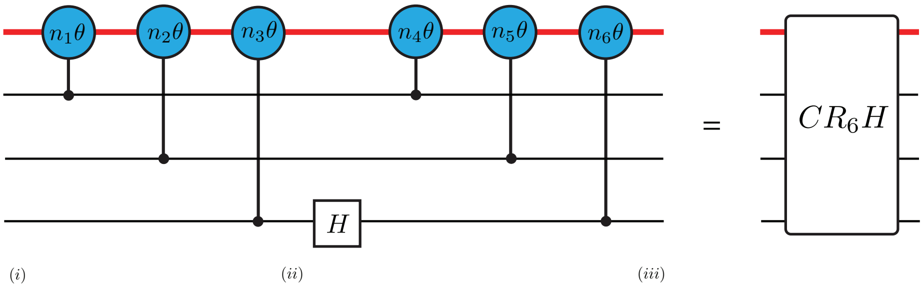

Figure 4.6: First attempt to construct a three qubit gate using a single probe beam and controlled rotations.

At point (iii), after the final three controlled rotations, we have

$$\begin{align}
&\frac{1}{\sqrt{2}}\Big(c_0\big(|000\rangle|\alpha\rangle+|001\rangle|\alpha e^{in_6\theta}\rangle\big)+c_1\big(|000\rangle|\alpha e^{in_3\theta}\rangle-|001\rangle|\alpha e^{i(n_3+n_6)\theta}\rangle\big) \nonumber\\
&+c_2\big(|010\rangle|\alpha e^{i(n_2+n_5)\theta}\rangle+|011\rangle|\alpha e^{i(n_2+n_5+n_6)\theta}\rangle\big) \tag{4.32}\\
&+c_3\big(|100\rangle|\alpha e^{i(n_1+n_4)\theta}\rangle+|101\rangle|\alpha e^{i(n_1+n_4+n_6)\theta}\rangle\big) \nonumber\\
&+c_4\big(|010\rangle|\alpha e^{i(n_2+n_3+n_5)\theta}\rangle-|011\rangle|\alpha e^{i(n_2+n_3+n_5+n_6)\theta}\rangle\big) \nonumber\\
&+c_5\big(|100\rangle|\alpha e^{i(n_1+n_3+n_4)\theta}\rangle-|101\rangle|\alpha e^{i(n_1+n_3+n_4+n_6)\theta}\rangle\big) \nonumber\\
&+c_6\big(|110\rangle|\alpha e^{i(n_1+n_2+n_4+n_5)\theta}\rangle+|111\rangle|\alpha e^{i(n_1+n_2+n_4+n_5+n_6)\theta}\rangle\big) \nonumber\\
&+c_7\big(|110\rangle|\alpha e^{i(n_1+n_2+n_3+n_4+n_5)\theta}\rangle-|111\rangle|\alpha e^{i(n_1+n_2+n_3+n_4+n_5+n_6)\theta}\rangle\big)\Big). \tag{4.33}
\end{align}$$

To distinguish the red from green terms in Eqn. 4.33 by performing a homodyne detection on the probe beam, we would require the probe beam states for the red terms to each be centred along a straight line in phase space and the probe beam states for the green terms to be centred along a different, parallel line. To distinguish the red from green terms in Eqn. 4.33 by performing a photon number detection on the probe beam, we would require the probe beam states for the red terms to each be centred along a circle centred at the origin and the probe beam states for the green terms to be centred along a concentric circle to the red state probe beam states. However, there is no choice for n_1, n_2, n_3, n_5, n_5 and n_6 that would allow the red terms to be distinguished from the green terms by either photon number detection or homodyne detection of the probe beam.

4.2.2 Success Probability

Motivated by the results on measuring the parity of n qubit with just a single probe beam, controlled rotations and displacements, presented in Section 4.1, we investigate the use of displacements in conjunction with controlled rotations to distinguish the red from green terms in Eqn. 4.33. When we use displacements and controlled rotations, the maximum success probability of inducing our three qubit gate is 1/2.

At point (*iii*) in Fig. 4.6 our probe beam is in one of the sixteen possible states $|\alpha e^{in_j\theta}\rangle$, where $n_j \in \{0, n_6, n_3+n_6, \cdots, n_1+n_2+n_3+n_4+n_5+n_6\}$. To pick out both the red and green terms in Eqn. 4.33, we assume the probe beam states for the red terms are taken to the set of states R_1 and the probe beam states for the green terms are taken to the set of states R_2. R_1 and R_2 could either be sets of states along parallel lines or concentric circles in phase space. The first step in distinguishing the red and green states is to displace the probe mode in Eqn. 4.33 by some amount $\alpha(A_1+iB_1)$, and then apply three controlled rotations to the probe beam, conditioned to each qubit, such that each displaced probe beam state picks up the corresponding phase $e^{i\chi_j\theta}$, as shown in Fig. 4.7. Our new probe beams would look like:

$$|\alpha e^{i\chi_j\theta}(e^{in_j\theta}+A_1+iB_1)\rangle \tag{4.34}$$

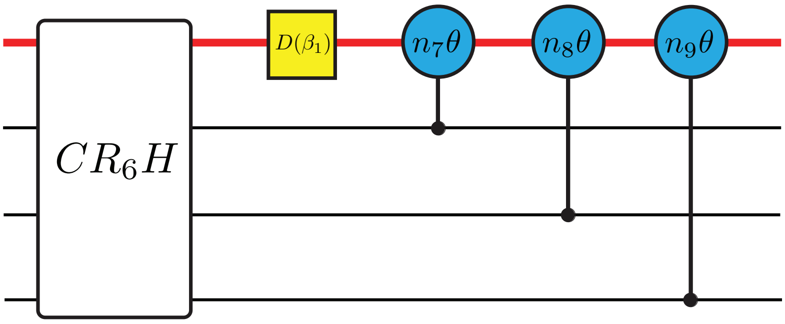

Figure 4.7: The first step in distinguishing the red from green terms in Eqn. 4.33. Here $\beta_1 = \alpha(A_1+iB_1)$ and CR_6H is given in Fig. 4.6.

Since we require each probe beam state in Eqn. 4.33 to move to a particular point in phase space, we will need to solve 16 simultaneous equations. We therefore require sixteen variables to solve for, in this case the variable take the form of 16 displacements, as shown in figure 4.8. The equations to be solved are:

$$\alpha e^{i\chi_j\theta}\Big(\cdots e^{i\chi_j\theta}\big(e^{i\chi_j\theta}\big(e^{in_j\theta}+A_1+iB_1\big)+A_2+iB_2\big)\cdots+A_{16}+iB_{16}\Big)=R_j \tag{4.35}$$

where R_j is an element of either R_1 or R_2.

Since this is a linear problem, we need to invert a 32×32 matrix with elements only dependent on $e^{i\chi_j\theta}$, independent of the initial positions of the probe beams, $\alpha e^{in_j\theta}$. This is not possible if we want to pick out both the red and green terms since $e^{i\chi_j\theta}$ for one of the red terms is equal to $e^{i\chi_j\theta}$ for at least

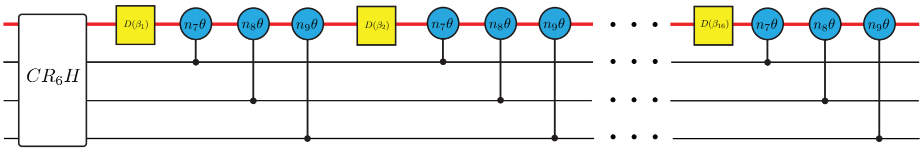

Figure 4.8: An attempt to distinguish the red from green terms in Eqn. 4.33. Here $\beta_1 = \alpha(A_1 + iB_1)$, $\beta_2 = \alpha(A_2 + iB_2)$, $\cdots$, $\beta_{16} = \alpha(A_{16} + iB_{16})$

one of the green terms. The matrix to be inverted would be singular, half of the rows would be repeated. That is, the rows corresponding to $c_0|000\rangle$ would be identical to the rows corresponding to $c_1|000\rangle$, and so on. We can therefore either pick out the red terms or the green terms in Eqn. 4.33, not both, thus our success probability is 1/2.

We now want to find what combination of controlled rotations and displacements will allow us to pick out only the red terms from Eqn. 4.33. The number of displacements we require will depend on what type of detection we wish to perform on the probe beam and what controlled rotations are applied between the displacements. After we have initiated the probe beam with Fig. 4.6 and applied the first displacement, we have three possible choices for the following controlled rotations. We can either apply one, two or three controlled rotations.

4.2.3 Displacements with 1 Controlled Rotation

If we condition the controlled rotation between displacements on the first qubit in Eqn. 4.33, we have two cases to consider: $|0\rangle$ and $|1\rangle$. If we want to use only this qubit to pick out the red terms, we will need to choose n_1, n_2, n_3, n_4, n_5 and n_6 in Eqn. 4.33 such that the probe beams for the states $c_1|001\rangle$, $c_2|010\rangle$ and $c_4|011\rangle$ all go to $|\alpha\rangle$ and the probe beams for the states $c_3|100\rangle$, $c_5|101\rangle$, $c_6|111\rangle$ and $c_7|110\rangle$ go to $|\alpha e^{ip\theta}\rangle$, for some p.

First we consider the c_1, c_2 and c_4 terms:

$$\begin{aligned} n_3 + n_6 &= 0 \\ n_2 + n_5 &= 0 \\ n_2 + n_3 + n_5 + n_6 &= 0 \end{aligned} \tag{4.36}$$

which gives $n_3 = -n_6$ and $n_2 = -n_5$.

Next, we consider the c_3, c_5, c_6 and c_7 terms:

$$\begin{aligned} n_1 + n_4 &= p \\ n_1 + n_3 + n_4 + n_6 &= p \\ n_1 + n_2 + n_4 + n_5 + n_6 &= p \\ n_1 + n_2 + n_3 + n_4 + n_5 &= p. \end{aligned} \tag{4.37}$$

Solving these in conjunction with Eqn. 4.36 gives $n_2 = n_3 = n_5 = n_6 = 0$ and $n_1 + n_4 = p$. With this solution it is not possible to pick the red terms from the green terms with displacements and controlled rotations, as Eqn. 4.33 would become

$$\begin{aligned}&\frac{1}{\sqrt{2}}\Big(c_0\big(|000\rangle|\alpha\rangle + |001\rangle|\alpha\rangle\big) + c_1\big(|000\rangle|\alpha\rangle - |001\rangle|\alpha\rangle\big) + c_2\big(|010\rangle|\alpha\rangle + |011\rangle|\alpha\rangle\big)\\ &+ c_3\big(|100\rangle|\alpha e^{ip\theta}\rangle + |101\rangle|\alpha e^{ip\theta}\rangle\big) + c_4\big(|010\rangle|\alpha\rangle - |011\rangle|\alpha\rangle\big)\\ &+ c_5\big(|100\rangle|\alpha e^{ip\theta}\rangle - |101\rangle|\alpha e^{ip\theta}\rangle\big) + c_6\big(|110\rangle|\alpha e^{ip\theta}\rangle + |111\rangle|\alpha e^{ip\theta}\rangle\big)\\ &+ c_7\big(|110\rangle|\alpha e^{ip\theta}\rangle - |111\rangle|\alpha e^{ip\theta}\rangle\big)\Big). \qquad (4.38)\end{aligned}$$

If we were to ignore Eqn. 4.37, we would be able to move the red term probe beams to five points in phase space. With this solution it is not possible to pick the red terms from the green terms with displacements and controlled rotations, as Eqn. 4.33 would become

$$\begin{aligned}&\frac{1}{\sqrt{2}}\Big(c_0\big(|000\rangle|\alpha\rangle + |001\rangle|\alpha e^{-in_3\theta}\rangle\big) + c_1\big(|000\rangle|\alpha e^{in_3\theta}\rangle - |001\rangle|\alpha\rangle\big)\\ &+ c_2\big(|010\rangle|\alpha\rangle + |011\rangle|\alpha e^{-in_3\theta}\rangle\big) + c_3\big(|100\rangle|\alpha e^{i(n_1+n_4)\theta}\rangle + |101\rangle|\alpha e^{i(n_1-n_3+n_4)\theta}\rangle\big)\\ &+ c_4\big(|010\rangle|\alpha e^{in_3\theta}\rangle - |011\rangle|\alpha\rangle\big) + c_5\big(|100\rangle|\alpha e^{i(n_1+n_3+n_4)\theta}\rangle - |101\rangle|\alpha e^{i(n_1+n_4)\theta}\rangle\big)\\ &+ c_6\big(|110\rangle|\alpha e^{i(n_1+n_4)\theta}\rangle + |111\rangle|\alpha e^{i(n_1-n_3+n_4)\theta}\rangle\big)\\ &+ c_7\big(|110\rangle|\alpha e^{i(n_1+n_3+n_4)\theta}\rangle - |111\rangle|\alpha e^{i(n_1+n_4)\theta}\rangle\big)\Big). \qquad (4.39)\end{aligned}$$

The reason some of the red terms will always be indistinguishable from some of the green terms in both Eqn. 4.38 and Eqn. 4.39, no matter how many displacements and controlled rotations we apply, is because at least one of green terms with the first qubit in the state $|x\rangle$, where $x \in \{0, 1\}$, has the same probe beam as at least one of the red terms with the first qubit in the state $|x\rangle$. Since we are only using controlled rotations between displacements condition on this first qubit, there is no way to distinguish these green and red terms, leading to gate failure.

4.2.4 Displacements with 2 Controlled Rotations

If we condition the controlled rotations between displacements on the first two qubits in Eqn. 4.33, we have four cases to consider: $|00\rangle, |01\rangle, |10\rangle$ and $|11\rangle$. We will need to choose n_1, n_2, n_3, n_4, n_5 and n_6 such that the probe beams for the states $c_0|000\rangle$ and $c_1|001\rangle$ go to $|\alpha\rangle$, the probe beams for the states $c_2|011\rangle$ and $c_4|010\rangle$ go to $|\alpha e^{ia\theta}\rangle$, the probe beams for the states $c_3|100\rangle$ and $c_5|101\rangle$ go to $|\alpha e^{ib\theta}\rangle$ and the probe beams for the states $c_6|111\rangle$ and $c_7|110\rangle$ go to $|\alpha e^{ic\theta}\rangle$, for some a, b and c.

First we consider the c_1 term:

$$n_3 + n_6 = 0 \rightarrow n_3 = -n_6 \qquad (4.40)$$

Next, we consider the c_2 and c_4 terms:

$$\begin{gathered} n_2 + n_5 = a \\ n_2 + n_3 + n_5 + n_6 = a \end{gathered} \tag{4.41}$$

which gives $n_2 = a - n_5$. Next, we consider the c_3 and c_5 terms:

$$\begin{gathered} n_1 + n_4 = b \\ n_1 + n_3 + n_4 + n_6 = b \end{gathered} \tag{4.42}$$

which gives $n_1 = b - n_4$. Finally, we consider the c_6 and c_7 terms:

$$\begin{gathered} n_1 + n_2 + n_4 + n_5 + n_6 = c \\ n_1 + n_2 + n_3 + n_4 + n_5 = c \end{gathered} \tag{4.43}$$

which gives $n_6 = 0$. With these solutions it is not possible to pick out the red from the green terms in Eqn. 4.33, as can be seen below in Eqn. 4.44:

$$\begin{aligned} &\frac{1}{\sqrt{2}}\Big(c_0\big(|000\rangle|\alpha\rangle + |001\rangle|\alpha\rangle\big) + c_1\big(|000\rangle|\alpha\rangle - |001\rangle|\alpha\rangle\big) + c_2\big(|010\rangle|\alpha e^{ia\theta}\rangle + |011\rangle|\alpha e^{ia\theta}\rangle\big) \\ &+ c_3\big(|100\rangle|\alpha e^{ib\theta}\rangle + |101\rangle|\alpha e^{ib\theta}\rangle\big) + c_4\big(|010\rangle|\alpha e^{ia\theta}\rangle - |011\rangle|\alpha e^{ia\theta}\rangle\big) \\ &+ c_5\big(|100\rangle|\alpha e^{ib\theta}\rangle - |101\rangle|\alpha e^{ib\theta}\rangle\big) + c_6\big(|110\rangle|\alpha e^{i(a+b)\theta}\rangle + |111\rangle|\alpha e^{i(a+b)\theta}\rangle\big) \\ &+ c_7\big(|110\rangle|\alpha e^{i(a+b)\theta}\rangle - |111\rangle|\alpha e^{i(a+b)\theta}\rangle\big)\Big). \end{aligned} \tag{4.44}$$

This is due to the fact that at least one of the green terms with the first two qubits in the state $|xy\rangle$, where $x, y \in \{0, 1\}$, has a the same probe beam as at least one of the red terms with the first two qubits in the state $|xy\rangle$. If we ignore Eqn. 4.43 we would be able to pick out the red from the green terms in Eqn. 4.33. That is, we could add displacements and additional controlled rotations such that the red $c_0, c_1, c_2, c_3, c_4, c_5$ and c_6 terms all go to one circle in phase space, and the red c_7 term goes to another circle. Provided these two circles are distinct from all the green term probe beam states, we would be able to use homodyne detection or photon number detection on the probe beam to pick out the red terms. Ignoring Eqn. 4.43 takes Eqn. 4.33 to Eqn. 4.45:

$$\begin{aligned} &\frac{1}{\sqrt{2}}\Big(c_0\big(|000\rangle|\alpha\rangle + |001\rangle|\alpha e^{in_6\theta}\rangle\big) + c_1\big(|000\rangle|\alpha e^{-in_6\theta}\rangle - |001\rangle|\alpha\rangle\big) \qquad (4.45) \\ &+ c_2\big(|010\rangle|\alpha e^{ia\theta}\rangle + |011\rangle|\alpha e^{i(a+n_6)\theta}\rangle\big) + c_3\big(|100\rangle|\alpha e^{ib\theta}\rangle + |101\rangle|\alpha e^{i(b+n_6)\theta}\rangle\big) \\ &+ c_4\big(|010\rangle|\alpha e^{i(a-n_6)\theta}\rangle - |011\rangle|\alpha e^{ia\theta}\rangle\big) + c_5\big(|100\rangle|\alpha e^{i(b-n_6)\theta}\rangle - |101\rangle|\alpha e^{ib\theta}\rangle\big) \\ &+ c_6\big(|110\rangle|\alpha e^{i(a+b)\theta}\rangle + |111\rangle|\alpha e^{i(a+b+n_6)\theta}\rangle\big) + c_7\big(|110\rangle|\alpha e^{i(a+b-n_6)\theta}\rangle - |111\rangle|\alpha e^{i(a+b)\theta}\rangle\big)\Big). \end{aligned}$$

Transforming the probe beam for the red $c_0, c_1, c_2, c_3, c_4, c_5$ and c_6 states to the common point $\alpha(R_1 + iR_2)$ requires solving 4 simultaneous equations. We therefore need four displacements, as shown in Fig. 4.9.

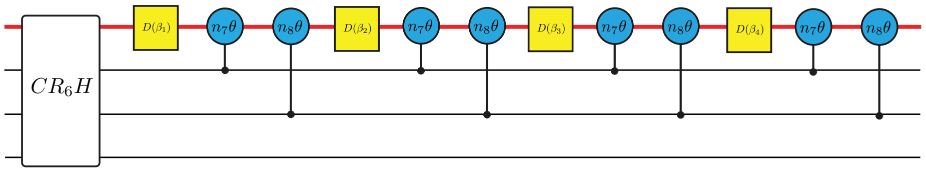

Figure 4.9: Picks out the red terms in Eqn. 4.45. Here $\beta_1 = \alpha(A_1+iB_1)$, $\beta_2 = \alpha(A_2+iB_2)$, $\beta_3 = \alpha(A_3+iB_3)$ and $\beta_4 = \alpha(A_4+iB_4)$.

Displacements

The 4 (complex) equations we need to solve are

$$\begin{aligned}\alpha e^{i\chi_j\theta}\big(e^{i\chi_j\theta}\big(e^{i\chi_j\theta}\big(e^{i\chi_j\theta}\big(e^{in_j\theta}+A_1+iB_1\big)+A_2+iB_2\big) \qquad (4.46)\\ +A_3+iB_3\big)+A_4+iB_4\big)=\alpha\big(R_1+iR_2\big)\end{aligned}$$

where $n_j \in \{0, a, b, a+b+n_6\}$, $\chi_j \in \{0, n_8, n_7, n_7+n_8\}$ and $A_k, B_k \in \mathbb{R}$ for $k = 1, 2, 3, 4$. Breaking Eqn. 4.46 into real and imaginary parts gives the 8 equations:

$$\begin{aligned}A_4\cos(\chi_j\theta)+A_3\cos(2\chi_j\theta)+A_2\cos(3\chi_j\theta)+A_1\cos(4\chi_j\theta)-B_4\sin(\chi_j\theta)-B_3\sin(2\chi_j\theta)\\ -B_2\sin(3\chi_j\theta)-B_1\sin(4\chi_j\theta)=R_1-\cos\big((n_j+4\chi_j)\theta\big) \qquad (4.47)\\ A_4\sin(\chi_j\theta)+A_3\sin(2\chi_j\theta)+A_2\sin(3\chi_j\theta)+A_1\sin(4\chi_j\theta)+B_4\cos(\chi_j\theta)+B_3\cos(2\chi_j\theta)\\ +B_2\cos(3\chi_j\theta)+B_1\cos(4\chi_j\theta)=R_2-\sin\big((n_j+4\chi_j)\theta\big). \qquad (4.48)\end{aligned}$$

Solving Eqns. 4.47 and 4.48 for $A_1, B_1, A_2, B_2, A_3, B_3, A_4, B_4$ gives:

$$\begin{aligned}A_1 = \frac{\csc\left(\frac{n_7\theta}{2}\right)\csc\left(\frac{n_8\theta}{2}\right)}{4\left(\cos\left(n_7\theta\right)-\cos\left(n_8\theta\right)\right)}\Bigg(\big(-\sin\left(n_7\theta\right)+\sin\left(n_8\theta\right)+\sin\left(\left(b+n_7-n_8\right)\theta\right)\\ -\sin\left(\left(a-n_7+n_8\right)\theta\right)\big)\sin\left(\frac{\theta}{2}\left(n_7+n_8\right)\right)\\ -\sin\left(\frac{\theta}{2}\left(n_7-n_8\right)\right)\sin\left(\left(a+b+n_6+n_7+n_8\right)\theta\right)\Bigg) \qquad (4.49)\end{aligned}$$

$$\begin{aligned}B_1 = \frac{\csc\left(\frac{n_7\theta}{2}\right)\csc\left(\frac{n_8\theta}{2}\right)}{8\left(\cos\left(n_7\theta\right)-\cos\left(n_8\theta\right)\right)}\Bigg(\sin\left(\frac{\theta}{2}\left(2b+n_7-3n_8\right)\right)-\sin\left(\left(b+\frac{3n_7}{2}-\frac{n_8}{2}\right)\theta\right)\\ +\sin\left(\left(a+b+n_6+\frac{3n_7}{2}+\frac{n_8}{2}\right)\theta\right)-\sin\left(\frac{\theta}{2}\left(2a-3n_7+n_8\right)\right)\\ -\sin\left(\frac{\theta}{2}\left(3n_7+n_8\right)\right)+\sin\left(\left(a-\frac{n_7}{2}+\frac{3n_8}{2}\right)\theta\right)-\sin\left(\left(a+b+n_6+\frac{n_7}{2}+\frac{3n_8}{2}\right)\theta\right)\\ +\sin\left(\frac{\theta}{2}\left(n_7+3n_8\right)\right)\Bigg) \qquad (4.50)\end{aligned}$$

$$
\begin{aligned}
A_2 = {} & \frac{\csc\left(\frac{n_7\theta}{2}\right)\csc\left(\frac{n_8\theta}{2}\right)}{4\left(\cos\left(n_7\theta\right)-\cos\left(n_8\theta\right)\right)}\Bigg(\sin\left(\frac{\theta}{2}\left(n_7+n_8\right)\right)\big(-\sin\left(\left(b+n_7\right)\theta\right)-\sin\left(\left(b+2n_7\right)\theta\right) \\
& +\sin\left(\left(n_7-n_8\right)\theta\right)-\sin\left(\left(b+n_7-n_8\right)\theta\right)+\sin\left(\left(a+n_8\right)\theta\right)+\sin\left(\left(a-n_7+n_8\right)\theta\right) \\
& +\sin\left(\left(a+2n_8\right)\theta\right)\big)+\sin\left(\frac{\theta}{2}\left(n_7-n_8\right)\right)\big(\sin\left(\left(a+b+n_6+n_7+n_8\right)\theta\right) \\
& +\sin\left(\left(a+b+n_6+2n_7+n_8\right)\theta\right)+\sin\left(\left(a+b+n_6+n_7+2n_8\right)\theta\right)\big)\Bigg)
\end{aligned}
\tag{4.51}
$$

$$
\begin{aligned}
B_2 = {} & \frac{\csc\left(\frac{n_7\theta}{2}\right)\csc\left(\frac{n_8\theta}{2}\right)}{2\left(\cos\left(n_7\theta\right)-\cos\left(n_8\theta\right)\right)}\Bigg(\frac{1}{4}\sin\left(\frac{\theta}{2}\left(n_7-3n_8\right)\right) \\
& +\cos\left(\frac{n_8\theta}{2}\right)\cos\left(\frac{\theta}{2}\left(2a+b+n_6+n_7+4n_8\right)\right)\sin\left(\frac{\theta}{2}\left(b+n_6\right)\right) \\
& -\frac{1}{4}\sin\left(\frac{\theta}{2}\left(2b+n_7-3n_8\right)\right)+\frac{1}{2}\sin\left(\frac{\theta}{2}\left(n_7-n_8\right)\right) \\
& -\frac{1}{4}\sin\left(\frac{\theta}{2}\left(2b+n_7-n_8\right)\right)+\frac{1}{4}\sin\left(\frac{\theta}{2}\left(3n_7-n_8\right)\right) \\
& +\frac{1}{2}\cos\left(\frac{n_7\theta}{2}\right)\left(\sin\left(\left(a-n_7+\frac{n_8}{2}\right)\theta\right)+\sin\left(\left(b+2n_7+\frac{n_8}{2}\right)\theta\right)\right. \\
& \left.-\sin\left(\left(a+b+n_6+2n_7+\frac{n_8}{2}\right)\theta\right)\right)\Bigg)
\end{aligned}
\tag{4.52}
$$

$$
\begin{aligned}
A_3 = {} & \frac{\csc\left(\frac{n_7\theta}{2}\right)\csc\left(\frac{n_8\theta}{2}\right)}{4\left(\cos\left(n_7\theta\right)-\cos\left(n_8\theta\right)\right)}\Bigg(\sin\left(\frac{\theta}{2}\left(n_7+n_8\right)\right)\big(\sin\left(\left(b+n_7\right)\theta\right)+\sin\left(\left(b+2n_7\right)\theta\right) \\
& +\sin\left(\left(n_7-n_8\right)\theta\right)-\sin\left(\left(a+n_8\right)\theta\right)+\sin\left(\left(b+2n_7+n_8\right)\theta\right)-\sin\left(\left(a+2n_8\right)\theta\right) \\
& -\sin\left(\left(a+n_7+2n_8\right)\theta\right)\big)-\sin\left(\frac{\theta}{2}\left(n_7-n_8\right)\right)\big(\sin\left(\left(a+b+n_6+2n_7+n_8\right)\theta\right) \\
& +\sin\left(\left(a+b+n_6+n_7+2n_8\right)\theta\right)+\sin\left(\left(a+b+n_6+2\left(n_7+n_8\right)\right)\theta\right)\big)\Bigg)
\end{aligned}
\tag{4.53}
$$

$$
\begin{aligned}
B_3 = {} & \frac{\csc\left(\frac{n_7\theta}{2}\right)\csc\left(\frac{n_8\theta}{2}\right)}{8\left(\cos\left(n_7\theta\right)-\cos\left(n_8\theta\right)\right)}\left(\cos\left(\left(a+b+\frac{5n_7}{2}+\frac{3n_8}{2}\right)\theta\right)\sin\left(n_6\theta\right)\right. \\
& -4\cos\left(\frac{n_7\theta}{2}\right)\cos\left(\frac{\theta}{2}\left(2a+b+n_6+2n_7+5n_8\right)\right)\sin\left(\frac{\theta}{2}\left(b+n_6\right)\right) \\
& -\sin\left(\frac{\theta}{2}\left(n_7-3n_8\right)\right)-2\sin\left(\frac{\theta}{2}\left(n_7-n_8\right)\right)+\sin\left(\frac{\theta}{2}\left(2b+n_7-n_8\right)\right) \\
& -\sin\left(\frac{\theta}{2}\left(3n_7-n_8\right)\right)+\sin\left(\left(b+\frac{3n_7}{2}-\frac{n_8}{2}\right)\theta\right) \\
& -2\cos\left(\frac{n_8\theta}{2}\right)\left(\sin\left(\left(a-\frac{n_7}{2}+n_8\right)\theta\right)+\sin\left(\left(b+\frac{5n_7}{2}+n_8\right)\theta\right)\right) \\
& \left.+\cos\left(n_6\theta\right)\sin\left(\left(a+b+\frac{5n_7}{2}+\frac{3n_8}{2}\right)\theta\right)+\sin\left(\left(a+b+n_6+\frac{5n_7}{2}+\frac{n_8}{2}\right)\theta\right)\right)
\end{aligned} \tag{4.54}
$$

$$
\begin{aligned}
A_4 = {} & \frac{\csc\left(\frac{n_7\theta}{2}\right)\csc\left(\frac{n_8\theta}{2}\right)}{4\left(\cos\ \left(n_7\theta\right)-\cos\left(n_8\theta\right)\right)}\left(\sin\left(\frac{\theta}{2}\left(n_7+n_8\right)\right)\left(-\sin\left(n_7\theta\right)+\sin\left(n_8\theta\right)\right.\right. \\
& \left.-\sin\left(\left(b+2n_7+n_8\right)\theta\right)+\sin\left(\left(a+n_7+2n_8\right)\theta\right)\right) \\
& \left.+\sin\left(\frac{\theta}{2}\left(n_7-n_8\right)\right)\sin\left(\left(a+b+n_6+2\left(n_7+n_8\right)\right)\theta\right)\right)
\end{aligned} \tag{4.55}
$$

$$
\begin{aligned}
B_4 = {} & \frac{\csc\left(\frac{n_7\theta}{2}\right)\csc\left(\frac{n_8\theta}{2}\right)}{8\left(\cos\left(n_7\theta\right)-\cos\left(n_8\theta\right)\right)}\left(2\cos\left(\frac{\theta}{2}\left(a+n_7+3n_8\right)\right)\sin\left(\frac{a\theta}{2}\right)\right. \\
& +\sin\left(\frac{\theta}{2}\left(3n_7+n_8\right)\right)-\sin\left(\frac{\theta}{2}\left(2b+3n_7+n_8\right)\right)+\sin\left(\left(b+\frac{5n_7}{2}+\frac{3n_8}{2}\right)\theta\right) \\
& -\sin\left(\left(a+b+n_6+\frac{5n_7}{2}+\frac{3n_8}{2}\right)\theta\right)-\sin\left(\left(a+\frac{3n_7}{2}+\frac{5n_8}{2}\right)\theta\right) \\
& \left.+\sin\left(\left(a+b+n_6+\frac{3n_7}{2}+\frac{5n_8}{2}\right)\theta\right)\right)
\end{aligned} \tag{4.56}
$$

where without loss of generality we have set $R_1 = R_2 = 0$. With these displacements Fig. 4.9 transforms Eqn. 4.45 to Eqn. 4.57.

$$
\begin{aligned}
& \frac{1}{\sqrt{2}}\Big(c_0\big(|000\rangle|0\rangle+|001\rangle|\alpha(e^{in_6\theta}-1)\rangle\big)+c_1\big(|000\rangle|\alpha(e^{-in_6\theta}-1)\rangle-|001\rangle|0\rangle\big) \\
& +c_2\big(|010\rangle|0\rangle+|011\rangle|\alpha(e^{in6\theta}-1)e^{i(a+4n_8)\theta}\rangle\big)+c_3\big(|100\rangle|0\rangle+|101\rangle|\alpha(e^{in_6\theta}-1)e^{i(b+4n_7)\theta}\rangle\big) \\
& +c_4\big(|010\rangle|\alpha(e^{-in_6\theta}-1)e^{i(a+n_8)\theta}\rangle-|011\rangle|0\rangle\big)+c_5\big(|100\rangle|\alpha(e^{-in_6\theta}-1)e^{i(b+4n_7)\theta}\rangle-|101\rangle|0\rangle\big) \\
& +c_6\big(|110\rangle|\alpha(1-e^{in_6\theta})e^{i(a+b+4n_7+4n_8)\theta}\rangle+|111\rangle|0\rangle\big) \\
& +c_7\big(|110\rangle|-2i\alpha\sin(n_6\theta)e^{i(a+b+4n_7+4n_8)\theta})\rangle-|111\rangle|\alpha(1-e^{in_6\theta})e^{i(a+b+4n_7+4n_8)\theta}\rangle\big)\Big).
\end{aligned} \tag{4.57}
$$

Homodyne Detection

If we set $a = -4n_8$ and $b = -4n_7$, Eqn. 4.57 becomes

$$\begin{aligned}
&\frac{1}{\sqrt{2}}\Big(c_0\big(|000\rangle|0\rangle + |001\rangle|\alpha(e^{in_6\theta}-1)\rangle\big) + c_1\big(|000\rangle|\alpha(e^{-in_6\theta}-1)\rangle - |001\rangle|0\rangle\big)\\
&+ c_2\big(|010\rangle|0\rangle + |011\rangle|\alpha(e^{in6\theta}-1)\rangle\big) + c_3\big(|100\rangle|0\rangle + |101\rangle|\alpha(e^{in_6\theta}-1)\rangle\big)\\
&+ c_4\big(|010\rangle|\alpha(e^{-in_6\theta}-1)\rangle - |011\rangle|0\rangle\big) + c_5\big(|100\rangle|\alpha(e^{-in_6\theta}-1)\rangle - |101\rangle|0\rangle\big) \qquad (4.58)\\
&+ c_6\big(|110\rangle|\alpha(1-e^{in_6\theta})\rangle + |111\rangle|0\rangle\big) + c_7\big(|110\rangle|-2i\alpha\sin(n_6\theta)\rangle - |111\rangle|\alpha(1-e^{in_6\theta})\rangle\big)\Big).
\end{aligned}$$

We see that the probe beam states for each of the red terms in Eqn. 4.58 is along the imaginary axis. We can homodyne detect the probe beam along the x-axis to pick out the red terms. Ideally the green term probe beams would be far from the red probe beams $|0\rangle$ and $|-2i\alpha\sin(n_6\theta)\rangle$.

When we homodyne detect along the x-direction there are five states that need to be considered: $|0\rangle$, $|-2i\alpha\sin(n_6\theta)\rangle$, $|\alpha(e^{in_6\theta}-1)\rangle$, $|\alpha(e^{-in_6\theta}-1)\rangle$ and $|\alpha(1-e^{in_6\theta})\rangle$. Using Eqn. 2.51 we project onto $\langle x|$:

$$\begin{aligned}
\langle x|0\rangle &= f(x,0)\\
\langle x|-2i\alpha\sin(n_6\theta)\rangle &= e^{i\phi_1(x)}f(x,0) \qquad (4.59)\\
\langle x|\alpha(e^{in_6\theta}-1)\rangle &= e^{i\phi_2(x)}f(x,\alpha\sqrt{(\cos(n_6\theta)-1)^2+\sin^2(n_6\theta)}\sin(n_6\theta/2))\\
\langle x|\alpha(e^{-in_6\theta}-1)\rangle &= e^{i\phi_3(x)}f(x,\alpha\sqrt{(\cos(n_6\theta)-1)^2+\sin^2(n_6\theta)}\sin(n_6\theta/2)))\\
\langle x|\alpha(1-e^{in_6\theta})\rangle &= e^{i\phi_4(x)}f(x,\alpha\sqrt{(\cos(n_6\theta)-1)^2+\sin^2(n_6\theta)}\sin(n_6\theta/2)))
\end{aligned}$$

where $\phi_1(x) = -2\alpha x\sin(n_6\theta)$ and we have used the fact that

$$\begin{aligned}
e^{in_6\theta}-1 =& \sqrt{(\cos(n_6\theta)-1)^2+\sin^2(n_6\theta)}\exp\left(i\arctan\left(\frac{\sin(n_6\theta)}{\cos(n_6\theta)-1}\right)\right)\\
&\cos\left(\arctan\left(\frac{\sin(n_6\theta)}{\cos(n_6\theta)-1}\right)\right) = \sin\left(\frac{n_6\theta}{2}\right).
\end{aligned}$$

The green term probe beam phases $e^{i\phi_j(x)}$ for $j = 2,3,4$ are not important and can be ignored.

In order to use homodyne detection of the probe beam to pick out the red terms in Eqn. 4.58, we require the peaks from the curves $f(x,0)$ and $f(x,\alpha\sqrt{(\cos(n_6\theta)-1)^2+\sin^2(n_6\theta)}\sin(n_6\theta/2)))$ to be far apart:

$$2\alpha\sqrt{(\cos(n_6\theta)-1)^2+\sin^2(n_6\theta)}\sin(n_6\theta/2)) \gg 1. \qquad (4.60)$$

Assuming θ is small we use Eqns. 2.33 and 2.34 to approximate $\cos(n_6\theta) \approx$

$1 - n_6^2\theta^2/2$ and $\sin(n_6\theta) \approx n_6\theta - n_6^3\theta^3/6$, giving

$$\begin{aligned} \alpha\sqrt{(1 - n_6^2\theta^2/2 - 1)^2 + n_6^2\theta^2 n_6\theta} \gg 1 \\ \alpha\theta^2 \gg \frac{1}{n_6^2}. \end{aligned} \tag{4.61}$$

The is the same scaling as the parity gate from [49]. The free parameter n_6 can be chosen to decrease the probability of error. The larger n_6 is, the further the distance between the peaks $f(x,0)$ and $f(x,\alpha\sqrt{(\cos(n_6\theta)-1)^2 + \sin^2(n_6\theta)}\sin(n_6\theta/2)))$ becomes.

Photon Number Detection

If we displace the probe beam in Eqn. 4.58 such that $|0\rangle$ and $|-2i\alpha\sin(n_6\theta)\rangle$ are equidistant from the x axis, we can apply a photon number detection to the probe beam to pick out the red terms. The necessary displacement is $D(\beta) = D(i\alpha\sin(n_6\theta))$. As with the homodyne detection case, we need to consider the five probe beam states:

$$\begin{aligned} |0\rangle &\rightarrow |i\alpha\sin(n_6\theta)\rangle \\ |-2i\alpha\sin(n_6\theta)\rangle &\rightarrow |-i\alpha\sin(n_6\theta)\rangle \\ |\alpha(e^{in_6\theta}-1)\rangle &\rightarrow |\alpha\big(\cos(n_6\theta) - 1 + 2i\sin(n_6\theta)\big)\rangle \\ |\alpha(e^{-in_6\theta}-1)\rangle &\rightarrow |\alpha(\cos(n_6\theta)-1)\rangle \\ |\alpha(1-e^{in_6\theta})\rangle &\rightarrow |\alpha(1-\cos(n_6\theta))\rangle. \end{aligned} \tag{4.62}$$

In order to use photon number detection of the probe beam to pick out the red terms in Eqn. 4.58, we require the number of photons in the states $|\alpha\big(\cos(n_6\theta) - 1 + 2i\sin(n_6\theta)\big)\rangle$, $|\alpha(\cos(n_6\theta)-1)\rangle$ and $|\alpha(1-\cos(n_6\theta))\rangle$ to be different to the number of photons in the states $|\pm i\alpha\sin(n_6\theta)\rangle$. Assuming θ is small we use Eqns. 2.33 and 2.34 to find:

$$\begin{aligned} \alpha^2\sin^2(n_6\theta) &\approx \alpha^2\big(n_6^2\theta^2 - n_6^4\theta^4/3\big) \\ \alpha^2\big((\cos(n_2\theta)-1)^2 + 4\sin^2(n_6\theta)\big) &\approx \alpha^2\big(4n_6^2\theta^2 - 13n_6^4\theta^4/12\big) \\ \alpha^2\big(\cos(n_6\theta)-1\big)^2 &\approx \alpha^2 n_6^4\theta^4/4 \\ \alpha^2\big(1-\cos(n_6\theta)\big)^2 &\approx \alpha^2 n_6^4\theta^4/4. \end{aligned} \tag{4.63}$$

If we assume $\theta^4 \approx 0$, we require a photon number detection of the probe beam that can distinguish between 0, $\alpha^2 n_6^2\theta^2$ and $4\alpha^2 n_6^2\theta^2$ photons. Since we expect a photon number detector to easily distinguish between 0 and n photons, for $n > 1$, we require the difference in the photon numbers $\alpha^2 n_6^2\theta^2$ and $4\alpha^2 n_6^2\theta^2$ to be large:

$$\begin{aligned} 3\alpha^2 n_6^2\theta^2 &\gg 1 \\ \alpha\theta &\gg \frac{1}{\sqrt{3}n_6}. \end{aligned} \tag{4.64}$$

The is the same scaling as the parity gate from [92, 93]. The free parameter n_6 can be chosen to decrease the probability of error. The larger n_6 is, the greater the difference between the photon numbers $\alpha^2 n_6^2 \theta^2$ and $4\alpha^2 n_6^2 \theta^2$ becomes.

Phase Correction

After we measure the probe probe beam in Fig. 4.9 we have effectively induced the transformation of Eqn. 4.27 into the red terms in Eqn. 4.58. If we homodyne detect we will have the phase $e^{i\phi_1(x)}$ on the state $c_7|110\rangle$ that we will need to correct for. There is no phase shift associated with displacing the probe beam by $D(i\alpha\sin(n_6\theta))$ before we apply a photon number detection to the probe beam, since $\mathrm{Im}\left[(i\alpha\sin(n_6\theta))\,(2i\alpha\sin(n_6\theta))\right] = 0$. Regardless of which measurement process we apply to the probe beam, we need to first deal with the phase shifts associated with the displacements $\alpha\left(A_1 + iB_1\right), \alpha\left(A_2 + iB_2\right), \alpha\left(A_3 + iB_3\right)$ and $\alpha\left(A_4 + iB_4\right)$.

After we measure the probe beam in Fig. 4.9, the output state is given by (after the application of IIZ):

$$\begin{aligned} e^{i\varphi_1}(c_0|000\rangle + c_1|001\rangle) + e^{i\varphi_2}(c_2|010\rangle + c_4|011\rangle) + e^{i\varphi_3}(c_3|100\rangle + c_5|101\rangle) \\ - e^{i\varphi_4}c_6|111\rangle + e^{i\varphi_5}c_7|110\rangle. \end{aligned} \tag{4.65}$$

We can correct for $\varphi_1, \varphi_2, \varphi_3$ without knowing their form by applying the phase shifters

$$\begin{aligned} |1\rangle_1 &\rightarrow e^{i(\varphi_1-\varphi_3)}|1\rangle_1 \\ |1\rangle_2 &\rightarrow e^{i(\varphi_1-\varphi_2)}|1\rangle_2 \end{aligned} \tag{4.66}$$

$$\tag{4.67}$$

on qubits 1 and 2. Eqn. 4.65 becomes

$$\begin{aligned} c_0|000\rangle + c_1|001\rangle + c_2|010\rangle + c_4|011\rangle + c_3|100\rangle + c_5|101\rangle \\ - e^{i(\varphi_4+\varphi_1-\varphi_2-\varphi_3)}c_6|111\rangle + e^{i(\varphi_5+\varphi_1-\varphi_2-\varphi_3)}c_7|110\rangle. \end{aligned} \tag{4.68}$$

To correct for the phase shifts on the c_6 and c_7 term we need to find the form of φ_4 and φ_5. Using Eqn. 2.26 we can find the form of φ_j from Eqn. 4.46.

$$\varphi_j = f_1\left(\chi_j\theta\right)\cos(n_j\theta) + f_2\left(\chi_j\theta\right)\sin(n_j\theta) + f_3\left(\chi_j\theta\right) \tag{4.69}$$

where

$$
\begin{aligned}
f_1(\chi_j\theta) &= \alpha^2 \left(B_1 + B_2\cos(\chi_j\theta) + B_3\cos(2\chi_j\theta) + B_4\cos(3\chi_j\theta) - A_2\sin(\chi_j\theta)\right.\\
&\qquad\qquad \left.-A_3\sin(2\chi_j\theta) - A_4\sin(3\chi_j\theta)\right)\\
f_2(\chi_j\theta) &= -\alpha^2 \left(A_1 + A_2\cos(\chi_j\theta) + A_3\cos(2\chi_j\theta) + A_4\cos(3\chi_j\theta) + B_2\sin(\chi_j\theta)\right.\\
&\qquad\qquad \left.+B_3\sin(2\chi_j\theta) + B_4\sin(3\chi_j\theta)\right) \qquad (4.70)\\
f_3(\chi_j\theta) &= \alpha^2 \left((-B_1A_2 + A_1B_2 - B_2A_3 + A_2B_3 - B_3A_4 + A_3B_4)\cos(\chi_j\theta)\right.\\
&\quad + (-B_1A_3 + A_1B_3 - B_2A_4 + A_2B_4)\cos(2\chi_j\theta) + (-B_1A_4 + A_1B_4)\cos(3\chi_j\theta)\\
&\quad - (A_2(A_1 + A_3) + B_2(B_1 + B_3) + A_3A_4 + B_3B_4)\sin(\chi_j\theta)\\
&\quad \left.-(A_1A_3 + B_1B_3 + A_2A_4 + B_2B_4)\sin(2\chi_j\theta) - (A_1A_4 + B_1B_4)\sin(3\chi_j\theta)\right).
\end{aligned}
$$

Notice that the functions $f_1()$, $f_2()$ and $f_3()$ are independent $n_j\theta$, the controlled rotations applied in Fig. 4.6. When we consider the form of φ_4 we know that $n_j = n_6 - 4(n_7 + n_8)$ and $\chi_j = n_7 + n_8$. When we consider the form of φ_5 we know that $n_j = -\left(n_6 + 4(n_7 + n_8)\right)$ and $\chi_j = n_7 + n_8$.

$$
\begin{aligned}
\varphi_4 &= f_1\left((n_7 + n_8)\theta\right)\cos((n_6 - 4(n_7 + n_8))\theta) \qquad (4.71)\\
&\quad + f_2\left((n_7 + n_8)\theta\right)\sin((n_6 - 4(n_7 + n_8))\theta) + f_3\left((n_7 + n_8)\theta\right)\\
\varphi_5 &= f_1\left((n_7 + n_8)\theta\right)\cos(-(n_6 + 4(n_7 + n_8))\theta)\\
&\quad + f_2\left((n_7 + n_8)\theta\right)\sin(-(n_6 + 4(n_7 + n_8))\theta) + f_3\left((n_7 + n_8)\theta\right).
\end{aligned}
$$

We can therefore write φ_4 and φ_5 as:

$$
\begin{aligned}
\varphi_4 &= f_4 + f_5 \qquad (4.72)\\
\varphi_5 &= f_4 - f_5
\end{aligned}
$$

where

$$
\begin{aligned}
f_4 &= f_1\left((n_7 + n_8)\theta\right)\cos(-4(n_7 + n_8)\theta)\cos(n_6\theta) + f_2\left((n_7 + n_8)\theta\right)\sin(-4(n_7 + n_8)\theta)\cos(n_6\theta)\\
&\qquad + f_3\left((n_7 + n_8)\theta\right)\\
f_5 &= f_2\left((n_7 + n_8)\theta\right)\cos(-4(n_7 + n_8)\theta)\sin(n_6\theta) - f_1\left((n_7 + n_8)\theta\right)\sin(-4(n_7 + n_8)\theta)\sin(n_6\theta).
\end{aligned}
$$

Eqn. 4.68 becomes

$$
\begin{aligned}
&c_0|000\rangle + c_1|001\rangle + c_2|010\rangle + c_4|011\rangle + c_3|100\rangle + c_5|101\rangle\\
&\qquad - e^{i(f_4+f_5+\varphi_1-\varphi_2-\varphi_3)}c_6|111\rangle + e^{i(f_4-f_5+\varphi_1-\varphi_2-\varphi_3)}c_7|110\rangle. \qquad (4.73)
\end{aligned}
$$

If we replace CR_6H in Fig. 4.9 with Fig. 4.10, we can correct for the f_5 phase term in Eqn. 4.73. That is, if we use Fig. 4.10 instead of Fig. 4.6, the initial state in Eqn. 4.45 becomes

$$\frac{1}{\sqrt{2}}\Big(c_0\big(|000\rangle|\alpha\rangle + e^{-i\phi}|001\rangle|\alpha e^{in_6\theta}\rangle\big) + c_1\big(e^{i\phi}|000\rangle|\alpha e^{-in_6\theta}\rangle - |001\rangle|\alpha\rangle\big) \tag{4.74}$$
$$+ c_2\big(|010\rangle|\alpha e^{ia\theta}\rangle + e^{-i\phi}|011\rangle|\alpha e^{i(a+n_6)\theta}\rangle\big) + c_3\big(|100\rangle|\alpha e^{ib\theta}\rangle + e^{-i\phi}|101\rangle|\alpha e^{i(b+n_6)\theta}\rangle\big)$$
$$+ c_4\big(e^{i\phi}|010\rangle|\alpha e^{i(a-n_6)\theta}\rangle - |011\rangle|\alpha e^{ia\theta}\rangle\big) + c_5\big(e^{i\phi}|100\rangle|\alpha e^{i(b-n_6)\theta}\rangle - |101\rangle|\alpha e^{ib\theta}\rangle\big)$$
$$+ c_6\big(|110\rangle|\alpha e^{i(a+b)\theta}\rangle + e^{-i\phi}|111\rangle|\alpha e^{i(a+b+n_6)\theta}\rangle\big) + c_7\big(e^{i\phi}|110\rangle|\alpha e^{i(a+b-n_6)\theta}\rangle - |111\rangle|\alpha e^{i(a+b)\theta}\rangle\big)\Big)$$

and the final state before probe beam detection in Eqn. 4.58 becomes

$$\frac{1}{\sqrt{2}}\Big(c_0\big(|000\rangle|0\rangle + e^{-i\phi}|001\rangle|\alpha(e^{in_6\theta} - 1)\rangle\big) + c_1\big(e^{i\phi}|000\rangle|\alpha(e^{-in_6\theta} - 1)\rangle - |001\rangle|0\rangle\big)$$
$$+ c_2\big(|010\rangle|0\rangle + e^{-i\phi}|011\rangle|\alpha(e^{in6\theta} - 1)\rangle\big) + c_3\big(|100\rangle|0\rangle + e^{-i\phi}|101\rangle|\alpha(e^{in_6\theta} - 1)\rangle\big)$$
$$+ c_4\big(e^{i\phi}|010\rangle|\alpha(e^{-in_6\theta} - 1)\rangle - |011\rangle|0\rangle\big) + c_5\big(e^{i\phi}|100\rangle|\alpha(e^{-in_6\theta} - 1)\rangle - |101\rangle|0\rangle\big) \tag{4.75}$$
$$+ c_6\big(|110\rangle|\alpha(1 - e^{in_6\theta})\rangle + e^{-i\phi}|111\rangle|0\rangle\big) + c_7\big(e^{i\phi}|110\rangle|-2i\alpha\sin(n_6\theta)\rangle - |111\rangle|\alpha(1 - e^{in_6\theta})\rangle\big)\Big).$$

After we detect the probe beam, we now have

$$e^{i\varphi_1}(c_0|000\rangle + c_1|001\rangle) + e^{i\varphi_2}(c_2|010\rangle + c_4|011\rangle) + e^{i\varphi_3}(c_3|100\rangle + c_5|101\rangle)$$
$$- e^{i(\varphi_4-\phi)}c_6|111\rangle + e^{i(\varphi_5+\phi)}c_7|110\rangle. \tag{4.76}$$

Once we correct for the phases φ_1, φ_2 and φ_3, we have

$$c_0|000\rangle + c_1|001\rangle + c_2|010\rangle + c_4|011\rangle + c_3|100\rangle + c_5|101\rangle$$
$$+ e^{i\tilde{\phi}}\left(-c_6|111\rangle + c_7|110\rangle\right). \tag{4.77}$$

where we have set ϕ in Fig. 4.10 to f_5 and $\tilde{\phi} = f_4 + \varphi_1 - \varphi_2 - \varphi_3$.

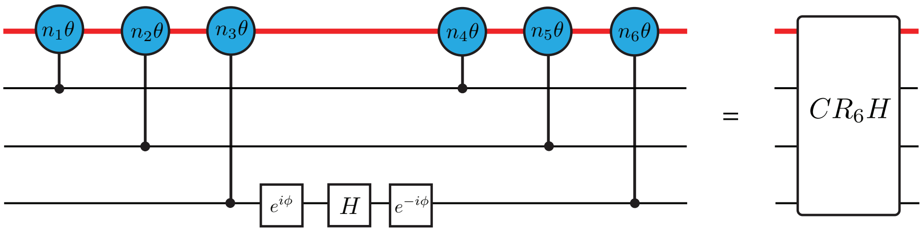

Figure 4.10: Probe beam preparation for our three qubit gate similar to Fig. 4.6 but with the phase shifters $\pm\phi$. When $\phi = f_5$ this can be used for phase correction.

If we consider transforming Eqn. 4.27 to Eqn. 4.77, we see that we have a controlled-controlled-(iY) gate as well as a controlled phase gate (with phase $\tilde{\phi}$) on qubits 1 and 2. While at first, this phase ($\tilde{\phi}$) appears to be a hinderance that needs to be corrected with a controlled phase gate on qubits 1 and 2, we can in fact use it to convert this three qubit gate into a Toffoli gate.

If we expand $\tilde{\phi}$ using Eqns. 2.33 and 2.34 we find

$$\tilde{\phi} \approx \frac{n_6}{n_7 n_8 \left(n_7 + n_8\right)} \frac{\alpha^2}{\theta}. \tag{4.78}$$

Since we require either $\alpha\theta^2 \gg \frac{1}{n_6^2}$ or $\alpha\theta \gg \frac{1}{\sqrt{3}n_6}$, we know that the quantity in Eqn. 4.78 is $\gg 1$. Given that we will know what α and θ are before we attempt the three qubit gate, we can set n_6, n_7 and n_8 such that

$$\frac{n_6}{n_7 n_8 \left(n_7 + n_8\right)} \frac{\alpha^2}{\theta} = p\frac{\pi}{2} \tag{4.79}$$

where p is a positive integer not equal to 0. Eqn. 4.77 would then becomes

$$\begin{aligned} c_0|000\rangle + c_1|001\rangle + c_2|010\rangle + c_4|011\rangle + c_3|100\rangle + c_5|101\rangle \\ - ic_6|111\rangle + ic_7|110\rangle \end{aligned} \tag{4.80}$$

which is locally equivalent to the Toffoli gate.

We now need to consider the phase shifts resulting from the probe beam measurement. When we homodyne detect the probe beam, Eqn. 4.80 becomes

$$\begin{aligned} c_0|000\rangle + c_1|001\rangle + c_2|010\rangle + c_4|011\rangle + c_3|100\rangle + c_5|101\rangle \\ - ic_6|111\rangle + ie^{i\phi_1(x)}c_7|110\rangle. \end{aligned} \tag{4.81}$$

Unfortunately, we cannot correct for this phase with just single qubit phase shifters. To transform Eqn. 4.81 into Eqn. 4.80 we would require a controlled phase gate. However, even without this controlled phase shift correction gate, a three qubit gate that transforms Eqn. 4.27 into 4.81 is as powerful in terms of entangling power, as a Toffoli gate.

When we perform a photon number detection on the probe beam, Eqn. 4.80 becomes

$$\begin{aligned} c_0|000\rangle + c_1|001\rangle + c_2|010\rangle + c_4|011\rangle + c_3|100\rangle + c_5|101\rangle \\ - ic_6|111\rangle + ic_7|110\rangle \end{aligned} \tag{4.82}$$

or

$$\begin{aligned} c_0|000\rangle + c_1|001\rangle + c_2|010\rangle + c_4|011\rangle + c_3|100\rangle + c_5|101\rangle \\ - ic_6|111\rangle - ic_7|110\rangle \end{aligned} \tag{4.83}$$

depending on whether we measured an even number of photons (Eqn. 4.82) or an odd number (Eqn. 4.83). The gate we induce is therefore the Toffoli gate 1/4 of the time and the controlled-controlled-(iY) gate 1/4 of the tim, where the controlled-controlled-(iY) gate is as powerful in terms of entangling power, as a Toffoli gate.

If we just concentrate on the Toffoli gate, we find that our successful probability of 25% is an improvement on the two leading LOQC Toffoli scheme [106, 107].

The coincidence basis Toffoli gate proposed in [106] succeeds with a probability of 0.75/%. However, this gate is destructive, as with the CNOT gates in Sections 2.7.2 and 2.7.3, since we need to measure the output qubits to detect the presence of a single photon. The Toffoli gate proposed in [107] succeeds with a probability of 1/64.

4.2.5 Displacements with 3 Controlled Rotations

In the last Section we showed that we could pick out the red terms in Eqn. 4.33 using either homodyne detection, provided $\alpha\theta^2 \gg 1/n_6^2$, or photon number detection, provided $\alpha\theta \gg \frac{1}{\sqrt{3}n_6}$. After we prepared the probe beam state using Fig. 4.6, we used displacements and additional controlled rotations conditioned on just the first two qubits to transform the probe beam states for the red terms in Eqn. 4.33 to just two, distinct states. If we instead use displacements and additional controlled rotations conditioned on all three qubits, we can transform the probe beam states for the red terms in Eqn. 4.33 to just one state. In this Section we investigate whether increasing the number of displacements improves the scaling in Eqn. 4.61 and 4.64.

Since we wish to transform each red term probe beam in Eqn. 4.33 to the state $\alpha\,(R_1 + R_2)$, we need to consider eight displacements, as shown in Fig. 4.11. We use Fig. 4.6 to prepare the probe beam state as in Eqn. 4.45, where $n_2 + n_5 = a$ and $n_1 + n_4 = b$.

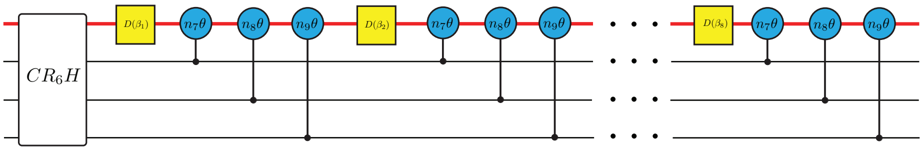

Figure 4.11: Picks out the red terms in Eqn. 4.33. Here $\beta_k = \alpha(A_k + iB_k)$, where $k = 1, 2, \cdots, 8$ and $A_k, B_k \in \mathbb{R}$.

Without loss of generality we set $R_1 = R_2 = 0$. The 8 (complex) equations we need to solve are

$$\begin{aligned}\alpha e^{i\chi_j\theta}\big(e^{i\chi_j\theta}\big(e^{i\chi_j\theta}\big(e^{i\chi_j\theta}\big(e^{i\chi_j\theta}\big(e^{i\chi_j\theta}\big(e^{i\chi_j\theta}\big(e^{i\chi_j\theta}\big(e^{in_j\theta} &+ A_1 + iB_1\big) + A_2 + iB_2\big)\\ &+ A_3 + iB_3\big) + A_4 + iB_4\big)\\ &+ A_5 + iA_5\big) + A_6 + iA_6\big)\\ &+ A_7 + iA_7\big) + A_8 + iA_8\big) = 0\end{aligned} \tag{4.84}$$

where $n_j \in \{0, a, b, a+b+n_6, a+b-n_6\}$ and $\chi_j \in \{0, n_7, n_8, n_9, n_7+n_8, n_7+n_9, n_8+n_9, n_7+n_8+n_9\}$. Breaking Eqn. 4.84 into real and imaginary parts gives the 16 equations:

$$
\begin{aligned}
A_8\cos(\chi_j\theta) &+ A_7\cos(2\chi_j\theta) + A_6\cos(3\chi_j\theta) + A_5\cos(4\chi_j\theta) + A_4\cos(5\chi_j\theta) \\
&+ A_3\cos(6\chi_j\theta) + A_2\cos(7\chi_j\theta) + A_1\cos(8\chi_j\theta) \qquad (4.85) \\
&- B_8\sin(\chi_j\theta) - B_7\sin(2\chi_j\theta) - B_6\sin(3\chi_j\theta) - B_5\sin(4\chi_j\theta) - B_4\sin(5\chi_j\theta) \\
&- B_3\sin(6\chi_j\theta) - B_2\sin(7\chi_j\theta) - B_1\sin(8\chi_j\theta) = -\cos\big((n_j + 8\chi_j)\theta\big) \\
A_8\sin(\chi_j\theta) &+ A_7\sin(2\chi_j\theta) + A_6\sin(3\chi_j\theta) + A_5\sin(4\chi_j\theta) + A_4\sin(5\chi_j\theta) \\
&+ A_3\sin(6\chi_j\theta) + A_2\sin(7\chi_j\theta) + A_1\sin(8\chi_j\theta) \qquad (4.86) \\
&+ B_8\cos(\chi_j\theta) + B_7\cos(2\chi_j\theta) + B_6\cos(3\chi_j\theta) + B_5\cos(4\chi_j\theta) + B_4\cos(5\chi_j\theta) \\
&+ B_3\cos(6\chi_j\theta) + B_2\cos(7\chi_j\theta) + B_1\cos(8\chi_j\theta) = -\sin\big((n_j + 8\chi_j)\theta\big).
\end{aligned}
$$

To solve for the 8 displacements requires the inversion of a non-sparse 16×16 matrix. We investigate the solution to Eqns. 4.85 and 4.86 numerically. When we homodyne detect the probe beam the scaling is of the form $\alpha\theta^2 \gg 1$, as in Eqn. 4.61 and when perform a photon number measurement on the probe beam the scaling is of the form $\alpha\theta \gg 1$, as in Eqn. 4.64.

When we use Fig. 4.11 to pick out the red terms from Eqn. 4.33 it is not clear that the phases associated with the displacements $\alpha(A_k + iB_k)$, where $k = 1, 2, \cdots, 8$, can be corrected with only single qubit phase shifters.

4.2.6 Multi-qubit Gate

We can generalise the idea of picking out the red terms from Eqn. 4.29 to picking out the red terms from a state with m qubits. Since it is not clear how to correct the phases associated with the displacments in Section 4.2.5, we base our m qubit gate on Section 4.2.4.

For example, consider the 4 qubit case. We can prepare the state

$$
\begin{aligned}
&\Big(c_0|0000\rangle + c_1|0001\rangle + c_2|0010\rangle + c_3|0100\rangle + c_4|1000\rangle + c_5|0011\rangle + c_6|0101\rangle + c_7|1001\rangle \\
&+ c_8|0110\rangle + c_9|1010\rangle + c_{10}|1100\rangle + c_{11}|0111\rangle + c_{12}|1011\rangle + c_{13}|1101\rangle + c_{14}|1110\rangle \\
&+ c_{15}|1111\rangle\Big)|\alpha\rangle \qquad (4.87)
\end{aligned}
$$

in an analogous way to Fig. 4.10, shown in Fig. 4.12. Here $\sum_{i=0}^{15} |c_i|^2 = 1$.

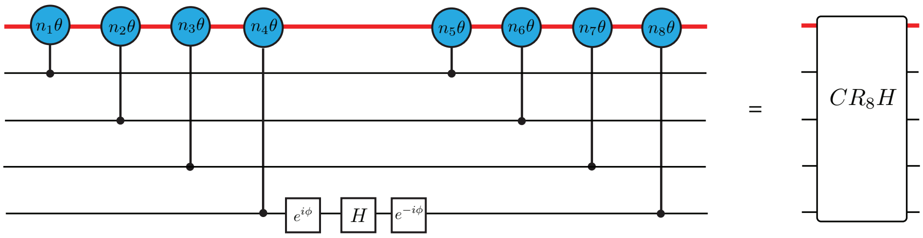

Figure 4.12: Probe beam preparation for a 4 qubit gate.

Fig. 4.12 takes Eqn. 4.87 to

$$\begin{aligned}
&\frac{1}{\sqrt{2}}\Big(c_0\big(|0000\rangle|\alpha\rangle + |0001\rangle|\alpha e^{in_8\theta}\rangle\big) + c_1\big(|0000\rangle|\alpha e^{-in_8\theta}\rangle - |0001\rangle|\alpha\rangle\big)\\
&+ c_2\big(|0010\rangle|\alpha e^{ic\theta}\rangle + |0011\rangle|\alpha e^{i(c+n_8)\theta}\rangle\big) \qquad (4.88)\\
&+ c_3\big(|0100\rangle|\alpha e^{ib\theta}\rangle + |0101\rangle|\alpha e^{i(b+n_8)\theta}\rangle\big)\\
&+ c_4\big(|1000\rangle|\alpha e^{ia\theta}\rangle + |1001\rangle|\alpha e^{i(a+n_8)\theta}\rangle\big)\\
&+ c_5\big(|0010\rangle|\alpha e^{i(c-n_8)\theta}\rangle - |0011\rangle|\alpha e^{ic\theta}\rangle\big)\\
&+ c_6\big(|0100\rangle|\alpha e^{i(b-n_8)\theta}\rangle - |0101\rangle|\alpha e^{ib\theta}\rangle\big)\\
&+ c_7\big(|1000\rangle|\alpha e^{i(a-n_8)\theta}\rangle - |1001\rangle|\alpha e^{ia\theta}\rangle\big)\\
&+ c_8\big(|0110\rangle|\alpha e^{i(b+c)\theta}\rangle + |0111\rangle|\alpha e^{i(b+c+n_8)\theta}\rangle\big)\\
&+ c_9\big(|1010\rangle|\alpha e^{i(a+c)\theta}\rangle + |1011\rangle|\alpha e^{i(a+c+n_8)\theta}\rangle\big)\\
&+ c_{10}\big(|1100\rangle|\alpha e^{i(a+b)\theta}\rangle + |1101\rangle|\alpha e^{i(a+b+n_8)\theta}\rangle\big)\\
&+ c_{11}\big(|0110\rangle|\alpha e^{i(b+c-n_8)\theta}\rangle - |0111\rangle|\alpha e^{i(b+c)\theta}\rangle\big)\\
&+ c_{12}\big(|1010\rangle|\alpha e^{i(a+c-n_8)\theta}\rangle - |1011\rangle|\alpha e^{i(a+c)\theta}\rangle\big)\\
&+ c_{13}\big(|1100\rangle|\alpha e^{i(a+b-n_8)\theta}\rangle - |1101\rangle|\alpha e^{i(a+b)\theta}\rangle\big)\\
&+ c_{14}\big(|1110\rangle|\alpha e^{i((a+b+c)\theta}\rangle + |1111\rangle|\alpha e^{i(a+b+c+n_8)\theta}\rangle\big)\\
&+ c_{15}\big(|1110\rangle|\alpha e^{i(a+b+c-n_8)\theta}\rangle - |1111\rangle|\alpha e^{i(a+b+c)\theta}\rangle\big)\Big)
\end{aligned}$$

where we have set $n_1 + n_5 = a$, $n_2 + n_6 = b$ and $n_3 + n_7 = c$. We see that this is analogous to Eqn. 4.45. That is, we see that each of the red terms with the first three qubits equal to $|xyz\rangle$, where $x, y, x \in \{0,1\}$, has the same probe beam, with the exception of the $c_{14}|111\rangle$ and $c_{15}|1110\rangle$ terms. Once we add displacements and additional controlled rotations conditioned on the first three qubits, we can take each of the probe beam states for the red terms $c_0, \cdots, c_{14}$ to $\alpha\,(R_1 + iR_2)$ and the red term $c_{15}|1110\rangle$ probe beam to another point, distinct from the probe beam states for each of the green terms. We would require 8 displacements to pick out the red terms in Eqn 4.88. As in Section 4.2.4, when perform a photon number detection on the probe beam, the phases associated with the displacements can be set such that the four qubit gate we induce is a controlled-controlled-controlled-X gate a $1/4$ of the time and controlled-controlled-controlled-iY $1/4$ of the time.

To apply an m qubit gate we would need to prepare the probe beam with $2m$ controlled rotations, as shown in Fig. 4.13. To pick out the red terms from the resulting state, we would require 2^{m-1} displacements and $(m-1)2^{m-1}$ additional controlled rotations, as shown in Fig. 4.14. This would require solving 2^m simultaneous equations. If we perform a photon number detection on the coherent probe beam we can always correct the phases associated with the displacements, as in Section 4.2.4.

The m qubit gate proposed in Fig. 4.14 succeeds as an m-qubit Toffoli with a probability of 25% and as an m-qubit controlled iY with a probability of 25%. Since this success probability is constant it is an improvement on [106], which succeeds with a probability of $\left(\frac{1}{1+2^{\frac{1}{m}}}\right)^{2m}$, and [107], which succeeds with a probability of $\frac{1}{(p_1)^{2n-3}}$, where p_1 is the success probability of a probabilistic CNOT gate. However, the resources required for both [106] and [107] scale linearly, whereas the resources for the Toffoli gate in Fig. 4.14 scale exponentially with the number of qubits.

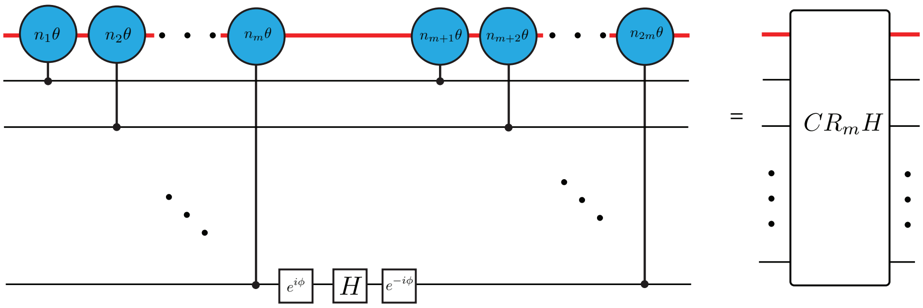

Figure 4.13: Probe beam preparation for an m qubit gate.

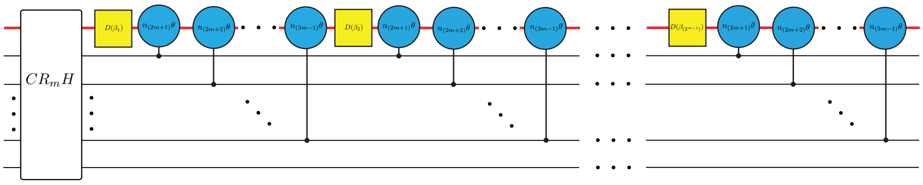

Figure 4.14: Picks out the red terms for an m qubit state. Here $\beta_k = \alpha(A_k + iB_k)$, where $k = 1, 2, \cdots, 2^{m-1}$ and $A_k, B_k \in \mathbb{R}$.

Chapter 5

Qubus Computation: Single Bit Teleportations

In Chapter 4 we described extensions to the qubus computation scheme that were centred around applying displacements to a single coherent quantum bus mode. In this Chapter we build on the ideas from Section 2.8.6 by considering multiple probe modes, concentrating on the use of teleportations in qubus computation.

As discussed in Section 2.5.4, we can teleport [80] an unknown qubit with two classical bits and a maximally entangled Bell state shared between the sender and receiver. Teleportation was used extensively in Section 2.5.4 when a two qubit gate using only linear optics with single photon sources and photon detection was described, teleporting the qubits through the gate [32]. Teleportations have also been shown to be useful for fault tolerance. In [108], Zhou *et al.* extended the significance of teleportation by showing how so called *single bit teleportations* could be used to construct fault tolerant encoded operations. In this Chapter we investigate the use of single bit teleportations for qubus computation.

In Section 5.1 we extend the results presented in Section 4.1 by showing a fault tolerant method of measuring the syndromes for any stabilizer code. We use single bit teleportations to transfer between two different forms of quantum logic, allowing for a linear saving in resources compared to a general CNOT construction. This scheme exploits the fact that entanglement is easy to create with coherent cat states, such as $|\alpha\rangle + |\alpha e^{i\theta}\rangle$, and single qubit operations are easily performed on polarisation logic.

The relative ease with which we can transfer between different forms of quantum logic prompts the next point addressed in this chapter: whether we can perform a universal set of gates on qubus by using single qubit teleportation gates. In Section 5.3 we show that a coherent state computation scheme using single qubit teleportation gates is the most efficient to date.

A question that naturally arises when looking at single bit teleportations for qubus computation is whether large entangled states, such as cluster states [44, 46, 47], could be produced efficiently. In Section 5.4 we show how we can efficiently construct large cluster states using single bit teleportations. In both Section 5.3 and 5.4 we analyse a non-ideal choice of system parameters and propose a method to boost the gate performance under such a choice of parameters.

5.1 Fault Tolerant Stabilizer Measurement with Controlled Rotations

In Section 4.1 we described a scheme to measure the syndromes of any stabilizer code by measuring the parity of n qubits. This scheme involved only one coherent probe beam coupled to our encoded state via controlled rotations. While only using one probe beam has practical advantages, it does not allow for a fault tolerant measurement of stabilizer syndromes. Since this coherent probe beam is coupled to more than one of the physical qubits, there is the possibility that a single error on the probe beam could cause a number of errors on the physical qubits that is greater than the number of errors the code can correct. For example, the probe beam may suffer a photon loss error [109] during one of the controlled rotations. This single error could then propagate to many phase errors on the physical qubits.

To find a fault tolerant method to measure the syndromes for any stabilizer code using qubus computation we use the scheme first proposed by Shor [21], shown in Fig. 5.1. This scheme incorporates Greenberger-Horne-Zeilinger (GHZ) ancilla states $\left(|0\rangle^{\otimes n} + |1\rangle^{\otimes n}\right)/\sqrt{2}$ with CNOT and Hadamard gates to fault tolerantly measure the generators of any stabilizer group. A single error on any one of the ancilla modes leads to at most one error on our encoded state. Fig. 5.1 shows the measurement of the Pauli operator $ZZZZ$, which as mentioned in Section 4.1.1, is equivalent to measuring the parity of the four qubits.

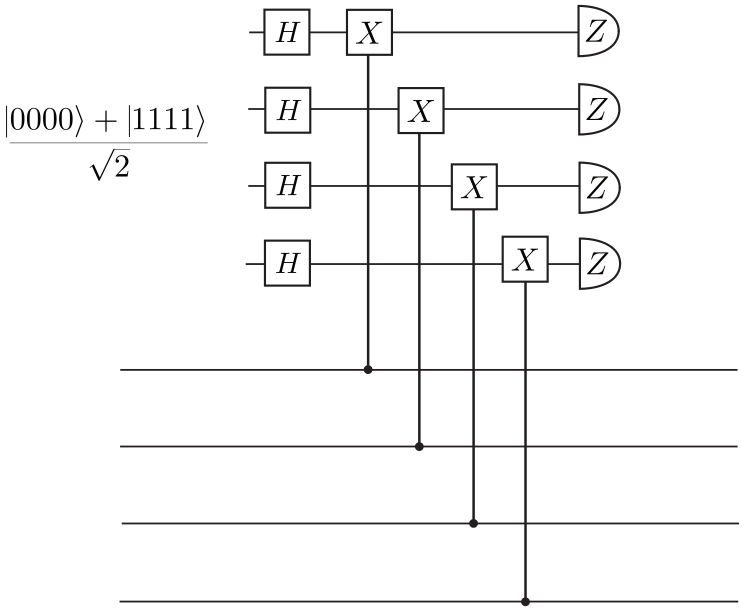

Figure 5.1: Measures the parity of four qubits [21].

To measure the stabilizer group generators of a QEC code with controlled rotations fault tolerantly, we modify the fault tolerant circuit proposed by Shor [21] by replacing the ancilla GHZ state with a coherent cat state $\left(|\alpha\rangle^{\otimes n} + |\alpha e^{i\theta}\rangle^{\otimes n}\right)/\sqrt{2}$. Since the ancilla modes are now coherent probe beams, we also need to modify the Hadamard and CNOT gates as well as the Z basis qubit measurements.

In Fig. 5.2 we show Fig. 5.1 modified to measure the parity of four qubits with controlled rotations fault tolerantly. We have replaced the CNOT gates with controlled rotations. It is worth noting that the substitution of a CNOT gate with a single controlled rotation is only valid here since the probe beam is measured immediately after the controlled rotation. We have replaced the Hadamard gates with gates that induce a Hadamard transformation on $|\alpha\rangle, |\alpha e^{i\theta}\rangle$ logic. That is:

$$\begin{aligned} \widetilde{H}|\alpha\rangle &= \frac{1}{\sqrt{2}}\left(|\alpha\rangle + |\alpha e^{i\theta}\rangle\right) \\ \widetilde{H}|\alpha e^{i\theta}\rangle &= \frac{1}{\sqrt{2}}\left(|\alpha\rangle - |\alpha e^{i\theta}\rangle\right). \end{aligned} \tag{5.1}$$

To measure the parity of the 4 qubits in Fig. 5.2 we need to distinguish between $|\alpha\rangle$ and $|\alpha e^{\pm i\theta}\rangle$, labelled as a $\widetilde{Z}$. We can use homodyne detection on the probe beam, in which case we would require $\alpha\theta^2 \gg 1$, or we can displace by $D(-\alpha)$ and perform a photon number detection on the probe beam, in which case we would require $\alpha\theta \gg 1$. In either case, we can only distinguish between $|\alpha\rangle$ and $|\alpha e^{\pm i\theta}\rangle$, $|\alpha e^{\pm i\theta}\rangle$ are indistinguishable. This type of measurement is essential to

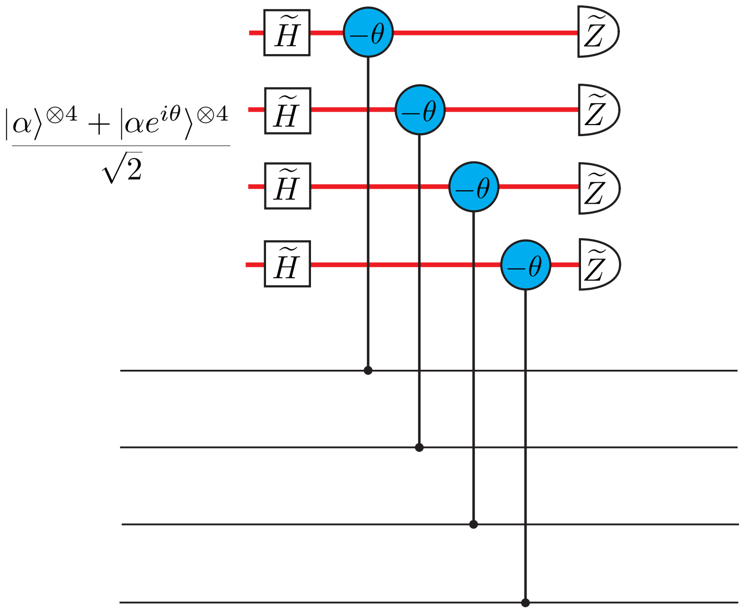

Figure 5.2: A modified version on Fig. 5.1 to measure the parity of four qubits with controlled rotations fault tolerantly.

detect the parity.

As in Section 4.1, when measuring the $ZZZZ$ syndrome for the [[7, 1, 3]] stabilizer code [105], an even parity measurement indicates no error and an odd parity measurement indicates the presence of a single X error. We have two cases to consider:

$$c_0|0000\rangle + c_1|1100\rangle + c_2|0011\rangle + c_3|1001\rangle + c_4|0110\rangle + c_5|1010\rangle + c_6|0101\rangle + c_7|1111\rangle \tag{5.2}$$

$$d_0|1000\rangle + d_1|0100\rangle + d_2|0010\rangle + d_3|0001\rangle + d_4|0111\rangle + d_5|1011\rangle + d_6|1101\rangle + d_7|1110\rangle \tag{5.3}$$

where $c_0, \cdots, c_{15}$ and $d_0, \cdots, d_{15}$ are arbitrary. After the application of the $\widetilde{H}$ operations in Fig. 5.2, the probe beams become

$$\frac{1}{\sqrt{2}}\big(|\alpha,\alpha,\alpha,\alpha\rangle + |\alpha,\alpha,\alpha e^{i\theta},\alpha e^{i\theta}\rangle + |\alpha e^{i\theta},\alpha e^{i\theta},\alpha,\alpha\rangle + |\alpha e^{i\theta},\alpha,\alpha,\alpha e^{i\theta}\rangle \\ + |\alpha,\alpha e^{i\theta},\alpha e^{i\theta},\alpha\rangle + |\alpha e^{i\theta},\alpha,\alpha e^{i\theta},\alpha\rangle + |\alpha,\alpha e^{i\theta},\alpha,\alpha e^{i\theta}\rangle + |\alpha e^{i\theta},\alpha e^{i\theta},\alpha e^{i\theta},\alpha e^{i\theta}\rangle\big). \tag{5.4}$$

Each of the even states in Eqn. 5.2 leaves the probe beam in Eqn. 5.4 unaltered as far as the Z measurement is concerned. However, there will be phase shifts associated with measuring the probe beams via homodyne or photon number detection. We can identify these phase shifts by considering each of the states in Eqn. 5.2 separately, as shown in Table 5.1, where the probe beam after the controlled rotations is of the form:

$$
\begin{aligned}
&\frac{1}{\sqrt{2}}\big(|\alpha,\alpha,\alpha,\alpha\rangle + |\alpha,\alpha,\alpha e^{g_1 i\theta},\alpha e^{g_2 i\theta}\rangle + |\alpha e^{g_3 i\theta},\alpha e^{g_4 i\theta},\alpha,\alpha\rangle + |\alpha e^{g_5 i\theta},\alpha,\alpha,\alpha e^{g_6 i\theta}\rangle \\
&\quad + |\alpha,\alpha e^{g_7 i\theta},\alpha e^{g_8 i\theta},\alpha\rangle + |\alpha e^{g_9 i\theta},\alpha,\alpha e^{g_{10} i\theta},\alpha\rangle + |\alpha,\alpha e^{g_{11} i\theta},\alpha,\alpha e^{g_{12} i\theta}\rangle \\
&\quad + |\alpha e^{g_{13} i\theta},\alpha e^{g_{14} i\theta},\alpha e^{g_{15} i\theta},\alpha e^{g_{16} i\theta}\rangle\big). \qquad (5.5)
\end{aligned}
$$

	g_1	g_2	g_3	g_4	g_5	g_6	g_7	g_8	g_9	g_{10}	g_{11}	g_{12}	g_{13}	g_{14}	g_{15}	g_{16}
c_0	+	+	+	+	+	+	+	+	+	+	+	+	+	+	+	+
c_1	+	+	-	-	-	+	-	+	-	+	-	+	-	-	+	+
c_2	-	-	+	+	+	-	+	-	+	-	+	-	+	+	-	-
c_3	+	-	-	+	-	-	+	+	-	+	+	-	-	+	+	-
c_4	-	+	+	-	+	+	-	-	+	-	-	+	+	-	-	+
c_5	-	+	-	+	-	+	+	-	-	-	+	+	-	+	-	+
c_6	+	-	+	-	+	-	-	+	+	+	-	-	+	-	+	-
c_7	-	-	-	-	-	-	-	-	-	-	-	-	-	-	-	-

Table 5.1: Shows the effect each of the even states in Eqn. 5.2, represented by the coefficients $c_0, \cdots, c_7$, has on the ancilla probe beams after the controlled rotations in Fig 5.2. The coefficients $g_1, \cdots, g_{16}$ refer to the sign on the induced coherent state phase in Eqn. 5.5.

As is evident from Eqn. 5.5, there will be 8 possible measurement outcomes when there is no error on our code block in Fig. 5.2. When we homodyne detect along the x-direction an outcome with $x > x_0$ indicates $|\alpha\rangle$ and an outcome with $x < x_0$ indicates $|\alpha e^{\pm i\theta}\rangle$, where $x_0 = \alpha\,(1 + \cos(\theta))$. The 8 possible measurements with the associated phases for homodyne detection are given by

$$
\begin{aligned}
|\alpha,\alpha,\alpha,\alpha\rangle: \quad & c_0|0000\rangle + c_1|1100\rangle + c_2|0011\rangle + c_3|1001\rangle + c_4|0110\rangle + c_5|1010\rangle \\
& + c_6|0101\rangle + c_7|1111\rangle \qquad (5.6) \\
|\alpha,\alpha,\alpha e^{\pm i\theta},\alpha e^{\pm i\theta}\rangle: \quad & e^{2i\phi(x)}\left(c_0|0000\rangle + c_1|1100\rangle\right) + e^{-2i\phi(x)}\left(c_2|0011\rangle + c_7|1111\rangle\right) \\
& + c_3|1001\rangle + c_4|0110\rangle + c_5|1010\rangle + c_6|0101\rangle \\
|\alpha e^{\pm i\theta},\alpha e^{\pm i\theta},\alpha,\alpha\rangle: \quad & e^{2i\phi(x)}\left(c_0|0000\rangle + c_2|0011\rangle\right) + e^{-2i\phi(x)}\left(c_1|1100\rangle + c_7|1111\rangle\right) \\
& + c_3|1001\rangle + c_4|0110\rangle + c_5|1010\rangle + c_6|0101\rangle \\
|\alpha e^{\pm i\theta},\alpha,\alpha,\alpha e^{\pm i\theta}\rangle: \quad & e^{2i\phi(x)}\left(c_0|0000\rangle + c_4|0110\rangle\right) + e^{-2i\phi(x)}\left(c_3|1001\rangle + c_7|1111\rangle\right) \\
& + c_1|1100\rangle + c_2|0011\rangle + c_5|1010\rangle + c_6|0101\rangle \\
|\alpha,\alpha e^{\pm i\theta},\alpha e^{\pm i\theta},\alpha\rangle: \quad & e^{2i\phi(x)}\left(c_0|0000\rangle + c_3|1001\rangle\right) + e^{-2i\phi(x)}\left(c_4|0110\rangle + c_7|1111\rangle\right) \\
& + c_1|1100\rangle + c_2|0011\rangle + c_5|1010\rangle + c_6|0101\rangle \\
|\alpha e^{\pm i\theta},\alpha,\alpha e^{\pm i\theta},\alpha\rangle: \quad & e^{2i\phi(x)}\left(c_0|0000\rangle + c_6|0101\rangle\right) + e^{-2i\phi(x)}\left(c_5|1010\rangle + c_7|1111\rangle\right) \\
& + c_1|1100\rangle + c_2|0011\rangle + c_3|1001\rangle + c_4|0110\rangle \\
|\alpha,\alpha e^{\pm i\theta},\alpha,\alpha e^{\pm i\theta}\rangle: \quad & e^{2i\phi(x)}\left(c_0|0000\rangle + c_5|1010\rangle\right) + e^{-2i\phi(x)}\left(c_6|0101\rangle + c_7|1111\rangle\right) \\
& + c_1|1100\rangle + c_2|0011\rangle + c_3|1001\rangle + c_4|0110\rangle \\
|\alpha e^{\pm i\theta},\alpha e^{\pm i\theta},\alpha e^{\pm i\theta},\alpha e^{\pm i\theta}\rangle: \quad & e^{4i\phi(x)}c_0|0000\rangle + c_1|1100\rangle + c_2|0011\rangle + c_3|1001\rangle + c_4|0110\rangle \\
& + c_5|1010\rangle + c_6|0101\rangle + e^{-4i\phi(x)}c_7|1111\rangle
\end{aligned}
$$

where $\phi(x) = \alpha\sin(\theta)\big(x - 2\alpha\cos(\theta)\big)$.

Each of the odd states in Eqn. 5.3 leaves the probe beam in Eqn. 5.4 in the form:

$$
\begin{aligned}
&\frac{1}{\sqrt{2}}\big(|\alpha e^{h_1 i\theta},\alpha,\alpha,\alpha\rangle + |\alpha,\alpha e^{h_2 i\theta},\alpha,\alpha\rangle + |\alpha,\alpha,\alpha e^{h_3 i\theta},\alpha\rangle + |\alpha,\alpha,\alpha,\alpha e^{h_4 i\theta}\rangle \\
&\quad + |\alpha,\alpha e^{h_5 i\theta},\alpha e^{h_6 i\theta},\alpha e^{h_7 i\theta}\rangle + |\alpha e^{h_8 i\theta},\alpha,\alpha e^{h_9 i\theta},\alpha e^{h_{10} i\theta}\rangle + |\alpha e^{h_{11} i\theta},\alpha e^{h_{12} i\theta},\alpha,\alpha e^{h_{13} i\theta}\rangle \\
&\quad + |\alpha e^{h_{14} i\theta},\alpha e^{h_{15} i\theta},\alpha e^{h_{16} i\theta},\alpha\rangle\big), \qquad (5.7)
\end{aligned}
$$

which, as far as the Z measurement is concerned, is identical for each of the odd states. The phase shifts associated with measuring the probe beams via homodyne or photon number detection can be identified by considering each of the states in Eqn. 5.3 separately, as shown in Table 5.2.

When there is a single X error on our code block in Fig. 5.2, there will be 8 possible measurement outcomes, each of which can be obtained from Eqn. 5.7. The 8 possible measurements with the associated phases for homodyne detection are given by

	h_1	h_2	h_3	h_4	h_5	h_6	h_7	h_8	h_9	h_{10}	h_{11}	h_{12}	h_{13}	h_{14}	h_{15}	h_{16}
d_0	-	+	+	+	+	+	+	-	+	+	-	+	+	-	+	+
d_1	+	-	+	+	-	+	+	+	+	+	+	-	+	+	-	+
d_2	+	+	-	+	+	-	+	+	-	+	+	+	+	+	+	-
d_3	+	+	+	-	+	+	-	+	+	-	+	+	-	+	+	+
d_4	+	-	-	-	-	-	-	+	-	-	+	-	-	+	-	-
d_5	-	+	-	-	+	-	-	-	-	-	-	+	-	-	+	-
d_6	-	-	+	-	-	+	-	-	+	-	-	-	-	-	-	+
d_7	-	-	-	+	-	-	+	-	-	+	-	-	+	-	-	-

Table 5.2: Shows the effect each of the odd states in Eqn. 5.3, represented by the coefficients $d_0, \cdots, d_7$, has on the ancilla probe beams after the controlled rotations in Fig 5.2. The coefficients $h_1, \cdots, h_{16}$ refer to the sign on the induced coherent state phase in Eqn. 5.7.

$$\begin{aligned}
|\alpha e^{\pm i\theta}, \alpha, \alpha, \alpha\rangle : \quad & e^{-i\phi(x)}\left(d_0|1000\rangle + d_5|1011\rangle + d_6|1101\rangle + d_7|1110\rangle\right) \\
& + e^{i\phi(x)}\left(d_1|0100\rangle + d_2|0010\rangle + d_3|0001\rangle + d_4|0111\rangle\right) \\
|\alpha, \alpha e^{\pm i\theta}, \alpha, \alpha\rangle : \quad & e^{-i\phi(x)}\left(d_1|0100\rangle + d_4|0111\rangle + d_6|1101\rangle + d_7|1110\rangle\right) \\
& + e^{i\phi(x)}\left(d_0|1000\rangle + d_2|0010\rangle + d_3|0001\rangle + d_5|1011\rangle\right) \\
|\alpha, \alpha, \alpha e^{\pm i\theta}, \alpha\rangle : \quad & e^{-i\phi(x)}\left(d_2|0010\rangle + d_4|0111\rangle + d_5|1011\rangle + d_7|1110\rangle\right) \\
& + e^{i\phi(x)}\left(d_0|1000\rangle + d_1|0100\rangle + d_3|0001\rangle + d_6|1101\rangle\right) \\
|\alpha, \alpha, \alpha, \alpha e^{\pm i\theta}\rangle : \quad & e^{-i\phi(x)}\left(d_3|0001\rangle + d_4|0111\rangle + d_5|1011\rangle + d_7|1110\rangle\right) \\
& + e^{i\phi(x)}\left(d_0|1000\rangle + d_1|0100\rangle + d_2|0010\rangle + d_7|1110\rangle\right) \\
|\alpha e^{\pm i\theta}, \alpha, e^{\pm i\theta}\alpha e^{\pm i\theta}, \alpha\rangle : \quad & e^{-i\phi(x)}\left(d_4|0111\rangle + d_5|1011\rangle + d_6|1101\rangle\right) + e^{-3i\phi(x)}d_7|1110\rangle \\
& + e^{i\phi(x)}\left(d_0|1000\rangle + d_1|0100\rangle + d_2|0010\rangle\right) + e^{3i\phi(x)}d_3|0001\rangle \\
|\alpha e^{\pm i\theta}, \alpha e^{\pm i\theta}, \alpha, \alpha e^{\pm i\theta}\rangle : \quad & e^{-i\phi(x)}\left(d_4|0111\rangle + d_5|1011\rangle + d_7|1110\rangle\right) + e^{-3i\phi(x)}d_6|1101\rangle \\
& + e^{i\phi(x)}\left(d_0|1000\rangle + d_1|0100\rangle + d_3|0001\rangle\right) + e^{3i\phi(x)}d_2|0010\rangle \\
|\alpha e^{\pm i\theta}, \alpha, \alpha e^{\pm i\theta}, \alpha e^{\pm i\theta}\rangle : \quad & e^{-i\phi(x)}\left(d_4|0111\rangle + d_6|1101\rangle + d_7|1110\rangle\right) + e^{-3i\phi(x)}d_5|1011\rangle \\
& + e^{i\phi(x)}\left(d_0|1000\rangle + d_2|0010\rangle + d_3|0001\rangle\right) + e^{3i\phi(x)}d_1|0100\rangle \\
|\alpha, \alpha e^{\pm i\theta}, \alpha e^{\pm i\theta}, \alpha e^{\pm i\theta}\rangle : \quad & e^{-i\phi(x)}\left(d_5|1011\rangle + d_6|1101\rangle + d_7|1110\rangle\right) + e^{-3i\phi(x)}d_4|0111\rangle \\
& + e^{i\phi(x)}\left(d_1|0100\rangle + d_2|0010\rangle + d_3|0001\rangle\right) + e^{3i\phi(x)}d_0|1000\rangle .
\end{aligned} \tag{5.8}$$

The phases in Eqns. 5.6 and 5.8 can be corrected by applying the phase shifter $e^{2i\phi(x)}$ to each mode in the code block corresponding to a homodyne measurement with $x < x_0$.

When the coherent probe beam is displaced by $D(-\alpha)$ and a photon number detection is performed, there will be phases associated with measuring an odd number of photons, as described in Section 2.8.6. We can perform a similar analysis to Eqns. 5.6 and 5.8 to show that the -1 phase factor can be corrected by applying the phase shifter $e^{i\pi}$ to each mode in the code block corresponding to the detection of an odd number of photons.

We can extend the party measurement of 4 qubits in Fig. 5.2 to the parity measurement of n qubits by using the coherent probe beam $\left(|\alpha\rangle^{\otimes n} + |\alpha e^{i\theta}\rangle^{\otimes n}\right)/\sqrt{2}$ in conjunction with n $\widetilde{H}$ gates, n controlled rotations and n $\widetilde{Z}$ measurements. As we described in Section 4.1.1, this provides a method to measure the syndromes for any stabilizer code.

Before we can claim that the generalisation of Fig. 5.2 can measure the parity of n qubits we need to provide a method of preparing the ancilla state $\left(|\alpha\rangle^{\otimes n} + |\alpha e^{i\theta}\rangle^{\otimes n}\right)/\sqrt{2}$ and a method to induce the gate $\widetilde{H}$ on $|\alpha\rangle, |\alpha e^{i\theta}\rangle$ logic.

5.1.1 Ancilla State Preparation

Consider the circuit shown in Fig. 5.3

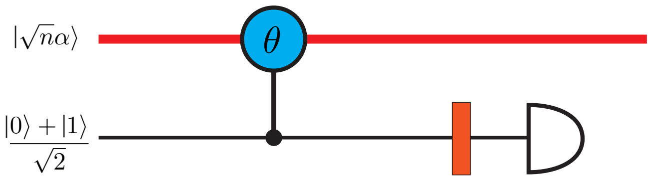

Figure 5.3: Circuit to construct $|\sqrt{n}\alpha\rangle \pm |e^{i\theta}\sqrt{n}\alpha\rangle$. The polariser transforms $|0\rangle \rightarrow (|0\rangle + |1\rangle/\sqrt{2}$ and $|1\rangle \rightarrow (-|0\rangle + |1\rangle/\sqrt{2}$.

After we detect the polarisation in the H/V basis we have the state $|\sqrt{n}\alpha\rangle \pm |e^{i\theta}\sqrt{n}\alpha\rangle$. If this state is incident on an n-port symmetric beam splitter, where the other $n-1$ input ports are the vacuum, the output is the cat state $\left(|\alpha\rangle^{\otimes n} \pm |\alpha e^{i\theta}\rangle^{\otimes n}\right)/\sqrt{2}$ [110, 111].

The -1 phase factor resulting from measuring $|0\rangle$ in Fig. 5.3 would ideally be corrected before we use the n port beam splitter. However, applying a Pauli Z gate on $|\alpha\rangle, |\alpha e^{i\theta}\rangle$ logic such that $\widetilde{Z}|\alpha\rangle = |\alpha\rangle$ and $\widetilde{Z}|\alpha e^{i\theta}\rangle = -|\alpha e^{i\theta}\rangle$, is difficult. We can avoid explicitly applying $\widetilde{Z}$ by keeping track of this necessary correction, which is called the Pauli frame [112, 113], compensating for it in subsequent measurements.

In order for the generalisation of the scheme presented Fig. 5.2 to be truly fault tolerant we need to verify that our cat state output from the n port beam splitter is error free using techniques outlined in [25], as discussed in [52].

5.1.2 Hadamard Gates on $|\alpha\rangle, |\alpha e^{i\theta}\rangle$ Logic

We can construct the $\widetilde{H}$ gate defined in Eqn. 5.1 by using single bit teleportations [108]. In Fig. 5.4 we show two teleportation schemes using controlled rotations.

In Fig. 5.4(a) we teleport from polarisation logic to $|\alpha\rangle, |\alpha e^{i\theta}\rangle$ logic. Directly before the X basis measurement on the polarisation qubit we have

$$|+\rangle \left(c_0|\alpha\rangle + c_1|\alpha e^{i\theta}\rangle\right) + |-\rangle \left(c_0|\alpha\rangle - c_1|\alpha e^{i\theta}\rangle\right). \tag{5.9}$$

If we measure $|-\rangle$ we need to perform a $\widetilde{Z}$ correction, as with the ancilla cat state preparation.

In Fig. 5.4(b) we teleport from $|\alpha\rangle, |\alpha e^{i\theta}\rangle$ logic into polarisation. Directly before the $\widetilde{Z}$ measurement on the probe beam we have

$$\frac{1}{\sqrt{2}} \left(c_0|0\rangle + c_1|1\rangle\right) |\alpha\rangle + \frac{1}{\sqrt{2}} \left(c_0|1\rangle|\alpha e^{-i\theta}\rangle + c_1|0\rangle|\alpha e^{i\theta}\rangle\right). \tag{5.10}$$

After we measure the probe beam we need to perform an X correction when we either homodyne detect $x < x_0$ or measure a number of photons greater than 0. This X correction is easily performed on polarisation logic.

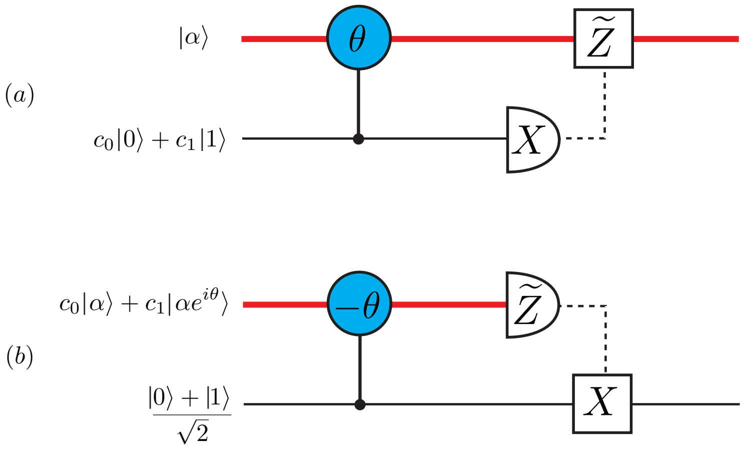

Figure 5.4: One bit teleportations [108] using controlled rotations. **(a)** Teleports from polarisation logic to $|\alpha\rangle, |\alpha e^{i\theta}\rangle$ logic. **(b)** Teleports from $|\alpha\rangle, |\alpha e^{i\theta}\rangle$ logic to polarisation.

To perform the $\widetilde{H}$ gates in Fig. 5.2 we first teleport each probe beam into polarisation logic using Fig 5.4(b). We perform the Hadamard gate on the polarisation qubits and then teleport back to the $|\alpha\rangle, |\alpha e^{i\theta}\rangle$ logic using Fig 5.4(a). We do not need to perform the $\widetilde{Z}$ corrections since we use the Pauli frame.

5.1.3 Resource Comparison

The resources required to measure a weight n Pauli operator are $3n+1$ controlled rotations, $n+1$ ancillary photons, $2n$ $\widetilde{Z}$ measurements and $n+1$ photon number measurements.

If we were to directly implement Shor's circuit in Fig. 5.1 with the qubus CNOT gate described in Section 2.8.4 [49], we would require $4(2n-1)$ controlled rotations, $2(2n-1)$ $\widetilde{Z}$ measurements, $2n-1$ ancillary photons and $2n-1$ photon number measurements to measure a weight n Pauli operator. This is due to the fact that each qubus CNOT requires 4 controlled rotations, 1 single photon ancilla, 1 single photon measurement and 2 $\widetilde{Z}$ measurements. And we require $n-1$ CNOT gates to construct the GHZ state in addition to the n required for the parity measurement.

By using coherent cat states in the place of the GHZ states in Shor's fault tolerant scheme we find we require $5(n-1)$ fewer controlled rotations, $2(n-1)$ fewer $\widetilde{Z}$ measurements, $n-2$ fewer ancillary photons and $n-2$ photon number measurements. This is a linear saving in resources, which is significant for physical implementations.

5.2 Single bit teleportations

In this Section we analyse the performance of the single bit teleportations in Fig. 5.4 under non-ideal values of α and θ. We quantify the performance by calculating the process fidelity, described in Section 2.3. These results will be the basis for the fidelity calculations in Section 5.3 when we construct a universal set of gates on $|\alpha\rangle, |\alpha e^{i\theta}\rangle$ logic and in Section 5.4 when construct cluster states using single bit teleportations.

When we calculate the process fidelity for Fig. 5.4(a) we consider the first mode of the maximally entangled state $(|00\rangle + |11\rangle)/\sqrt{2}$ incident on the polarisation mode. This state becomes

$$|\psi_{\pm}\rangle = \frac{1}{\sqrt{2}}\left(|0,\alpha\rangle \pm |1,\alpha e^{i\theta}\rangle\right) \tag{5.11}$$

where the ± depends on the polarisation $x-$basis measurement outcome. Even when the values of α and θ are such that either $\alpha\theta^2 \not\gg 1$ or $\alpha\theta \not\gg 1$, the process fidelity is 1.

When we calculate the process fidelity for Fig. 5.4(b) we at first consider the first mode of the state $\left(|\alpha,\alpha\rangle + |\alpha e^{i\theta},\alpha e^{i\theta}\rangle\right)/\sqrt{2}$ incident on the probe beam mode. However, since

$$|\langle\alpha|\alpha e^{i\theta}\rangle|^2 = e^{-2|\alpha|^2(\cos(\theta)-1)} \approx e^{-|\alpha|^2\theta^2} \quad \text{for small} \quad \theta, \tag{5.12}$$

when $\alpha\theta \not\gg 1$, $\left(|\alpha,\alpha\rangle + |\alpha e^{i\theta},\alpha e^{i\theta}\rangle\right)/\sqrt{2}$ is not a maximally entangled state. For this reason we instead consider the first mode of the state

$$\left(|\alpha,0\rangle + |\alpha e^{i\theta},1\rangle\right)/\sqrt{2} \tag{5.13}$$

incident on the probe beam mode in Fig. 5.4(b). Eqn. 5.13 is also not a maximally entangled state, but it is as close as we can get when we assume

$|\langle\alpha|\alpha e^{i\theta}\rangle|^2 \not\approx 0$. Ideally, we would expect the output to be the maximally entangled state $(|00\rangle + |11\rangle)/\sqrt{2}$. When we do not place any restrictions on α and θ, the state output from Fig. 5.4(b) is the unnormalised state

$$|\psi_1\rangle = \frac{f(x,\alpha)}{2}\left(|00\rangle + |11\rangle\right) + \frac{f(x,\alpha\cos(\theta))}{2}\left(e^{i\phi(x)}|01\rangle + e^{-i\phi(x)}|10\rangle\right), \quad (5.14)$$

where $f(x,\beta)$ and $\phi(x)$ are as defined in Eqns. 2.51 and 2.52, respectively, and we assume $\widetilde{Z}$ is a homodyne measurement. When we measure $x > x_0 = \alpha\left(1+\cos(\theta)\right)$ no correction is necessary, when we measure $x < x_0$, we apply a phase shifter $e^{-i\phi(x)}$ to mode 1 followed by a polarisation bit flip. The normalised output, averaged over all x outcomes is given by

$$\rho_1 = \int_{x_0}^{\infty} |\psi_1\rangle\langle\psi_1|dx + \int_{-\infty}^{x_0}\left(U_1 \otimes \mathbb{1}\right)|\psi_1\rangle\langle\psi_1|\left(U_1^\dagger \otimes \mathbb{1}\right)dx \quad (5.15)$$

where U_1 corresponds to the single qubit corrections necessary when we measure $x < x_0$. In the case that $\alpha\theta^2 \gg 1$ this would simply be that state $(|00\rangle + |11\rangle)/\sqrt{2}$. Given that

$$\int_{x_0}^{\infty}\left(f(x,\alpha)\right)^2 dx = \int_{-\infty}^{x_0}\left(f(x,\alpha\cos(\theta))\right)^2 dx = \frac{1}{2}\text{Erfc}\left[-\frac{x_d}{2\sqrt{2}}\right]$$
$$\int_{x_0}^{\infty}\left(f(x,\alpha\cos(\theta))\right)^2 dx = \int_{-\infty}^{x_0}\left(f(x,\alpha)\right)^2 dx = \frac{1}{2}\text{Erfc}\left[\frac{x_d}{2\sqrt{2}}\right] \quad (5.16)$$

where $x_d = 2\alpha(1-\cos(\theta)) \approx \alpha\theta^2$ for small θ, the process fidelity is calculated to be

$$F_1(x_d) = \frac{1}{2}\left(1 + \text{Erf}\left[\frac{x_d}{2\sqrt{2}}\right]\right). \quad (5.17)$$

This process fidelity is shown in Fig. 5.5. When x_d approaches 0 the output from our single bit teleportation circuit in Fig. 5.4(b) is the maximally mixed state, indicated in Fig. 5.5 by the process fidelity of 1/2. As x_d increases, the distance between the peaks for the curves $f(x,\alpha)$ and $f(x,\alpha\cos(\theta))$ increases, leading to more efficient homodyne detection and a process fidelity that approaches 1.

5.2.1 Post-selected teleportation

To deal with the $x_d \not\gg 1$ case, we can post-select the homodyne measurement result to increase the process fidelity, at the expense of reducing the success probability. This involves ignoring homodyne measurement outcomes that are close to x_0. That is, we only allow homodyne measurement outcomes that are greater than $x_0 + y$ or less than $x_0 - y$. The normalised output from Fig. 5.4(b), given that the first mode of Eqn. 5.13 is incident on the probe beam mode, is given by

$$\rho_2 = \frac{\rho_2'}{\text{Tr}\left[\rho_2'\right]} \quad (5.18)$$

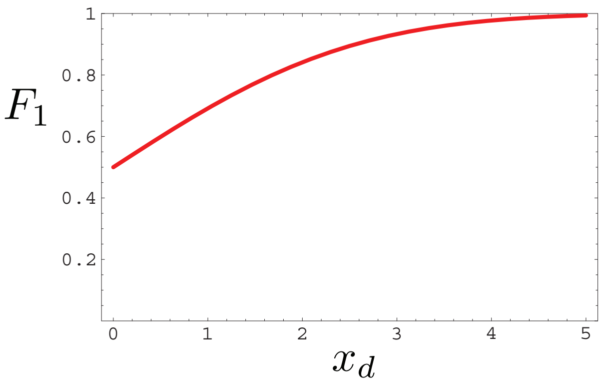

Figure 5.5: Process fidelity $F_1(x_d)$ for the single bit teleportation in Fig. 5.4(b) as a function of x_d.

where

$$\rho_2' = \int_{x_0+y}^{\infty} |\psi_1\rangle\langle\psi_1| dx + \int_{-\infty}^{x_0-y} \Big(U_1 \otimes 1\!\!1\Big) |\psi_1\rangle\langle\psi_1| \Big(U_1^\dagger \otimes 1\!\!1\Big) dx. \tag{5.19}$$

Given that

$$\begin{aligned} \int_{x_0+y}^{\infty} \left(f(x,\alpha)\right)^2 dx = \int_{-\infty}^{x_0-y} \left(f(x,\alpha\cos(\theta))\right)^2 dx = \frac{1}{2}\text{Erfc}\left[\frac{2y-x_d}{2\sqrt{2}}\right] \\ \int_{x_0+y}^{\infty} \left(f(x,\alpha\cos(\theta))\right)^2 dx = \int_{-\infty}^{x_0-y} \left(f(x,\alpha)\right)^2 dx = \frac{1}{2}\text{Erfc}\left[\frac{2y+x_d}{2\sqrt{2}}\right], \end{aligned} \tag{5.20}$$

the probability of success and conditional process fidelity are calculated to be

$$\begin{aligned} P_2(x_d,y) &= \frac{1}{2}\left(\text{Erfc}\left[\frac{2y-x_d}{2\sqrt{2}}\right] + \text{Erfc}\left[\frac{2y+x_d}{2\sqrt{2}}\right]\right) \\ F_2(x_d,y) &= \frac{\text{Erfc}\left[\frac{2y-x_d}{2\sqrt{2}}\right]}{\text{Erfc}\left[\frac{2y-x_d}{2\sqrt{2}}\right] + \text{Erfc}\left[\frac{2y+x_d}{2\sqrt{2}}\right]}. \end{aligned} \tag{5.21}$$

In the case that $y = 0$, $P_2(x_d, 0) = 1$ and $F_2(x_d, 0) = F_1(x_d)$. In Fig. 5.6 we show a range contour lines for $F_2(x_d, y)$ and $P_2(x_d, y)$. For example, when $x_d = 2$ and $y = 0.4$, we have a process fidelity of 0.9 and success probability of 0.8.

We consider the limit of $y \to \infty$ for both $P_2(x_d, y)$ and $F_2(x_d, y)$:

$$\begin{aligned} \lim_{y\to\infty} P_2(x_d,y) &= 0 \\ \lim_{y\to\infty} F_2(x_d,y) &= \frac{1}{1+\frac{\text{Erfc}\left[\frac{2y+x_d}{2\sqrt{2}}\right]}{\text{Erfc}\left[\frac{2y-x}{2\sqrt{2}}\right]}} = 1 \end{aligned} \tag{5.22}$$

where

$$\lim_{y\to\infty} \text{Erfc}\,[y \pm x] = 0 \tag{5.23}$$
$$\lim_{y\to\infty} \frac{\text{Erfc}\,[y+x]}{\text{Erfc}\,[y-x]} = 0$$

for $x > 0$. This is as expected since when we ignore an increasing range of homodyne outcomes, no matter how low x_d has become, we will eventually start accepting homodyne results from the tails of the Gaussian curves $f(x, \alpha)$ and $f(x, \alpha\cos(\theta))$. In the limit of $y \to \infty$ we effectively ignore all measurement results, leading to a 0 success probability.

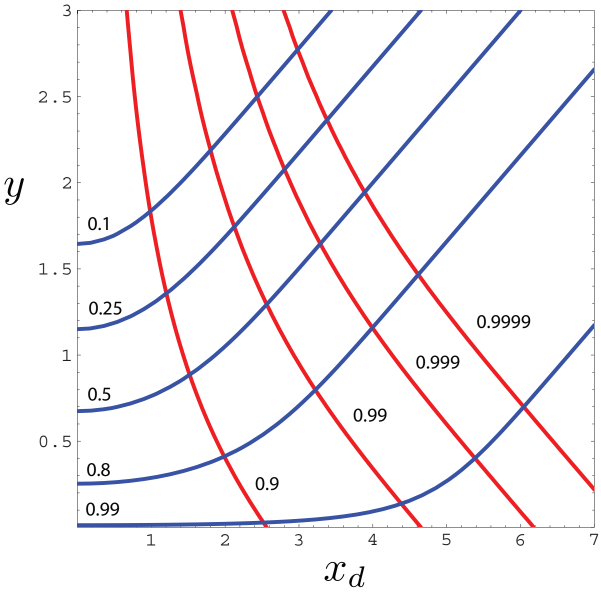

Figure 5.6: Contour lines for the process fidelity $F_2(x_d, y)$ (in red) and the success probability $P_2(x_d, y)$ (in blue) for the post-selected single bit teleportation in Fig. 5.4(b).

5.3 Universal Computation with Qubus Logic

In [114, 111, 110] a scheme to implement a universal set of gates on coherent state logic defined by $|0\rangle_L = |-\alpha'\rangle$ and $|1\rangle_L = |\alpha'\rangle$ was shown. This scheme used partial Bell state measurements and a resource of cat states. To perform a universal set of gates a total of 16 ancilla cat states are necessary. When $\alpha' \geq 2$, the qubits $|-\alpha'\rangle$ and $|\alpha'\rangle$ are approximately orthogonal since $|\langle\alpha'| - \alpha'\rangle|^2 = e^{-4\alpha'^2} \leq 10^{-6}$.

Using the single bit teleportations in Fig. 5.4 we can implement a universal set of gates on what we term *qubus logic*, defined by $|\mathbf{0}\rangle_L = |\alpha\rangle$ and $|\mathbf{1}\rangle_L = |\alpha e^{\pm i\theta}\rangle$, where as mentioned previously, the measurement $\widetilde{Z}$ cannot distinguish $|\alpha e^{i\theta}\rangle$ from $|\alpha e^{-i\theta}\rangle$. Qubits defined in this way are approximately orthogonal provided $\alpha\theta \gg 1$, since $|\langle\alpha|e^{i\theta}\alpha\rangle|^2 = e^{-2|\alpha|^2(\cos\theta-1)} \approx e^{-|\alpha|^2\theta^2}$, for small θ. If $\alpha\theta \geq 3.4$, then $|\langle\alpha|e^{i\theta}\alpha\rangle|^2 \leq 10^{-6}$. Qubus qubits are equivalent to coherent state qubits since a displacement and a phase shifter can convert between the two types of logic. That is, an arbitrary qubit $d_0|\alpha\rangle + d_1|\alpha e^{i\theta}\rangle$ can be displaced by $D(-\alpha\cos\left(\frac{\theta}{2}\right)e^{i\frac{\theta}{2}})$ to give

$$d_0|\alpha\big(1 - e^{i\frac{\theta}{2}}\cos(\theta/2)\big)\rangle + d_1 e^{\frac{i}{2}\alpha^2\sin(\theta)}|\alpha\big(e^{i\theta} - e^{i\frac{\theta}{2}}\cos(\theta/2)\big)\rangle. \tag{5.24}$$

We know from Section 2.1.5 that a phase shifter takes $|\alpha\rangle$ to $|e^{i\phi}\alpha\rangle$, so we can apply the phase shifter $e^{\frac{i}{2}(\pi-\theta)}$ to Eqn. 5.24 to get $d_0|\alpha\sin\left(\frac{\theta}{2}\right)\rangle + d_1 e^{\frac{i}{2}\alpha^2\sin(\theta)}|-\alpha\sin\left(\frac{\theta}{2}\right)\rangle$. To transform qubus encoding into coherent state encoding we require $\alpha' = \alpha\sin\left(\frac{\theta}{2}\right) \approx \alpha\theta/2$, for small θ. The $e^{\frac{i}{2}\alpha^2\sin(\theta)}$ phase factor can be taken care of once we use a single bit teleportation, as will be explained in the next Section. If $\alpha' \geq 2$ then we require $\alpha\theta \geq 4$, which is already satisfied by the orthogonality condition: $\alpha\theta \gg 1$.

We compare the qubus encoding scheme with the coherent state encoding scheme by counting the number of controlled rotations we require per gate. This is fair comparison since the cat state ancillas required in the coherent state scheme, $(|-\alpha'\rangle + |\alpha'\rangle)/\sqrt{2}$, can be constructed using Fig. 5.4(a) with $c_0 = c_1 = 1/\sqrt{2}$ and $\alpha' = \alpha\sqrt{(1-\cos(\theta))/2} \approx \alpha\theta/2$. We therefore consider the 16 ancilla cat states required in [111] for a universal set of gates to be equivalent to 16 controlled rotations.

As mentioned in Section 2.5.2, a universal set of gates comprises of all single qubit rotations and an entangling gate, such as the CSIGN gate. In the next Section we will describe a method to perform any single qubit gate on qubus qubits. In Section 5.3.2 we describe a method to perform a CSIGN on qubus qubits.

5.3.1 Single Qubit Gates

We can perform an arbitrary single qubit unitary U to the qubit $d_0|\alpha\rangle + d_1|\alpha e^{i\theta}\rangle$ by first teleporting the from qubus logic into polarisation, applying the unitary U to the polarisation qubit and then teleporting back to qubus logic, as shown in Fig. 5.7. When we perform the second single bit teleportation we will need to correct for a $\widetilde{Z}$ qubus logic error half of the time. This can be delayed until we teleport to polarisation logic for the next single qubit operation. If it happens that this single qubit rotation is the last step of an algorithm, we know that this $\widetilde{Z}$ error will not effect the outcome of a homodyne measurement, so in this case this correction can be ignored. To perform an arbitrary single qubit unitary we have only use two controlled rotations.

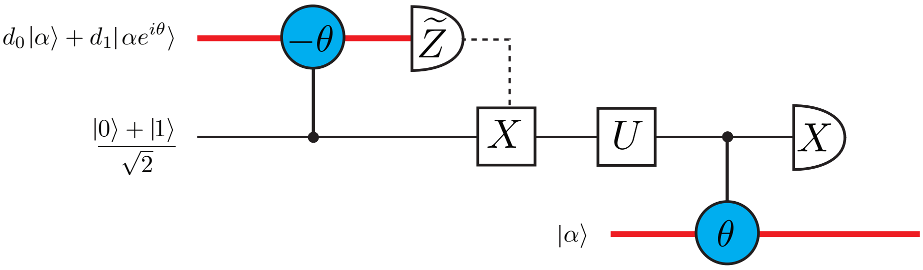

Figure 5.7: Applies an arbitrary single qubit unitary to the qubit $d_0|\alpha\rangle + d_1|\alpha e^{i\theta}\rangle$.

As in [111], to perform a bit flip we can simply apply the phase shifter $e^{-i\theta}$ to convert $d_0|\alpha\rangle + d_1|\alpha e^{i\theta}\rangle$ to $d_0|\alpha e^{-i\theta}\rangle + d_1|\alpha\rangle$.

In case that $x_d \not\gg 1$, only the first teleportation in Fig. 5.7 is affected, so we can quantify the gate performance as in Section 5.2, increasing the process fidelity via post-selection as in Section 5.2.1.

5.3.2 Two Qubit Gates

We can perform a CSIGN gate between the qubus qubits $d_0|\alpha\rangle + d_1|\alpha e^{i\theta}\rangle$ and $h_0|\alpha\rangle + h_1|\alpha e^{i\theta}\rangle$ by first teleporting them onto the entangled polarisation state $\frac{1}{2}(|00\rangle + |01\rangle + |10\rangle - |11\rangle) = (\mathbb{1} \otimes H)(|00\rangle + |11\rangle)/\sqrt{2}$ and then teleporting back into qubus logic. This is shown in Fig. 5.8. Directly before we measure the polarisation qubits in the $x-$basis we have

$$\begin{aligned}
&\frac{1}{2}|{+}{+}\rangle \left(c_0h_0|\alpha,\alpha\rangle + c_0h_1|\alpha,\alpha e^{i\theta}\rangle + c_1h_0|\alpha e^{i\theta},\alpha\rangle - c_1h_1|\alpha e^{i\theta},\alpha e^{i\theta}\rangle\right) \\
&+\frac{1}{2}|{+}{-}\rangle \left(c_0h_0|\alpha,\alpha\rangle - c_0h_1|\alpha,\alpha e^{i\theta}\rangle + c_1h_0|\alpha e^{i\theta},\alpha\rangle + c_1h_1|\alpha e^{i\theta},\alpha e^{i\theta}\rangle\right) \\
&+\frac{1}{2}|{-}{+}\rangle \left(c_0h_0|\alpha,\alpha\rangle + c_0h_1|\alpha,\alpha e^{i\theta}\rangle - c_1h_0|\alpha e^{i\theta},\alpha\rangle + c_1h_1|\alpha e^{i\theta},\alpha e^{i\theta}\rangle\right) \\
&+\frac{1}{2}|{-}{-}\rangle \left(c_0h_0|\alpha,\alpha\rangle - c_0h_1|\alpha,\alpha e^{i\theta}\rangle - c_1h_0|\alpha e^{i\theta},\alpha\rangle - c_1h_1|\alpha e^{i\theta},\alpha e^{i\theta}\rangle\right).
\end{aligned} \tag{5.25}$$

As in the single qubit unitary case, we may need to perform a $\widetilde{Z}$ corrections to the resulting qubus state depending on the polarisation measurement outcome, however this can be delayed until the next time we teleport into polarisation.

The entangled polarisation resource state $(|00\rangle + |11\rangle)/\sqrt{2}$ can be constructed by first constructing the state $\left(|\alpha,\alpha\rangle + |\alpha e^{i\theta},\alpha e^{i\theta}\rangle\right)/\sqrt{2}$, as in Section 5.1.1, then teleporting each mode using Fig. 5.4(b) into polarisation. This process requires three controlled rotations.

To apply a CSIGN gate to qubus qubits we have used a total seven controlled rotations.

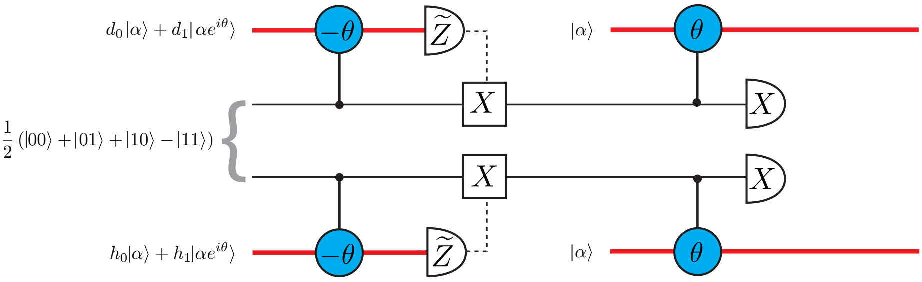

Figure 5.8: Applies a CSIGN gate between the qubits $d_0|\alpha\rangle + d_1|\alpha e^{i\theta}\rangle$ and $h_0|\alpha\rangle + h_1|\alpha e^{i\theta}\rangle$.

We quantify the effect the condition $x_d \ggg 1$ has on Fig. 5.8 by considering the first two modes of the state

$$\frac{1}{2}\left(|\alpha,\alpha\rangle|00\rangle + |\alpha,\alpha e^{i\theta}\rangle|01\rangle + |\alpha, e^{i\theta}\alpha\rangle|10\rangle + |\alpha e^{i\theta},\alpha e^{i\theta}\rangle|11\rangle\right) \tag{5.26}$$

incident on the left hand probe beam modes. Since the condition $x_d \ggg 1$ only affects the homodyne detections, we only need to consider teleporting the first two modes of Eqn. 5.26 onto the polarisation state $\frac{1}{2}(|00\rangle + |01\rangle + |10\rangle - |11\rangle)$. This is given by

$$\begin{aligned}
|\psi_3\rangle = \frac{1}{4}\Big\{ & f(x,\alpha)f(x',\alpha)\left(|00\rangle|00\rangle + |01\rangle|01\rangle + |10\rangle|10\rangle - |11\rangle|11\rangle\right) \qquad (5.27)\\
& + f(x,\alpha)f(x',\alpha\cos(\theta))\left(e^{-i\phi(x')}\left(|01\rangle|00\rangle - |11\rangle|10\rangle\right) + e^{i\phi(x')}\left(|00\rangle|01\rangle + |10\rangle|11\rangle\right)\right)\\
& + f(x,\alpha\cos(\theta))f(x',\alpha)\left(e^{-i\phi(x)}\left(|10\rangle|00\rangle - |11\rangle|01\rangle\right) + e^{i\phi(x)}\left(|00\rangle|10\rangle + |01\rangle|11\rangle\right)\right)\\
& + f(x,\alpha\cos(\theta))f(x',\alpha\cos(\theta))\Big(e^{i(\phi(x)+\phi(x'))}|00\rangle|11\rangle + e^{i(\phi(x)-\phi(x'))}|01\rangle|10\rangle\\
& \qquad + e^{i(\phi(x')-\phi(x))}|10\rangle|01\rangle - e^{-i(\phi(x)+\phi(x'))}|11\rangle|00\rangle\Big)\Big\}
\end{aligned}$$

where x and x' correspond to outcomes of the top and bottom homodyne detections in Fig. 5.8. Since there are two homodyne detections we need to consider the four cases: (i) $x > x_0$ and $x' > x_0$ with no correction; (ii) $x > x_0$ and $x' < x_0$ with the correction $U_2 = \mathbb{1} \otimes Z_{2\phi(x')}X$; (iii) $x < x_0$ and $x' > x_0$ with the correction $U_3 = Z_{2\phi(x)}X \otimes \mathbb{1}$; (iv) $x < x_0$ and $x' < x_0$ with the correction $U_4 = Z_{2\phi(x)}X \otimes Z_{2\phi(x')}X$. The normalised output is given by

$$\begin{aligned}\rho_3 = &\int_{x_0}^{\infty}\int_{x_0}^{\infty} |\psi_3\rangle\langle\psi_3| dx dx' + \int_{x_0}^{\infty}\int_{-\infty}^{x_0} (\mathbb{1}\otimes U_2)\, |\psi_3\rangle\langle\psi_3| \left(\mathbb{1}\otimes U_2^{\dagger}\right) dx dx' \\ &+ \int_{-\infty}^{x_0}\int_{x_0}^{\infty} (\mathbb{1}\otimes U_3)\, |\psi_3\rangle\langle\psi_3| \left(\mathbb{1}\otimes U_3^{\dagger}\right) dx dx' \\ &+ \int_{-\infty}^{x_0}\int_{-\infty}^{x_0} (\mathbb{1}\otimes U_4)\, |\psi_3\rangle\langle\psi_3| \left(\mathbb{1}\otimes U_4^{\dagger}\right) dx dx'.\end{aligned} \tag{5.28}$$

When $x_d \gg 1$ we expect Eqn. 5.26 to be transformed to

$$\frac{1}{2}\left(|00\rangle|00\rangle + |01\rangle|01\rangle + |10\rangle|10\rangle - |11\rangle|11\rangle\right). \tag{5.29}$$

Using Eqns. 5.28, 5.29 and 5.16 we calculate the process fidelity to be

$$F_3 = \frac{1}{4}\left(1 + \mathrm{Erf}\left[\frac{x_d}{2\sqrt{2}}\right]\right)^2. \tag{5.30}$$

This process fidelity is shown in Fig. 5.9. To improve this process fidelity we can

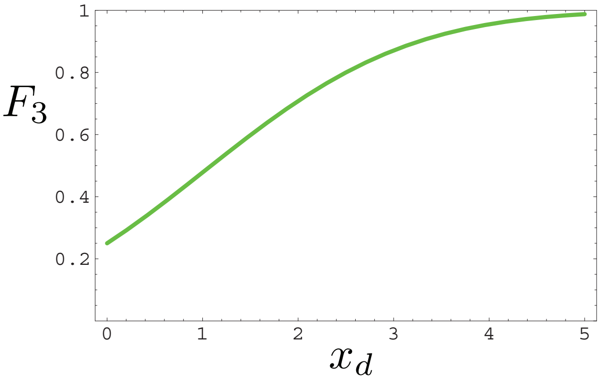

Figure 5.9: Process fidelity $F_3(x_d)$ for the CSIGN gate in Fig. 5.8 as a function of x_d.

post-select the homodyne detections, as in Section 5.2.1. When we only allow homodyne outcomes greater than $x_0 + y$ or less than $x_- - y$, the normalised output becomes

$$\rho_4 = \frac{\rho_4'}{\mathrm{Tr}\,[\rho_4']} \tag{5.31}$$

where

$$\begin{aligned}\rho_4' = &\int_{x_0+y}^{\infty}\int_{x_0+y}^{\infty} |\psi_3\rangle\langle\psi_3| dx dx' + \int_{x_0+y}^{\infty}\int_{-\infty}^{x_0-y} (\mathbb{1}\otimes U_2)\, |\psi_3\rangle\langle\psi_3| \left(\mathbb{1}\otimes U_2^{\dagger}\right) dx dx' \\ &+ \int_{-\infty}^{x_0-y}\int_{x_0+y}^{\infty} (\mathbb{1}\otimes U_3)\, |\psi_3\rangle\langle\psi_3| \left(\mathbb{1}\otimes U_3^{\dagger}\right) dx dx' \\ &+ \int_{-\infty}^{x_0-y}\int_{-\infty}^{x_0-y} (\mathbb{1}\otimes U_4)\, |\psi_3\rangle\langle\psi_3| \left(\mathbb{1}\otimes U_4^{\dagger}\right) dx dx'.\end{aligned} \tag{5.32}$$

Using Eqn. 5.20 we calculate the probability of success and conditional process fidelity to be

$$P_4(x_d, y) = \frac{1}{4}\left(\text{Erfc}\left[\frac{2y - x_d}{2\sqrt{2}}\right] + \text{Erfc}\left[\frac{2y + x_d}{2\sqrt{2}}\right]\right)^2 \tag{5.33}$$

$$F_4(x_d, y) = \left(\frac{\text{Erfc}\left[\frac{2y-x_d}{2\sqrt{2}}\right]}{\text{Erfc}\left[\frac{2y-x_d}{2\sqrt{2}}\right] + \text{Erfc}\left[\frac{2y+x_d}{2\sqrt{2}}\right]}\right)^2.$$

In Fig. 5.10 we show a range contour lines for $F_4(x_d, y)$ and $P_4(x_d, y)$. For example, when $x_d = 2.6$ and $y = 0.35$, we have a process fidelity of 0.9 and success probability of 0.8.

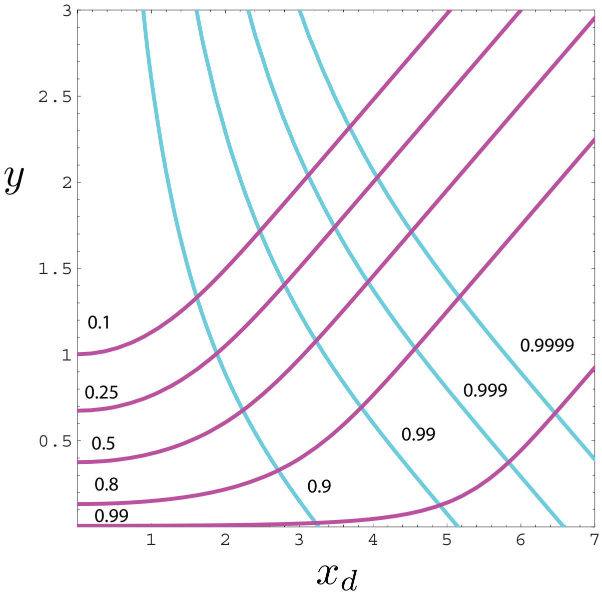

Figure 5.10: Contour lines for the process fidelity $F_4(x_d, y)$ (in cyan) and the success probability $P_4(x_d, y)$ (in magenta) for the post-selected CSIGN gate Fig. 5.8.

5.3.3 Comparison

To perform a CSIGN gate on qubus qubits we required seven controlled rotations, three for the entanglement production and four for the gate operation. To perform an arbitrary single qubit gate we required two controlled rotations. We therefore need nine controlled rotations to perform an entangling two qubit gate and an arbitrary single qubit rotation. This is in contrast to the sixteen ancilla cat states required for the coherent state model in [114, 111, 110], requiring eight for a CSIGN and eight for an arbitrary single qubit gate.

5.4 Cluster state generation

In this Section we describe a method to produce cluster states [44]. We begin by generalising the ancilla preparation state from Section 5.1.1 to prepare arbitrarily large polarisation GHZ states. Since GHZ states are locally equivalent to star cluster states [115, 116], we can join these GHZ states using the CNOT gates from [49, 92], or the probabilistic fusion gates from [47], to produce cluster states that would allow universal quantum computation.

At first glance we can simply produce GHZ states of arbitrary size using controlled rotations and only one coherent probe beam, as shown in Fig. 5.11. This is similar to the scheme by Jin *et al.* [117].

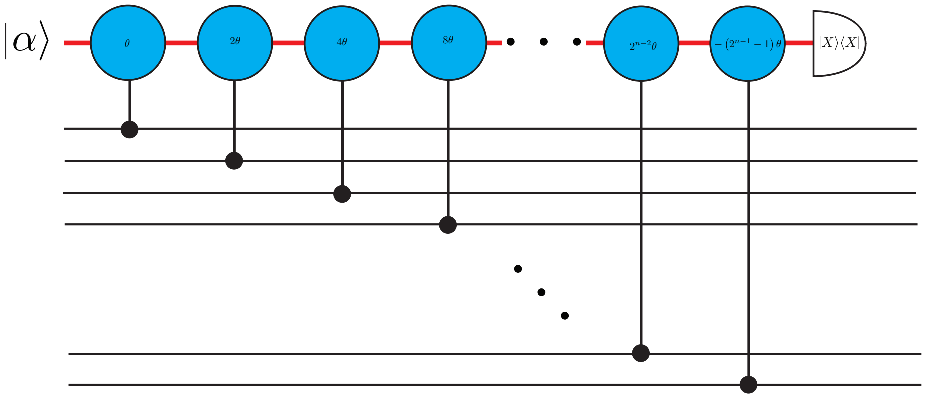

Figure 5.11: Produces an n qubit GHZ state.

If we have n copies of $(|0\rangle + |1\rangle)/\sqrt{2}$ incident on Fig. 5.11, we see that directly before we homodyne detect the probe beam, we have 2^{n-1} circles in phase space. Homodyne detection will give 2^{n-1} outcomes, each needing one or more bit flip corrections to produce the GHZ state $(|0\rangle^{\otimes n} + |1\rangle^{\otimes n})/\sqrt{2}$. The problem with this scheme is that it requires an exponential number of controlled rotations. As n increases, the size of the required controlled rotations also increases exponentially. For small n this is not an issue, however, if we consider

$\theta \approx 0.01$, once n reaches 10 we would require controlled rotations, such as $2^{n-3}\theta$, on the order of π.

5.4.1 GHZ state production

In Section 5.1.1 we described a scheme to produce the state $\left(|\alpha\rangle^{\otimes n} + |\alpha e^{i\theta}\rangle^{\otimes n}\right)/\sqrt{2}$ using a single controlled rotation, a single photon ancilla in the state $\left(|0\rangle + |1\rangle\right)/\sqrt{2}$ and the coherent state $|\sqrt{n}\alpha\rangle$. If we now teleport each of the n modes using Fig. 5.4(b), we obtain the state $\left(|0\rangle^{\otimes n} + |1\rangle^{\otimes n}\right)/\sqrt{2}$. We can think of this process as transforming the state $\left(|0\rangle + |1\rangle\right)/\sqrt{2} \to \left(|0\rangle^{\otimes n} + |1\rangle^{\otimes n}\right)/\sqrt{2}$. The resources we have used to produce this n qubit GHZ state are $n+1$ controlled rotations, $n+1$ single photon ancilla states, 1 photon detection and n homodyne detections.

We quantify the effect the condition $x_d \not\gg 1$ has on producing an n qubit GHZ state by using the first mode of the maximally entangled state $\left(|00\rangle + |11\rangle\right)/\sqrt{2}$ in conjunction with $|\sqrt{n}\alpha\rangle$ to produce the state $\left(|0\rangle^{\otimes(n+1)} + |1\rangle^{\otimes(n+1)}\right)/\sqrt{2}$. Given that the state output from the n single bit teleporters is a generalisation of Eqn. 5.27, we calculate the process fidelity to be

$$F_5(x_d) = \frac{1}{2^n}\left(1 + \text{Erf}\left[\frac{x_d}{2\sqrt{2}}\right]\right)^n. \tag{5.34}$$

In Fig. 5.12 we show the process fidelity for the construction of GHZ states of various sizes. Notice that as n increases, the process fidelity for a set x_d decreases. As the size of the GHZ state we wish to construct increases, the condition $x_d \not\gg 1$ takes a larger toll on the state production.

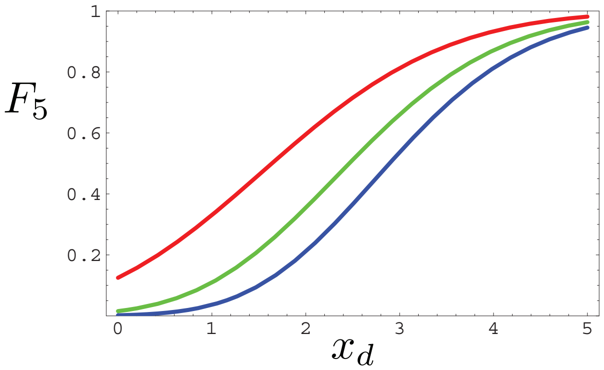

Figure 5.12: Process fidelity $F_5(x_d)$ for the construction of GHZ states. In red we show $F_5(x_d)$ for $n = 3$, in green we show $F_5(x_d)$ for $n = 6$ and in blue we show $F_5(x_d)$ for $n = 9$.

In a similar way to Eqn. 5.33, we can increase the process fidelity by post selecting the homodyne measurements. We calculate the probability of success and conditional process fidelity to be

$$P_6(x_d, y) = \frac{1}{2^n}\left(\text{Erfc}\left[\frac{2y - x_d}{2\sqrt{2}}\right] + \text{Erfc}\left[\frac{2y + x_d}{2\sqrt{2}}\right]\right)^n \tag{5.35}$$

$$F_6(x_d, y) = \left(\frac{\text{Erfc}\left[\frac{2y-x_d}{2\sqrt{2}}\right]}{\text{Erfc}\left[\frac{2y-x_d}{2\sqrt{2}}\right] + \text{Erfc}\left[\frac{2y+x_d}{2\sqrt{2}}\right]}\right)^n .$$

In Figs. 5.13 and 5.14 we show a range of contour lines for $F_6(x_d, y)$ and $P_6(x_d, y)$ for the $n = 3$ and $n = 9$ cases, respectively. Notice that as we increase n, the conditional process fidelity contours shift to the right, indicating the need for higher x_d values. As n increases, the success probability contours move to the bottom right, indicating a reduction in success probability. This is due to the fact that the negative effect post-selection has on the success probability increases with n.

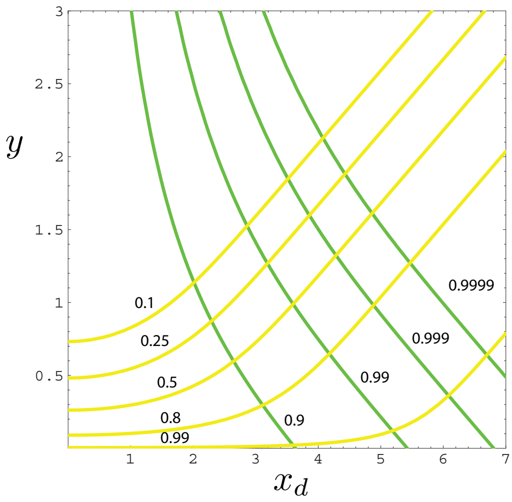

Figure 5.13: Contour lines for the process fidelity $F_6(x_d, y)$ (in green) and the success probability $P_6(x_d, y)$ (in yellow) for the post-selected construction of $\left(|0\rangle^{\otimes 3} + |1\rangle^{\otimes 3}\right)/\sqrt{2}$.

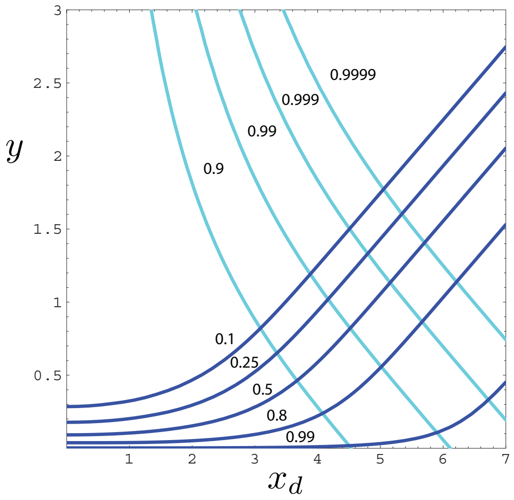

Figure 5.14: Contour lines for the process fidelity $F_6(x_d, y)$ (in cyan) and the success probability $P_6(x_d, y)$ (in blue) for the post-selected construction of $\left(|0\rangle^{\otimes 9} + |1\rangle^{\otimes 9}\right)/\sqrt{2}$.

The trend of the condition $x_d \ggg 1$ taking a larger toll on more complex operations is shown in Fig. 5.15, where we show the process fidelity for the single qubit teleportation in Fig. 5.4(b), the two qubit qubus gate in Fig. 5.8 and the $n = 3$ and $n = 9$ GHZ construction cases.

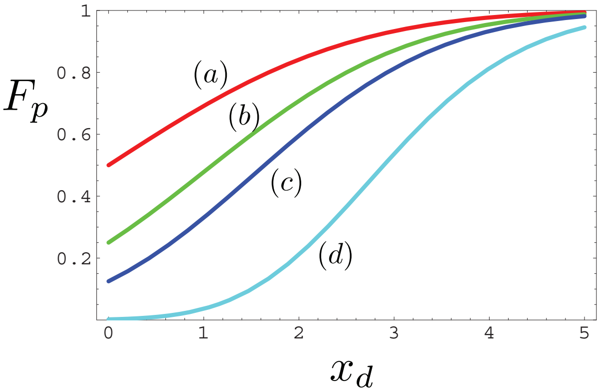

Figure 5.15: **(a)** Process fidelity $F_1(x_d)$ for the single bit teleportation in Fig. 5.4(b); **(b)** Process fidelity $F_3(x_d)$ for the qubus CSIGN in Fig. 5.8; **(c)** Process fidelity $F_5(x_d)$ for the producing the GHZ state $\left(|0\rangle^{\otimes 3} + |1\rangle^{\otimes 3}\right)/\sqrt{2}$; **(d)** Process fidelity $F_5(x_d)$ for the producing the GHZ state $\left(|0\rangle^{\otimes 9} + |1\rangle^{\otimes 9}\right)/\sqrt{2}$

Fig. 5.16 shows that as the complexity of the system we consider increases, we require higher values for x_d. The success probability also suffers as the complexity increases, since we require more post-selection for more complex systems, leading to a negative impact on the success probability.

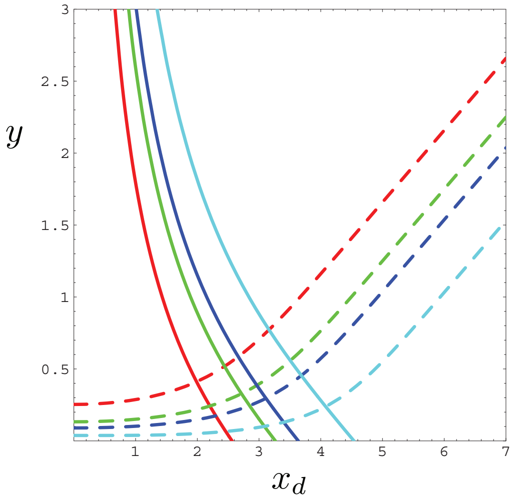

Figure 5.16: Contour lines for a conditional process fidelity of 0.9 (solid lines) and a success probability of 0.8 (dashed lines). The post-selected single bit teleportation in Fig. 5.4(b) is shown in red, the post-selected qubus CSIGN gate in Fig. 5.8 is shown in green, the post-selected $\left(|0\rangle^{\otimes 3}+|1\rangle^{\otimes 3}\right)/\sqrt{2}$ state production is shown in blue and the post-selected $\left(|0\rangle^{\otimes 9}+|1\rangle^{\otimes 9}\right)/\sqrt{2}$ state production is shown in cyan.

Chapter 6

Optical Quantum Zeno Gate

In Section 2.9 we saw the Franson *et al.* proposal [50, 101] of how an evanescent coupling of photonic qubits in a dual core optical fibre could be used to construct an all optical CSIGN. Unwanted two photon terms were a result of this evanescent coupling and could be suppressed via the quantum Zeno effect [102]. This involved *breaking* the optical fibre into N segments and absorbing the two photon terms in between each segment. As N approached ∞ we obtained a CSIGN, up to local phase gates and a SWAP operation, both easily performed on optical qubits. The two photon absorption supplied the necessary non-linearity for the optical qubits to interact.

The method by which we *absorbed* the two photon terms in Section 2.9 was an ideal, artificial approach. We saw in Eqn. 2.146 that we manually eliminated the two photon terms in between coupling segments. In a realistic model of this gate, the two photon absorption must be modelled with the methods presented in Section 2.1.7, that is, using a master equations similar to that in Eqn. 2.61. This is the first aim of this Chapter, to model the optical Zeno gate presented in [50, 101] with realistic two photon absorption.

In such a realistic scenario, single photon loss will be the dominant form of decoherence [50, 101], something that cannot be ignored. As a naive example, consider the state $|11\rangle$ incident on the optical Zeno gate in Section 2.9. After an application of the interaction Hamiltonian in Eqn. 2.141 for a time t, this state becomes a superpostition of $|11\rangle$, $|20\rangle$ and $|02\rangle$, as seen in Eqn. 2.142. If we were to lose a single photon from either mode, we would have a density matrix that now had terms such as $|01\rangle\langle 01|$, $|10\rangle\langle 10|$ and $|00\rangle\langle 00|$. This means the the basis state $|11\rangle$ could now be confused with the basis states $|00\rangle$, $|01\rangle$ or $|10\rangle$. This adds to the first aim of this Chapter: to model the Zeno gate in [50, 101] with both realistic two photon absorption and single photon loss. In [101] it was suggested that the two photon absorption could be made four to five orders of magnitude greater than the single photon loss. Using this we want to examine how close a realistic model for the optical Zeno gate is to an ideal CSIGN. To realistically model single photon loss we use a master equation similar to Eqn. 2.56 in Section 2.1.7. To measure the *closeness* we will use the process fidelity, introduced in Section 2.3.

We model the optical Zeno gate with realistic two photon absorption and single photon loss in two ways. First, to model continuous two photon and single photon loss we solve a master equation containing terms for the evanescent coupling, the two photon absorption and the single photon loss. This method involves solving a set of coupled ordinary differential equations (ODEs). Second, we break the system into N evanescently coupled segments. In between each segment we model the single photon loss and two photon absorption via a master equation. The coupled segments are modelled as weakly reflecting beam splitters. To solve for the output of the N'th beam splitter we need to solve a set of recurrence equations along with the coupled ODEs from the first method. This second approach is the more experimentally feasible method, being similar to work done be Kwiat *et al.* [118].

The second aim of this Chapter is to show that the optical Zeno gate can still succeed with a high fidelity once single photon loss is introduced. We do this by encoding the optical qubits in two levels [48]. First, each qubit will be encoded with the generalised parity code described in Section 2.7.6. Next, these encoded parity qubits will be redundantly encoded. We will show that by encoding out qubits in such a way we can indeed overcome the effects of single photon loss such that our resource usage is much less than that required for an equivalent LOQC scheme shown in [87].

6.1 Continuous Two Photon Absorption and Single Photon Loss

In this Section we consider the Franson *et al.* [50, 101] optical Zeno CSIGN gate with realistic, continuous two photon absorption and single photon loss.

In Section 2.9 we showed the Franson *et al.* [50, 101] scheme to perform a CSIGN on the arbitrary two qubit state $c_0|00\rangle + c_1|01\rangle + c_2|10\rangle + c_3|11\rangle$, where $|c_0|^2 + |c_1|^2 + |c_2|^2 + |c_3|^2 = 1$, $|0\rangle = |\text{vac}\rangle$ and $|1\rangle = \hat{a}^\dagger|\text{vac}\rangle$. This gate acted on *single* rail logic [119, 120], as opposed to the dual rail logic described in Section 2.5.1. Since the desired gate is a CSIGN and not a CNOT, we could equally well have applied it to modes 1 and 3 of the arbitrary two qubit dual rail state $c_0|0101\rangle + c_1|0110\rangle + c_2|1001\rangle + c_3|1010\rangle$. In this way we see that the optical Zeno CSIGN gate in [50, 101] can work on either single or dual rail logic.

The device we consider in this Section is shown in Fig. 6.1. Here we consider dual rail logic in the form of polarisation: $|0\rangle_L = |H\rangle$ and $|1\rangle_L = |V\rangle$. If we have the state $c_0|HH\rangle + c_1|HV\rangle + c_2|VH\rangle + c_3|VV\rangle$ incident on Fig. 6.1, only the state $|VV\rangle$ will obtain a phase shift since this is the only state that has two photons inside the interaction medium.

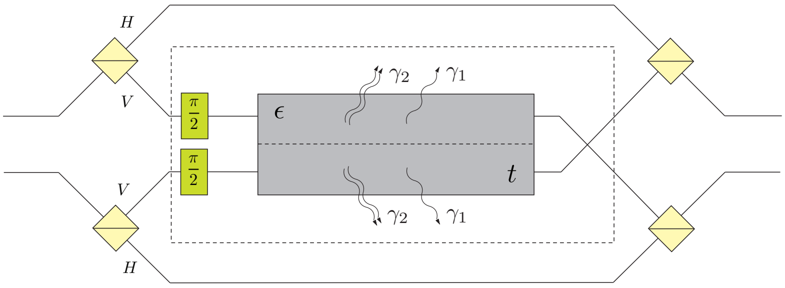

Figure 6.1: Key parameters of the system. The gate between the qubits is created by an interaction between the vertical polarisation modes inside the device. The modes interact with a strength ϵ, for a time t. While passing through the medium the modes undergo single photon loss and two photon absorption with the rates γ_1 and γ_2, respectively. The whole gate forms a dual-rail CSIGN gate for polarisation encoded qubits while the region inside the dashed box forms a single-rail encoded CSIGN gate.

As in Section 2.9, we consider the evanescent coupling Hamiltonian

$$\hat{H}_I = \epsilon(\hat{a}_1^\dagger \hat{a}_2 + \hat{a}_1 \hat{a}_2^\dagger) \tag{6.1}$$

where $\hat{a}_1$ ($\hat{a}_2$) is the annihilation operator for the top (bottom) mode in Fig. 6.1. This is just the beam splitter Hamiltonian given in Eqn. 2.29 in Section 2.1.5 with $\theta = \epsilon t$ and $\vartheta = 0$ ($\phi = -\pi/2$ in Eqn. 2.36).

Incorporating continuous two-photon absorption and single photon loss as in Section 2.1.7 gives the master equation:

$$\begin{aligned}\frac{d\rho}{dt} &= i\left[\rho, \hat{H}_I\right] + \sum_{j=1}^{2} \frac{\gamma_1^{(j)}}{2}(2\hat{a}_j\rho\hat{a}_j^\dagger - \hat{a}_j^\dagger\hat{a}_j\rho - \rho\hat{a}_j^\dagger\hat{a}_j) + \sum_{j=1}^{2} \frac{\gamma_2^{(j)}}{2}(2\hat{a}_j^2\rho\hat{a}_j^{\dagger 2} - \hat{a}_j^{\dagger 2}\hat{a}_j^2\rho - \rho\hat{a}_j^{\dagger 2}\hat{a}_j^2) \\ &= i\epsilon\big(\rho\hat{a}_1^\dagger\hat{a}_2 + \rho\hat{a}_2^\dagger\hat{a}_1 - \hat{a}_1^\dagger\hat{a}_2\rho - \hat{a}_2^\dagger\hat{a}_1\rho\big) + \sum_{j=1}^{2} \frac{\gamma_1^{(j)}}{2}(2\hat{a}_j\rho\hat{a}_j^\dagger - \hat{a}_j^\dagger\hat{a}_j\rho - \rho\hat{a}_j^\dagger\hat{a}_j) \qquad (6.2) \\ &\qquad + \sum_{j=1}^{2} \frac{\gamma_2^{(j)}}{2}(2\hat{a}_j^2\rho\hat{a}_j^{\dagger 2} - \hat{a}_j^{\dagger 2}\hat{a}_j^2\rho - \rho\hat{a}_j^{\dagger 2}\hat{a}_j^2)\end{aligned}$$

where $\rho \equiv \rho(t)$ is the density matrix at time t, $\gamma_2^{(j)}$ describes the two photon absorption in core j and $\gamma_1^{(j)}$ describes the single photon loss in core j. By describing single photon loss and two photon absorption in this way we must ensure that the Born-Markov approximation holds for our system. Single photons can be lost at any point in our system, and as such we expect single photon loss to have a negligible effect on the state of the environment. Since single photons are scattered in any direction we do not expect the environment to have any memory of single photon loss events. If we could somehow arrange for the environment to keep track of where and when single photons were lost we could correct for this decoherence. We consider two photons to be absorbed by a continuum of three level atoms as in [50], where the three energy levels are such that a single photon cannot be absorbed. When two photons are absorbed the atoms decay sufficiently rapidly such that the environment has no memory. The photons resulting from this decay have a different frequency to our qubit photons.

We simplify the system by assuming the two photon absorption in mode 1 is equal to that in mode 2, similarly for the single photon loss: $\gamma_2^{(1)} = \gamma_2^{(2)} = \gamma_2$ and $\gamma_1^{(1)} = \gamma_1^{(2)} = \gamma_1$. We also parameterise the system by rescaling the interaction time as $t = \tau/\gamma_1$ and introduce the scaled interaction strength $\kappa = \epsilon/\gamma_1$ and ratio of two-photon absorption to single-photon loss $\gamma = \gamma_2/\gamma_1$. This gives the master equation:

$$\begin{aligned}\frac{d\rho}{d\tau} &= i\kappa\big(\rho\hat{a}_1^\dagger\hat{a}_2 + \rho\hat{a}_2^\dagger\hat{a}_1 - \hat{a}_1^\dagger\hat{a}_2\rho - \hat{a}_2^\dagger\hat{a}_1\rho\big) + \frac{1}{2}\sum_{j=1}^{2}(2\hat{a}_j\rho\hat{a}_j^\dagger - \hat{a}_j^\dagger\hat{a}_j\rho - \rho\hat{a}_j^\dagger\hat{a}_j) \qquad (6.3)\\ &\quad + \frac{\gamma}{2}\sum_{j=1}^{2}(2\hat{a}_j^2\rho\hat{a}_j^{\dagger 2} - \hat{a}_j^{\dagger 2}\hat{a}_j^2\rho - \rho\hat{a}_j^{\dagger 2}\hat{a}_j^2).\end{aligned}$$

In order to model a CSIGN we set $\kappa\tau = \epsilon t = \pi/2$, as in Section 2.9. Our system is now described by only two parameters: τ and γ.

Solving for a general ρ in Eqn. 6.3 is a difficult task. As mentioned in Section 2.1.7, the general solutions for both the on- and off-diagaonal density matrix elements for either the single photon loss master equation ($\kappa = 0$ and $\gamma_2^{(1)} = \gamma_2^{(2)} = 0$ in Eqn. 6.2) or the two photon absorption master equation ($\kappa = 0$ and $\gamma_1^{(1)} = \gamma_1^{(2)} = 0$ in Eqn. 6.2) are well known. A general solution to a master equation with both single photon loss and two photon absorption ($\kappa = 0$ in Eqn. 6.3) is not known. In [121, 66, 122], a solution for the diagonal density matrix elements for such a master equation was shown. We could use this in combination with [70, 71] to find both the on- and off-diagonal density matrix elements for the single photon loss and two photon absorption master equation. However, even with this we would not be able to solve Eqn. 6.3 directly since we need κ non-zero. Since the maximum number of photons in the system at any one time is two, we do not need to find a general solution to Eqn. 6.3. We can instead write down the thirty six couple ODEs and solve for these.

We start with the state

$$\begin{aligned}&c_0|HH\rangle + c_1|HV\rangle + c_2|VH\rangle + c_3|VV\rangle\\ &= \big(c_0|1001\rangle + c_1|1010\rangle + c_2|0101\rangle + c_3|0110\rangle\big)_{1234} \qquad (6.4)\end{aligned}$$

where only modes 2 and 3 goes through the interaction region in Fig. 6.1. Since the interaction Hamiltonian in Eqn. 6.1 can transform the state $|11\rangle$ to superposition of the state $|11\rangle, |02\rangle$ and $|20\rangle$, as seen in Eqn. 2.142 in Section 2.9, we know the set of all possible states found inside the interaction region is $\mathbb{B} \in \{|00\rangle, |01\rangle, |10\rangle, |11\rangle, |02\rangle, |20\rangle\}$. The density matrix inside the interaction medium is therefore:

$$\rho = \sum_{ij,kl \in \mathbb{B}} d_{ijkl} |ij\rangle\langle kl|. \tag{6.5}$$

We can write an ODE for each element of the density matrix by using the fact that

$$\begin{aligned} \langle mn|\dot{\rho}|pq\rangle &= \dot{d}_{mnpq} \qquad (6.6) \\ \langle mn|\rho|pq\rangle &= d_{mnpq}. \end{aligned}$$

Applying these to Eqn. 6.3 we have the following thirty six coupled ODEs:

$$\begin{aligned} \dot{d}_{mnpq} =& i\kappa\big(\sqrt{(p+1)q}\,d_{mn(p+1)(q-1)} + \sqrt{p(q+1)}\,d_{mn(p-1)(q+1)} - \sqrt{m(n+1)}\,d_{(m-1)(n+1)pq} \\ & - \sqrt{(m+1)n}\,d_{(m+1)(n-1)pq}\big) + \sqrt{(m+1)(p+1)}\,d_{(m+1)n(p+1)q} + \sqrt{(n+1)(q+1)}\,d_{m(n+1)p(q+1)} \\ & + \gamma\left(\sqrt{(m+1)(m+2)(p+1)(p+2)}\,d_{(m+2)n(p+2)q} + \sqrt{(n+1)(n+2)(q+1)(q+2)}\,d_{m(n+2)p(q+2)}\right) \\ & - \frac{1}{2}\big(m+p+n+q+\gamma[m(m-1)+p(p-1)+n(n-1)+q(q-1)]\big)d_{mnpq} \end{aligned} \tag{6.7}$$

where we have used Eqns. 2.4, 2.9 2.10 and 2.11 from Section 2.1.2 along with

$$\begin{aligned} \hat{a}^2|n\rangle &= \sqrt{n(n-1)}|n-2\rangle \\ (\hat{a}^\dagger)^2|n\rangle &= \sqrt{(n+1)(n+2)}|n+2\rangle \qquad (6.8) \\ (\hat{a}^\dagger)^2\hat{a}^2|n\rangle &= n(n-1)|n\rangle \\ \hat{a}^2(\hat{a}^\dagger)^2|n\rangle &= (n+1)(n+2)|n\rangle. \end{aligned}$$

Using the fact that $\rho = \rho^\dagger$ we can reduce the number of couple ODEs in Eqn. 6.7 to just twenty one. If we define the 21×1 vector

$$\vec{\rho} = \begin{bmatrix} d_{0000} \\ d_{0001} \\ \vdots \\ d_{2002} \\ d_{2020} \end{bmatrix}$$

we can rewrite Eqn. 6.7 as

$$\dot{\vec{\rho}}(t) = M\vec{\rho} \tag{6.9}$$

and solve by diagonalising the 21×21 matrix M:

$$\vec{\rho}(t) = \exp(Mt)\vec{\rho}(0) = P\exp(Dt)P^{-1}\vec{\rho}(0) \tag{6.10}$$

where $M = PDP^{-1}$, P is the matrix of eigenvectors for M, D is diagonal matrix made up of the eigenvectors for M and

$$\begin{aligned} \rho(0) &= \sum_{ij,kl\in\mathbb{B}} c_{ijkl}|ij\rangle\langle kl| \qquad (6.11) \\ \vec{\rho}(0) &= \begin{bmatrix} c_{0000} \\ c_{0001} \\ \vdots \\ c_{2002} \\ c_{2020} \end{bmatrix}. \end{aligned}$$

Finding the solution in Eqn. 6.10 is relatively straightforward numerically, however it is a daunting task analytically, since we need to invert the 21×21 matrix P. For this reason we instead break Eqn. 6.7 into subsystems and solve each separately.

For the case $m + n = 2$ and $p + q = 2$ in Eqn. 6.7 we have

$$\begin{aligned} \dot{d}_{1111} &= -2d_{1111} + i\sqrt{2}\kappa\big(d_{1102} + d_{1120} - d_{0211} - d_{2011}\big) \\ \dot{d}_{0211} &= -(2+\gamma)d_{0211} + i\sqrt{2}\kappa\big(d_{0202} + d_{0220} - d_{1111}\big) \\ \dot{d}_{0202} &= -2(1+\gamma)d_{0202} + i\sqrt{2}\kappa\big(d_{0211} - d_{1102}\big) \qquad (6.12) \\ \dot{d}_{2011} &= -(2+\gamma)d_{2011} + i\sqrt{2}\kappa\big(d_{2002} + d_{2020} - d_{1111}\big) \\ \dot{d}_{2002} &= -2(1+\gamma)d_{2002} + i\sqrt{2}\kappa\big(d_{2011} - d_{1102}\big) \\ \dot{d}_{2020} &= -2(1+\gamma)d_{2020} + i\sqrt{2}\kappa\big(d_{2011} - id_{1120}\big). \end{aligned}$$

Notice that the ODE $\dot{d}_{1111}$ has the term d_{1102}, which is not being solved explicitly. To get around this problem we break each density matrix element up into real and imaginary parts: $d_{mnpg} = \mathrm{Re}(d_{mnpg}) + i\,\mathrm{Im}(d_{mnpg})$. In this way we can write $d_{1102} = \mathrm{Re}(d_{0211}) - i\,\mathrm{Im}(d_{0211})$. Similarly for the terms d_{1120} and d_{0220}. We can solve Eqn. 6.12 using the method described in Eqn. 6.10 but now the matrix of eigenvectors to be inverted is only a 6×6 matrix and is easily inverted analytically.

For the case $m + n = 1$ and $p + q = 2$ in Eqn. 6.7 we have

$$\begin{aligned} \dot{d}_{0111} &= -\frac{3}{2}d_{0111} + i\kappa\big(\sqrt{2}d_{0102} + \sqrt{2}d_{0120} - d_{1011}\big) \\ \dot{d}_{0102} &= -\left(\frac{3}{2}+\gamma\right)d_{0102} + i\kappa\big(\sqrt{2}d_{0111} - d_{1002}\big) \\ \dot{d}_{0120} &= -\left(\frac{3}{2}+\gamma\right)d_{0120} + i\kappa\big(\sqrt{2}d_{0111} - d_{1020}\big) \qquad (6.13) \\ \dot{d}_{1011} &= -\frac{3}{2}d_{1011} + i\kappa\big(\sqrt{2}d_{1002} + \sqrt{2}d_{1020} - d_{0111}\big) \\ \dot{d}_{1002} &= -\left(\frac{3}{2}+\gamma\right)d_{1002} + i\kappa\big(\sqrt{2}d_{1011} - d_{0102}\big) \\ \dot{d}_{1020} &= -\left(\frac{3}{2}+\gamma\right)d_{1020} + i\kappa\big(\sqrt{2}d_{1011} - d_{0120}\big). \end{aligned}$$

We can solve the coupled ODEs in Eqn. 6.13 in a similar way to the solution for Eqn. 6.12.

For the case $m+n=1$ and $p+q=1$ in Eqn. 6.7 we have

$$\begin{aligned}\dot{d}_{0101} &= d_{1111}+2d_{0202}-d_{0101}+i\kappa\big(d_{0110}-d_{1001}\big)\\ \dot{d}_{1001} &= -d_{1001}+\sqrt{2}d_{1102}+\sqrt{2}d_{2011}+i\kappa\big(d_{1010}-d_{0101}\big)\\ \dot{d}_{1010} &= -d_{1010}+d_{1111}+2d_{2020}+i\kappa\big(d_{1001}-d_{0110}\big),\end{aligned}\tag{6.14}$$

for the case $m+n=0$ and $p+q=2$ in Eqn. 6.7 we have

$$\begin{aligned}\dot{d}_{0002} &= i\sqrt{2}\kappa d_{0011}-(1+\gamma)d_{0002}\\ \dot{d}_{0020} &= i\sqrt{2}\kappa d_{0011}-(1+\gamma)d_{0020}\\ \dot{d}_{0011} &= -d_{0011}+i\sqrt{2}\kappa\big(d_{0002}+d_{0020}\big),\end{aligned}\tag{6.15}$$

for the case $m+n=0$ and $p+q=1$ in Eqn. 6.7 we have

$$\begin{aligned}\dot{d}_{0001} &= -\frac{1}{2}d_{0001}+\sqrt{2}d_{0102}+d_{1011}+i\kappa d_{0010}\\ \dot{d}_{0010} &= -\frac{1}{2}d_{0010}+d_{0111}+\sqrt{2}d_{1020}+i\kappa d_{0001},\end{aligned}\tag{6.16}$$

and for the case $m+n=0$ and $p+q=0$ in Eqn. 6.7 we have

$$\dot{d}_{0000} = d_{0101}+d_{1010}+2\gamma\big(d_{0202}+d_{2020}\big).\tag{6.17}$$

Notice that the ODEs in Eqns. 6.14–6.17 are not homogeneous. We need to use the general method of diagonalisation [123] to solve these given the solutions to Eqns 6.12 and 6.13.

6.2 Beam Splitters with Continuous Two Photon Absorption and Single Photon Loss

In this Section we model the Franson *et al.* [50, 101] optical Zeno CSIGN gate as a linear array of partially transmitting beam splitters with continuous two photon absorption and single photon loss after each beam splitter. The results presented in this Section are similar to those in [124]. We solve for the output of the N'th beamsplitter and loss/absorption combination by solving a set of recurrence equations along with Eqn. 6.7 with $\kappa=0$.

First we show how we can directly model a CSIGN gate as a linear array of partially transmitting beam splitters with the two photon terms manually eliminated after each beam splitter.

6.2.1 Manual Two Photon Absorption

If we have a linear array of N beam splitters, as in Fig. 6.2, and we manually eliminate the two photon terms after each beam splitter, the middle two modes of Eqn. 6.4:

$$|\psi\rangle_{\text{input}} = c_0|00\rangle + c_1|01\rangle + c_2|10\rangle + c_3|11\rangle \tag{6.18}$$

where $|c_0|^2 + |c_1|^2 + |c_2|^2 + |c_3|^2 = 1$, become:

$$\begin{aligned}|\psi\rangle_{\text{input}} \rightarrow \frac{1}{\mathcal{N}}\Big(& c_0|00\rangle + c_1\big(\cos(N\theta)|01\rangle - e^{i\phi}\sin(N\theta)|10\rangle\big) \\ &+ c_2\big(\cos(N\theta)|10\rangle + e^{-i\phi}\sin(N\theta)|01\rangle\big) \\ &+ c_3\cos^N(2\theta)|11\rangle\Big)\end{aligned} \tag{6.19}$$

where

$$\mathcal{N} = \sqrt{|c_0|^2 + \big(1+\cos(\phi)\sin(2N\theta)\big)|c_1|^2 + \big(1-\cos(\phi)\sin(2N\theta)\big)|c_2|^2 + \cos^{2N}(2\theta)\,|c_3|^2}$$

and we have used the description of a beam beam splitter given in Section 2.1.5. Since we want a CSIGN gate, we first choose $N\theta = m\pi$, where $m = 1, 2, 3, \cdots$. This takes $|01\rangle \rightarrow \cos(m\pi)|01\rangle$ and $|10\rangle \rightarrow \cos(m\pi)|10\rangle$. If we choose m even we have

$$|\psi\rangle_{\text{input}} \rightarrow \frac{1}{\mathcal{N}}\left(c_0|00\rangle + c_1|01\rangle + c_2|10\rangle + c_3\cos^N\left(\frac{2m\pi}{N}\right)|11\rangle\right). \tag{6.20}$$

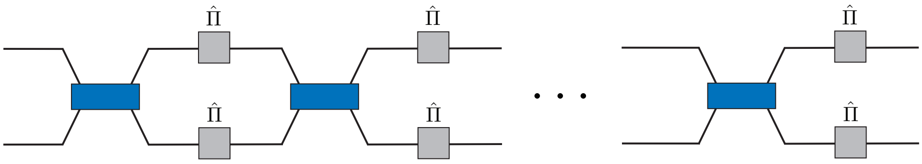

Figure 6.2: A linear array of N partially transmitting beam splitters, each followed by a manually elimination of any two photon terms. This performs a CSIGN on single rail logic. The projector $\hat{\Pi} = |0\rangle\langle 0| + |1\rangle\langle 1|$.

We need $\cos^N\left(\frac{2m\pi}{N}\right) = -1$. Using the fact that $\cos(\theta) = -\cos(\pi - \theta)$ we have

$$\cos^N\left(\frac{2m\pi}{N}\right) = (-1)^N\cos^N\left(\pi\left(1 - 2\frac{m}{N}\right)\right). \tag{6.21}$$

If we choose N odd we have

$$|\psi\rangle_{\text{input}} \rightarrow \frac{1}{\mathcal{N}}\left(c_0|00\rangle + c_1|01\rangle + c_2|10\rangle - c_3\cos^N\left(\pi\left(1 - 2\frac{m}{N}\right)\right)|11\rangle\right) \tag{6.22}$$

where $N = 1, 3, 5, \cdots$ and $m = 2, 4, 6, \cdots$. We want $\cos^N\left(\pi\left(1 - 2\frac{m}{N}\right)\right) \approx 1$. This is true if $\frac{m}{N} \approx \frac{1}{2}$. If we choose $N = 2m - 1$, we find that as m increases, our gate more closely resembles a CSIGN:

$$|\psi\rangle_{\text{input}} \rightarrow \frac{1}{\mathcal{N}}\left(c_0|00\rangle + c_1|01\rangle + c_2|10\rangle - c_3\cos^{2m-1}\left(\frac{\pi}{2m-1}\right)|11\rangle\right) \tag{6.23}$$

where $m = 2, 4, 6, \cdots$ and

$$\mathcal{N} = \sqrt{1 + |c_3|^2 \left(\cos^{4m-2} \left(\frac{\pi}{2m-1} \right) - 1 \right)}. \tag{6.24}$$

For m large enough this state becomes

$$c_0|00\rangle + c_1|01\rangle + c_2|10\rangle - c_3|11\rangle \tag{6.25}$$

since

$$\lim_{m\to\infty} \cos^{2m-1} \left(\frac{\pi}{2m-1} \right) = 1.$$

6.2.2 Continuous Two Photon Absorption and Single Photon Loss

To realistically model a CSIGN gate with a linear array of beam splitters we need to consider continuous two photon absorption after each beam splitter in Fig. 6.2, as in Fig. 6.3.

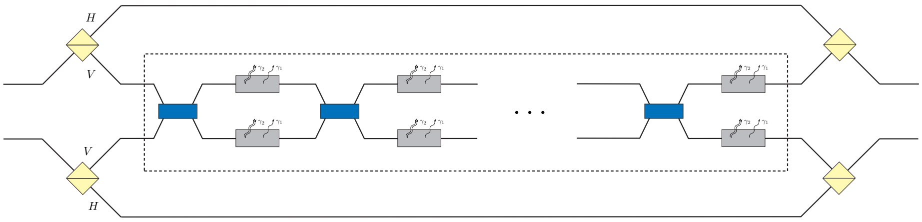

Figure 6.3: A linear array of N partially transmitting beam splitters, each followed by a realistic continuous two photon absorption and single photon loss. The whole gate forms a dual-rail CSIGN gate for polarisation encoded qubits while the region inside the dashed box forms a single-rail encoded CSIGN gate.

As with Section 6.1, single photon loss will be a dominant decoherence process in such a system. We model the continuous two photon absorption and single photon loss via the master equation 6.7 with $\kappa = 0$. In such a case the twenty one coupled ODEs in Eqns. 6.12–6.17 are easily solved and are given below:

For the case $\kappa = 0$, $m + n = 2$ and $p + q = 2$ in Eqn. 6.7 we have

$$\begin{aligned}
d_{1111}(\mathcal{T}) &= e^{-2\mathcal{T}} c_{1111} \\
d_{0211}(\mathcal{T}) &= e^{-(2+\gamma)\mathcal{T}} c_{0211} \\
d_{0202}(\mathcal{T}) &= e^{-2(1+\gamma)\mathcal{T}} c_{0202} \\
d_{2011}(\mathcal{T}) &= e^{-(2+\gamma)\mathcal{T}} c_{2011} \\
d_{2002}(\mathcal{T}) &= e^{-2(1+\gamma)\mathcal{T}} c_{2002} \\
d_{2020}(\mathcal{T}) &= e^{-2(1+\gamma)\mathcal{T}} c_{2020}.
\end{aligned} \tag{6.26}$$

For the case $\kappa = 0$, $m + n = 1$ and $p + q = 2$ in Eqn. 6.7 we have

$$\begin{aligned}
d_{0111}(\mathcal{T}) &= e^{-\frac{3}{2}\mathcal{T}} c_{0111} \\
d_{0102}(\mathcal{T}) &= e^{-(\frac{3}{2}+2\gamma)\mathcal{T}} c_{0102} \\
d_{0120}(\mathcal{T}) &= e^{-(\frac{3}{2}+2\gamma)\mathcal{T}} c_{0120} \\
d_{1011}(\mathcal{T}) &= e^{-\frac{3}{2}\mathcal{T}} c_{1011} \\
d_{1002}(\mathcal{T}) &= e^{-(\frac{3}{2}+2\gamma)\mathcal{T}} c_{1002} \\
d_{1020}(\mathcal{T}) &= e^{-(\frac{3}{2}+2\gamma)\mathcal{T}} c_{1020}.
\end{aligned} \tag{6.27}$$

For the case $\kappa = 0$, $m + n = 1$ and $p + q = 1$ in Eqn. 6.7 we have

$$\begin{aligned}
d_{0101}(\mathcal{T}) &= e^{-\mathcal{T}} c_{0101} + e^{-2\mathcal{T}}(e^{\mathcal{T}} - 1) c_{1111} + \frac{2e^{-2(1+\gamma)\mathcal{T}}(e^{(1+2\gamma)\mathcal{T}} - 1)}{1+2\gamma} c_{0202} \\
d_{1001}(\mathcal{T}) &= e^{-\mathcal{T}} c_{1001} + \frac{\sqrt{2}\left(e^{-\mathcal{T}} - e^{-(2+\gamma)\mathcal{T}}\right)}{1+\gamma} (c_{1102} + c_{2011}) \\
d_{1010}(\mathcal{T}) &= e^{-\mathcal{T}} c_{1010} + e^{-2\mathcal{T}}(e^{\mathcal{T}} - 1) c_{1111} + \frac{2e^{-2(1+\gamma)\mathcal{T}}(e^{(1+2\gamma)\mathcal{T}} - 1)}{1+2\gamma} c_{2020}.
\end{aligned} \tag{6.28}$$

For the case $\kappa = 0$, $m + n = 0$ and $p + q = 2$ in Eqn. 6.7 we have

$$\begin{aligned}
d_{0002}(\mathcal{T}) &= e^{-(1+\gamma)\mathcal{T}} c_{0002} \\
d_{0020}(\mathcal{T}) &= e^{-(1+\gamma)\mathcal{T}} c_{0020} \\
d_{0011}(\mathcal{T}) &= e^{-\mathcal{T}} c_{0011}.
\end{aligned} \tag{6.29}$$

For the case $\kappa = 0$, $m + n = 0$ and $p + q = 1$ in Eqn. 6.7 we have

$$\begin{aligned}
d_{0001}(\mathcal{T}) &= e^{-\frac{1}{2}\mathcal{T}} c_{0001} + e^{-\frac{1}{2}\mathcal{T}}(1 - e^{-\mathcal{T}}) c_{1011} - \frac{\sqrt{2}e^{-\frac{1}{2}\mathcal{T}}(e^{-(1+\gamma)\mathcal{T}} - 1)}{1+\gamma} c_{0102} \\
d_{0010}(\mathcal{T}) &= e^{-\frac{1}{2}\mathcal{T}} c_{0010} + e^{-\frac{1}{2}\mathcal{T}}(1 - e^{-\mathcal{T}}) c_{0111} - \frac{\sqrt{2}e^{-\frac{1}{2}\mathcal{T}}(e^{-(1+\gamma)\mathcal{T}} - 1)}{1+\gamma} c_{1020}.
\end{aligned} \tag{6.30}$$

For the case $\kappa = 0$, $m + n = 0$ and $p + q = 0$ in Eqn. 6.7 we have

$$\begin{aligned}
d_{0000}(\mathcal{T}) = {} & c_{0000} + (1 - e^{-\mathcal{T}})(c_{0101} + c_{1010}) + e^{-2\mathcal{T}}(e^{\mathcal{T}} - 1)^2 c_{1111} \\
& + \frac{2\gamma(1 - e^{-2(1+\gamma)\mathcal{T}}) + (1 - 2e^{-\mathcal{T}} + e^{-2(1+\gamma)\mathcal{T}})}{1+2\gamma} (c_{0202} + c_{2020})
\end{aligned} \tag{6.31}$$

where as in Section 6.1 we set $\mathcal{T} = \gamma_1 t$, $\gamma = \frac{\gamma_2}{\gamma_1}$ and the initial density matrix is given by in Eqn. 6.11. Since we want to induce a CSIGN on the state $|\psi\rangle_{\text{input}}$ given in Eqn. 6.18, we set $N = 2m - 1$, for even m, as in Section 6.2.1.

We start with the state $|\psi\rangle_{\text{input}}$ given in Eqn. 6.18 incident on the first beam splitter in Fig. 6.3. The output of this beam splitter is the initial density matrix for the first continuous two photon absorption and single photon loss process. The density matrix resulting from Eqns. 6.26–6.31 is now the incident state for the second beam splitter. We continue in the manner for N beam splitters. We now need to solve for the output of the $N'th$ beam splitter/absorption/loss combination. Since we will want to compare the CSIGN gate implemented in this Section with that in Section 6.1, the time the two photon absorption and single photon loss act on the two systems must be equal. For this reason we set $\mathcal{T} = \frac{\tau}{2m-1}$, where τ is the scaled total time the photons spend in the interaction medium in Fig. 6.3.

We solve for the output of the N'th beam splitter/absoprtion/loss combination by solving a set of recurrence equations. To find an analytical solution we must break the density matrix ρ into the six sub-blocks:

$$\begin{pmatrix}
d_{0000}^{(N)} & d_{0001}^{(N)} & d_{0010}^{(N)} & d_{0011}^{(N)} & d_{0020}^{(N)} & d_{0002}^{(N)} \\
d_{0100}^{(N)} & d_{0101}^{(N)} & d_{0110}^{(N)} & d_{0111}^{(N)} & d_{0120}^{(N)} & d_{0102}^{(N)} \\
d_{1000}^{(N)} & d_{1001}^{(N)} & d_{1010}^{(N)} & d_{1011}^{(N)} & d_{1020}^{(N)} & d_{1002}^{(N)} \\
d_{1100}^{(N)} & d_{1101}^{(N)} & d_{1110}^{(N)} & d_{1111}^{(N)} & d_{1120}^{(N)} & d_{1102}^{(N)} \\
d_{2000}^{(N)} & d_{2001}^{(N)} & d_{2010}^{(N)} & d_{2011}^{(N)} & d_{2020}^{(N)} & d_{2002}^{(N)} \\
d_{0200}^{(N)} & d_{0201}^{(N)} & d_{0210}^{(N)} & d_{0211}^{(N)} & d_{0220}^{(N)} & d_{0202}^{(N)}
\end{pmatrix}. \tag{6.32}$$

To solve for the terms in each sub-block we use Eqn, 2.36 in conjunction with Eqns. 6.26–6.31. There will be two types of solution here, those coming from the homogeneous ODEs in Eqns. 6.26, 6.27 and 6.29 and those coming from the non-homogeneous Eqns. 6.28, 6.30 and 6.31. That is, the red, green and cyan density matrix sub-blocks only depend on terms within their own initial density matrix sub-block. However, the blue, yellow and magenta density matrix sub-blocks depend on terms within their own initial density matrix sub-block and on terms from other initial density matrix sub-blocks.

The Red sub-block in Eqn. 6.32

For the two photon absorption and single photon loss given in Eqn. 6.26, we consider the density matrix block with the elements corresponding to $|11\rangle\langle 11|$, $|11\rangle\langle 02|$, $|11\rangle\langle 20|$, $|02\rangle\langle 11|$, $|02\rangle\langle 02|$, $|02\rangle\langle 20|$, $|20\rangle\langle 11|$, $|20\rangle\langle 02|$ and $|20\rangle\langle 20|$. Our initial state is given by $|\psi\rangle_{\text{input}}$ in Eqn. 6.18 and is pure. After a beam splitter, $|\psi\rangle_{\text{input}}$ becomes the pure state:

$$|\psi\rangle_{\text{input}} \rightarrow c_0'|00\rangle + c_1'|01\rangle + c_2'|10\rangle + c_3'|11\rangle + c_4'|20\rangle + c_5'|02\rangle. \tag{6.33}$$

After two photon absorption and single photon loss, the two photon terms in this state become

$$\begin{pmatrix} |c'_3|^2 & c'_3 c'^*_4 & c'_3 c'^*_5 \\ c'_4 c'^*_3 & |c'_4|^2 & c'_4 c'^*_5 \\ c'_5 c'^*_3 & c'_5 c'^*_4 & |c'_5|^2 \end{pmatrix} \rightarrow \begin{pmatrix} |c'_3|^2 e^{-2\mathcal{T}} & c'_3 c'^*_4 e^{-(2+\gamma)\mathcal{T}} & c'_3 c'^*_5 e^{-(2+\gamma)\mathcal{T}} \\ c'_4 c'^*_3 e^{-(2+\gamma)\mathcal{T}} & |c'_4|^2 e^{-2(1+\gamma)\mathcal{T}} & c'_4 c'^*_5 e^{-2(1+\gamma)\mathcal{T}} \\ c'_5 c'^*_3 e^{-(2+\gamma)\mathcal{T}} & c'_5 c'^*_4 e^{-2(1+\gamma)\mathcal{T}} & |c'_5|^2 e^{-2(1+\gamma)\mathcal{T}} \end{pmatrix} \tag{6.34}$$

where we have used Eqn. 6.26. The state on the right hand side is just the pure state $c'_3 e^{-\mathcal{T}}|11\rangle + c'_4 e^{-(1+\gamma)\mathcal{T}}|20\rangle + c'_5 e^{-(1+\gamma)\mathcal{T}}|02\rangle$. If we were now to put this state through another beam splitter followed by two photon loss and single photon absorption we would obtain a similar pure state. We can therefore write down what this density matrix sub-block looks like after N beam splitter/absorption/loss combinations:

$$\begin{aligned} \rho^{(m+n=2,\, p+q=2)}_{(N)} &= \begin{pmatrix} d^{(N)}_{1111} & d^{(N)}_{1120} & d^{(N)}_{1102} \\ d^{(N)}_{2011} & d^{(N)}_{2020} & d^{(N)}_{2002} \\ d^{(N)}_{0211} & d^{(N)}_{0220} & d^{(N)}_{0202} \end{pmatrix} \\ &= V_1 \cdot \begin{pmatrix} d^{(N-1)}_{1111} & d^{(N-1)}_{1120} & d^{(N-1)}_{1102} \\ d^{(N-1)}_{2011} & d^{(N-1)}_{2020} & d^{(N-1)}_{2002} \\ d^{(N-1)}_{0211} & d^{(N-1)}_{0220} & d^{(N-1)}_{0202} \end{pmatrix} \cdot V_1^\dagger \qquad (6.35) \\ &= (V_1)^N \cdot \begin{pmatrix} |c_3|^2 & c_3 c_4^* & c_3 c_5^* \\ c_4 c_3^* & |c_4|^2 & c_4 c_5^* \\ c_5 c_3^* & c_5 c_4^* & |c_5|^2 \end{pmatrix} \cdot \left(V_1^\dagger\right)^N \\ &= (V_1)^N \left(c_3|11\rangle + c_4|20\rangle + c_5|02\rangle\right)\left(c_3^*\langle 11| + c_4^*\langle 20| + c_5^*\langle 02|\right)\left(V_1^\dagger\right)^N \end{aligned}$$

where

$$V_1 = \begin{pmatrix} e^{-\mathcal{T}}\cos(2\theta) & \frac{1}{\sqrt{2}}e^{-\mathcal{T}}\sin(2\theta) & -\frac{1}{\sqrt{2}}e^{-\mathcal{T}}\sin(2\theta) \\ -\frac{1}{\sqrt{2}}e^{-(1+\gamma)\mathcal{T}}\sin(2\theta) & e^{-(1+\gamma)\mathcal{T}}\cos^2(\theta) & e^{-(1+\gamma)\mathcal{T}}\sin^2(\theta) \\ \frac{1}{\sqrt{2}}e^{-(1+\gamma)\mathcal{T}}\sin(2\theta) & e^{-(1+\gamma)\mathcal{T}}\sin^2(\theta) & e^{-(1+\gamma)\mathcal{T}}\cos^2(\theta) \end{pmatrix}.$$

V_1 is easily diagonalisable. In the case that $c_4 = c_5 = 0$ for $|\psi\rangle_{\text{input}}$, as in Eqn. 6.18, we can expand Eqn. 6.35 given V_1 to find:

$$\begin{aligned} d^{(N)}_{2020} &= d^{(N)}_{0202} \\ d^{(N)}_{2002} &= d^{(N)}_{0220} \\ d^{(N)}_{1120} &= d^{(N)}_{2011} = -d^{(N)}_{1102} = -d^{(N)}_{0211}. \end{aligned} \tag{6.36}$$

The Green sub-block in Eqn. 6.32

This case is similar to the previous case since we start with a pure state $|\psi\rangle_{\text{input}}$ and the transformations in Eqns. 2.36 and 6.27 leave the state pure. In Eqn. 6.33 we saw that $|\psi\rangle_{\text{input}}$ goes to $c'_0|00\rangle + c'_1|01\rangle + c'_2|10\rangle + c'_3|11\rangle + c'_4|20\rangle + c'_5|02\rangle$

after a beam splitter. We want to consider the green sub-block in Eqn. 6.32 for this state:

$$\big(c_3'|11\rangle + c_4'|20\rangle + c_5'|02\rangle\big)\big(c_1'^{*}\langle 01| + c_2'^{*}\langle 10|\big). \tag{6.37}$$

Using Eqn. 6.27, after two photon absorption and single photon loss this becomes

$$\begin{pmatrix} c_3'c_1'^{*}e^{-\frac{3}{2}\mathcal{T}} & c_3'c_2'^{*}e^{-\frac{3}{2}\mathcal{T}} \\ c_4'c_1'^{*}e^{-(\frac{3}{2}+2\gamma)\mathcal{T}} & c_4'c_2'^{*}e^{-(\frac{3}{2}+2\gamma)\mathcal{T}} \\ c_5'c_1'^{*}e^{-(\frac{3}{2}+2\gamma)\mathcal{T}} & c_5'c_2'^{*}e^{-(\frac{3}{2}+2\gamma)\mathcal{T}} \end{pmatrix} \tag{6.38}$$

which is equal to

$$\big(c_3'e^{-\mathcal{T}}|11\rangle + c_4'e^{-(1+\gamma)\mathcal{T}}|20\rangle + c_5'e^{-(1+\gamma)\mathcal{T}}|02\rangle\big)\big(c_1'^{*}e^{-\frac{1}{2}\mathcal{T}}\langle 01| + c_2'^{*}e^{-\frac{1}{2}\mathcal{T}}\langle 10|\big). \tag{6.39}$$

If we put this sub-block through another beam splitter followed by two photon loss and single photon absorption we would obtain a similar result. We can therefore write down what this density matrix sub-block looks like after N beam splitter/absorption/loss combinations:

$$\begin{aligned} \rho_{(N)}^{(m+n=2,\,p+q=1)} &= \begin{pmatrix} d_{1101}^{(N)} & d_{1110}^{(N)} \\ d_{2001}^{(N)} & d_{2010}^{(N)} \\ d_{0201}^{(N)} & d_{0210}^{(N)} \end{pmatrix} \\ &= V_2 \cdot \begin{pmatrix} d_{1101}^{(N-1)} & d_{1110}^{(N-1)} \\ d_{2001}^{(N-1)} & d_{2010}^{(N-1)} \\ d_{0201}^{(N-1)} & d_{0210}^{(N-1)} \end{pmatrix} \cdot V_3^{\dagger} \\ &= (V_2)^N \cdot \begin{pmatrix} c_3c_1^* & c_3c_2^* \\ c_4c_1^* & c_4c_2^* \\ c_5c_1^* & c_5c_2^* \end{pmatrix} \cdot \left(V_3^{\dagger}\right)^N \\ &= (V_2)^N \left(c_3|11\rangle + c_4|20\rangle + c_5|02\rangle\right)\left(c_1^*\langle 01| + c_2^*\langle 10|\right)\left(V_3^{\dagger}\right)^N \end{aligned} \tag{6.40}$$

where

$$\begin{aligned} V_2 &= V_1 \\ V_3 &= \begin{pmatrix} e^{-\frac{1}{2}\mathcal{T}}\cos(\theta) & e^{-\frac{1}{2}\mathcal{T}}\sin(\theta) \\ -e^{-\frac{1}{2}\mathcal{T}}\sin(\theta) & e^{-\frac{1}{2}\mathcal{T}}\cos(\theta) \end{pmatrix} \end{aligned} \tag{6.41}$$

and V_2 and V_3 are easily diagonalisable. In the case that $c_4 = c_5 = 0$ for $|\psi\rangle_{\text{input}}$, as Eqn. 6.18, we can expand Eqn. 6.40 given V_1 and V_3 to find

$$\begin{aligned} d_{2001}^{(N)} &= -d_{0201}^{(N)} \\ d_{2010}^{(N)} &= -d_{0210}^{(N)}. \end{aligned} \tag{6.42}$$

If the initial state $|\psi\rangle_{\text{input}}$ was not pure, given instead by general initial density matrix $\rho(0)$ in Eqn. 6.11, we would have to solve this case by solving the recurrence equation

$$\begin{bmatrix} d^{(N)}_{1101} \\ d^{(N)}_{1110} \\ d^{(N)}_{2001} \\ d^{(N)}_{2010} \\ d^{(N)}_{0201} \\ d^{(N)}_{0210} \end{bmatrix} = (W)^N \begin{bmatrix} c_{1101} \\ d_{1110} \\ c_{2001} \\ c_{2010} \\ c_{0201} \\ c_{0210} \end{bmatrix} \tag{6.43}$$

where

$$W = \begin{pmatrix} EAB & EAC & \frac{1}{\sqrt{2}}EDB & \frac{1}{\sqrt{2}}EDC & -\frac{1}{\sqrt{2}}EDB & -\frac{1}{\sqrt{2}}EDC \\ EAC & EAB & \frac{1}{\sqrt{2}}EDC & \frac{1}{\sqrt{2}}EDB & -\frac{1}{\sqrt{2}}EDC & -\frac{1}{\sqrt{2}}EDB \\ -\frac{1}{\sqrt{2}}FDB & -\frac{1}{\sqrt{2}}FDC & FB^3 & FB^2C & FC^2B & FC^3 \\ -\frac{1}{\sqrt{2}}FDC & -\frac{1}{\sqrt{2}}FDB & FB^2C & FB^3 & FC^3 & FC^2B \\ \frac{1}{\sqrt{2}}FDB & \frac{1}{\sqrt{2}}FDC & FC^2B & FC^2C & FB^3 & FB^2C \\ \frac{1}{\sqrt{2}}FDC & \frac{1}{\sqrt{2}}FDB & FC^2C & FC^2B & FB^2C & FB^3 \end{pmatrix},$$

$A = \cos(2\theta), B = \cos(\theta), C = \sin(\theta), D = \sin(2\theta), E = e^{-\frac{3}{2}\mathcal{T}}$ and $F = e^{-(\frac{3}{2}+\gamma)\mathcal{T}}$. This would involve diagonalising the 6×6 matrix W, the resulting 6'th order polynomial having no known analytical solutions. For this reason, we require the initial state $|\psi\rangle_{\text{input}}$ to be pure.

The Cyan sub-block in Eqn. 6.32

As with the previous two cases, if we start with the pure state $|\psi_{\text{input}}\rangle$, the transformations in Eqns. 2.36 and 6.29 leave this state pure. In this case we want to consider the cyan sub-block in Eqn. 6.32. The corresponding terms we need to consider from Eqn. 6.33 for $|\psi\rangle_{\text{input}}$ after a beam splitter are:

$$\big(c_3'|11\rangle + c_4'|20\rangle + c_5'|02\rangle\big)c_0^{'*}\langle 00|. \tag{6.44}$$

After two photon absorption and single photon loss this sub-block becomes

$$\big(c_3' e^{-\mathcal{T}}|11\rangle + c_4' e^{-(1+\gamma)\mathcal{T}}|20\rangle + c_5' e^{-(1+\gamma)\mathcal{T}}|02\rangle\big)c_0^{'*}\langle 00|. \tag{6.45}$$

We can write the sub-block after N beam splitter/absoprtion/loss combinations as

$$\begin{aligned}\rho_{(N)}^{(m+n=2,\, p+q=0)} = \begin{bmatrix} d_{1100}^{(N)} \\ d_{2000}^{(N)} \\ d_{0200}^{(N)} \end{bmatrix} &= V_4 \cdot \begin{bmatrix} d_{1100}^{(N-1)} \\ d_{2000}^{(N-1)} \\ d_{0200}^{(N-1)} \end{bmatrix} \\ &= (V_4)^N \cdot \begin{bmatrix} c_3 c_0^* \\ c_4 c_0^* \\ c_5 c_0^* \end{bmatrix} \\ &= (V_4)^N \Big(c_3|11\rangle + c_4|20\rangle + c_5|02\rangle \Big) c_0^* \langle 00| \end{aligned} \tag{6.46}$$

where $V_4 = V_1$. In the case that $c_4 = c_5 = 0$ for $|\psi\rangle_{\text{input}}$, as in Eqn. 6.18, we have

$$\rho_{(N)}^{(m+n=2,\, p+q=0)} = c_3 c_0^* \, (V_4)^N \, |11\rangle\langle 00|.$$

The Blue sub-block in Eqn. 6.32

In this case the fact that our initial state is pure does not help solve for the general form of the blue sub-block in Eqn. 6.32 after N beam splitter/absortpion/loss combinations. We need to use a more general recurrence relation than that used in the previous cases. To formulate this general recurrence relation we will express the blue density matrix sub-block after N beam splitter/absortpion/loss combinations in terms of density matrix sub-blocks after $N-1$ beam splitter/absortpion/loss combinations.

We denote the blue density matrix sub-block after N beam splitter/absortpion/loss combinations by:

$$\begin{bmatrix} d_{0101}^{(N)} \\ d_{0110}^{(N)} \\ d_{1001}^{(N)} \\ d_{1010}^{(N)} \end{bmatrix}. \tag{6.47}$$

If we examine Eqn. 6.28, we see that $d_{0101}^{(N)}$, $d_{0110}^{(N)}$, $d_{1001}^{(N)}$ and $d_{1010}^{(N)}$ depend on both $c_{0101}, c_{0110}, c_{1001}, c_{1010}$ and $c_{1111}, c_{1120}, c_{1102}, c_{2011}, c_{2020}, c_{2002}, c_{0211}, c_{0220}, c_{0202}$, where we use that fact that $d_{0110}(\mathcal{T}) = d_{1001}(\mathcal{T})^*$. That is, the red and blue sub-blocks of the density matrix directly after the N'th beam splitter, shown as point (i) in fig. 6.4, contribute the the blue density matrix sub-block after the N'th two photon absorption/single photon loss.

We can express this abstractly as $\vec{d}^{(N)} = U\vec{d}^{(N-1)} + \vec{v}^{(N)}$, where $\vec{v}^{(N)}$ in this case is comprised of the red sub-block terms after $N-1$ beam splitters/absoprttion/loss combinations and one additional beam splitter. If we

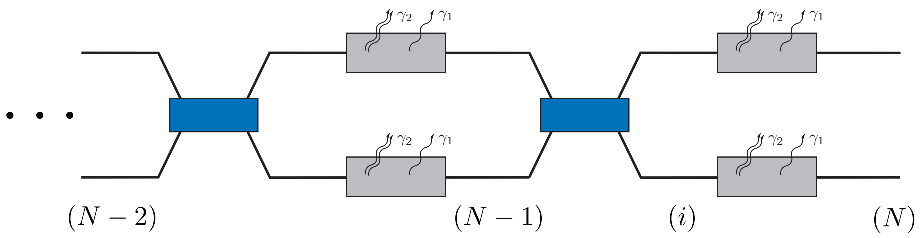

Figure 6.4: The (N-2)'th, (N-1)'th and (N)'th beam splitter/absoprtion/loss combination. At (i) there have been N beam splitters and only $N-1$ single photon losses and two photon absorption processes.

continue with the recurrence equation we see that

$$\vec{d}^{(N)} = U\vec{d}^{(N-1)} + \vec{v}^{(N)} = (U)^N \vec{d}^{(0)} + \sum_{i=1}^{N} (U)^{N-i}\, \vec{v}^{(i-1)}. \tag{6.48}$$

For the case of $\vec{d}^{(N)}$ equal to Eqn. 6.47 we have

$$\begin{bmatrix} d_{0101}^{(N)} \\ d_{0110}^{(N)} \\ d_{1001}^{(N)} \\ d_{1010}^{(N)} \end{bmatrix} = (V_5)^N \cdot \begin{bmatrix} |c_1|^2 \\ c_1 c_2^* \\ c_2 c_1^* \\ |c_2|^2 \end{bmatrix} + \sum_{i=1}^{N} (V_5)^{N-i} \cdot \vec{v}_{\text{blu}}^{(i-1)} \tag{6.49}$$

where $\vec{d}^{(0)} = (c_1|01\rangle + c_2|10\rangle)\,(c_1^*\langle 01| + c_2^*\langle 10|)$ and

$$V_5 = \begin{pmatrix} e^{-\mathcal{T}}\cos^2(\theta) & \frac{1}{2}e^{-\mathcal{T}}\sin(2\theta) & \frac{1}{2}e^{-\mathcal{T}}\sin(2\theta) & e^{-\mathcal{T}}\sin^2(\theta) \\ -\frac{1}{2}e^{-\mathcal{T}}\sin(2\theta) & e^{-\mathcal{T}}\cos^2(\theta) & -e^{-\mathcal{T}}\sin^2(\theta) & \frac{1}{2}e^{-\mathcal{T}}\sin(2\theta) \\ -\frac{1}{2}e^{-\mathcal{T}}\sin(2\theta) & -e^{-\mathcal{T}}\sin^2(\theta) & e^{-\mathcal{T}}\cos^2(\theta) & \frac{1}{2}e^{-\mathcal{T}}\sin(2\theta) \\ e^{-\mathcal{T}}\sin^2(\theta) & -\frac{1}{2}e^{-\mathcal{T}}\sin(2\theta) & -\frac{1}{2}e^{-\mathcal{T}}\sin(2\theta) & e^{-\mathcal{T}}\cos^2(\theta) \end{pmatrix}.$$

V_5 is easily diagonalisable. The vector $\vec{v}_{\text{blu}}^{(n)}$ is obtained from Eqns.2.36 and 6.26:

$$\vec{v}_{\text{blu}}^{(n)} = \begin{bmatrix} A_1 \\ A_2 \\ A_3 \\ A_4 \end{bmatrix} \tag{6.50}$$

where

$$\begin{aligned}
A_1 =&\frac{2e^{-2(1+\gamma)\mathcal{T}}(e^{(1+2\gamma)\mathcal{T}}-1)}{1+2\gamma}\Bigg(\cos^4(\theta)d^{(n)}_{0202}+\sin^4(\theta)d^{(n)}_{2020}+\frac{1}{2}\sin^2(2\theta)d^{(n)}_{1111}\\
&+\frac{1}{\sqrt{2}}\sin(2\theta)\sin^2(\theta)\Big(d^{(n)}_{1120}+d^{(n)}_{2011}\Big)+\frac{1}{\sqrt{2}}\sin(2\theta)\cos^2(\theta)\Big(d^{(n)}_{1102}+d^{(n)}_{0211}\Big)\\
&+\frac{1}{4}\sin^2(2\theta)\Big(d^{(n)}_{2002}+d^{(n)}_{0220}\Big)\Bigg)+e^{-2\mathcal{T}}(e^{\mathcal{T}}-1)\Bigg(\cos^2(2\theta)d^{(n)}_{1111}+\frac{1}{\sqrt{8}}\sin(4\theta)\Big(d^{(n)}_{1120}\\
&+d^{(n)}_{2011}-d^{(n)}_{1102}-d^{(n)}_{0211}\Big)+\frac{1}{2}\sin^2(2\theta)\Big(d^{(n)}_{0202}+d^{(n)}_{2020}-d^{(n)}_{0220}-d^{(n)}_{2002}\Big)\Bigg),\\
A_2 =&\frac{\sqrt{2}\big(e^{-\mathcal{T}}-e^{-(2+\gamma)\mathcal{T}}\big)}{1+\gamma}\Bigg(\cos^2(\theta)\Big(d^{(n)}_{1120}+d^{(n)}_{0211}\Big)-\sin^2(\theta)\Big(d^{(n)}_{1102}+d^{(n)}_{2011}\Big)\\
&\qquad\qquad+\frac{1}{\sqrt{2}}\sin(2\theta)\Big(d^{(n)}_{2020}-d^{(n)}_{0202}\Big)\Bigg),\\
A_3 =&\frac{\sqrt{2}\big(e^{-\mathcal{T}}-e^{-(2+\gamma)\mathcal{T}}\big)}{1+\gamma}\Bigg(\cos^2(\theta)\Big(d^{(n)}_{1102}+d^{(n)}_{2011}\Big)-\sin^2(\theta)\Big(d^{(n)}_{1120}+d^{(n)}_{0211}\Big)\\
&\qquad\qquad+\frac{1}{\sqrt{2}}\sin(2\theta)\Big(d^{(n)}_{2020}-d^{(n)}_{0202}\Big)\Bigg),
\end{aligned}$$

and

$$\begin{aligned}
A_4 =&\frac{2e^{-2(1+\gamma)\mathcal{T}}(e^{(1+2\gamma)\mathcal{T}}-1)}{1+2\gamma}\Bigg(\frac{1}{2}\sin^2(2\theta)d^{(n)}_{1111}+\cos^4(\theta)d^{(n)}_{2020}+\sin^4(\theta)d^{(n)}_{0202}\\
&-\frac{1}{\sqrt{2}}\sin(2\theta)\sin^2(\theta)\Big(d^{(n)}_{1102}+d^{(n)}_{0211}\Big)-\frac{1}{\sqrt{2}}\cos^2(\theta)\sin(2\theta)\Big(d^{(n)}_{2011}+d^{(n)}_{1120}\Big)\\
&+\frac{1}{4}\sin^2(2\theta)\Big(d^{(n)}_{2002}+d^{(n)}_{0220}\Big)\Bigg)+e^{-2\mathcal{T}}(e^{\mathcal{T}}-1)\Bigg(\cos^2(2\theta)d^{(n)}_{1111}+\frac{1}{\sqrt{8}}\sin(4\theta)\Big(d^{(n)}_{1120}\\
&+d^{(n)}_{2011}-d^{(n)}_{1102}-d^{(n)}_{0211}\Big)+\frac{1}{2}\sin^2(2\theta)\Big(d^{(n)}_{0202}+d^{(n)}_{2020}-d^{(n)}_{0220}-d^{(n)}_{2002}\Big)\Bigg).
\end{aligned}$$

In the case that $c_4 = c_5 = 0$ for $|\psi\rangle_{\text{input}}$, as Eqn. 6.18, we can use Eqn. 6.36 to simplify $\vec{v}^{(n)}_{\text{blu}}$:

$$\begin{aligned}
A_1 =&\frac{2e^{-2(1+\gamma)\mathcal{T}}(e^{(1+2\gamma)\mathcal{T}}-1)}{1+2\gamma}\Bigg(\Big(\cos^4(\theta)+\sin^4(\theta)\Big)d^{(n)}_{2020}+\frac{1}{2}\sin^2(2\theta)d^{(n)}_{1111}\\
&+\frac{1}{2}\sin^2(2\theta)d^{(n)}_{2002}\Bigg)+e^{-2\mathcal{T}}(e^{\mathcal{T}}-1)\Bigg(\cos^2(2\theta)d^{(n)}_{1111}+\sqrt{2}\sin(4\theta)d^{(n)}_{1120}\\
&+\sin^2(2\theta)\Big(d^{(n)}_{2020}-d^{(n)}_{2002}\Big)\Bigg),\\
A_2 =&0,\\
A_3 =&0\\
&\text{and}\\
A_4 =&A_1.
\end{aligned}$$

With this simplification we can generate an analytical expression for the sum in Eqn. 6.49.

The Yellow sub-block in Eqn. 6.32

We use the recurrence equation in Eqn. 6.48 to solve for the yellow sub-block in Eqn. 6.32.

We find

$$\begin{bmatrix} d^{(N)}_{0100} \\ d^{(N)}_{1000} \end{bmatrix} = (V_6)^N \cdot \begin{bmatrix} c_1 c_0^* \\ c_2 c_0^* \end{bmatrix} + \sum_{i=1}^{N} (V_6)^{N-i} \cdot \vec{v}^{\,(i-1)}_{\text{yel}} \tag{6.51}$$

where $\vec{d}^{(0)} = (c_1|01\rangle + c_2|10\rangle)\, c_0^* \langle 00|$, $V_6 = V_3$ (Eqn. 6.41) and

$$\vec{v}^{\,(n)}_{\text{yel}} = \begin{bmatrix} A_5 \\ A_6 \end{bmatrix} \tag{6.52}$$

where

$$\begin{aligned} A_5 = & \frac{\sqrt{2} e^{-\frac{1}{2}\mathcal{T}} (1 - e^{-(1+\gamma)\mathcal{T}})}{1+\gamma} \Big(\cos^3(\theta) d^{(n)}_{0201} + \sin^3(\theta) d^{(n)}_{2010} \\ & + \sin^2(\theta)\cos(\theta) \Big(d^{(n)}_{2001} + \sqrt{2} d^{(n)}_{1110} \Big) + \cos^2(\theta)\sin(\theta) \Big(d^{(n)}_{0210} + \sqrt{2} d^{(n)}_{1101} \Big) \Big) \\ & + e^{-\frac{1}{2}\mathcal{T}} (1 - e^{-\mathcal{T}}) \Big(\cos(2\theta) \Big(\cos(\theta) d^{(n)}_{1110} - \sin(\theta) d^{(n)}_{1101} \Big) \\ & + \frac{1}{\sqrt{2}} \sin(2\theta) \Big(\cos(\theta) (d^{(n)}_{2010} - d^{(n)}_{0210}) + \sin(\theta) (d^{(n)}_{0201} - d^{(n)}_{2001}) \Big) \Big) \end{aligned}$$

and

$$\begin{aligned} A_6 = & \frac{\sqrt{2} e^{-\frac{1}{2}\mathcal{T}} (1 - e^{-(1+\gamma)\mathcal{T}})}{1+\gamma} \Big(\cos^3(\theta) d^{(n)}_{2010} - \sin^3(\theta) d^{(n)}_{0201} \\ & - \cos^2(\theta)\sin(\theta) \Big(d^{(n)}_{2001} + \sqrt{2} d^{(n)}_{1110} \Big) + \sin^2(\theta)\cos(\theta) \Big(d^{(n)}_{0210} + \sqrt{2} d^{(n)}_{1101} \Big) \Big) \\ & + e^{-\frac{1}{2}\mathcal{T}} (1 - e^{-\mathcal{T}}) \Big(\cos(2\theta) \Big(\sin(\theta) d^{(n)}_{1110} + \cos(\theta) d^{(n)}_{1101} \Big) \\ & + \frac{1}{\sqrt{2}} \sin(2\theta) \Big(\sin(\theta) (d^{(n)}_{2010} - d^{(n)}_{0210}) + \cos(\theta) (d^{(n)}_{2001} - d^{(n)}_{0201}) \Big) \Big). \end{aligned}$$

In the case that $c_4 = c_5 = 0$ for $|\psi\rangle_{\text{input}}$, as Eqn. 6.18, we can use Eqn. 6.42 to simplify $\vec{v}^{\,(n)}_{\text{yel}}$:

$$\begin{aligned} A_5 = & \frac{\sqrt{2} e^{-\frac{1}{2}\mathcal{T}} (1 - e^{-(1+\gamma)\mathcal{T}})}{1+\gamma} \Big(\cos(2\theta) \Big(\cos(\theta) d^{(n)}_{0201} - \sin(\theta) d^{(n)}_{2010} \Big) \\ & + \frac{1}{\sqrt{2}} \sin(2\theta) \Big(\sin(\theta) d^{(n)}_{1110} + \cos(\theta) d^{(n)}_{1101} \Big) \\ & + e^{-\frac{1}{2}\mathcal{T}} (1 - e^{-\mathcal{T}}) \Big(\cos(2\theta) \Big(\cos(\theta) d^{(n)}_{1110} - \sin(\theta) d^{(n)}_{1101} \Big) \\ & + \sqrt{2} \sin(2\theta) \Big(\cos(\theta) d^{(n)}_{2010} + \sin(\theta) d^{(n)}_{0201} \Big) \Big) \end{aligned}$$

and

$$\begin{aligned}
A_6 =&\frac{\sqrt{2}e^{-\frac{1}{2}\mathcal{T}}(1-e^{-(1+\gamma)\mathcal{T}})}{1+\gamma}\Big(\cos(2\theta)\Big(\cos(\theta)d^{(n)}_{2010}+\sin(\theta)d^{(n)}_{0201}\Big)\\
&+\frac{1}{\sqrt{2}}\sin(2\theta)\Big(\sin(\theta)d^{(n)}_{1101}-\cos(\theta)d^{(n)}_{1110}\Big)\\
&+e^{-\frac{1}{2}\mathcal{T}}(1-e^{-\mathcal{T}})\Big(\cos(2\theta)\Big(\cos(\theta)d^{(n)}_{1101}+\sin(\theta)d^{(n)}_{1110}\Big)\\
&+\sqrt{2}\sin(2\theta)\Big(\cos(\theta)d^{(n)}_{0201}+\sin(\theta)d^{(n)}_{2010}\Big)\Big).
\end{aligned}$$

With this simplification we can generate an analytical expression for the sum in Eqn. 6.51.

The Magenta sub-block in Eqn. 6.32

We use the recurrence equation in Eqn. 6.48 to solve for the magenta sub-block in Eqn. 6.32. In this case $U=\mathbb{1}$ in Eqn. 6.48:

$$d^{(N)}_{0000}=c_0c_0^*+\sum_{i=1}^{N}v^{(i-1)}_{\text{mag}} \tag{6.53}$$

where

$$\begin{aligned}
v^{(n)}_{\text{mag}} =&(1-e^{-\mathcal{T}})\left(d^{(n)}_{1010}+d^{(n)}_{0101}\right)+(1-e^{-\mathcal{T}})^2\Big(\cos^2(2\theta)d^{(n)}_{1111}\\
&+\frac{1}{\sqrt{8}}\sin(4\theta)\Big(d^{(n)}_{2011}+d^{(n)}_{1120}-d^{(n)}_{0211}-d^{(n)}_{1102}\Big)\\
&+\frac{1}{2}\sin^2(2\theta)\Big(d^{(n)}_{0202}+d^{(n)}_{2020}-d^{(n)}_{0220}-d^{(n)}_{2002}\Big)\Big)\\
&+\frac{2\gamma(1-e^{-2(1+\gamma)\mathcal{T}})+(1-2e^{-\mathcal{T}}+e^{-2(1+\gamma)\mathcal{T}})}{1+2\gamma}\Big(\sin^2(2\theta)d^{(n)}_{1111}\\
&+\frac{1}{4}\Big(3+\cos(4\theta)\Big)\Big(d^{(n)}_{0202}+d^{(n)}_{2020}\Big)+\frac{1}{\sqrt{8}}\sin(4\theta)\Big(d^{(n)}_{1102}+d^{(n)}_{0211}-d^{(n)}_{2011}-d^{(n)}_{1120}\Big)\\
&+\frac{1}{2}\sin^2(2\theta)\Big(d^{(n)}_{0220}+d^{(n)}_{2002}\Big)\Big).
\end{aligned}$$

In the case that $c_4=c_5=0$ for $|\psi\rangle_{\text{input}}$, as Eqn. 6.18, we can use Eqn. 6.36 to simplify $v^{(n)}_{\text{mag}}$:

$$\begin{aligned}
v^{(n)}_{\text{mag}} =&(1-e^{-\mathcal{T}})\left(d^{(n)}_{1010}+d^{(n)}_{0101}\right)+(1-e^{-\mathcal{T}})^2\Big(\cos^2(2\theta)d^{(n)}_{1111}+\sqrt{2}\sin(4\theta)d^{(n)}_{1120}\\
&+\sin^2(2\theta)\Big(d^{(n)}_{2020}-d^{(n)}_{2002}\Big)\Big)\\
&+\frac{2\gamma(1-e^{-2(1+\gamma)\mathcal{T}})+(1-2e^{-\mathcal{T}}+e^{-2(1+\gamma)\mathcal{T}})}{1+2\gamma}\Big(\sin^2(2\theta)d^{(n)}_{1111}\\
&+\frac{1}{2}\Big(3+\cos(4\theta)\Big)d^{(n)}_{2020}-\sqrt{2}\sin(4\theta)d^{(n)}_{1120}+\sin^2(2\theta)d^{(n)}_{2002}\Big).
\end{aligned}$$

With this simplification we can generate an analytical expression for the sum due to the $d^{(n)}_{1111}, d^{(n)}_{2020}, d^{(n)}_{1120}, d^{(n)}_{2002}$ terms and the double sum due to the $d^{(n)}_{1010}, d^{(n)}_{0101}$ terms in Eqn. 6.53.

6.3 Process Fidelity

We now have two realistic models for the optical Zeno CSIGN gate proposed by Franson *et al.* in [50, 101]. We can either solve equations 6.12–6.17 to find density matrix $\rho_{\text{cont}}(t)$ at any time t within the interaction region in Fig. 6.1, or we can solve the recurrence equations 6.35–6.53 to find the density matrix $\rho_{\text{bs}}(t)$ after N beam spitter/absorption/loss combinations in Fig. 6.3, given there is continuous two photon absorption and single photon loss for a time t/N after each beam splitter.

We now want to quantify what effect realistic two photon absorption and single photon loss has on the CSIGN gate operation. We do this by measuring the *closeness* of our density matrix $\rho(t)$ to the density matrix resulting from an ideal CSIGN gate. We use the process fidelity for this, as described in Section 2.3.

For a single rail CSIGN, consider applying a CSIGN to modes 3 and 4 of $|\psi_{\text{SR}}\rangle$, where

$$|\psi_{\text{SR}}\rangle = \frac{1}{2}\sum_{a,b=0}^{1} |ab\rangle \otimes |ab\rangle = \frac{1}{2}\left(|00\rangle|00\rangle + |01\rangle|01\rangle + |10\rangle|10\rangle + |11\rangle|11\rangle\right)_{1234} \quad (6.54)$$

or in terms of an input density matrix this is equivalent to

$$\rho_{\text{SR}} = \frac{1}{4}\sum_{a,b,c,d=0}^{1} |ab\rangle\langle cd| \otimes |ab\rangle\langle cd|. \quad (6.55)$$

The output will be

$$\begin{aligned}\rho^{(CZ)}_{\text{SR}} &= \frac{1}{4}\sum_{a,b,c,d=0}^{1} |ab\rangle\langle cd| \otimes U_{\text{CZ}}|ab\rangle\langle cd|U^{\dagger}_{\text{CZ}} \\ &= \frac{1}{4}\sum_{a,b,c,d=0}^{1} (-1)^{ab+cd}\,|ab\rangle\langle cd| \otimes |ab\rangle\langle cd| \end{aligned} \quad (6.56)$$

where U_{CZ} is the unitary associated with a CSIGN, given in Eqn. 2.74

Next, consider modes 3 and 4 of Eqn. 6.55 incident on Fig. 6.1 or 6.3. The output will be

$$\rho^{(\mathcal{E})}_{\text{SR}} = \frac{1}{4}\sum_{a,b,c,d=0}^{1} |ab\rangle\langle cd| \otimes \mathcal{E}\left(|ab\rangle\langle cd|\right) \quad (6.57)$$

where $\mathcal{E}$ describes the action of Fig. 6.1 or 6.3 on modes 3 and 4 of the state $|\psi_{\text{SR}}\rangle$.

To calculate the process fidelity we work out the fidelity between ρ_{CZ} and $\rho_{\mathcal{E}}$, given the fact that $\rho_{\mathrm{SR}}^{(\mathrm{CZ})}$ is pure:

$$\begin{aligned}
F_{\mathrm{pro}}^{(\mathrm{SR})} &= \mathrm{Tr}\left[\rho_{\mathrm{SR}}^{(CZ)} \cdot \rho_{\mathrm{SR}}^{(\mathcal{E})}\right] \\
&= \frac{1}{16}\mathrm{Tr}\left[\sum_{a,b,c,d=0}^{1} (-1)^{ab+cd} |ab\rangle\langle cd| \otimes |ab\rangle\langle cd| \cdot \sum_{m,n,p,q=0}^{1} |mn\rangle\langle pq| \otimes \mathcal{E}\left(|mn\rangle\langle pq|\right)\right] \\
&= \frac{1}{16}\mathrm{Tr}\left[\sum_{a,b,c,d=0}^{1} (-1)^{ab+cd} |ab\rangle\langle cd| \cdot \mathcal{E}\left(|ab\rangle\langle cd|\right)\right] \qquad (6.58)
\end{aligned}$$

where we have used $\langle a|b\rangle = \delta_{ab}$. If we were to perform a single rail CSIGN, we would need arbitrary single qubits rotations which are quite difficult to perform, at best requiring applications of the CSIGN [120].

For a dual rail CSIGN, consider applying a CSIGN to modes 5,6,7 and 8 of $|\psi_{\mathrm{DR}}\rangle$, where

$$\begin{aligned}
|\psi_{\mathrm{DR}}\rangle &= \frac{1}{2}\left(|00\rangle_L|00\rangle_L + |01\rangle_L|01\rangle_L + |10\rangle_L|10\rangle_L + |11\rangle_L|11\rangle_L\right) \\
&= \frac{1}{2}\left(|0101\rangle|0101\rangle + |0110\rangle|0110\rangle + |1001\rangle|1001\rangle + |1010\rangle|1010\rangle\right)_{12345678} \\
&= \frac{1}{2}\sum_{a,b=0}^{1} |a\bar{a}b\bar{b}\rangle \otimes |a\bar{a}b\bar{b}\rangle \qquad (6.59)
\end{aligned}$$

and $\bar{a} = (a+1) \bmod 2$. Since a dual rail CSIGN is equivalent to a single rail CSIGN, this is equivalent to applying the single rail CSIGN to modes 5 and 7 of $|\psi_{\mathrm{DR}}\rangle$.

In terms of an input density matrix, $|\psi_{\mathrm{DR}}\rangle$ is equivalent to

$$\begin{aligned}
\rho_{\mathrm{DR}} &= \frac{1}{4}\sum_{a,b,c,d=0}^{1} |a\bar{a}b\bar{b}\rangle\langle c\bar{c}d\bar{d}| \otimes |a\bar{a}b\bar{b}\rangle\langle c\bar{c}d\bar{d}| \\
&= \frac{1}{4}\sum_{a,b,c,d=0}^{1} |ab\rangle\langle cd| \otimes |\overline{ab}\rangle\langle\overline{cd}| \otimes |ab\rangle\langle cd| \otimes |\overline{ab}\rangle\langle\overline{cd}| \qquad (6.60)
\end{aligned}$$

where we have reordered the modes in the second line. The output of the ideal CSIGN will be

$$\begin{aligned}
\rho_{\mathrm{DR}}^{(CZ)} &= \frac{1}{4}\sum_{a,b,c,d=0}^{1} |ab\rangle\langle cd| \otimes |\overline{ab}\rangle\langle\overline{cd}| \otimes U_{\mathrm{CZ}}|ab\rangle\langle cd|U_{\mathrm{CZ}}^{\dagger} \otimes |\overline{ab}\rangle\langle\overline{cd}| \\
&= \frac{1}{4}\sum_{a,b,c,d=0}^{1} (-1)^{ab+cd} |ab\rangle\langle cd| \otimes |\overline{ab}\rangle\langle\overline{cd}| \otimes |ab\rangle\langle cd| \otimes |\overline{ab}\rangle\langle\overline{cd}|. \qquad (6.61)
\end{aligned}$$

Next, consider the third sub-system of ρ_{DR} in Eqn. 6.60 incident on either Fig. 6.1 or 6.3. The output will be

$$\rho_{\mathrm{DR}}^{(\mathcal{E})} = \frac{1}{4}\sum_{a,b,c,d=0}^{1} |ab\rangle\langle cd| \otimes |\overline{ab}\rangle\langle\overline{cd}| \otimes \mathcal{E}\left(|ab\rangle\langle cd|\right) \otimes |\overline{ab}\rangle\langle\overline{cd}| \qquad (6.62)$$

where $\mathcal{E}$ describes the action of Fig. 6.1 or 6.3 on modes 5 and 7 of the state $|\psi_{\mathrm{DR}}\rangle$.

To calculate the process fidelity we work out the fidelity between ρ_{CZ} and $\rho_{\mathcal{E}}$, given the fact that $\rho_{\mathrm{DR}}^{(\mathrm{CZ})}$ is pure:

$$\begin{aligned}
F_{\mathrm{pro}}^{(\mathrm{DR})} &= \mathrm{Tr}\left[\rho_{\mathrm{DR}}^{(CZ)} \cdot \rho_{\mathrm{DR}}^{(\mathcal{E})}\right] \\
&= \frac{1}{16}\mathrm{Tr}\Bigg[\sum_{a,b,c,d=0}^{1} (-1)^{ab+cd} |ab\rangle\langle cd| \otimes |\overline{ab}\rangle\langle\overline{cd}| \otimes |ab\rangle\langle cd| \otimes |\overline{ab}\rangle\langle\overline{cd}| \\
&\qquad\qquad \cdot \sum_{m,n,p,q=0}^{1} |mn\rangle\langle pq| \otimes |\overline{mn}\rangle\langle\overline{pq}| \otimes \mathcal{E}\left(|mn\rangle\langle pq|\right) \otimes |\overline{mn}\rangle\langle\overline{pq}|\Bigg] \\
&= \frac{1}{16}\mathrm{Tr}\left[\sum_{a,b,c,d=0}^{1} (-1)^{ab+cd} |ab\rangle\langle cd| \cdot \mathcal{E}\left(|ab\rangle\langle cd|\right)\right]. \qquad (6.63)
\end{aligned}$$

We see that the process fidelity for the single rail case, $F_{\mathrm{pro}}^{(\mathrm{SR})}$ in Eqn. 6.58, is equal to the process fidelity for the dual rail case, $F_{\mathrm{pro}}^{(\mathrm{DR})}$ in Eqn. 6.63.

We calculate an analytical expression for the process fidelity $F_{\mathrm{pro}}^{(\mathrm{SR})}$ and plot it in Figs. 6.5–6.10 for both the continuous interaction case in Section 6.1 and the beam splitter case in Section 6.2.

If we consider the continuous interaction from Section 6.1 alone, we see the relationship of the process fidelity with τ for various γ values in Fig. 6.5.

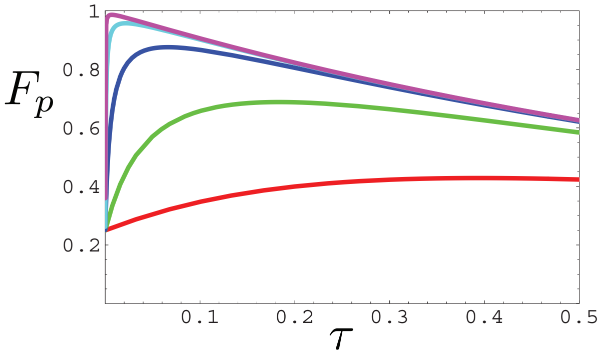

Figure 6.5: The process fidelity for the continuous interaction case, as solved for in Section 6.1. The Red curve represents $\gamma = 10$, the Green curve represents $\gamma = 100$, the Blue curve represents $\gamma = 1000$, the Cyan curve represents $\gamma = 10000$ and the Magenta curve represents $\gamma = 100000$.

If we consider the beam splitter case from Section 6.2 alone, we see the relationship of the process fidelity with τ for a varying number of beam splitters for constant γ in Fig. 6.6.

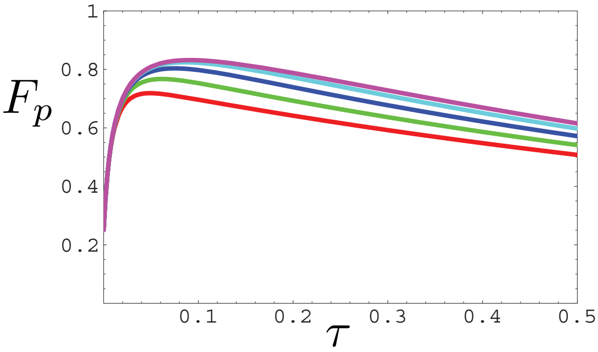

Figure 6.6: The process fidelity for the beam splitter case, as solved for in Section 6.2. Here γ was set to 500. The Red curve represents 7 beam splitters, the Green curve represents 11 beam splitters, the Blue curve represents 19 beam splitters, the Cyan curve represents 39 beam splitters and the Magenta curve represents 199 beam splitters.

Now, we consider the beam splitter case again but instead we vary γ with the number of beam splitters kept constant, as shown in Fig. 6.7

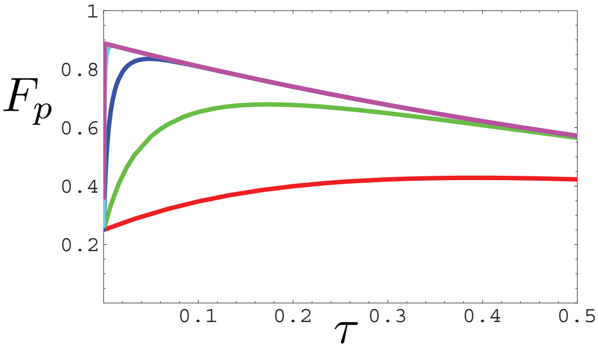

Figure 6.7: The process fidelity for the beam splitter case, as solved for in Section 6.2. Here we consider the 19 beam splitter case. The Red curve represents $\gamma = 10$, the Green curve represents $\gamma = 100$, the Blue curve represents $\gamma = 1000$, the Cyan curve represents $\gamma = 10000$ and the Magenta curve represents $\gamma = 100000$.

To compare the continuous interaction case to the beam splitter case we plot the process fidelity for both cases together in Fig. 6.8. Notice that for the $\gamma = 20$ case, the continuous interaction and beam splitter case are almost identical. As the γ increases, the continuous interaction case peaks to a higher fidelity than the beam splitter case and drops off at a slower rate.

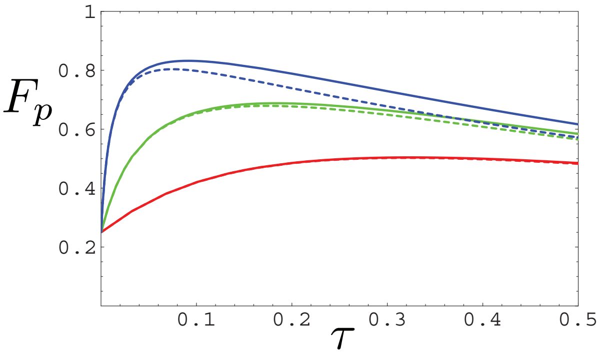

Figure 6.8: The process fidelity for both the continuous interaction and the beam splitter case. The continuous interaction case is given by the solid curves and the 19 beam splitter case is given by the dashed curves. The Red curve represents $\gamma = 20$, the Green curve represents $\gamma = 100$ and the Blue curve represents $\gamma = 500$.

Notice that for each case in Figs. 6.5–6.8, the fidelity peaked for some $\tau = \tau_{\text{opt}}$ value. Also notice that this peak never reached unity. We can explain the presence of the optimal τ_{opt} by considering the two extremes.

If the interaction time is too short, then there has been insufficient two photon absorption for the gate to operate as a CSIGN Consider the case that the gate does nothing to the input state given in Eqn. 6.55. If we calculate the process fidelity between ρ_{SR} and the ideal CSIGN density matrix $\rho_{\text{SR}}^{(CZ)}$ given in Eqn. 6.56, we find

$$\begin{aligned} F_{\text{pro}} &= \text{Tr}\left[\rho_{\text{SR}}^{(CZ)} \cdot \rho_{\text{SR}}\right] \\ &= \frac{1}{16}\text{Tr}\left[\sum_{a,b,c,d=0}^{1} (-1)^{ab+cd} |ab\rangle\langle cd| \otimes |ab\rangle\langle cd| \cdot \sum_{m,n,p,q=0}^{1} |mn\rangle\langle pq| \otimes |mn\rangle\langle pq|\right] \\ &= \frac{1}{16} \sum_{a,b,c,d=0}^{1} (-1)^{ab+cd} = \frac{1}{4}. \end{aligned} \tag{6.64}$$

This is the $\tau \to 0$ limit in each of the graphs in Figs. 6.5–6.9.

If the interaction time is too long, then single photon loss starts to dominate. That is, if single photon loss dominates then we expect the state $\rho_{\text{SR}}^{(\mathcal{E})}$ in Eqn. 6.57 to eventually become $\frac{1}{4}\sum_{a,b,c,d=0}^{1} |ab\rangle\langle cd| \otimes |00\rangle\langle 00|$. If we calculate the fidelity of this state with respect to the ideal CSIGN density matrix $\rho_{\text{SR}}^{(CZ)}$, we find

$$\begin{aligned} F_{\text{pro}} &= \frac{1}{16}\text{Tr}\left[\sum_{a,b,c,d=0}^{1} (-1)^{ab+cd} |ab\rangle\langle cd| \otimes |ab\rangle\langle cd| \cdot \sum_{m,n,p,q=0}^{1} |mn\rangle\langle pq| \otimes |00\rangle\langle 00|\right] \\ &= \frac{1}{16}. \end{aligned} \tag{6.65}$$

The fidelity for each of the graphs in Figs. 6.5–6.8 approaches $\frac{1}{16}$ as $\tau \to \infty$. This can be seen explicitly in Fig. 6.9.

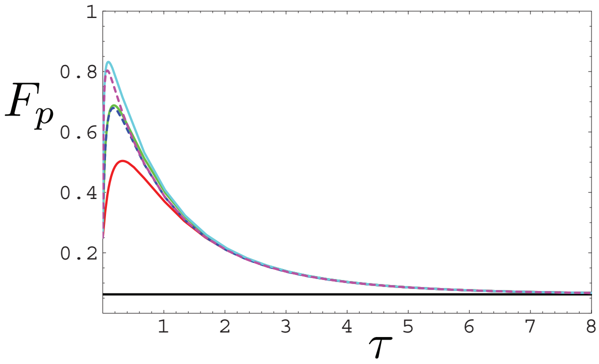

Figure 6.9: The long τ limit process fidelity for both the continuous interaction and the beam splitter case, as in Fig. 6.8. The continuous interaction case is given by the solid curves and the 19 beam splitter case is given by the dashed curves. The Red curve represents $\gamma = 20$, the Green curve represents $\gamma = 100$ and the Blue curve represents $\gamma = 500$. The solid **Black** line corresponds to $F_p = \frac{1}{16}$.

Since too short an interaction corresponds to insufficient two photon absorption, and too long an interaction time corresponds to single photon loss domination, it follows that there is a peak in the process fidelity for some $\tau = \tau_{\text{opt}}$. That is, there will be a peak when there has been enough two photon absorption for a CSIGN gate to be created and when single photon loss has not begun to dominate. In Fig. 6.10 we show how the optimised ($\tau = \tau_{\text{opt}}$) process fidelity scales with γ for both the continuous interaction and beam splitter case. Even at high γ values the process fidelity cannot reach unity because of the presence of singe photon loss. As the number of beam splitters increases the peak process fidelity becomes closer to the continuous interaction case. The beam splitter fidelity is always less than the continuous case since the beam splitter case only approximates a CSIGN gate. Only in the limit of a large number of beam splitters does the beam splitter case resemble a CSIGN, as described in Section 6.2.1.

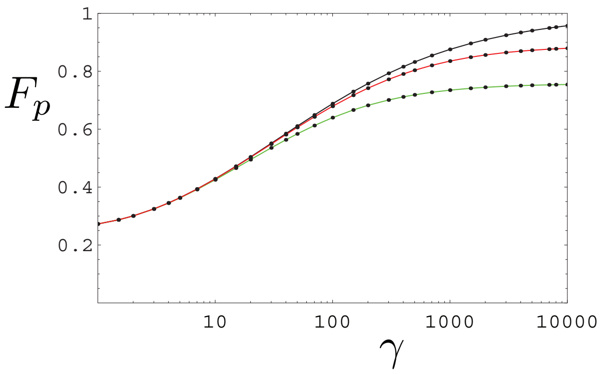

Figure 6.10: The scaling of the process fidelity with γ for $\tau = \tau_{\text{opt}}$ (separate optimisation for each point shown). The **Black** line represents the continuous interaction case, the Red line represents the 19 beam splitter case and the Green line represents the 7 beam splitter case.

6.3.1 Comparing the beam splitter case to the ideal beam splitter case

When we consider the beam splitter case in Fig. 6.6, 6.7 and 6.8, we worked out the process fidelity with respect to the ideal CSIGN, as shown in Eqns. 6.58 and 6.63. However, as shown in Section 6.2.1, the ideal beam splitter case is only a CSIGN for a large number of beam splitters. We can further analyse the beam splitter case by measuring the closeness of our density matrix $\rho_{\text{bs}}(t)$ worked out in Eqns. 6.35–6.53 to the ideal beam splitter case given in Eqn. 6.23.

We work out the process fidelity for the single rail case, since we know the single rail case is equivalent to the dual rail case:

$$\begin{aligned} F_{\text{pro}}^{(\text{SR:BS})} &= \text{Tr}\left[\rho_{\text{SR}}^{(BS)} \cdot \rho_{\text{SR}}^{(\mathcal{E})}\right] \\ &= \frac{1}{16}\text{Tr}\left[\rho_{\text{SR}}^{(BS)} \cdot \sum_{m,n,p,q=0}^{1} |mn\rangle\langle pq| \otimes \mathcal{E}\left(|mn\rangle\langle pq|\right)\right] \end{aligned} \tag{6.66}$$

where $\rho_{\text{SR}}^{(BS)} = |\psi_{\text{SR}}^{(BS)}\rangle\langle\psi_{\text{SR}}^{(BS)}|$ and $|\psi_{\text{SR}}^{(BS)}\rangle$ is the ideal beam splitter output state in Eqn. 6.23 given the maximally entangle input state in Eqn. 6.54:

$$|\psi_{\text{SR}}^{(BS)}\rangle = \frac{1}{\mathcal{N}}\left(|00\rangle|00\rangle + |01\rangle|01\rangle + |10\rangle|10\rangle - \cos^{2m-1}\left(-\frac{\pi}{2m-1}\right)|11\rangle|11\rangle\right) \tag{6.67}$$

where $m = 2, 4, 6, \cdots$ and

$$\mathcal{N} = \sqrt{1 + \frac{1}{4}\left(\cos^{4m-2}\left(-\frac{\pi}{2m-1}\right) - 1\right)}. \tag{6.68}$$

We calculate an analytical expression for the process fidelity $F_{\text{pro}}^{(\text{SR:BS})}$ and plot it in Figs. 6.11–6.15.

In Fig. 6.11 we see the relationship between the process fidelity and τ for various γ values with the number of beam splitters set at 99. Notice that as γ increases, the peak process fidelity increases. The peak fidelity is always less than unity due to the presence of single photon loss.

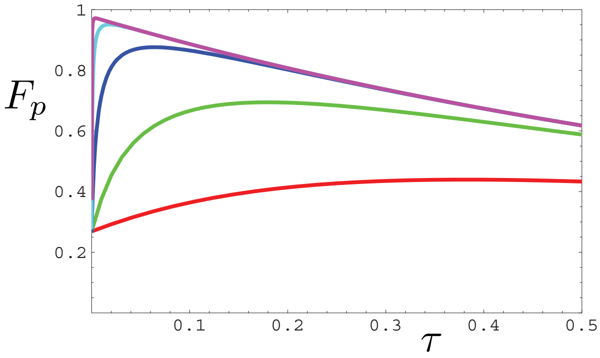

Figure 6.11: The process fidelity for comparison with the ideal beam splitter case. Here we consider the 99 beam splitter case. The Red curve represents $\gamma = 10$, the Green curve represents $\gamma = 100$, the Blue curve represents $\gamma = 1000$, the Cyan curve represents $\gamma = 10000$ and the Magenta curve represents $\gamma = 100000$.

In Fig. 6.11 the process fidelity approaches $\frac{1}{16}$ as $\tau \to \infty$, shown explicitly in Fig. 6.12. To show this we perform a similar calculation to that in Eqn. 6.65.

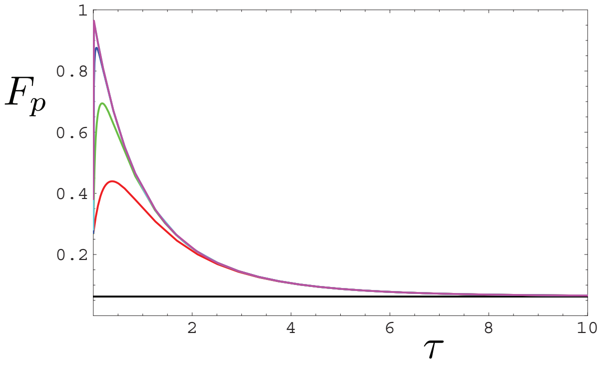

Figure 6.12: The long τ limit process fidelity for the beam splitter case, as in Fig. 6.11. Here we consider the 99 beam splitter case. The Red curve represents $\gamma = 10$, the Green curve represents $\gamma = 100$, the Blue curve represents $\gamma = 1000$, the Cyan curve represents $\gamma = 10000$ and the Magenta curve represents $\gamma = 100000$. The solid **Black** line corresponds to $F_p = \frac{1}{16}$.

In Fig. 6.13 we see the relationship between the process fidelity and τ for a varying number of beam splitters, with $\gamma = 500$. The peak fidelity increases as the number of beam splitters increases. Notice that this case is different to that in Fig. 6.6, in that the curves for different numbers of beam splitters cross. Also notice that none of the process fidelity curves approach $\frac{1}{4}$ as $\tau \to 0$. As $\tau \to 0$, the output of our gate will be close to the input ρ_{SR} given in Eqn. 6.55. If we work out the process fidelity between this state and $\rho_{\mathrm{SR}}^{(\mathrm{BS})}$ given in Eqn. 6.67, we find

$$\begin{aligned} F_{\mathrm{pro}} &= \mathrm{Tr}\left[\rho_{\mathrm{SR}}^{(BS)} \cdot \rho_{\mathrm{SR}}\right] \\ &= \frac{\left(\cos^N\left(\frac{\pi}{N}\right) - 3\right)^2}{4\left(3 + \cos^{2N}\left(\frac{\pi}{N}\right)\right)}. \end{aligned} \tag{6.69}$$

This shows that in the case that $\tau = 0$, the lower the number of beam splitters, the closer the output state is to $\rho_{\mathrm{SR}}^{(\mathrm{BS})}$. This is shown in Fig. 6.14. For example, for the 7 beam splitter case in Fig. 6.13, we see that the process fidelity for $\tau = 0$ is 0.5, which is confirmed in Fig. 6.14. However, the 11 beam splitter case has a process fidelity of 0.41 for $\tau = 0$. For a low number of beam splitters, the peak process fidelity is limited since there is insufficient interaction.

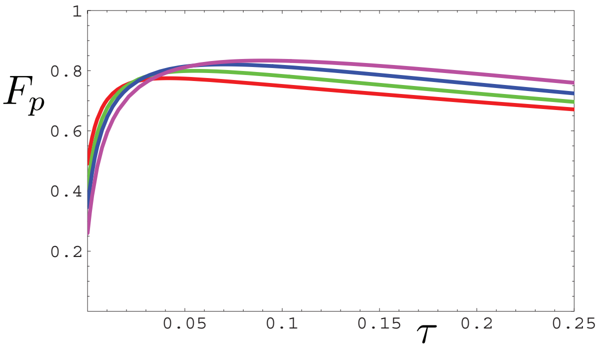

Figure 6.13: The process fidelity for comparison with the ideal beam splitter case. Here we consider the $\gamma = 500$. The Red curve represents 7 beam splitters, the Green curve represents 11 beam splitters, the Blue curve represents 19 beam splitters, and the Magenta curve represents 199 beam splitters.

In Fig. 6.15 we show how the optimised ($\tau = \tau_{opt}$) process fidelity scales with γ for this beam splitter comparison case. This figure emphasises the point made above, that lower beam splitter numbers are desired for smaller γ values.

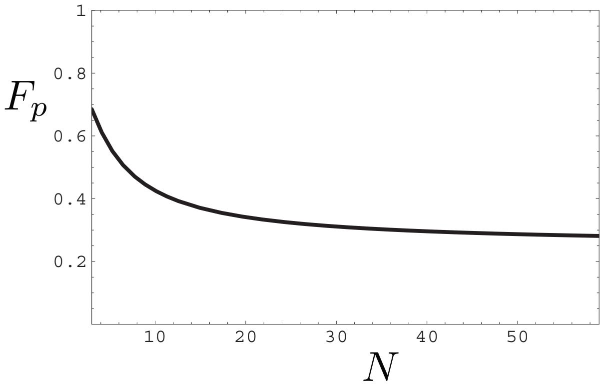

Figure 6.14: The process fidelity for $\tau = 0$ given in Eqn. 6.69 as we increase the number of beam splitters N.

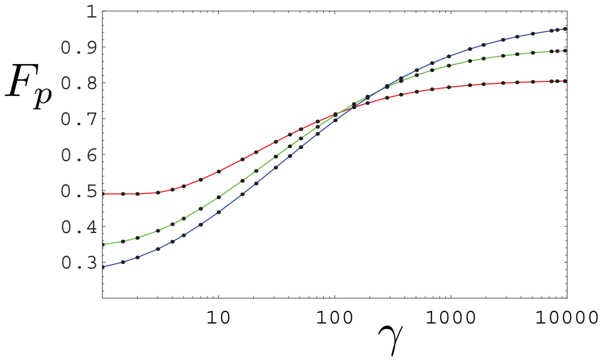

Figure 6.15: The scaling of the process fidelity with γ with $\tau = \tau_{\text{opt}}$ (separate optimisation for each point shown) for comparison with the ideal beam splitter case. The Red line represents 7 beam splitters, the Green line represents 19 beam splitters and the Blue line represents 99 beam splitters.

6.4 Encoding against Loss

In Section 2.7.6 we described a general parity encoding technique that was used in [87] to construct a LOQC CNOT that was more efficient that the original scheme in [31]. In [48] Ralph *et al.* used this parity encoding in conjunction with redundancy encoding to protect optical qubits against single photon loss, constructing a loss tolerant quantum memory. Such codes have already been demonstrated experimentally [125]. In this section we use the same parity and redundancy encoding as in [48] to recover from loss in both Fig. 6.1 and 6.3.

As described in Eqn. 2.105 in Section 2.7.6, the parity state $|0\rangle^{(n)}$ is the superposition of all possible even states of length n and the parity state $|1\rangle^{(n)}$

is the superposition of all possible odd states of length n:

$$\begin{aligned} |0\rangle^{(n)} &= \frac{1}{\sqrt{2}}\left(|+\rangle^{\otimes n} + |-\rangle^{\otimes n}\right) \\ |1\rangle^{(n)} &= \frac{1}{\sqrt{2}}\left(|+\rangle^{\otimes n} - |-\rangle^{\otimes n}\right). \end{aligned} \tag{6.70}$$

Adding redundancy to the encoding, a general encoded qubit is given by:

$$\alpha|0\rangle_L + \beta|1\rangle_L = \alpha|0\rangle^{(n)}|0\rangle^{(n)}\cdots + \beta|1\rangle^{(n)}|1\rangle^{(n)}\cdots \tag{6.71}$$

For the task at hand, two levels of parity encoding is sufficient. An encoded qubit is given by:

$$\alpha|0\rangle_L + \beta|1\rangle_L = \alpha|0\rangle^{(2)}|0\rangle^{(2)}\cdots + \beta|1\rangle^{(2)}|1\rangle^{(2)}\cdots \tag{6.72}$$

As a concrete example, consider only two levels of redundancy for the qubits $|\Psi\rangle_1$ and $|\Psi\rangle_2$:

$$\begin{aligned} |\Psi\rangle_1 &= \alpha|0\rangle^{(2)}|0\rangle^{(2)} + \beta|1\rangle^{(2)}|1\rangle^{(2)} \\ |\Psi\rangle_2 &= \gamma|0\rangle^{(2)}|0\rangle^{(2)} + \delta|1\rangle^{(2)}|1\rangle^{(2)} \end{aligned} \tag{6.73}$$

$$\begin{aligned} |\Psi\rangle_1|\Psi\rangle_2 &= \alpha\gamma|\underline{0000}\rangle + \alpha\delta|\underline{0011}\rangle + \beta\gamma|\underline{1100}\rangle + \beta\delta|\underline{1111}\rangle \\ &= \alpha\gamma|\underline{0}\rangle\left(|0000\rangle + |0011\rangle + |1100\rangle + |1111\rangle\right)_{1234}|\underline{0}\rangle \\ &\quad + \alpha\delta|\underline{0}\rangle\left(|0001\rangle + |0010\rangle + |1101\rangle + |1110\rangle\right)_{1234}|\underline{1}\rangle \\ &\quad + \beta\gamma|\underline{1}\rangle\left(|0100\rangle + |0111\rangle + |1000\rangle + |1011\rangle\right)_{1234}|\underline{0}\rangle \\ &\quad + \beta\delta|\underline{1}\rangle\left(|0101\rangle + |0110\rangle + |1001\rangle + |1010\rangle\right)_{1234}|\underline{1}\rangle \end{aligned} \tag{6.74}$$

where $|\underline{0}\rangle = |0\rangle^{(2)}$ and $|\underline{1}\rangle = |1\rangle^{(2)}$. After we perform a a CSIGN between modes 2 and 3 we have

$$\begin{aligned} |\Psi\rangle_1|\Psi\rangle_2 \rightarrow\; & \alpha\gamma|\underline{0}\rangle\left(|0000\rangle + |0011\rangle + |1100\rangle - |1111\rangle\right)_{1234}|\underline{0}\rangle \\ & + \alpha\delta|\underline{0}\rangle\left(|0001\rangle + |0010\rangle + |1101\rangle - |1110\rangle\right)_{1234}|\underline{1}\rangle \\ & + \beta\gamma|\underline{1}\rangle\left(|0100\rangle - |0111\rangle + |1000\rangle + |1011\rangle\right)_{1234}|\underline{0}\rangle \\ & + \beta\delta|\underline{1}\rangle\left(|0101\rangle - |0110\rangle + |1001\rangle + |1010\rangle\right)_{1234}|\underline{1}\rangle. \end{aligned} \tag{6.75}$$

This encoded state can recover from single photon loss on either mode 2 or 3. It can also recover from single photon loss on both modes 2 and 3. First, consider the no loss case.

No Loss

If we detect modes 2 and 3 in the ± basis we have

$$\begin{aligned} \rightarrow\; & \alpha\gamma|\underline{0}\rangle\left(A_1|00\rangle + A_2|01\rangle + A_3|10\rangle + A_4|11\rangle\right)_{14}|\underline{0}\rangle \\ & + \alpha\delta|\underline{0}\rangle\left(A_1|01\rangle + A_2|00\rangle + A_3|11\rangle + A_4|10\rangle\right)_{14}|\underline{1}\rangle \\ & + \beta\gamma|\underline{1}\rangle\left(B_1|00\rangle + B_2|01\rangle + B_3|10\rangle + B_4|11\rangle\right)_{14}|\underline{0}\rangle \\ & + \beta\delta|\underline{1}\rangle\left(B_1|01\rangle + B_2|00\rangle + B_3|11\rangle + B_4|10\rangle\right)_{14}|\underline{1}\rangle \end{aligned}$$

where the coefficients A_1, A_2, A_3, A_4, B_1, B_2, B_3 and B_4 are given in Table. 6.1.

	A_1	A_2	A_3	A_4	B_1	B_2	B_3	B_4
$\vert ++\rangle_{23}$	1	1	1	-1	1	-1	1	1
$\vert +-\rangle_{23}$	1	-1	1	1	1	1	1	-1
$\vert -+\rangle_{23}$	1	1	-1	1	-1	1	1	1
$\vert --\rangle_{23}$	1	-1	-1	-1	-1	-1	1	-1

Table 6.1: The results for the no loss case after we measure qubits 2 and 3 in the ± basis.

If we now detect modes 1 and 4 in the computational basis we have

$$\rightarrow C_1\alpha\gamma|\underline{00}\rangle + C_2\alpha\delta|\underline{01}\rangle + C_3\beta\gamma|\underline{10}\rangle + C_4\beta\delta|\underline{11}\rangle$$

where the coefficients C_1, C_2, C_3 and C_4 are given in Table 6.2.

		C_1	C_2	C_3	C_4
$\vert ++\rangle_{23}$	$\vert 00\rangle_{14}$	1	1	1	-1
	$\vert 01\rangle_{14}$	1	1	-1	1
	$\vert 10\rangle_{14}$	1	-1	1	1
	$\vert 11\rangle_{14}$	-1	1	1	1
$\vert +-\rangle_{23}$	$\vert 00\rangle_{14}$	1	-1	1	1
	$\vert 01\rangle_{14}$	-1	1	1	1
	$\vert 10\rangle_{14}$	1	1	1	-1
	$\vert 11\rangle_{14}$	1	1	-1	1
$\vert -+\rangle_{23}$	$\vert 00\rangle_{14}$	1	1	-1	1
	$\vert 01\rangle_{14}$	1	1	1	-1
	$\vert 10\rangle_{14}$	-1	1	1	1
	$\vert 11\rangle_{14}$	1	-1	1	1
$\vert --\rangle_{23}$	$\vert 00\rangle_{14}$	1	-1	-1	-1
	$\vert 01\rangle_{14}$	-1	1	-1	-1
	$\vert 10\rangle_{14}$	-1	-1	1	-1
	$\vert 11\rangle_{14}$	-1	-1	-1	1

Table 6.2: The results for the no loss case after we measure qubits 2 and 3 in the ± basis and qubits 1 and 4 in the computational basis.

In Table 6.2 we see that there is only ever a single -1 in each row, up to a global phase factor. Each case is a CSIGN gate, up to Z corrections. The CSIGN operation in this case is summarised in Fig. 6.16 with $A = Z$.

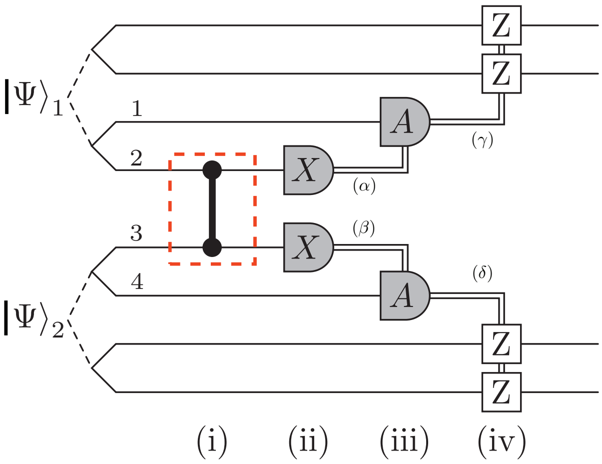

Figure 6.16: To perform an encoded CSIGN: (i) a pair of qubits goes through the nonlinear CSIGN and the photons may be lost in the interaction. We consider either Fig. 6.1 or 6.3 to be inside the Red box. (ii) Detect qubits 2 and 3 in the $|\pm\rangle$ (X) basis, giving α and β, respectively. (iii-a) If measurements indicated that no photons were lost, measure the remaining parity qubits in the computational ($A = Z$) basis. The CSIGN has been successfully performed. (iii-b) If measurements indicated loss, measure the remaining parity qubits in the $|\pm\rangle$ ($A = X$) basis to disantangle and attempt gate on the next redundantly encoded qubits. (iv) Depending on the measurement results phase corrections may need to be applied to remaining qubits. Note the double line indicates classical information.

Lose one photon

Next, consider the case that we lose a photon in mode 2 in Eqns. 6.74 and 6.75, $|\Psi\rangle_1|\Psi\rangle_2$ becomes $|\Omega_1\rangle\langle\Omega_1| + |\Omega_2\rangle\langle\Omega_2|$, where

$$\begin{aligned}|\Omega_1\rangle =&\alpha\gamma|\underline{0}\rangle\Big(|0\phi 00\rangle + |0\phi 11\rangle\Big)_{1234}|\underline{0}\rangle + \alpha\delta|\underline{0}\rangle\Big(|0\phi 01\rangle + |0\phi 10\rangle\Big)_{1234}|\underline{1}\rangle \qquad (6.76)\\ &+\beta\gamma|\underline{1}\rangle\Big(|1\phi 00\rangle + |1\phi 11\rangle\Big)_{1234}|\underline{0}\rangle + \beta\delta|\underline{1}\rangle\Big(|1\phi 01\rangle + |1\phi 10\rangle\Big)_{1234}|\underline{1}\rangle,\\ |\Omega_2\rangle =&\alpha\gamma|\underline{0}\rangle\Big(|1\phi 00\rangle + D_1|1\phi 11\rangle\Big)_{1234}|\underline{0}\rangle + \alpha\delta|\underline{0}\rangle\Big(|1\phi 01\rangle + D_1|1\phi 10\rangle\Big)_{1234}|\underline{1}\rangle\\ &+\beta\gamma|\underline{1}\rangle\Big(|0\phi 00\rangle + D_1|0\phi 11\rangle\Big)_{1234}|\underline{0}\rangle + \beta\delta|\underline{1}\rangle\Big(|0\phi 01\rangle + D_1|0\phi 10\rangle\Big)_{1234}|\underline{1}\rangle,\end{aligned}$$

$|\phi\rangle = |\text{vac}\rangle$, $D_1 = 1$ if loss occurred before the application of the CSIGN and $D_1 = -1$ if it occurred after. We model the loss via Eqn. 2.60 in Section 2.1.7 with $t \to \infty$. In the case that $t \not\to \infty$, as will be considered later in this section, the mixed state resulting will have both vacuum and the initial state terms.

If we detect mode 3 in the $\pm$ basis we have $\frac{1}{2}|\Omega_3\rangle\langle\Omega_3| + \frac{1}{2}|\Omega_4\rangle\langle\Omega_4|$, where

$$\begin{aligned}|\Omega_3\rangle &= \alpha\Big(\gamma|\underline{00}\rangle + E_1\delta|\underline{01}\rangle\Big)\Big(|00\rangle + E_1|01\rangle\Big)_{14} + \beta\Big(\gamma|\underline{10}\rangle + E_1\delta|\underline{11}\rangle\Big)\Big(|10\rangle + E_1|11\rangle\Big)_{14},\\ |\Omega_4\rangle &= \alpha\Big(\gamma|\underline{00}\rangle + E_2\delta|\underline{01}\rangle\Big)\Big(|10\rangle + E_2|11\rangle\Big)_{14} + \beta\Big(\gamma|\underline{10}\rangle + E_2\delta|\underline{11}\rangle\Big)\Big(|00\rangle + E_2|01\rangle\Big)_{14},\end{aligned}$$

$E_2 = D_1E_1$, $E_1 = 1$ when we measure $|+\rangle_3$ and $E_1 = -1$ when we measure

$|-\rangle_3$. If we now detect modes 1 and 4 in the ± basis, we have

$$\frac{1}{2\sqrt{2}}\Big(F_1\alpha\gamma|\underline{00}\rangle + F_2\alpha\delta|\underline{01}\rangle + F_3\beta\gamma|\underline{10}\rangle + F_4\beta\delta|\underline{11}\rangle\Big) \tag{6.77}$$

where the coefficients F_1, F_2, F_3 and F_4 are given in Table 6.3.

		F_1	F_2	F_3	F_4
D_1=1	$\lvert++\,+\rangle_{134}$	$\sqrt{2}$	$\sqrt{2}$	$\sqrt{2}$	$\sqrt{2}$
	$\lvert++\,-\rangle_{134}$	0	0	0	0
	$\lvert-+\,+\rangle_{134}$	$\sqrt{2}$	$\sqrt{2}$	-$\sqrt{2}$	-$\sqrt{2}$
	$\lvert-+\,-\rangle_{134}$	0	0	0	0
	$\lvert+-\,+\rangle_{134}$	0	0	0	0
	$\lvert+-\,-\rangle_{134}$	$\sqrt{2}$	$\sqrt{2}$	$\sqrt{2}$	$\sqrt{2}$
	$\lvert--\,+\rangle_{134}$	0	0	0	0
	$\lvert--\,-\rangle_{134}$	$\sqrt{2}$	$\sqrt{2}$	-$\sqrt{2}$	-$\sqrt{2}$
$D_1 = -1$	$\lvert++\,+\rangle_{134}$	1	1	1	1
	$\lvert++\,-\rangle_{134}$	1	1	1	1
	$\lvert-+\,+\rangle_{134}$	1	1	-1	-1
	$\lvert-+\,-\rangle_{134}$	1	1	-1	-1
	$\lvert+-\,+\rangle_{134}$	1	1	1	1
	$\lvert+-\,-\rangle_{134}$	1	1	1	1
	$\lvert--\,+\rangle_{134}$	1	1	-1	-1
	$\lvert--\,-\rangle_{134}$	1	1	-1	-1

Table 6.3: The results for loss on mode 2, after we measure qubits 1, 3 and 4 in the ± basis.

We see that we have lost a level of redundancy. This is summarised in Fig. 6.16 with both modes 1 and 4 detected in the X basis ($A = X$).

Lose two photons

Next, consider the case that we lose a photon from both mode 2 and 3 in Eqn. 6.74 and 6.75, $|\Psi\rangle_1|\Psi\rangle_2$ becomes $|\Omega_5\rangle\langle\Omega_5| + |\Omega_6\rangle\langle\Omega_6| + |\Omega_7\rangle\langle\Omega_7| + |\Omega_8\rangle\langle\Omega_8|$, where

$$\begin{aligned}
|\Omega_5\rangle &= \alpha\gamma|\underline{00}\rangle|00\rangle_{14} + \alpha\delta|\underline{01}\rangle|01\rangle_{14} + \beta\gamma|\underline{10}\rangle|10\rangle_{14} + \beta\delta|\underline{11}\rangle|11\rangle_{14},\\
|\Omega_6\rangle &= \alpha\gamma|\underline{00}\rangle|01\rangle_{14} + \alpha\delta|\underline{01}\rangle|00\rangle_{14} + \beta\gamma|\underline{10}\rangle|11\rangle_{14} + \beta\delta|\underline{11}\rangle|10\rangle_{14},\\
|\Omega_7\rangle &= \alpha\gamma|\underline{00}\rangle|10\rangle_{14} + \alpha\delta|\underline{01}\rangle|11\rangle_{14} + \beta\gamma|\underline{10}\rangle|00\rangle_{14} + \beta\delta|\underline{11}\rangle|01\rangle_{14},\\
|\Omega_8\rangle &= \alpha\gamma|\underline{00}\rangle|11\rangle_{14} + \alpha\delta|\underline{01}\rangle|10\rangle_{14} + \beta\gamma|\underline{10}\rangle|01\rangle_{14} + \beta\delta|\underline{11}\rangle|00\rangle_{14}.
\end{aligned}$$

This is independent of whether a loss occurred before or after the CSIGN

If we now detect modes 1 and 4 in the ± basis we have

$$\frac{1}{2}\Big(\alpha\gamma|\underline{00}\rangle + G_1\alpha\delta|\underline{01}\rangle + G_2\beta\gamma|\underline{10}\rangle + G_3\beta\delta|\underline{11}\rangle\Big) \tag{6.78}$$

where the coefficients G_1, G_2 and G_3 are given in Table 6.4.

	G_1	G_2	G_3
$\vert{+}{+}\rangle_{14}$	1	1	1
$\vert{+}{-}\rangle_{14}$	-1	1	-1
$\vert{-}{+}\rangle_{14}$	1	-1	-1
$\vert{-}{-}\rangle_{14}$	-1	-1	1

Table 6.4: The results for loss on modes 2 and 3, after we measure qubits 1 and 4 in the ± basis.

This is summarised in Fig. 6.16 with both modes 1 and 4 detected in the X basis ($A = X$).

6.4.1 Process Fidelity

As mentioned in the previous Section, since we are dealing with photon loss from a single mode, we encode our qubits with $n = 2$ in Eqn. 6.71. The number of redundancy levels is set to q. Similar to Eqns. 6.73 and 6.74, our encoded state looks like

$$|\psi_{\text{enc}}\rangle_{\text{in}} = \eta_{00}|\underline{0}\rangle^{\otimes q}|\underline{0}\rangle^{\otimes q} + \eta_{01}|\underline{0}\rangle^{\otimes q}|\underline{1}\rangle^{\otimes q} + \eta_{10}|\underline{1}\rangle^{\otimes q}|\underline{0}\rangle^{\otimes q} + \eta_{11}|\underline{1}\rangle^{\otimes q}|\underline{1}\rangle^{\otimes q} \tag{6.79}$$

$$\begin{aligned} &= \frac{1}{2}|\eta_{00}\rangle\Big(|00\rangle + |11\rangle\Big)_{12}\Big(|00\rangle + |11\rangle\Big)_{34} \\ &\quad + \frac{1}{2}|\eta_{01}\rangle\Big(|00\rangle + |11\rangle\Big)_{12}\Big(|01\rangle + |10\rangle\Big)_{34} \\ &\quad + \frac{1}{2}|\eta_{10}\rangle\Big(|01\rangle + |10\rangle\Big)_{12}\Big(|00\rangle + |11\rangle\Big)_{34} \\ &\quad + \frac{1}{2}|\eta_{11}\rangle\Big(|01\rangle + |10\rangle\Big)_{12}\Big(|01\rangle + |10\rangle\Big)_{34} \\ &= |\chi_{00}\rangle|00\rangle_{23} + |\chi_{01}\rangle|01\rangle_{23} + |\chi_{10}\rangle|10\rangle_{23} + |\chi_{11}\rangle|11\rangle_{23} \end{aligned}$$

where $|\underline{0}\rangle = |0\rangle^{(2)}$, $|\underline{1}\rangle = |1\rangle^{(2)}$, $\sum_{ij=0}^{1}|\eta_{ij}|^2 = 1$,

$$|\eta_{ab}\rangle = \eta_{ab}|\underline{a}\rangle^{\otimes(q-1)}|\underline{b}\rangle^{\otimes(q-1)} \tag{6.80}$$

with $a, b \in \{0, 1\}$ and

$$|\chi_{ab}\rangle = \frac{1}{2}\sum_{m,n=0}^{1}|\eta_{mn}\rangle X^a \otimes X^b|mn\rangle_{14}. \tag{6.81}$$

For example, $|\chi_{00}\rangle = \frac{1}{2}\Big(|\eta_{00}\rangle|00\rangle_{14}+|\eta_{01}\rangle|01\rangle_{14}+|\eta_{10}\rangle|10\rangle_{14}+|\eta_{11}\rangle|11\rangle_{14}\Big)$. The input state incident on Fig. 6.16 now looks like

$$\begin{aligned} |\psi_{\text{enc}}\rangle_{\text{in}} &= \sum_{a,b=0}^{1} |\chi_{ab}\rangle|ab\rangle_{23} \qquad (6.82) \\ \rho_{\text{in}} &= \sum_{a,b,c,d=0}^{1} |\chi_{ab}\rangle\langle\chi_{cd}| \otimes |ab\rangle\langle cd| \end{aligned}$$

where modes 2 and 3 are incident on the CSIGN in Fig. 6.16. At the point in between (i) and (ii) in Fig. 6.16 we can write the density matrix in a similar way to Eqn. 6.62:

$$\rho_{\text{out}} = \sum_{a,b,c,d=0}^{1} |\chi_{ab}\rangle\langle\chi_{cd}| \otimes |\overline{ab}\rangle\langle\overline{cd}| \otimes \mathcal{E}\left(|ab\rangle\langle cd|\right) \qquad (6.83)$$

where we have written modes 2 and 3 in the dual rail basis.

Next, we need to measure modes 2 and 3 in the ± basis to detect for loss. If we measure $|\text{vac}\rangle$ we measure qubits 1 and 4 in the ± basis to obtain a state with one less redundancy level then attempt a CSIGN on the next redundantly encoded photon. If we detect no loss, we measure modes 1 and 4 in the computational basis. To calculate the process fidelity we just consider the case when we detect no loss.

After detecting modes 2 and 3 in the ± basis Eqn. 6.83 becomes

$$\rho_{\text{out}}^{\alpha\beta} = \sum_{a,b,c,d=0}^{1} |\chi_{ab}\rangle\langle\chi_{cd}| \otimes \operatorname{Tr}\left[M^{\alpha\beta}\Big(|\overline{ab}\rangle\langle\overline{cd}| \otimes \mathcal{E}\left(|ab\rangle\langle cd|\right)\Big)\right] \qquad (6.84)$$

where

$$M^{\alpha\beta} = Z^{\alpha} \otimes Z^{\beta}|++\rangle\langle++|Z^{\alpha} \otimes Z^{\beta},$$

$M^{\pm} = |\pm\rangle\langle\pm| = \frac{1}{2}\left(|0\rangle\langle 0| \pm |0\rangle\langle 1| \pm |1\rangle\langle 0| + |1\rangle\langle 1|\right)$, $\alpha, \beta \in \{0,1\}$ and we have used the fact that $M^{\alpha\beta}M^{\alpha\beta} = M^{\alpha\beta}$. We know that $Z^{\alpha}|s\rangle = (-1)^{\alpha s}|s\rangle$ and $|++\rangle\langle++| = \frac{1}{4}\sum_{stuv=0}^{1}|st\rangle\langle uv|$ so we can rewrite $M^{\alpha\beta}$ as

$$\begin{aligned} M^{\alpha\beta} &= \frac{1}{4}\sum_{stuv=0}^{1} Z^{\alpha} \otimes Z^{\beta}|st\rangle\langle uv|Z^{\alpha} \otimes Z^{\beta} \qquad (6.85) \\ &= \frac{1}{4}\sum_{stuv=0}^{1} (-1)^{\alpha(s+u)+\beta(t+v)}\,|st\rangle\langle uv| \\ &= \frac{1}{4}\sum_{stuv=0}^{1} (-1)^{\alpha(s+u)+\beta(t+v)}\,|\overline{st}\rangle\langle\overline{uv}| \otimes |st\rangle\langle uv| \end{aligned}$$

where we have written $M^{\alpha\beta}$ in the dual rail basis in the last line. $\rho_{\text{out}}^{\alpha\beta}$ becomes

$$\rho_{\text{out}}^{\alpha\beta} = \frac{1}{4} \sum_{a,b,c,d=0}^{1} (-1)^{\alpha(a+c)+\beta(b+d)} \, |\chi_{ab}\rangle\langle\chi_{cd}| \langle ab|\mathcal{E}\left(|ab\rangle\langle cd|\right)|cd\rangle. \tag{6.86}$$

Since we are only considering the case when we detect no photon loss, we detect modes 1 and 4 in $|\chi_{ab}\rangle$ in the computational basis. Using Eqn. 6.81, $\rho_{\text{out}}^{\alpha\beta}$ becomes

$$\begin{aligned}\rho_{\text{out}}^{\alpha\beta\gamma\delta} = \frac{1}{16} \sum_{\substack{a,b,c,d,\\ m,n,p,q}=0}^{1} & (-1)^{\alpha(a+c)+\beta(b+d)} \, |\eta_{ab}\rangle\langle\eta_{cd}| \mathrm{Tr}\left[|\gamma\delta\rangle\langle\gamma\delta| X^a \otimes X^b |mn\rangle\langle pq| X^c \otimes X^d\right] \\ & \times \langle ab|\mathcal{E}\left(|ab\rangle\langle cd|\right)|cd\rangle \end{aligned} \tag{6.87}$$

where $\gamma, \delta \in \{0,1\}$. We use the fact that $X^a|m\rangle = |m \oplus a\rangle$, where the addition $\oplus$ is modulo 2: $a \oplus b = (a+b) \bmod 2$. So $\langle\gamma\delta|X^a \otimes X^b|mn\rangle = \delta_{\gamma\oplus a,m}\delta_{\delta\oplus b,n}$. $\rho_{\text{out}}^{\alpha\beta\gamma\delta}$ becomes

$$\rho_{\text{out}}^{\alpha\beta\gamma\delta} = \frac{1}{16} \sum_{a,b,c,d=0}^{1} (-1)^{\alpha(a+c)+\beta(b+d)} \, |\eta_{\gamma\oplus a,\delta\oplus b}\rangle\langle\eta_{\gamma\oplus c,\delta\oplus d}| \langle ab|\mathcal{E}\left(|ab\rangle\langle cd|\right)|cd\rangle. \tag{6.88}$$

Note, at this stage, one might think that both X and Z corrections are necessary for each detection outcome. However, if we examine the form of $|\eta_{ab}\rangle$ in Eqn. 6.80 we see that only Z corrections are necessary, as was shown in Table 6.2 and Fig. 6.16.

We want to work out the process fidelity, so the input state $|\psi_{\text{enc}}\rangle_{\text{in}}$ in Eqn. 6.79 will have $\eta_{00} = \eta_{01} = \eta_{10} = \eta_{11} = \frac{1}{2}$ and $q \to 2q$. That is, instead of $|\eta_{ab}\rangle$ we will use

$$|\tilde{\eta}_{ab}\rangle = \frac{1}{2} \left(|a\rangle^{(2)}\right)^{\otimes(q-1)} \left(|a\rangle^{(2)}\right)^{\otimes(q)} \left(|b\rangle^{(2)}\right)^{\otimes(q-1)} \left(|b\rangle^{(2)}\right)^{\otimes(q)}. \tag{6.89}$$

We can apply corrections to $\rho_{\text{out}}^{\alpha\beta\gamma\delta}$ due to the computational basis and $\pm$ basis measurements. In this case we use X corrections even though only Z corrections are necessary.

$$\begin{aligned}\rho_{\text{out}} = \frac{1}{16} \sum_{a,b,c,d=0}^{1} & \left(Z^\alpha \otimes Z^\beta\right)\left(X^\gamma \otimes X^\delta\right) |\tilde{\eta}_{\gamma\oplus a,\delta\oplus b}\rangle\langle\tilde{\eta}_{\gamma\oplus c,\delta\oplus d}| \left(X^\gamma \otimes X^\delta\right)\left(Z^\alpha \otimes Z^\beta\right) \\ & \times (-1)^{\alpha(a+c)+\beta(b+d)} \langle ab|\mathcal{E}\left(|ab\rangle\langle cd|\right)|cd\rangle \\ = \frac{1}{16} \sum_{a,b,c,d=0}^{1} & \left((-1)^{\alpha(a+c)+\beta(b+d)}\right)^2 |\tilde{\eta}_{ab}\rangle\langle\tilde{\eta}_{cd}| \langle ab|\mathcal{E}\left(|ab\rangle\langle cd|\right)|cd\rangle \\ = \frac{1}{16} \sum_{a,b,c,d=0}^{1} & \langle ab|\mathcal{E}\left(|ab\rangle\langle cd|\right)|cd\rangle |\tilde{\eta}_{ab}\rangle\langle\tilde{\eta}_{cd}| \end{aligned} \tag{6.90}$$

where we can easily apply the X and Z corrections to the redundant parity encoding as described in Section 2.7.6. Since we are only considering the case when we detect no photon loss, the density matrix ρ_{out} is not normalised. The trace gives the probability of no loss on one redundancy level of encoding, that is, the probability of measuring $+$ or $-$ at point (ii) in Fig. 6.16:

$$P_{\text{av}} = \text{Tr}\left[\rho_{\text{out}}\right] = \frac{1}{64}\sum_{ab=0}^{1} \langle ab|\mathcal{E}\left(|ab\rangle\langle ab|\right)|ab\rangle.$$

Notice that neither ρ_{out} nor P_{av} is dependent on the measurement outcomes $\alpha, \beta, \gamma, \delta$. Since there are sixteen possible measurement outcomes, the total success probability is given by

$$P_{\text{av}} = \frac{1}{4}\sum_{a,b=0}^{1} \langle ab|\mathcal{E}\left(|ab\rangle\langle ab|\right)|ab\rangle. \tag{6.91}$$

The probability of failure on m redundancy levels of encoding is $(1 - P_{\text{av}})^m$. The normalised output density matrix is

$$\rho_{\text{out}} = \frac{\frac{1}{4}\sum_{a,b,c,d}\langle ab|\mathcal{E}\left(|ab\rangle\langle cd|\right)|cd\rangle|\tilde{\eta}_{ab}\rangle\langle\tilde{\eta}_{cd}|}{\sum_{a,b}\langle ab|\mathcal{E}\left(|ab\rangle\langle ab|\right)|ab\rangle}. \tag{6.92}$$

To work out the process fidelity we note that an ideal CSIGN transforms the state in Eqn. 6.79, using $|\tilde{\eta}_{ab}\rangle$ instead of $|\eta_{ab}\rangle$, to

$$|\psi_{\text{CSign}}\rangle = \sum_{a,b=0}^{1} (-1)^{ab}|\tilde{\eta}_{ab}\rangle. \tag{6.93}$$

We work out the process fidelity to be

$$F_{\text{pro}}^{\text{enc}} = \frac{\frac{1}{4}\sum_{a,b,c,d}(-1)^{ab+cd}\langle ab|\mathcal{E}\left(|ab\rangle\langle cd|\right)|cd\rangle}{\sum_{a,b}\langle ab|\mathcal{E}\left(|ab\rangle\langle ab|\right)|ab\rangle}. \tag{6.94}$$

Along with the success probability P_{av}, we can also work out a worst case success probability by considering just the state $|VV\rangle$ incident on Fig. 6.1 or Fig. 6.3. This is the only state that allows a loss of one photon in both modes. The worst case success probability is given by

$$P_{\text{wt}} = \text{Tr}\Big[|11\rangle\langle 11|\mathcal{E}\left(|11\rangle\langle 11|\right)\Big] = \langle 11|\mathcal{E}\left(|11\rangle\langle 11|\right)|11\rangle. \tag{6.95}$$

We calculate analytical expressions for the process fidelity $F_{\text{pro}}^{\text{enc}}$, the success probability P_{av} and the worst case success probability P_{wt} and plot them in Figs. 6.17–6.29 for both the continuous interaction case in Section 6.1 and the beam splitter case in Section 6.2.

In Figs. 6.17 and 6.18 we show the improvements one level of parity encoding has over the no encoding case of Figs. 6.5 and 6.7, respectively.

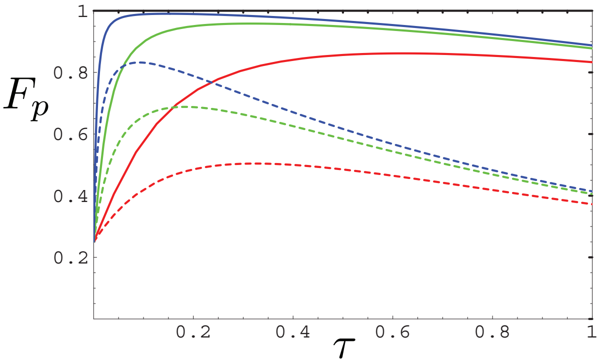

Figure 6.17: The process fidelity $F_{\text{pro}}^{\text{enc}}$ for the continuous interaction case for one level of parity encoding (solid lines) and no encoding (dashed lines), as in Fig. 6.5. The Red curves represent $\gamma = 20$, the Green curves represent $\gamma = 100$ and the Blue curves represent $\gamma = 500$.

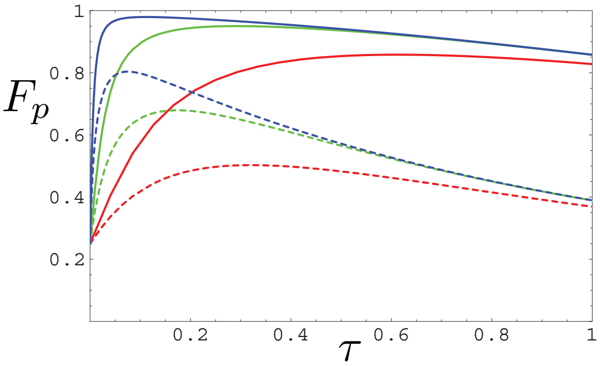

Figure 6.18: The process fidelity $F_{\text{pro}}^{\text{enc}}$ for the case case for one level of parity encoding (solid lines) and no encoding (dashed lines), as in Fig. 6.7. Here we consider the 19 beam splitter case. The Red curves represent $\gamma = 20$, the Green curves represent $\gamma = 100$ and the Blue curves represent $\gamma = 500$.

In both Figs. 6.17 and 6.18, the process fidelity with encoding is considerably higher than the no encoding case. Notice however that when we do include encoding, the process fidelity peaks at some optimal τ value and then drops off. This is contrary to what we would expect. In Fig. 6.19 we show the peak process fidelity for each of the cases shown in Fig. 6.17 and 6.18. This figure clearly shows the advantage in using encoding.

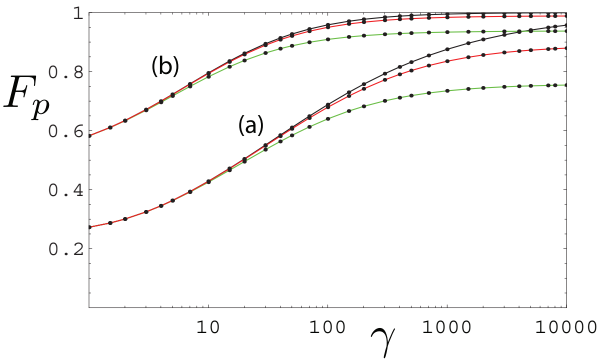

Figure 6.19: The scaling of the process fidelity with γ for $\tau = \tau_{\text{opt}}$ (separate optimisation for each point shown). The **Black** lines represent the continuous interaction case, the Red lines represent the 19 beam splitter case and the Green lines represent the 7 beam splitter case. In part (a) the case in Fig. 6.10 is shown. In part (b), the encoded case is considered.

In Figs. 6.20–6.23 we show the probability P_{av} and worst case probability P_{wt} for both the continuous interaction case (Fig. 6.20) and the beam splitter case (Fig. 6.21). Notice that for each case P_{wt} is less than P_{av}, as expected.

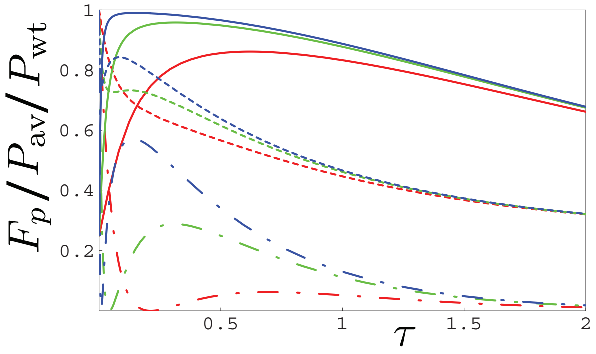

Figure 6.20: The process fidelity $F_{\text{pro}}^{\text{enc}}$ for the continuous interaction case for one level of parity encoding (solid lines), P_{av} (dashed line) and P_{wt} (dashed-dotted line). The Red curves represent $\gamma = 20$, the Green curves represent $\gamma = 100$ and the Blue curves represent $\gamma = 500$.

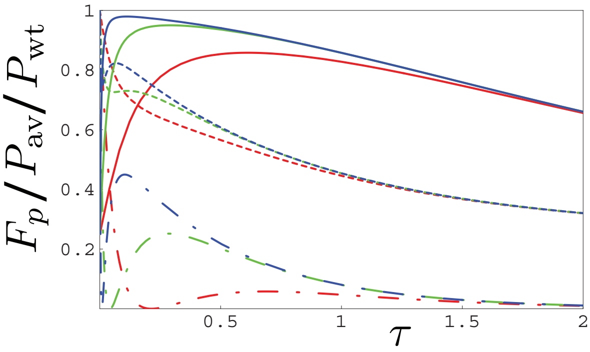

Figure 6.21: The process fidelity $F_{\rm pro}^{\rm enc}$ for the beam splitter case for one level of parity encoding (solid lines), $P_{\rm av}$ (dashed line) and $P_{\rm wt}$ (dashed-dotted line). Here we consider the 19 beam splitter case. The Red curves represent $\gamma = 20$, the Green curves represent $\gamma = 100$ and the Blue curves represent $\gamma = 500$.

As τ increases, both the encoded process fidelity and $P_{\rm av}$ approach 1/4, and $P_{\rm wt}$ approaches 0, as seen in Fig. 6.22 for the continuous interaction case and Fig. 6.23 for the beam splitter case. When we expand the sum for $P_{\rm av}$ in Eqn. 6.91 we see that $P_{\rm av} = \frac{1}{4}\Big(\langle 00|\mathcal{E}(|00\rangle\langle 00|)|00\rangle + \langle 01|\mathcal{E}(|01\rangle\langle 01|)|01\rangle + \langle 10|\mathcal{E}(|10\rangle\langle 10|)|10\rangle + \langle 11|\mathcal{E}(|11\rangle\langle 11|)|11\rangle\Big)$, and as shown in Eqn. 6.65 in Section 6.3, as $\tau \to \infty$, that is, as the single photon loss begins to dominate, $\mathcal{E}(|ab\rangle\langle ab|) \to |00\rangle\langle 00| = |\mathrm{vac}\rangle\langle \mathrm{vac}|$, for $a, b \in \{0, 1\}$. This fact explains why $F_{\rm pro}^{\rm enc}$ drops off as τ increases, as can be seen when we expand the sum in Eqn. 6.94 for $F_{\rm pro}^{\rm enc}$.

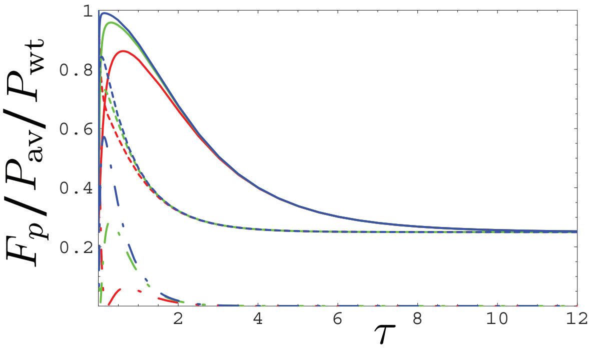

Figure 6.22: The process fidelity $F_{\rm pro}^{\rm enc}$ for the continuous interaction case for one level of parity encoding (solid lines), $P_{\rm av}$ (dashed line) and $P_{\rm wt}$ (dashed-dotted line) as in Fig. 6.20 for long τ. The Red curves represent $\gamma = 20$, the Green curves represent $\gamma = 100$ and the Blue curves represent $\gamma = 500$.

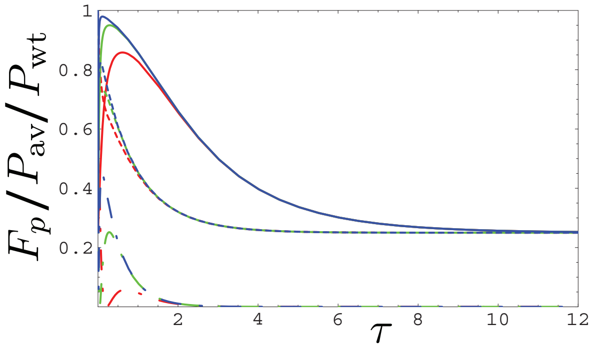

Figure 6.23: The process fidelity $F^{\rm enc}_{\rm pro}$ for the beam splitter case for one level of parity encoding (solid lines), $P_{\rm av}$ (dashed line) and $P_{\rm wt}$ (dashed-dotted line), as in Fig. 6.21 for long τ. Here we consider the 19 beam splitter case. The Red curves represent $\gamma = 20$, the Green curves represent $\gamma = 100$ and the Blue curves represent $\gamma = 500$.

For the small τ case we see that both $P_{\rm av}$ and $P_{\rm wt}$ dip, as shown in Fig. 6.24 for the continuous interaction case and Fig. 6.25 for the beam splitter case. Before the dip, both $P_{\rm av}$ and $P_{\rm wt}$ approach 1 as $\tau \to 0$. This is expected, since insufficient time for the two photon absorption to act results in the identity, as shown in Eqn. 6.64 in Section 6.3. If we look at the form of both $P_{\rm av}$ and $P_{\rm wt}$ in Eqn. 6.91 and 6.95, respectively, we see that for $\mathcal{E} = \mathbb{1}$, both are equal to 1.

The dip shown for $P_{\rm av}$ in Figs. 6.24 and 6.25 is approximately 3/4. As γ decreases, $P_{\rm av}$ dips further below 3/4. The dip shown for $P_{\rm wt}$ in Figs. 6.24 and 6.25 is 0. If we explicitly calculate the form of $P_{\rm av}$ and $P_{\rm wt}$ for the continuous interaction case we see that

$$\begin{aligned} \langle 00|\mathcal{E}\Big(|00\rangle\langle 00|\Big)|00\rangle &= 1 \\ \langle 01|\mathcal{E}\Big(|01\rangle\langle 01|\Big)|01\rangle &= e^{-\tau} \\ \langle 10|\mathcal{E}\Big(|10\rangle\langle 10|\Big)|10\rangle &= e^{-\tau} \\ \langle 11|\mathcal{E}\Big(|11\rangle\langle 11|\Big)|11\rangle &= A_{11} \end{aligned} \tag{6.96}$$

where

$$A_{11} = A^{-3} e^{-(2+\gamma)\tau}\left(A(A^2+2\pi^2)\cosh(A) + \gamma\tau A^2\sinh(A) - 2A\pi^2\right)$$

and

$$A = \sqrt{\gamma^2\tau^2 - 4\pi^2}.$$

If we explicitly calculate the form of $P_{\rm av}$ and $P_{\rm wt}$ for the beam splitter case we see that

$$\begin{aligned}
\langle 00|\mathcal{E}\Big(|00\rangle\langle 00|\Big)|00\rangle &= 1 \\
\langle 01|\mathcal{E}\Big(|01\rangle\langle 01|\Big)|01\rangle &= e^{-(2m-1)\tau} \\
\langle 10|\mathcal{E}\Big(|10\rangle\langle 10|\Big)|10\rangle &= e^{-(2m-1)\tau} \\
\langle 11|\mathcal{E}\Big(|11\rangle\langle 11|\Big)|11\rangle &= B_{11}
\end{aligned} \tag{6.97}$$

where

$$\begin{aligned}
B_{11} = 2^{1-4m}\Bigg\{ & B_1(1+e^{2\gamma\tau})\cos\left(\frac{4m\pi}{2m-1}\right) + e^{\gamma\tau}\Bigg(\sqrt{2}BB_2(e^{\gamma\tau}-1)\cos\left(\frac{2m\pi}{2m-1}\right) \\
& + 2B_1\cosh(\gamma\tau) - 4\left(2B_-^{2m+1}B_+^{2m+1}\sin^2\left(\frac{2m\pi}{2m-1}\right) + B_1\right)\Bigg)\Bigg\}(B_+B_-B)^{-2}
\end{aligned}$$

and

$$\begin{aligned}
B &= e^{-\gamma\tau}\sqrt{1-6e^{\gamma\tau}+e^{2\gamma\tau}+(1+e^{\gamma\tau})^2\cos\left(\frac{4m\pi}{2m-1}\right)} \\
B_\pm &= e^{-\tau}\left((1+e^{-\gamma\tau})\cos\left(\frac{2m\pi}{2m-1}\right) \pm \frac{B}{\sqrt{2}}\right) \\
B_1 &= B_-^2B_+^{4m} + B_-^{4m}B_+^2 \\
B_2 &= B_-^2B_+^{4m} - B_-^{4m}B_+^2.
\end{aligned}$$

We expect $P_{\mathrm{wt}} = \langle 11|\mathcal{E}\Big(|11\rangle\langle 11|\Big)|11\rangle$ to dip to 0. As $\tau \to 0$ our gate takes $|11\rangle$ to $|11\rangle$. After the two photon absorption has had enough time to act, we expect our gate to take $|11\rangle$ to $-|11\rangle$. This means, somewhere in between, the amplitude for $|11\rangle$ will be 0. This is confirmed by looking at A_{11} and B_{11} numerically, each go to 0 for a particular small τ. This, in conjunction with the fact that $\langle 01|\mathcal{E}\big(|01\rangle\langle 01|\big)|01\rangle \approx 1$ and $\langle 10|\mathcal{E}\big(|10\rangle\langle 10|\big)|10\rangle \approx 1$ for small τ, explains why P_{av} dips to 3/4 in Figs. 6.24 and 6.25.

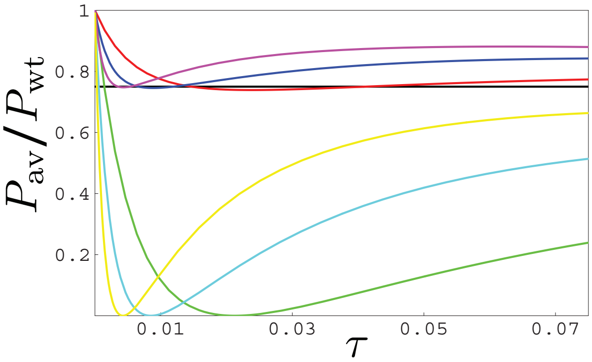

Figure 6.24: P_{av} and P_{wt} as in Fig. 6.20 for short τ. The Red curve shows P_{av} for $\gamma = 200$, the Blue curves shows P_{av} for $\gamma = 500$ and the Magenta curve shows P_{av} for $\gamma = 1000$. The Green curve shows P_{wt} for $\gamma = 200$, the Cyan curve shows P_{wt} for $\gamma = 500$ and the Yellow curve shows P_{wt} for $\gamma = 1000$. The **Black** line shows probability equal to 3/4.

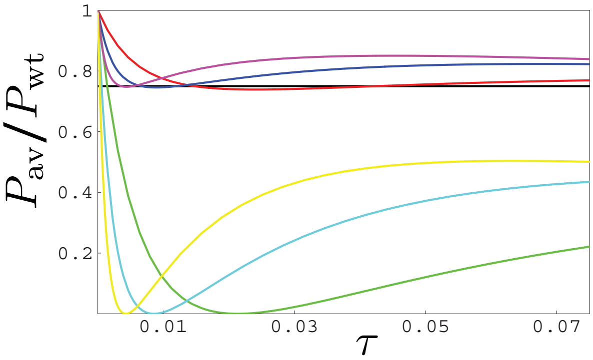

Figure 6.25: P_{av} and P_{wt} as in Fig. 6.21 for short τ. The Red curve shows P_{av} for $\gamma = 200$, the Blue curves shows P_{av} for $\gamma = 500$ and the Magenta curve shows P_{av} for $\gamma = 1000$. The Green curve shows P_{wt} for $\gamma = 200$, the Cyan curve shows P_{wt} for $\gamma = 500$ and the Yellow curve shows P_{wt} for $\gamma = 1000$. The **Black** line shows probability equal to 3/4.

In Fig. 6.26 we compare $P_{\rm av}$ and $P_{\rm wt}$ for the continuous interaction case with $P_{\rm av}$ and $P_{\rm wt}$ for the beam splitter case. As we increase γ, we need more beam splitters to approach the continuous interaction case. This is also true for $F^{\rm enc}_{\rm pro}$, as shown in Fig. 6.27.

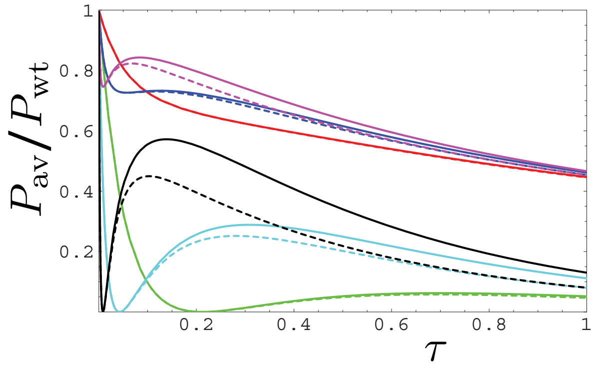

Figure 6.26: $P_{\rm av}$ and $P_{\rm wt}$ for both the continuous interaction (solid lines) and 19 beam splitter case (dashed lines). The Red curve shows $P_{\rm av}$ for $\gamma = 20$, the Blue curves shows $P_{\rm av}$ for $\gamma = 100$ and the Magenta curve shows $P_{\rm av}$ for $\gamma = 500$. The Green curve shows $P_{\rm wt}$ for $\gamma = 20$, the Cyan curve shows $P_{\rm wt}$ for $\gamma = 100$ and the **Black** curve shows $P_{\rm wt}$ for $\gamma = 500$.

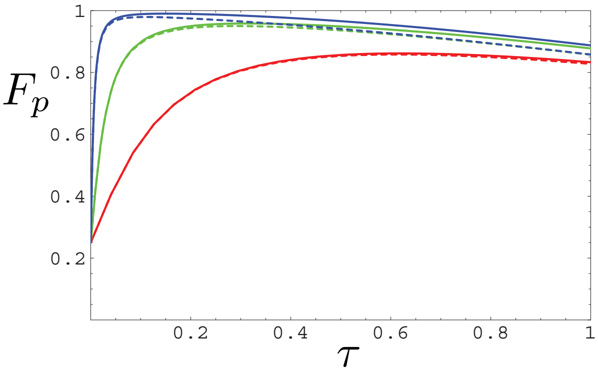

Figure 6.27: $F^{\rm enc}_{\rm pro}$ for both the continuous interaction (solid lines) and 19 beam splitter case (dashed lines). The Red curves represent $\gamma = 20$, the Green curves represent $\gamma = 100$ and the Blue curves represent $\gamma = 500$.

In Fig. 6.28 we see how the beam splitter case approaches the continuous interaction case as we increasing the number of beam splitters by looking at $F_{\rm pro}^{\rm enc}$, $P_{\rm av}$ and $P_{\rm wt}$.

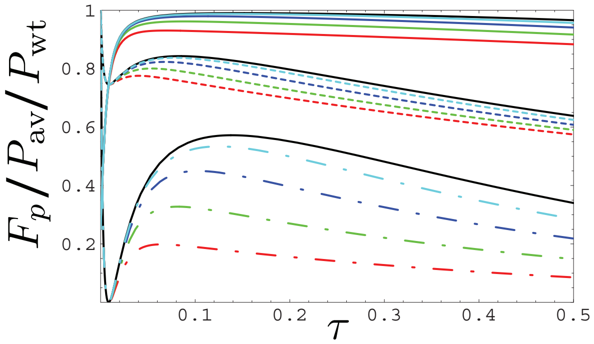

Figure 6.28: The process fidelity $F_{\rm pro}^{\rm enc}$ for one level of parity encoding (solid lines), $P_{\rm av}$ (dashed line) and $P_{\rm wt}$ (dashed-dotted line). Here we consider the $\gamma = 500$ case. The Red curves represent 7 beam splitters, the Green curves represent 11 beam splitters, the Blue curves represent 19 beam splitters, the Cyan curves represent 39 beam splitters and the **Black** curves represent the continuous interaction case.

In Fig. 6.29 we show the peak process fidelity for one level of encoding with the corresponding $P_{\rm av}$ and $P_{\rm wt}$. At γ values of approximately 1000, the peak process fidelity is above 99%.

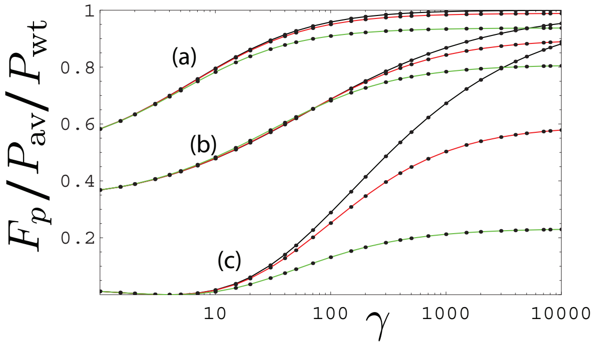

Figure 6.29: The scaling of the process fidelity $F_{\rm pro}^{\rm enc}$ with γ for $\tau = \tau_{\rm opt}$ is shown in part (a) (separate optimisation for each point shown). In parts (b) and (c) the corresponding $P_{\rm av}$ and $P_{\rm wt}$ are shown, respectively. The **Black** lines represent the continuous interaction case, the Red lines represent the 19 beam splitter case and the Green lines represent the 7 beam splitter case.

6.5 Balanced Solution

The fact that the process fidelity in the previous section drops off after some optimal τ value can be rectified by including loss in both modes of the dual rail qubits in Figs. 6.1 and 6.3, not just within the interaction region, as shown in Figs. 6.30 and 6.31. That is, consider the state $c_{00}|HH\rangle + c_{01}|HV\rangle + c_{10}|VH\rangle + c_{11}|VV\rangle$ incident on Fig. 6.1 or 6.3. The amplitude of $|HH\rangle$ is independent of τ, however the amplitudes for $|HV\rangle, |VH\rangle$ and $|VV\rangle$ approach 0 as $\tau \to \infty$, with $|VV\rangle$ dropping off the fastest. This results in our output density matrix having a relatively large $|HH\rangle\langle HH|$ term. If we include loss in the horizontal modes, each term in the output density matrix will fall off at the same rate, thus increasing the process fidelity as τ increases. Including loss in the horizontal mode will result in the success probability decreasing at a faster rate.

Since the photons in the horizontal modes in Fig. 6.1 and 6.3 never interact with any other photons, there is only ever 0 or 1 photon in these modes. Given that the initial density matrix for one of the horizontal modes is $c_{00}(t)|0\rangle\langle 0| + c_{01}(t)|0\rangle\langle 1| + c_{10}(t)|1\rangle\langle 0| + c_{11}(t)|1\rangle\langle 1|$, where $c_{00} + c_{11} = 1$, we can work out what the density matrix looks like after a time t with single photon loss of strength γ_1 by using Eqn. 2.59 in Section 2.1.7 with n set to 1:

$$\rho(t) = \left(c_{00} + c_{11}\left(1 - e^{-\gamma_1 t}\right)\right)|0\rangle\langle 0| + e^{-\gamma_1 t/2}\left(c_{01}|0\rangle\langle 1| + c_{10}|1\rangle\langle 0|\right) + c_{11}e^{-\gamma_1 t}. \quad (6.98)$$

In terms of a quantum operation $\mathcal{E}_H$ this is:

$$\mathcal{E}_H\left(|a\rangle\langle b|\right) = \kappa^{(1)}_{ab}|a\rangle\langle b| + \kappa^{(2)}_{ab}|a-1\rangle\langle b-1| \quad (6.99)$$

where $\kappa^{(1)}_{00} = 1$, $\kappa^{(1)}_{01} = \kappa^{(1)}_{10} = e^{-\tau/2}$, $\kappa^{(1)}_{11} = e^{-\tau}$, $\kappa^{(2)}_{00} = \kappa^{(2)}_{01} = \kappa^{(2)}_{10} = 0$, $\kappa^{(2)}_{11} = 1 - e^{-\tau}$ and we have re-scaled t as before: $t = \tau/\gamma_1$. Applying this to two horizontally polarised modes gives:

$$\begin{aligned}\mathcal{E}_H\left(|ab\rangle\langle cd|\right) &= \left(\kappa^{(1)}_{ac}|a\rangle\langle c| + \kappa^{(2)}_{ac}|a-1\rangle\langle c-1|\right) \otimes \left(\kappa^{(1)}_{bd}|b\rangle\langle d| + \kappa^{(2)}_{bd}|b-1\rangle\langle d-1|\right)\\ &= \kappa^{(1)}_{ac}\kappa^{(1)}_{bd}|a,\, b\rangle\langle c,\, d| + \kappa^{(1)}_{ac}\kappa^{(2)}_{bd}|a,\, b-1\rangle\langle c,\, d-1| \quad (6.100)\\ &+ \kappa^{(2)}_{ac}\kappa^{(1)}_{bd}|a-1,\, b\rangle\langle c-1,\, d| + \kappa^{(2)}_{ac}\kappa^{(2)}_{bd}|a-1,\, b-1\rangle\langle c-1,\, d-1|.\end{aligned}$$

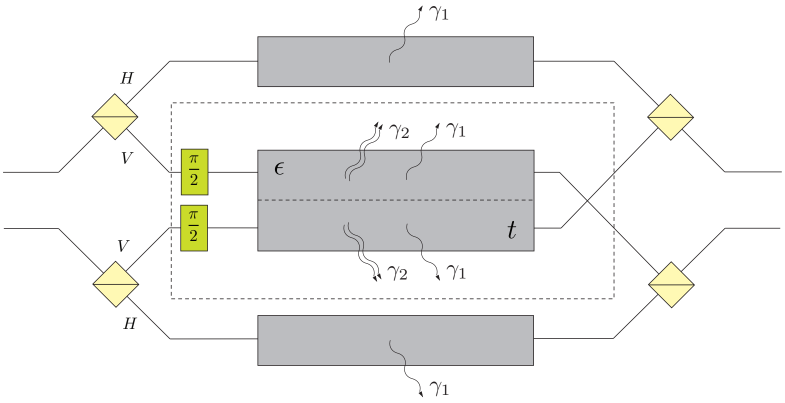

Figure 6.30: Incorporating loss on the horizontal modes in Fig. 6.1 to *balance* the system.

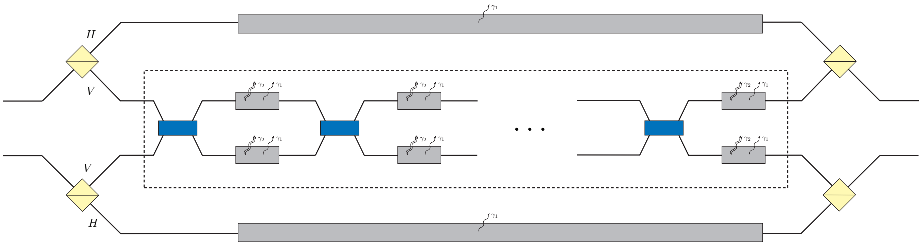

Figure 6.31: Incorporating loss on the horizontal modes in Fig. 6.3 to *balance* the system.

With this in mind, the output density matrix in Eqn. 6.83 can be modified to include single photon loss on the horizontal modes:

$$\rho_{\text{out}} = \sum_{a,b,c,d=0}^{1} |\chi_{ab}\rangle\langle\chi_{cd}| \otimes \mathcal{E}_H\left(|\overline{ab}\rangle\langle\overline{cd}|\right) \otimes \mathcal{E}\left(|ab\rangle\langle cd|\right). \tag{6.101}$$

This is the output density matrix for both Fig. 6.30 and Fig. 6.31.

We can expand this using Eqn. 6.100

$$\begin{aligned}\rho_{\text{out}} = &\sum_{a,b,c,d=0}^{1} |\chi_{ab}\rangle\langle\chi_{cd}| \otimes \kappa^{(1)}_{\overline{ac}}\kappa^{(1)}_{\overline{bd}} |\overline{ab}\rangle\langle\overline{cd}| \otimes \mathcal{E}\left(|ab\rangle\langle cd|\right) \\ &+ \sum_{a,c=0}^{1} |\chi_{a0}\rangle\langle\chi_{c0}| \otimes \kappa^{(1)}_{\overline{ac}}\kappa^{(2)}_{11} |\overline{a}0\rangle\langle\overline{c}0| \otimes \mathcal{E}\left(|a0\rangle\langle c0|\right) \\ &+ \sum_{b,d=0}^{1} |\chi_{0b}\rangle\langle\chi_{0d}| \otimes \kappa^{(2)}_{11}\kappa^{(1)}_{\overline{bd}} |0\overline{b}\rangle\langle0\overline{d}| \otimes \mathcal{E}\left(|0b\rangle\langle0d|\right) \\ &+ |\chi_{00}\rangle\langle\chi_{00}| \otimes \left(\kappa^{(2)}_{11}\right)^2 |00\rangle\langle00| \otimes \mathcal{E}\left(|00\rangle\langle00|\right).\end{aligned} \tag{6.102}$$

After detecting modes 2 and 3 in the ± basis Eqn. 6.101 becomes

$$\begin{aligned}
\rho_{\text{out}}^{\alpha\beta} &= \sum_{a,b,c,d=0}^{1} |\chi_{ab}\rangle\langle\chi_{cd}| \otimes \operatorname{Tr}\left[M^{\alpha\beta}\Big(\mathcal{E}_H\left(|\overline{ab}\rangle\langle\overline{cd}|\right) \otimes \mathcal{E}\left(|ab\rangle\langle cd|\right)\Big)\right] \qquad (6.103)\\
&= \frac{1}{4}\sum_{\substack{a,b,c,d,\\ s,t,u,v}=0}^{1} (-1)^{\alpha(s+u)\beta(t+v)}\, |\chi_{ab}\rangle\langle\chi_{cd}|\langle\overline{uv}|\mathcal{E}_H\left(|\overline{ab}\rangle\langle\overline{cd}|\right)|\overline{st}\rangle\\
&\qquad\qquad\qquad\qquad \times \langle uv|\mathcal{E}\left(|ab\rangle\langle cd|\right)|st\rangle\\
&= \frac{1}{4}\sum_{s,t,u,v=0}^{1} (-1)^{\alpha(s+u)\beta(t+v)}\, \langle\overline{uv}uv|\rho_{\text{out}}|\overline{st}st\rangle
\end{aligned}$$

where $M^{\alpha\beta}$ is given in Eqn. 6.85. Using Eqn. 6.102 we find

$$\rho_{\text{out}}^{\alpha\beta} = \frac{1}{4}\sum_{a,b,c,d=0}^{1} (-1)^{\alpha(a+c)\beta(b+d)}\, |\chi_{ab}\rangle\langle\chi_{cd}|\kappa_{\overline{ac}}^{(1)}\kappa_{\overline{bd}}^{(1)}\langle ab|\mathcal{E}\left(|ab\rangle\langle cd|\right)|cd\rangle, \quad (6.104)$$

since $|\overline{st}st\rangle, |\overline{uv}uv\rangle \in \{|0011\rangle, |0110\rangle, |1001\rangle, |1100\rangle\}$ and $\mathcal{E}$ transforms terms to a sum of terms with equal or lower photon number. For instance, consider

$$\begin{aligned}
&\langle\overline{uv}uv|\sum_{a,c=0}^{1} |\overline{a}0\rangle\langle\overline{c}0| \otimes \mathcal{E}\left(|a0\rangle\langle c0|\right)|\overline{st}st\rangle\\
&= \langle\overline{uv}uv||10\rangle\langle 10| \otimes \mathcal{E}\left(|00\rangle\langle 00|\right) + |10\rangle\langle 00| \otimes \mathcal{E}\left(|00\rangle\langle 10|\right)\\
&\quad + |00\rangle\langle 10| \otimes \mathcal{E}\left(|10\rangle\langle 00|\right) + |00\rangle\langle 00| \otimes \mathcal{E}\left(|10\rangle\langle 10|\right)|\overline{st}st\rangle\\
&= 0
\end{aligned}$$

where $\mathcal{E}\left(|00\rangle\langle 00|\right) = |00\rangle\langle 00|$, $\mathcal{E}\left(|10\rangle\langle 00|\right)$ is a sum of the terms $|00\rangle\langle 00|$, $|10\rangle\langle 00|$ and $|01\rangle\langle 00|$, $\mathcal{E}\left(|00\rangle\langle 10|\right)$ is a sum of the terms $|00\rangle\langle 00|$, $|00\rangle\langle 10|$ and $|00\rangle\langle 01|$ and $\mathcal{E}\left(|10\rangle\langle 10|\right)$ is a sum of the terms $|00\rangle\langle 00|$, $|10\rangle\langle 00|$, $|01\rangle\langle 00|$, $|00\rangle\langle 10|$, $|00\rangle\langle 01|$, $|01\rangle\langle 01|$, $|01\rangle\langle 10|$, $|10\rangle\langle 01|$ and $|10\rangle\langle 10|$. This is true for all possible $\langle\overline{uv}uv|$ and $|\overline{st}st\rangle$.

Notice that $\rho_{\text{out}}^{\alpha\beta}$ shown in Eqn. 6.104 is equivalent to $\rho_{\text{out}}^{\alpha\beta}$ in Eqn. 6.86 up to the the factor $\kappa_{\overline{ac}}^{(1)}\kappa_{\overline{bd}}^{(1)}$. This mean we can proceed with the computation basis measurement of modes 1 and 4 and the calculation of the process fidelity and probability of success as before by just including the factor $\kappa_{\overline{ac}}^{(1)}\kappa_{\overline{bd}}^{(1)}$.

The new probability of success will be

$$P_{\text{av}}^{\text{B}} = \frac{1}{4}\sum_{a,b=0}^{1} \kappa_{\overline{aa}}^{(1)}\kappa_{\overline{bb}}^{(1)}\langle ab|\mathcal{E}\left(|ab\rangle\langle ab|\right)|ab\rangle, \qquad (6.105)$$

the normalised output density matrix, after the ± and computation basis measurements is given by

$$\rho_{\text{out}}^{\text{B}} = \frac{\frac{1}{4}\sum_{a,b,c,d}\kappa_{\overline{ac}}^{(1)}\kappa_{\overline{bd}}^{(1)}\langle ab|\mathcal{E}\left(|ab\rangle\langle cd|\right)|cd\rangle|\tilde{\eta}_{ab}\rangle\langle\tilde{\eta}_{cd}|}{\sum_{a,b}\kappa_{\overline{aa}}^{(1)}\kappa_{\overline{bb}}^{(1)}\langle ab|\mathcal{E}\left(|ab\rangle\langle ab|\right)|ab\rangle} \qquad (6.106)$$

and the process fidelity is given by

$$F_{\text{pro}}^{\text{B}} = \frac{\frac{1}{4}\sum_{a,b,c,d}(-1)^{ab+cd}\,\kappa_{\overline{ac}}^{(1)}\kappa_{\overline{bd}}^{(1)}\langle ab|\mathcal{E}\left(|ab\rangle\langle cd|\right)|cd\rangle}{\sum_{a,b}\kappa_{\overline{aa}}^{(1)}\kappa_{\overline{bb}}^{(1)}\langle ab|\mathcal{E}\left(|ab\rangle\langle ab|\right)|ab\rangle}. \tag{6.107}$$

We calculate analytical expressions for the process fidelity $F_{\text{pro}}^{\text{B}}$ and the success probability $P_{\text{av}}^{\text{B}}$and plot them in Figs. 6.32–6.44 for both the continuous interaction case in Section 6.1 and the beam splitter case in Section 6.2.

In Figs. 6.32 and 6.33 we compare the balanced encoded results in Eqns. 6.105 and 6.107 with the unbalanced encoded results in Eqns. 6.91 and 6.94 and the unencoded result in Eqn. 6.63 for both the continuous interaction and the beam splitter case. In both cases, once we include loss in the horizontal mode, the process fidelity increases with τ, not dropping off after some optimal τ. As a consequence, the success probability falls off faster than the unbalanced encoded case.

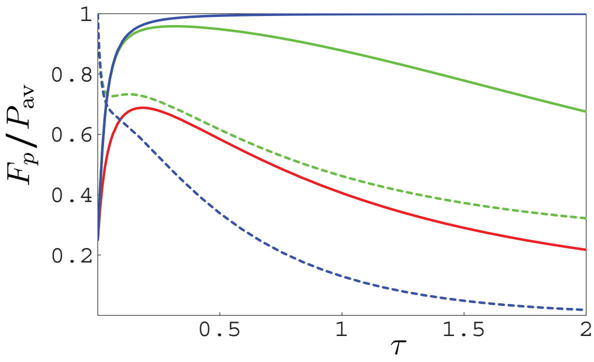

Figure 6.32: The process fidelity F_{pro} (solid lines) and probability of success P_{av} (dashed lines) for the continuous interaction case. Here we consider the $\gamma = 100$ case. The Red curve represents the no encoding case of Section 6.3, the Green curves represent the encoding case of Section 6.4.1 and the Blue curves represent the encoding case with single photon loss in the horizontal mode from Eqns. 6.105 and 6.107.

In Figs. 6.34 and 6.35 the process fidelity $F_{\text{pro}}^{\text{B}}$ and success probability P_{av}^{B} are shown for increasing γ. As we would expect, for a given τ the process fidelity increases with γ. The success probability dips to approximately 3/4 as in the unbalanced encoded case shown in Figs. 6.24 and 6.25. As τ increases the success probability also approaches 1/4.

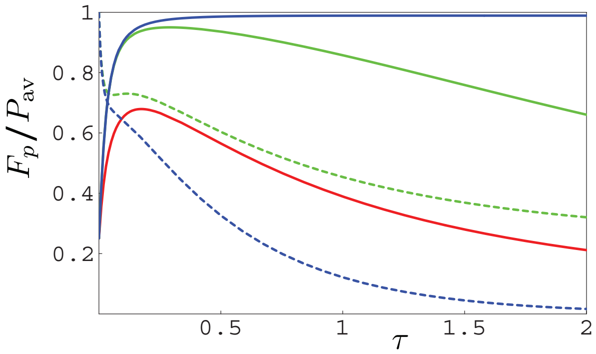

Figure 6.33: The process fidelity F_{pro} (solid lines) and probability of success P_{av} (dashed lines) for the beam splitter case. Here we consider the 19 beam splitter, $\gamma = 100$ case. The Red curve represents the no encoding case of Section 6.3, the Green curves represent the encoding case of Section 6.4.1 and the Blue curves represent the encoding case with single photon loss in the horizontal mode from Eqns. 6.105 and 6.107.

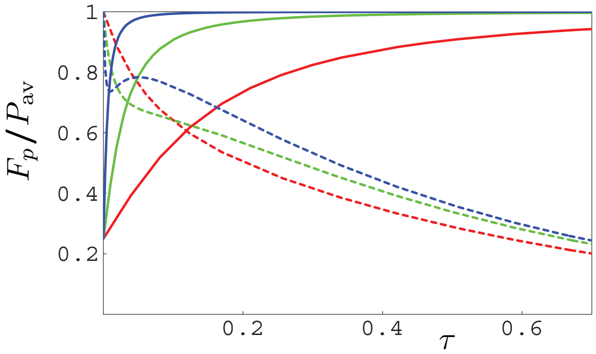

Figure 6.34: The process fidelity $F^{\text{B}}_{\text{pro}}$ (solid lines) and probability of success P^{B}_{av} (dashed lines) for the continuous interaction case with single photon loss in the horizontal mode. The Red curves represent $\gamma = 20$, the Green curves represent $\gamma = 100$ and the Blue curves represent $\gamma = 500$.

In Figs. 6.36 and 6.37 we show how the continuous interaction case compares to a particular number beam splitter case as we vary γ. As we increase γ, we need more beam splitters to approach the continuous interaction case.

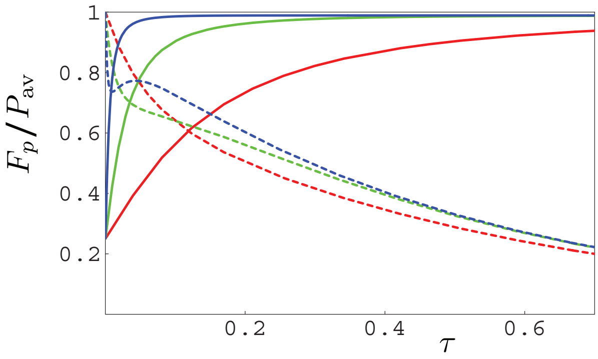

Figure 6.35: The process fidelity $F^{\text{B}}_{\text{pro}}$ (solid lines) and probability of success P^{B}_{av} (dashed lines) for the beam splitter case with single photon loss in the horizontal mode. Here we consider the 19 beam splitter case. The Red curves represent $\gamma = 20$, the Green curves represent $\gamma = 100$ and the Blue curves represent $\gamma = 500$.

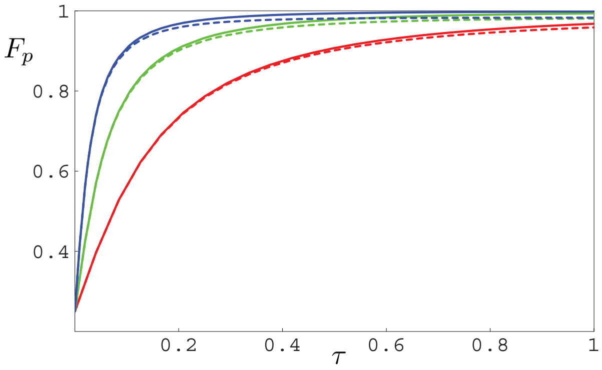

Figure 6.36: The process fidelity $F^{\text{B}}_{\text{pro}}$ for both the continuous interaction case (solid lines) and the beam splitter case (dashed lines). Here we consider the 15 beam splitter case. The Red curves represent $\gamma = 20$, the Green curves represent $\gamma = 50$ and the Blue curves represent $\gamma = 100$.

In Fig. 6.38 we compare the continuous interaction case with the beam splitter case for a particular γ. As we increase the number of beam splitters, the beam splitter process fidelity approaches the continuous interaction case faster than the probability of success.

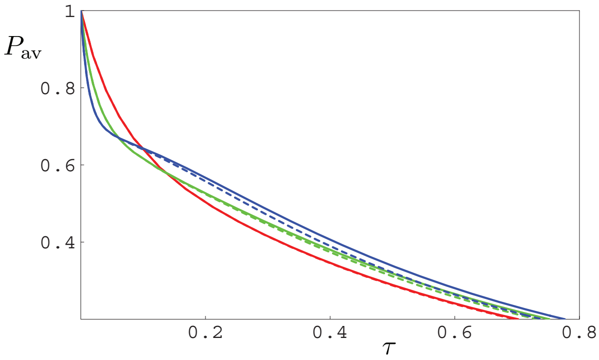

Figure 6.37: The probability of success P_{av}^{B} for both the continuous interaction case (solid lines) and the beam splitter case (dashed lines). Here we consider the 15 beam splitter case. The Red curves represent $\gamma = 20$, the Green curves represent $\gamma = 50$ and the Blue curves represent $\gamma = 100$.

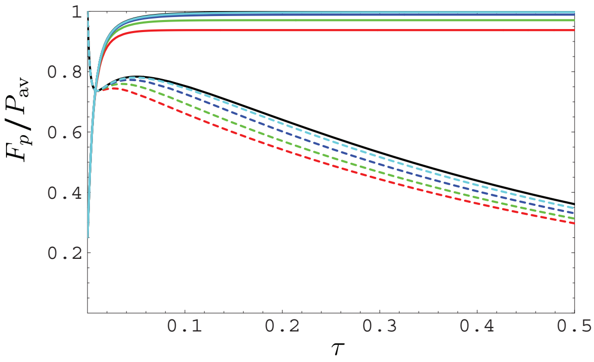

Figure 6.38: The process fidelity $F_{\text{pro}}^{\text{B}}$ and success probability P_{av}^{B} for both the continuous interaction case (solid lines) and the beam splitter case (dashed lines). Here we consider the $\gamma = 500$ case. The Red curves represent 7 beam splitters, the Green curves represent 11 beam splitters, the Blue curves represent 19 beam splitters, the Cyan curves represent 39 beam splitters and the **Black** curves represent the continuous interaction case.

In Figs. 6.39 and 6.40 we show the scaling of the process fidelity $F_{\text{pro}}^{\text{B}}$ and success probability P_{av}^{B} with γ for the continuous interaction case. We find the values of γ and τ for which the success probability is 25%, 50% and 64% and calculate the corresponding process fidelity, shown as part (a) in Fig. 6.39. In a similar way, we find the values of γ and τ for which the process fidelity is 99.9% and calculate the corresponding success probability, shown as part (b) in Fig. 6.39. Notice that a process fidelity of 99.9% is attainable for all γ, although some γ values result in a success probability of approximately 0. The success probability reaches a peak value after it dips to 3/4, as can be seen when $\gamma = 500$ in Figs 6.34 and 6.35. If there is insufficient two photon absorption, the the peak in success probability is not directly visible, such is the case for $\gamma \lesssim 250$. The peak success probability in these cases can be found by looking at the first and second derivative, with respect to τ. In part (c) in Fig. 6.39, we show the maximum success probability and corresponding process fidelity for $\gamma > 250$. Notice that the success probability curves from parts (b) and (c) converge for large γ. This is magnified in Fig. 6.40.

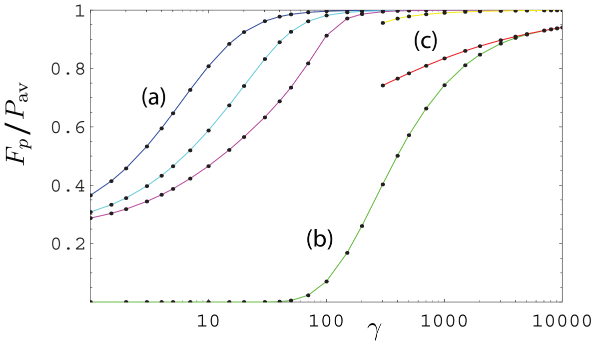

Figure 6.39: The scaling of the process fidelity $F^{\rm B}_{\rm pro}$ and success probability $P^{\rm B}_{\rm av}$ with γ for the continuous interaction case (separate optimisation for each point shown). Part (a) shows $F^{\rm B}_{\rm pro}$ for $P^{\rm B}_{\rm av} = 25\%$ (Blue), $P^{\rm B}_{\rm av} = 50\%$ (Cyan) and $P^{\rm B}_{\rm av} = 64\%$ (Magenta). Part (b) shows $P^{\rm B}_{\rm av}$ for $F^{\rm B}_{\rm pro} = 99.9\%$. Part (c) shows maximum success probability $P^{\rm B}_{\rm av}$ in Red and the corresponding process fidelity $F^{\rm B}_{\rm pro}$ in Yellow.

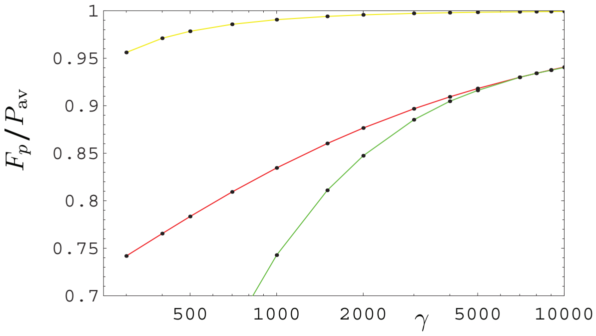

Figure 6.40: The scaling of the process fidelity $F^{\rm B}_{\rm pro}$ and success probability $P^{\rm B}_{\rm av}$ with γ for the continuous interaction case (separate optimisation for each point shown). Here we show parts (b) and (c) of Fig. 6.39 magnified. In Green we have $P^{\rm B}_{\rm av}$ for $F^{\rm B}_{\rm pro} = 99.9\%$. In Red we have the maximum success probability $P^{\rm B}_{\rm av}$ and in Yellow we have the corresponding process fidelity $F^{\rm B}_{\rm pro}$.

In part (b) of Fig. 6.39 we showed the success probability for the continuous interaction case, given that the process fidelity was 99.9%. We could have instead considered any process fidelity arbitrarily close to 1. This is not true for the beam splitters case. Depending on the number of beam splitters considered, the process fidelity reaches a maximum, not necessarily equal 1. This is shown in Fig. 6.41. Notice that a process fidelity above 99% is only possible if the number of beam splitters is ≥ 23, and a process fidelity above 99.9% is only possible if the number of beam splitters is ≥ 67. The results in the figure are independent of γ. That is, for a given value of γ, the process fidelity will reach the maximum predicted in Fig. 6.41 for some τ value. If we increase the value of γ, the value of τ at which the process fidelity first reaches its maximum will decrease.

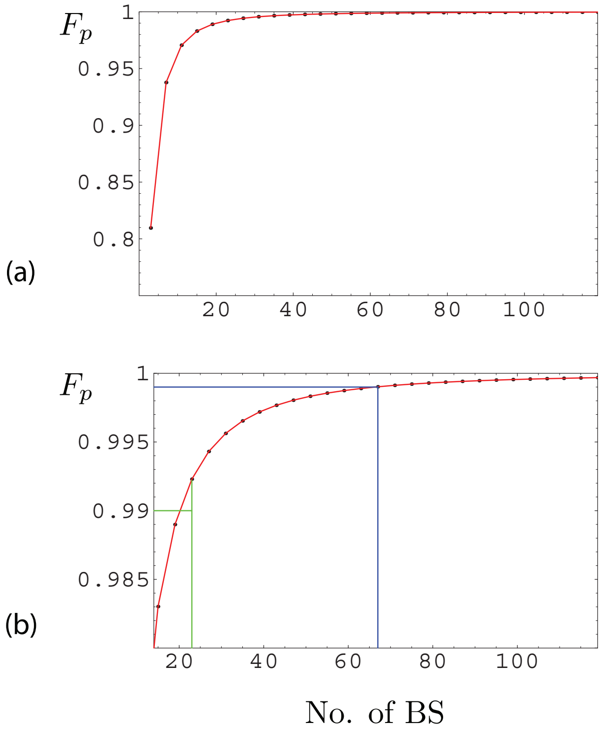

Figure 6.41: In part (a) we show the maximum process fidelity $F_{\text{pro}}^{\text{B}}$ for a given number of beam splitters (separate optimisation for each point shown). In part (b) we magnify part (a) showing when the process fidelity reaches 99% in Greens and when the process fidelity reaches 99.9% in Blue.

The maximum process fidelity for a given number of beam splitters shown in Fig. 6.41 corresponds to the peak process fidelity for the unbalanced encoded beam splitter case in Fig. 6.29(a).

In Fig. 6.42 we find the values of γ and τ for which the process fidelity is 99.9% and calculate the corresponding success probability for both the continuous interaction and beam splitter case.

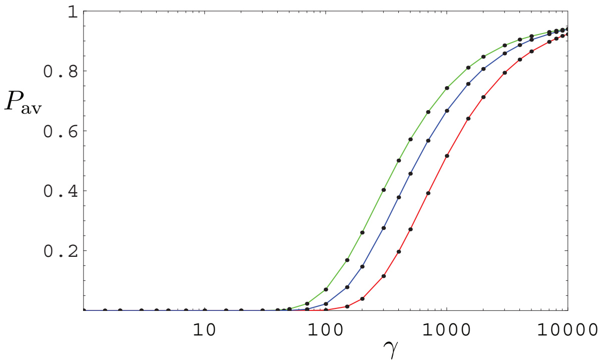

Figure 6.42: The success probability $P^{\mathrm{B}}_{\mathrm{av}}$ for $F^{\mathrm{B}}_{\mathrm{pro}} = 99.9\%$ with the continuous interaction case in Green, the 67 beam splitter case in Red and the 79 beam splitter case in Blue (separate optimisation for each point shown).

In Fig. 6.43 we find the values of γ and τ for which the success probability is 25%, 50% and 64%, respectively, and calculate the corresponding process fidelity, for both the continuous interaction and beam splitter case. Notice that for each of these cases, the process fidelity for the beam splitter case reaches the maximum predicted in Fig. 6.41.

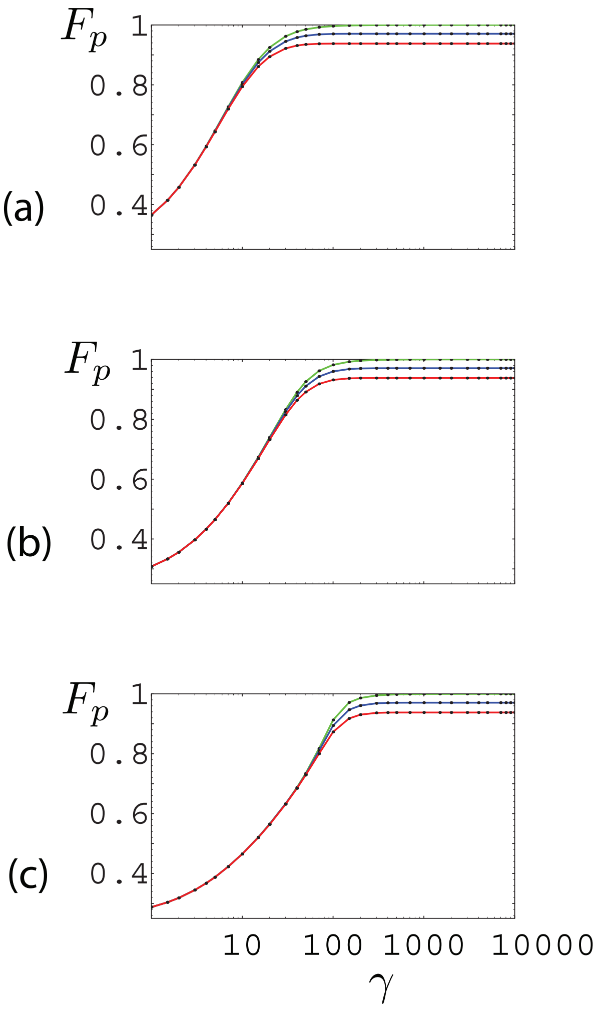

Figure 6.43: The process fidelity $F_{\text{pro}}^{\text{B}}$ for $P_{\text{av}}^{\text{B}} = 25\%$ (part (a)), $P_{\text{av}}^{\text{B}} = 50\%$ (part (b)) and $P_{\text{av}}^{\text{B}} = 64\%$ (part (c)) The continuous interaction case is shown in Green, the 7 beam splitter case is shown in Red and the 11 beam splitter case is shown in Blue (separate optimisation for each point shown).

In Fig. 6.44 we show how the maximum success probability for the continuous interaction case compares with the beam splitters case along with the corresponding process fidelities.

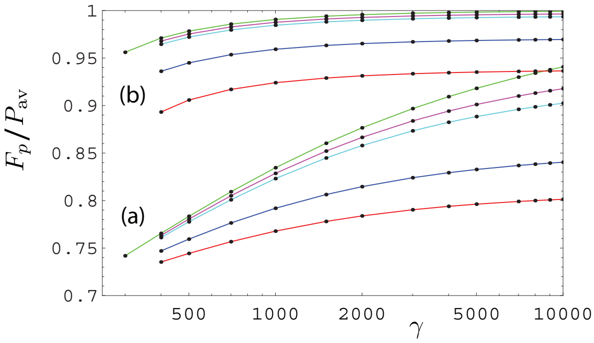

Figure 6.44: The scaling of the process fidelity $F^{\mathrm{B}}_{\mathrm{pro}}$ and success probability $P^{\mathrm{B}}_{\mathrm{av}}$ with γ for both the continuous interaction and beam splitter case (separate optimisation for each point shown). In part (a) we have the maximum success probability $P^{\mathrm{B}}_{\mathrm{av}}$ for the continuous interaction case in Green, the 7 beam splitter case in Red, the 11 beam splitter case in Blue, the 27 beam splitter case in Cyan and the 39 beam splitter case in Magenta. In part (b) we have the corresponding process fidelity $F^{\mathrm{B}}_{\mathrm{pro}}$ for each case.

6.6 LOQC Comparison

In order to gauge the amount of resources our encoded optical Zeno CSIGN gate consumes, we compare our gate with a competing LOQC scheme. The gate suggested by Gilchrist *et al.* in [87], described in Section 2.7.6, uses the same parity encoding presented in Section 6.4 to increase the probability of success above that of the original LOQC scheme [31], as shown in Fig. 2.32.

We compare the two gates by looking at the average number of photons consumed during the gates operation, $\bar{n}$. To do this, we assume that each gate operates above a total failure probability P_0, below which the gate destroys the quantum information. We impose the restriction that the two qubit gate must work with process fidelity of at least 99.9%. For the encoded Zeno gate, this will have implications on what values both P_0 and $\bar{n}$ can take. Since there is no inherent variable controlling the process fidelity for the LOQC scheme, we assume that the linear optics, entangled ancilla and photon detectors are all such that $F_p \geq 99.9\%$.

The probability of failure for the LOQC CNOT gate in Fig. 2.29(b) is $P_0^{(\mathrm{L})} = (3/4)^{n/2}$, where we assume $n/2$ photons are present in both the control and target qubits. This is equivalent to $n/2 = \log\left(P_0^{(\mathrm{L})}\right)/\log(3/4)$. Since each fusion gate in Fig. 2.29(b) operates with a success probability of $1/2$, the two fusion gate system operates with a success probability of $1/4$. We therefore expect 12 photons to be consumed by the two fusion gates, 4 from each of the control, target and ancilla qubits. A parity measurement is made on the control qubit, consuming another $n/2 - 4$ photons. For the LOQC gate we find the average number of photons consumed to be

$$\bar{n}_{\mathrm{L}} = 12 + \frac{n}{2} - 4 = 8 + \frac{n}{2} = 8 + \frac{\log\left(P_0^{(\mathrm{L})}\right)}{\log\left(3/4\right)}. \tag{6.108}$$

For the Zeno gate, each CSIGN attempt shown in Fig. 6.16 consumes 4 photons. If we take the probability of success to be P_{av}, the average number of photons consumed by the Zeno gate is

$$\bar{n}_{\mathrm{Z}} = \frac{4}{P_{\mathrm{av}}}. \tag{6.109}$$

As mentioned in Section 6.4.1, the probability of failure on m redundancy levels of encoding is

$$P_0^{(\mathrm{Z})} = \left(1 - P_{\mathrm{av}}\right)^m. \tag{6.110}$$

If we combine Eqns. 6.109 and 6.110 we have

$$\bar{n}_{\mathrm{Z}} = \frac{4}{1 - \left(P_0^{(\mathrm{Z})}\right)^{\frac{1}{m}}}. \tag{6.111}$$

In Fig. 6.45 we plot both $\bar{n}_{\mathrm{L}}$ and $\bar{n}_{\mathrm{Z}}$ as a function of P_0. For $P_0 \lesssim 10^{-1}$ the Zeno scheme always consumes less resources than the LOQC scheme.

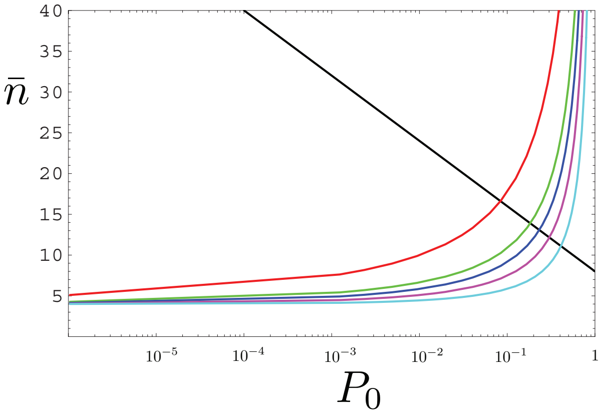

Figure 6.45: The scaling of the average number of photons consumed per gate ($\bar{n}$) with the probability of total failure (P_0). The **Black** line shows $\bar{n}_{\mathrm{L}}$. The Red, Green, Blue, Magenta and Cyan lines show $\bar{n}_{\mathrm{Z}}$ with 8, 4, 3, 2, and 1 levels of redundancy, respectively.

For the Zeno gate, both the process fidelity and success probability are governed by γ and τ. For the unbalanced encoded case in Section 6.4.1 we need to find τ_{opt} for a particular γ that gives the target process fidelity of 99.9%. In this way we find the success probability P_{av}, dictating $\bar{n}_Z$ and $P_0^{(\text{Z})}$ via Eqns. 6.109 and 6.110. For the continuous interaction case, only γ values greater than 4825 give the target fidelity. This is shown in parts (b)–(f) of Fig. 6.46. In Fig. 6.41 we noted that at least 67 beam splitters were necessary for $F_p \geq 99.9\%$ in the balanced case. This is also true for the unbalanced encoded case. In Fig. 6.47 we compare the continuous interaction and beam splitter cases for the unbalanced Zeno gate.

For the balanced case in Section 6.5 we need to find the smallest τ such that the target fidelity is met, for a given γ. This gives the success probability P_{av} which once again dictates $\bar{n}_Z$ and $P_0^{(\text{Z})}$. In the continuous interaction case, for any given γ there is always a τ for which $F_p \geq 99.9\%$, as noted in part (b) of Fig. 6.39. If the number of beam splitters is at least 67 this is also the case, as shown in Fig. 6.41. For a particular level of redundancy, the points $(P_0, \bar{n})$ will always be on the same curves as in Fig. 6.45. The value of γ and whether we are considering the continuous interaction or beam splitter case will govern where on these curves each point is located. This is shown in parts (g)–(k) of Fig. 6.46 and in Fig. 6.48 for the continuous interaction case and in Figs. 6.49 and 6.50 for the beam splitter case.

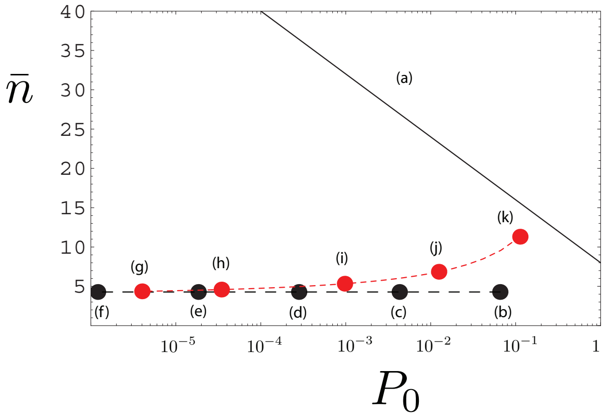

Figure 6.46: The scaling of the average number of photons consumed per gate operation ($\bar{n}$) with the probability of total failure (P_0), for a target fidelity of $F_p = 99.9\%$. The solid **Black** line in part (a) shows the LOQC case. The dashed **Black** line shows the unbalanced Zeno gate with $\gamma = 4825$ and the dashed Red line shows the balanced Zeno gate, both for the continuous interaction case. Point (b) shows the unbalanced case with no redundancy encoding, points (c)–(f) show the unbalanced case with 1–4 levels of redundancy encoding. Points (g)–(k) show the balanced case with 4 levels of redundancy encoding, for γ equal to 5000, 2500, 1000, 500, 250, respectively.

In Fig. 6.46 we show how $\bar{n}$ scales with P_0 for both the unbalanced and balanced continuous interaction case, given a target fidelity of $F_p = 99.9\%$. For the unbalanced case, given that $\gamma = 4825$, we can reduce the total failure probability by increasing the number of levels of redundant encoding, without increasing $\bar{n}$. For the balanced case we see that by increasing γ, we can reduce both the total failure probability and the average number of photons consumed per gate operation. With 4 levels of redundancy encoding, the $\gamma = 250$ case is close to using as many resources as the LOQC scheme.

In Fig. 6.47 we examine the beam splitter case for the unbalanced Zeno gate. As mentioned above, we need at least 67 beam splitters for the target fidelity to be reached. If we consider this minimum number of beam spliiters, we require $\gamma \geq 64000$ for the target fidelity to be reached. We show this in the lower part of Fig. 6.47. Notice that as we increase the number of beam splitters we approach the continuous interaction case. If we reduce γ by an order of magnitude, we would need to increase the number of beam splitters to 135 for the target fidelity to be reached. This is shown in the upper part of Fig. 6.47. As in Fig. 6.46, we can reduce the total failure probability by increasing the number of levels of redundant encoding. Notice that as γ increases the spread between the beam splitter continuous interaction cases decreases.

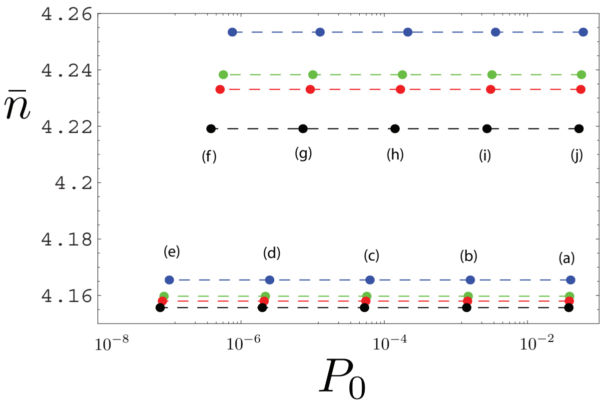

Figure 6.47: The scaling of the average number of photons consumed per gate operation ($\bar{n}$) with the probability of total failure (P_0), for a target fidelity of $F_p = 99.9\%$, for the unbalanced Zeno gate. The lower four lines show the $\gamma = 64000$ case with the continuous interaction case shown in **Black**, the 67 beam splitter case shown in Blue, the 71 beam splitter case shown in Green and the 79 beam splitter case shown in Red. The upper four lines show the $\gamma = 6400$ case with the continuous interaction case shown in **Black**, the 135 beam splitter case shown in Blue, the 147 beam splitter case shown in Green and the 159 beam splitter case shown in Red. Points (a) and (j) show no redundancy encoding. Points (b)–(e) show 1–4 levels of redundancy encoding and points (f)–(i) show 4–1 levels of redundancy encoding.

In Fig. 6.48 we examine the continuous interaction case for the balanced Zeno gate, showing how the number of levels of redundant encoding improves the total failure probability for a given γ. We see that when we have only 1 level of redundancy encoding, for $\gamma = 250$, the Zeno gate uses more resources than the LOQC scheme.

In Figs. 6.49 and 6.50 we examine the beam splitter case for the balanced Zeno gate. As we decrease the number of beam splitters, we move from left to

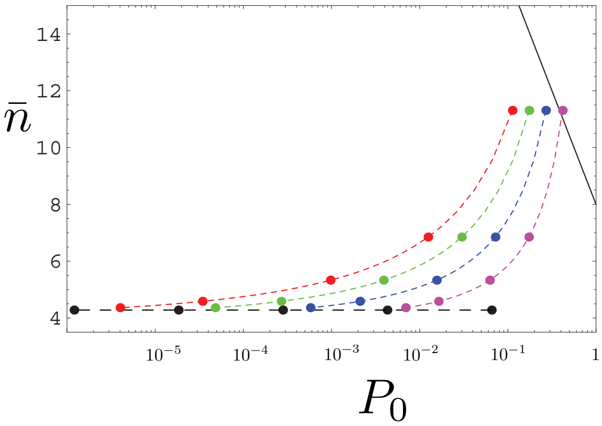

Figure 6.48: The scaling of the average number of photons consumed per gate operation ($\bar{n}$) with the probability of total failure (P_0), for a target fidelity of $F_p = 99.9\%$, for the continuous interaction balanced Zeno gate. The solid **Black** line shows the LOQC case. The dashed **Black** line shows the unbalanced Zeno gate with $\gamma = 4825$. The dashed Magenta, Blue, Green and Red lines show the balanced Zeno gate with 1, 2, 3 and 4 levels of redundancy encoding, respectively. Each of these lines shows the points corresponding to γ=5000, 2500, 1000, 500 and 250, from left to right.

right along the curves in Fig. 6.45, for a given γ. This can be seen in Fig. 6.49 for the case of 4 levels of redundancy encoding. Notice that for the 67 and 79 beam splitter case, when $\gamma = 250$, we use more resources than the LOQC scheme. In Fig. 6.50 we show how the beam splitter case compares to the continuous interaction case when we have 4, 3, 2, and 1 level of redundancy encoding. As we would expect, for each specific case, that is, for either the continuous interaction case or a given number of beam splitters, and a particular γ, $\bar{n}$ is constant as we increase the level of redundancy of encoding, with P_0 decreasing. When we have 4, 3, 2, or 1 level of redundancy encoding in Fig. 6.50, both the 67 and 79 beam splitter case use more resources when $\gamma = 250$.

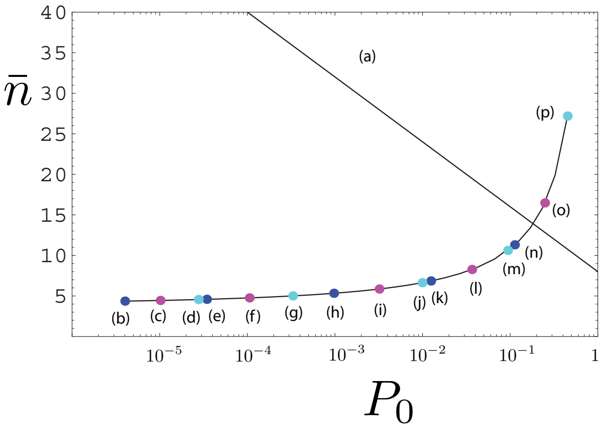

Figure 6.49: The scaling of the average number of photons consumed per gate operation ($\bar{n}$) with the probability of total failure (P_0), for a target fidelity of $F_p = 99.9\%$, for both the continuous interaction and beam splitter balanced Zeno gate with 4 levels of redundancy encoding. The solid **Black** line in part (a) shows the LOQC case. The Blue points represent the continuous interaction case, the Magenta points represent the 79 beam splitter case and the Cyan points represent the 67 beam splitter case. $\gamma = 5000$ for points (b)–(d), $\gamma = 2500$ for points (e)–(g), $\gamma = 1000$ for points (h)–(j), $\gamma = 500$ for points (k)–(m) and $\gamma = 250$ for points (n)–(p).

In Fig. 6.51 we investigate how the number of beam splitters changes the point at which the balanced Zeno gate and the LOQC scheme use the same number of resources. We consider 4 levels of redundancy encoding. As the number of beam splitters decreases, the value of γ at which the resource usage for the two schemes is equal increases. This is shown explicitly in Fig. 6.52.

In Fig. 6.52 we pick out the values of γ for which the balanced Zeno scheme and the LOQC scheme consume the same resources. For a given number of beam splitters, if γ is less than that shown on each curve, then the LOQC scheme uses less resources, if it is greater, the balanced Zeno gate uses less resources. As the the number of beam splitters is increased, we approach the continuous interaction (CI) case, shown on the right. We consider 8, 4, 3, 2 and 1 level of redundancy encoding. As we would expect, as the level of encoding increases for a given number of beam splitters, the value of γ for which the two schemes use the same number of resources decreases. The values of $\bar{n}$ and P_0 for which the resource consumption is the same for both schemes is shown in Table 6.5, for each levels of redundancy encoding.

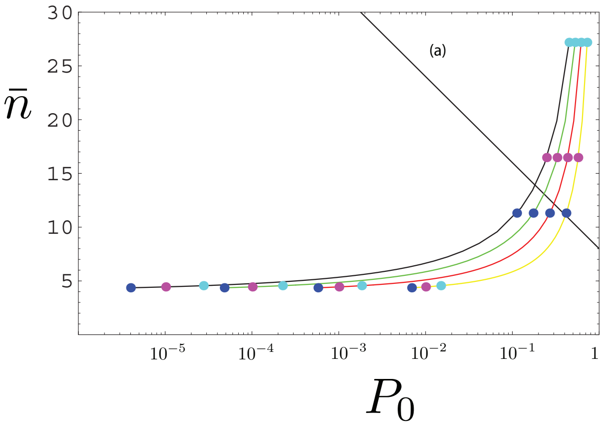

Figure 6.50: The scaling of the average number of photons consumed per gate operation ($\bar{n}$) with the probability of total failure (P_0), for a target fidelity of $F_p = 99.9\%$, for both the continuous interaction and beam splitter balanced Zeno gate. The solid **Black** line in part (a) shows the LOQC case. The Blue points represent the continuous interaction case, the Magenta points represent the 79 beam splitter case and the Cyan points represent the 67 beam splitter case. The **Black**, Green, Red and Yellow curves correspond to 4, 3, 2, and 1 level of redundancy encoding, respectively. On each curve the three left points show the $\gamma = 5000$ case and the three right points show the $\gamma = 250$ case.

No. levels of redundancy	P_0	$\bar{n}$
1	0.412	11.17
2	0.304	12.22
3	0.234	13.13
4	0.184	13.94
8	0.084	16.65

Table 6.5: P_0 and $\bar{n}$ when the balanced Zeno gate and LOQC scheme consume the same resources.

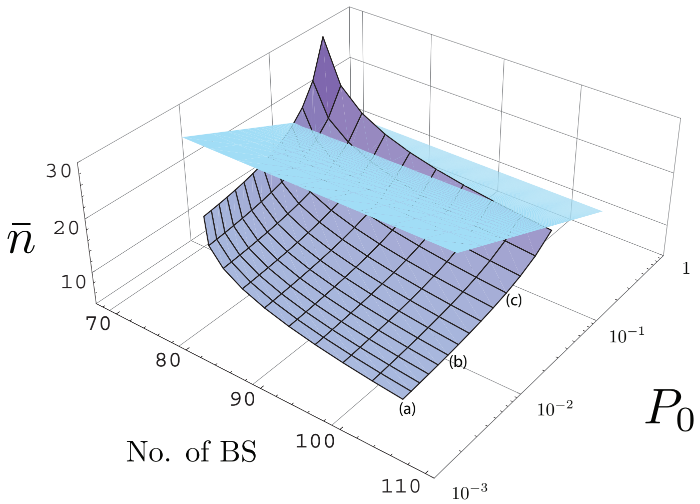

Figure 6.51: The scaling of the average number of photons consumed per gate operation ($\bar{n}$) with both the probability of total failure (P_0) and the number of beam splitters, for a target fidelity of $F_p = 99.9\%$. Here we consider 4 levels of redundancy encoding in the balanced Zeno gate. We consider 10 different beam splitter cases, ranging from the 67 beam splitter case through to the 103 beam splitter case, increasing by increments of 4 beam splitters. Parallel to the "No. of BS" axis we plot lines of constant γ, starting with $\gamma = 250$ at point (a) and increasing by 50 until $\gamma = 900$. Points (b) and (c) show the curves with $\gamma = 500$ and 750, respectively. The Cyan plane shows the LOQC case.

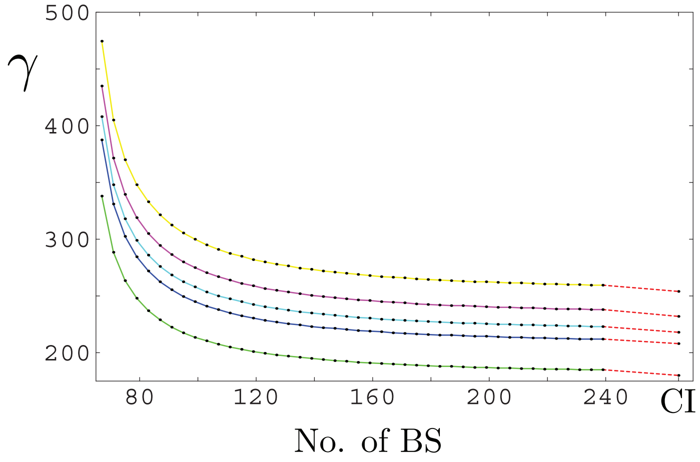

Figure 6.52: The relationship between the number of beam splitters and γ when the resources consumed by the balanced Zeno gate is equal to that consumed by the LOQC scheme. The Green, Blue, Cyan, Magenta and Yellow curves show 8, 4, 3, 2 and 1 level of redundancy encoding, respectively. We consider 44 different beam splitter cases, ranging from the 67 beam splitter case through to the 239 beam splitter case, increasing by increments of 4 beam splitters. The continuous interaction (CI) case is shown on the right for each redundancy level.

Chapter 7

Summary of Results

In this thesis we presented results from three areas of photonic quantum computing.

First, we presented a photon-number QND detector with a success probability that asymptotically approaches 1. This photon-number QND detector detects the presence of a single photon in an arbitrary polarisation state when the input state is a sum of vacuum and multi-photon terms. For the success probability to asymptotically approach 1, we use the entangled resources states $|\mathrm{QND}t_n\rangle$, similar to the $|t_n\rangle$ states. The circuit for this photon-number QND detector is a new type of optical teleporter. When we compare our optical teleporter with the original LOQC teleporter [31], given a success probability of $\left(\frac{n}{n+1}\right)^2$, our teleporter requires n^2-2n-1 less entangling operations in general and $2n-1$ less entangling operations when n is small [83].

Second, we presented results centred around qubus computation [49, 93]. We show a scheme to measure the party of n qubit states. When n is even we require one coherent probe beam, $n+1$ optical displacements and $n(n+2)$ controlled rotations. When n is odd we require one coherent probe beam, $n+2$ optical displacements and $n(n+3)$ controlled rotations. In each case we need to measure the probe beam, either by performing a photon number or homodyne detection. We extended these results, showing a fault tolerant method to measure the parity of n qubits. This scheme required $3n+1$ controlled rotations, $n+1$ ancillary photons, $2n$ probe beam measurements and $n+1$ photon number measurements. A direct breakdown of the Shor fault tolerant circuit [21] into CNOT gates would require $4(2n-1)$ controlled rotations, $2(2n-1)$ probe beam measurements, $2n-1$ ancillary photons and $2n-1$ photon number measurements.

We constructed a three qubit gate that functions as a Toffoli gate 25% of the time and as a controlled-controlled-iY gate 25% of the time. This three qubit gate required one quantum bus probe beam, 14 controlled rotations, 4 optical displacements and a photon number detection of the probe beam. We extended this three qubit to an m qubit gate that functions as an m-qubit Toffoli gate 25% of the time and as an m-qubit controlled iY gate 25%. However, the resources scale exponentially with m, requiring one probe beam, $2m + (m - 1)2^{m-1}$ controlled rotations, 2^{m-1} optical displacements and a photon number detection of the probe beam.

We used single bit teleportations [108] to construct a universal set of gates on qubus logical states, similar to the coherent logic states in [111]. This scheme required 2 controlled rotations to perform arbitrary single qubit gate and 7 controlled rotations to perform a CSIGN gate. This is in contrast to the 8 controlled rotations required for a CSIGN and 8 controlled rotations required for an arbitrary single qubit gate in [111]. We also used single teleportations to construct n qubit polarisation GHZ states, states that can be used to construct cluster states. To construct an n qubit polarisation GHZ states we required $n + 1$ controlled rotations, $n + 1$ single photon ancilla state, 1 photon number detection and n homodyne detections. For both qubus logical gates and GHZ production we showed a method of boosting the fidelity by post-selection.

Third, we presented results centred around the Franson *et al.* optical Zeno gate [50]. We modelled realistic two photon absorption and included realistic single photon loss for this gate, showing that the fidelity of the gate is severely effected by single photons loss. We show that we can increase the fidelity by encoding against single photon loss, using a generalised parity code and using redundancy encoding [87, 48]. We show that by encoding our qubits in such a way, we overcome the effects of single photon loss such that our resource usage is much less than that required for an equivalent LOQC scheme [87].

Bibliography

[1] P. Benioff. The computer as a physical system: A microscopic quantum mechanical Hamiltonian model of computers as represented by Turing machines. *J. Stat. Phys.*, 22:563, 1980.

[2] R.P. Feynman. Simulating physics with computers. *Int. J. Theor. Phys.*, 21:467, 1982.

[3] D. Deutsch. Quantum theory, the Church-Turing principle and the universal quantum computer. *Proc. R. Soc. Lond. A*, 400:97, 1985.

[4] R.P. Feynman. Quantum mechanical computers. *Theor. Phys.*, 16:507, 1986.

[5] D. Deutsch. Quantum computational networks. *Proc. R. Soc. Lond. A*, 425:73, 1989.

[6] D. Deutsch. Rapid solution of problems by quantum computation. *Proc. R. Soc. Lond. A*, 553:73, 1992.

[7] S. Lloyd. A potentially realizable quantum computer. *Science*, 261:1569, 1993.

[8] S. Lloyd. Envisioning a quantum supercomputer. *Science*, 263:695, 1994.

[9] S. Lloyd. Almost any quantum logic gate is universal. *Phys. Rev. Lett.*, 74:4091, 1995.

[10] D.P. DiVincenzo. Two-bit gates are universal for quantum computation. *Phys. Rev. A*, 51:1015, 1995.

[11] P.W. Shor. Algorithms for quantum computation: Discrete logarithms and factoring. In *Proc. 35th Annual Symposium on Foundations of Computer Science*, page 124. IEEE Press, Los Alamitos, CA, 1994. quant-ph/9508027.

[12] L.K. Grover. A fast quantum mechanical algorithm for database search. In *Proc. 28th Annual ACM Symposium on the Theory of Computing*, page 212. AGM Press, New York, 1996. quant-ph/9605043.

[13] L.K. Grover. Quantum mechanics helps in searching for a needle in a haystack. *Phys. Rev. Lett.*, 79:325, 1997.

[14] S. Lloyd. Universal quantum simulators. *Science*, 273:1073, 1996.

[15] C. Zalka. Efficient simulation of quantum systems by quantum computers. *Proc. R. Soc. Lond. A*, 454:313, 1998.

[16] P.W. Shor. Scheme for reducing decoherence in quantum computer memory. *Phys. Rev. A*, 52:R2493, 1995.

[17] A.M. Steane. Error correcting codes in quantum theory. *Phys. Rev. Lett.*, 77:793, 1996.

[18] R. Laflamme, C. Miquel, J.P. Paz, and W.H. Zurek. Perfect quantum error correcting code. *Phys. Rev. Lett.*, 77:198, 1996.

[19] D. Gottesman. Class of quantum error-correctin codes saturating the quantum hamming bound. *Phys. Rev. A*, 54:1862, 1996.

[20] C.H. Bennett, D.P. DiVincenzo, J.A. Smolin, and W.K. Wootters. Mixed-state entanglement and quantum error correction. *Phys. Rev. A*, 54:3824, 1996.

[21] P.W. Shor. Fault-tolerant quantum computation. In *Proc. 37th Annual Symposium on Foundations of Computing*, page 56. IEEE Press, Los Alamitos, CA, 1996. quant-ph/9605011.

[22] J.I. Cirac, T. Pellizzari, and P. Zoller. Enforcing coherent evolution in dissipative quantum dynamics. *Science*, 273:1207, 1996.

[23] W.H. Zurek and R. Laflamme. Quantum logical operations on encoded qubits. *Phys. Rev. Lett.*, 77:4683, 1996.

[24] D.P. DiVincenzo and P.W. Shor. Fault-tolerant error correction with efficient quantum codes. *Phys. Rev. Lett.*, 77:3260, 1996.

[25] J. Preskill. Fault-tolerant quantum computation. quant-ph/9712048, 1997.

[26] D. Gottesman. Theory of fault-tolerant quantum computation. *Phys. Rev. A*, 57:127, 1998.

[27] D.P. DiVincenzo. The physical implementation of quantum computation. *Fortschr. Phys.*, 48:771, 2000.

[28] G.J. Milburn. Quantum optical Fredkin gate. *Phys. Rev. Lett.*, 62:2124, 1989.

[29] Y. Yamamoto, M. Kitagawa, and K. Igeta. Quantum mechanical aspects of optical communication and optical computing. In Y. W. Chan, A. F. Leung, C. N. Yang, and K. Young, editors, *Proceedings of the 3rd Asia Pacific Physics Conference*, page 779. World Scientific, Singapore, 1988.

[30] I.L. Chuang and Y. Yamamoto. Simple quantum computer. *Phys. Rev. A*, 52:3489, 1995.

[31] E. Knill, R. Laflamme, and G.J. Milburn. A scheme for efficient quantum computation with linear optics. *Nature*, 409:46, 2001.

[32] D. Gottesman and I.L. Chuang. Demonstrating the viability of universal quantum computation using teleportation and single- qubit operations. *Nature*, 402:390, November 1999.

[33] E. Knill, R. Laflamme, and G.J. Milburn. Thresholds for linear optics quantum computation. quant-ph/0006120, 2000.

[34] T.B. Pittman, B.C. Jacobs, and J.D. Franson. Probabilistic quantum logic operations using polarizing beam splitters. *Phys. Rev. A*, 64:062311, 2001.

[35] T.C. Ralph, A.G. White, W.J. Munro, and G.J. Milburn. Simple scheme for efficient linear optics quantum gates. *Phys. Rev. A*, 65:012314, 2001.

[36] T.B. Pittman, M.J. Fitch, B.C. Jacobs, and J.D. Franson. Experimental controlled-not logic gate for single photons in the coincidence basis. *Phys. Rev. A*, 68:032316, 2003.

[37] T.C. Ralph, N.K. Langford, T.B. Bell, and A.G. White. Linear optical controlled-not gate in the coincidence basis. *Phys. Rev. A*, 65:062324, 2002.

[38] E. Knill. Bounds on the probability of success of postselected nonlinear sign shifts implemented with linear optics. *Phys. Rev. A*, 68:2003, 2003.

[39] E. Knill. Quantum gates using linear optics and postselection. *Phys. Rev. A*, 66:052306, 2002.

[40] S. Scheel and N. Lütkenhaus. Upper bounds on success probabilities in linear optics. *New J. Phys*, 6:51, 2004.

[41] J. Eisert. Optimising linear optics quantum gates. *Phys. Rev. Lett.*, 95:040502, 2005.

[42] M. Silva, M. Rötteler, and C. Zalka. Thresholds for linear optics quantum computing with photon loss at the detectors. *Phys. Rev. A*, 72:032307, 2005.

[43] A.J.F. Hayes, A. Gilchrist, C. R. Myers, and T. C. Ralph. Utilizing encoding in scalable linear optics quantum computing. *J. Opt. B: Quantum Semiclass. Opt.*, 6:533, 2004.

[44] R. Raussendorf and H.J. Briegel. A one-way quantum computer. *Phys. Rev. A*, 86:5188, 2001.

[45] N. Yoran and B. Reznik. Deterministic linear optics quantum computation with single photon qubits. *Phys. Rev. Lett.*, 91:037903, 2003.

[46] M.A. Nielsen. Optical quantum computation using cluster states. *Phys. Rev. Lett.*, 93:040503, 2004.

[47] D.E. Brown and T. Rudolph. Resource-efficient linear optical quantum computation. *Phys. Rev. Lett.*, 95:010501, 2005.

[48] T.C. Ralph, A.J.F. Hayes, and A. Gilchrist. Loss-tolerant optical qubits. *Phys. Rev. Lett.*, 95:100501, 2000.

[49] K. Nemoto and W.J. Munro. Nearly deterministic linear optical controlled-not gate. *Phys. Rev. Lett.*, 93:250502, 2004.

[50] J.D. Franson, B.C. Jacobs, and T.B. Pittman. Quantum computing using single photons and the Zeno effect. *Phys. Rev. A*, 70:062302, 2004.

[51] C.R. Myers and R. Laflamme. Linear optics quantum computation: an overview. In G. Casati, D.L. Shepelyansky, and P. Zoller, editors, *Proc. International School of Physics "Enrico Fermi", Course CLXII on "Quantum Computers, Algorithms and Chaos", Varenna, Italy*, page 45. Societa Italiana di Fisica Bologna-Italy, 2006. quant-ph/0512104.

[52] C.R. Myers, M. Silva, K. Nemoto, and W. J. Munro. Stabilizer quantum error correction with quantum bus computation. *Phys. Rev. A*, 76:012303, 2007.

[53] C.R. Myers and A. Gilchrist. Photon-loss-tolerant Zeno controlled-sign gate. *Phys. Rev. A*, 75:052339, 2007.

[54] J.D. Jackson. *Classical Electrodynamics*. Wiley, 3rd edition, 1999.

[55] D.F. Walls and G.J. Milburn. *Quantum Optics*. Springer-Verlag, Berlin, 1994.

[56] M.O. Scully and M.S. Zubairy. *Quantum Optics*. Cambridge University Press, Cambridge, 1997.

[57] C.W. Gardiner and P. Zoller. *Quantum Noise*. Springer-Verlag, Berlin, 2000.

[58] U.M. Titulaer and R.J. Glauber. Density operators for coherent fields. *Phys. Rev.*, 145:1041, 1966.

[59] P.P. Rohde and T.C. Ralph. Frequency and temporal effects in linear optical quantum computing. *Phys. Rev. A*, 71:032320, 2005.

[60] R.J. Glauber. Coherent and incoherent states of the radiation field. *Phys. Rev.*, 131:2766, 1963.

[61] W.H. Louisell. *Quantum Statistical Properties of Radiation.* John Wiley & Sons, New York, 1990.

[62] S.M. Barnett and P.M. Radmore. *Methods in Theoretical Quantum Optics.* Clarendon Press, Oxford, 1997.

[63] S.D. Barrett, P. Kok, K. Nemoto, R.G. Beausoleil, W.J. Munro, and T.P. Spiller. Symmetry analyzer for nondestructive Bell-state detection using weak nonlinearities. *Phys. Rev. A*, 71:060302(R), 2005.

[64] H.-P. Breuer and F. Petruccione. *The Theory of Open Quantum Systems.* Oxford University Press, Oxford, 2002.

[65] K.J. McNeil and D.F. Walls. A master equation approach to nonlinear optics. *J. Phys. A: Math., Nucl. Gen.*, 7(5):617, 1974.

[66] V.V. Dodonov and S.S. Mizrahi. Competition between one- and two-photon absorption processes. *J. Phys. A: Math. Gen.*, 30:2915, 1997.

[67] H.J. Carmichael. *Statistical Methods in Quantum Optics 1.* Springer-Verlag, Berlin, 2002.

[68] S.M.D. Phoenix. Wave-packet evolution in the damped oscillator. *Phys. Rev. A*, 41:5132, 1990.

[69] H.D. Simaan and R. Loudon. Quantum statistics of single-beam two-photon absorption. *J. Phys. A: Math., Nucl. Gen.*, 8(4):539, 1975.

[70] H.D. Simaan and R. Loudon. Off-diagonal density matrix for single-beam two-photon absorbed light. *J. Phys. A: Math., Nucl. Gen.*, 1(2):435, 1978.

[71] L. Gilles and P.L. Knight. Two-photon absorption and nonclassical states of light. *Phys. Rev. A*, 48:1582, 1993.

[72] R.W. Boyd. *Nonlinear Optics.* Academic Press, Amsterdam, 2nd edition, 2003.

[73] A. Gilchrist, N.K. Langford, and M.A. Nielsen. Distance measures to compare real and ideal quantum processes. *Phys. Rev. A*, 71:062310, 2005.

[74] A. Jamiołkowski. Linear transformations which preserve trace and positive semidefiniteness of operators. *Rep. Math. Phys.*, 3:275, 1972.

[75] M. Horodecki, P. Horodecki, and R. Horodecki. General teleportation channel, singlet fraction, and quasidistillation. *Phys. Rev. A*, 60:1888, 1999.

[76] N. Lütkenhaus, J. Calsamiglia, and K.A. Suominen. Bell measurements for teleportation. *Phys. Rev. A*, 59:3295, 1999.

[77] M. Reck, A. Zeilinger, H.J. Bernstein, and P. Bertani. Experimental realization of any discrete unitary operator. *Phys. Rev. Lett.*, 73:58, 1998.

[78] N.J. Cerf, C. Adami, and P.G. Kwiat. Optical simulation of quantum logic. *Phys. Rev. A*, 57:R1477, 1998.

[79] M.A. Nielsen and I.L.. Chuang. *Quantum Computation and Quantum Information.* Cambridge University Press, 2000.

[80] C.H. Bennett, G. Brassard, C. Crépeau, R. Jozsa, A. Peres, and W. Wootters. Teleporting an uknown quantum state via dual classical and Einstein-Podolsky-Rosem channels. *Phys. Rev. Lett.*, 70(13):1895, March 1993.

[81] E. Knill, R. Laflamme, and G.J. Milburn. Efficient linear optics quantum computation. quant-ph/0006088, 2000.

[82] E. Knill, R. Laflamme, and G.J. Milburn. A scheme for efficient quantum computation with linear optics: Supplementary information. *Nature*, 409:46, January 2001.

[83] J.D. Franson, M.M. Donegan, and B.C. Jacobs. Generation of entangled ancilla states for use in linear optics quantum computing. *Phys. Rev. A*, 69:52328, 2004.

[84] E. Knill. Linear optics quantum computation: Overview lecture and lectures i-v. In *ITP Program on Quantum Information: Entanglement, Decoherence and Chaos*, page 779, 2001. http://online.itp.ucsb.edu/online/qinfo01.

[85] E. Knill and R. Laflamme. Theory of quantum error-correcting codes. *Phys. Rev. A*, 55:900, 1997.

[86] D. Gottesman. *Stabilizer Codes and Quantum Error Correction.* PhD thesis, California Institute of Technology, Pasadena, CA, 1997. quant-ph/9705052.

[87] A. Gilchrist, A.J.F. Hayes, and T.C. Ralph. Efficient parity encoded optical quantum computing. *Phys. Rev. A*, 75:052328, 2007.

[88] P. Kok, H. Lee, and J.P. Dowling. Single-photon quantum-non-demolition detectors constructed with linear optics and projective measurements. *Phys. Rev. A*, 66:063814, 2002.

[89] C.M. Caves, K.S. Thorne, R.W.D Drever, V.D. Sandberg, and M. Zimmermann. On the measurement of a weak classical force coupled to a quantum-mechanical oscillator. I. Issues of principle. *Rev. Mod. Phys.*, 52(2):341, April 1980.

[90] V.B. Braginsky and F.Ya. Khalili. *Quantum Measurement.* Cambridge University Press, Cambridge, 1992.

[91] G.J. Pryde, J.L. O'Brien, A.G. White, S.D. Bartlett, and T.C. Ralph. Measuring a photonic qubit without destroying it. *Phys. Rev. Lett.*, 92:190402, 2004.

[92] W.J. Munro, K. Nemoto, and T.P. Spiller. Weak nonlinearities: A new route to optical quantum computation. *New J. Phys*, 7:137, 2005.

[93] T.P. Spiller, K. Nemoto, S.L. Braunstein, W.J. Munro, P. van Loock, and G.J. Milburn. Quantum computation by communication. *New J. Phys*, 8:30, 2006.

[94] R.W. Boyd. Order-of-magnitude estimates of the nonlinear optical susceptibility. *J. Mod. Opt.*, 46:367, 1999.

[95] N. Imoto, H.A. Haus, and Y. Yamamoto. Quantum nondemolition measurement of the photon number via the optical Kerr effect. *Phys. Rev. A*, 32:2287, 1985.

[96] H. Schmidt and A. Imamoğlu. Giant Kerr nonlinearities obtained by electromagnetically induced transparency. *Opt. Lett.*, 21:1936, 1996.

[97] S. E. Harris and L.V. Hau. Nonlinear optics at low light levels. *Phys. Rev. Lett.*, 82:4611, 1999.

[98] J.H. Shapiro and M. Razavi. Continuous-time cross-phase modulation and quantum computation. *New J. Phys*, 9:16, 2007.

[99] W.J. Munro, K. Nemoto, T.P. Spiller, S.D. Barret, P. Kok, and R.G. Beausoleil. Efficient optical quantum information processing. *J. Opt. B: Quantum Semiclass. Opt.*, 7:S135, 2005.

[100] F. Yamaguchi, K Nemoto, and W.J. Munro. Quantum error correction via robust probe modes. *Phys. Rev. A*, 73:060302(R), 2006.

[101] J.D. Franson and S.M. Hendrickson. Optical transparency using interference between two modes of a cavity. *Phys. Rev. A*, 74:053817, 2006.

[102] B. Misra and E.C.G. Sudarshan. The Zeno's paradox in quantum theory. *J. Math. Phys.*, 18:756, 1977.

[103] F.M. Spedalieri, H. Lee, M. Florescu, K.T. Kapale, U. Yurtsever, and J.P. Dowling. Exploiting the quantum Zeno effect to beat photon loss in linear optical quantum information processors. quant-ph/0408026, 2004.

[104] C.K. Hong, Z.Y. Ou, and L. Mandel. Measurement of subpicosecond time intervals between two photons by interference. *Phys. Rev. Lett.*, 59(18):2044, November 1987.

[105] A.M. Steane. Multiple particle interference and quantum error correction. *Proc. Roy. Soc. Lond., Ser. A*, 452:2551, 1996.

[106] J. Fiurášek. Linear-optics quantum Toffoli and Fredkin gates. *Phys. Rev. A*, 73:062313, 2006.

[107] T.C. Ralph, K.J. Resch, and A. Gilchrist. Efficient Toffoli gates using qudits. *Phys. Rev. A*, 75:022313, 2007.

[108] X. Zhou, D.W. Leung, and I.L. Chuang. Methodology for quantum logic gate construction. *Phys. Rev. A*, 62:052316, 2000.

[109] H. Jeong. Using weak nonlinearity under decoherence for macroscopic entanglement generation and quantum computation. *Phys. Rev. A*, 72:034305, 2005.

[110] A. Gilchrist, K. Nemoto, W.J. Munro, T.C. Ralph, S. Glancy, S.L. Braunstein, and G.J. Milburn. Schrödinger cats and their power for quantum information processing. *J. Opt. B: Quantum Semiclass. Opt.*, 6:S828, 2004.

[111] T.C. Ralph, A. Gilchrist, G.J. Milburn, W.J. Munro, and S. Glancy. Quantum computation with optical coherent states. *Phys. Rev. A*, 68:042319, 2003.

[112] A.M. Steane. Overhead and noise threshold of fault-tolerant quantum error correction. *Phys. Rev. A*, 68:042322, 2003.

[113] E. Knill. Scalable quantum computing in the presence of large detected-error rates. *Phys. Rev. A*, 71:042322, 2005.

[114] T.C. Ralph, W.J. Munro, and G.J. Milburn. Quantum computation with coherent states, linear interactions and superposed resources. *Proc. SPIE*, 4917:1, 2002.

[115] M. Hein, W .Dür, J. Eisert, R. Raussendorf, M. Van den Nest, and H.-J. Briegel. Entanglement in graph states and its applications. Lecture notes for the International School of Physics "Enrico Fermi" on "Quantum Computers, Algorithms and Chaos", Varenna, Italy, July, 2005, quant-ph/0602096, 2005.

[116] E.T. Campbell, J. Fitzsimons, S.C. Benjamin, and P. Kok. Efficient growth of complex graph states via imperfect path erasure. quant-ph/0702209, 2007.

[117] G.-S. Jin, Y. Lin, and B. Wu. Generating multiphoton Greenberger-Horne-Zeilinger states with weak cross-Kerr nonlinearity. *Phys. Rev. A*, 75:054302, 2007.

[118] P.G. Kwiat, A.G. White, J.R. Mitchell, O. Nairz, G. Weihs, H. Weinfurter, and A. Zeilinger. High-efficiency quantum interrogation measurements via the quantum Zeno effect. *Phys. Rev. Lett.*, 83:4725, 1999.

[119] H.-W. Lee and J. Kim. Quantum teleportation and Bell's inequality using single-particle entanglement. *Phys. Rev. A*, 63:012305, 2001.

[120] A.P. Lund and T.C. Ralph. Nondeterministic gates for photonic single-rail quantum ligic. *Phys. Rev. A*, 66:032307, 2002.

[121] A. Bandilla. Change of the photon statistics by one-photon absorption and by simultaneous one-photon and two-photon absorption. *Opt. Comm.*, 23(3):299, 1977.

[122] V.V. Dodonov and S.S. Mizrahi. Exact stationary photon distributions due to competition between one- and two-photon absorption and emission. *J. Phys. A: Math. Gen.*, 30:5657, 1997.

[123] E. Kreyszig. *Advanced Engineering Mathematics.* John Wiley & Sons, Inc., Singapore, 8th edition, 1999.

[124] P.M. Leung and T.C. Ralph. Improving the fidelity of optical Zeno gates via distillation. *Phys. Rev. A*, 74:062325, 2005.

[125] J.L. O'Brien, G.J. Pryde, A.G. White, and T.C. Ralph. High-fidelity z-measurement error correction of optical qubits. *Phys. Rev. A*, 71:060303(R), 2005.